Beyond the Confines of the Ore Deposit: Mapping Low Temperature Hydrothermal Alteration Above, Within, and Beneath Carlin-type Gold Deposits

by

Ayesha Doris Ahmed

B.Sc., The University of British Columbia, 2008

A THESIS SUBMITTED IN PARTIAL FULFILLMENT OF THE
REQUIREMENTS FOR THE DEGREE OF

MASTER OF SCIENCE

in

The Faculty of Graduate Studies

(Geological Sciences)

THE UNIVERSITY OF BRITISH COLUMBIA

(Vancouver)

October 2010

ABSTRACT

Multiple analytical techniques were employed to investigate distal patterns in low temperature hydrothermal fluid flow into and out of Carlin-type gold deposits in two study areas: the Leeville deposit and the Shoshone range including the Pipeline, Gold Acres and Elder Creek deposits. Previous studies indicate that gold is hosted in lower Paleozoic carbonate rocks overlain by thick sequences of similarly aged siliciclastic rocks. Patterns in $\delta^{18}O$ depletion (<20‰$_{VSMOW}$), and Au, As, Sb, Hg, Tl, and Te concentrations in lower Paleozoic carbonate rock identified three disconnected lateral fluid pathways into the Pipeline deposit: a main conduit providing gold-bearing fluid to the main ore body, the Abyss fault located ~300m below the main ore zone, and the RMT located underneath the Abyss fault. Following gold precipitation in the Pipeline deposit, gold-depleted fluids were likely exhausted laterally, at least initially, along the same structures as those that allowed fluid to enter the deposit. Upon intersecting the RMT fault, fluid either exploited the fault to reach surface, or transgressed overlying siliciclastic rocks via small scale faults and fractures. $\delta^{18}O$ and δD values of H_2O in equilibrium clay minerals, and the concentration and crystallinity of illite outlined multiple zones of hydrothermal alteration in surface rocks from both the Shoshone Range and Leeville study areas, however no genetic link was established to Carlin-type gold mineralization at depth. Similarities in trace element geochemistry, ore assemblage, and alteration assemblages however, suggest that the Elder Creek deposit may represent low temperature (200°C) gold mineralization resulting from the exhaust of Carlin-type ore forming fluid. The region above the surface projection of the Leeville deposit exhibits multiple zones of hydrothermal fluid upflow resulting in pervasive illitization of surface siliciclastic rocks. The Pipeline/ Gold Acres also contain abundant crystalline illite. The presence of highly crystalline illite highlights zones of focused fluid upflow, typically along faults and other secondary permeability structures such as breccias.

PREFACE

Dr. K.H. Hickey identified and designed the research program. The research, sampling, and data accumulation were performed by A. Ahmed in consultation with K.H. Hickey, S.L. and Barker. Chapters 3 and 4 of the thesis are intended for publication in a scientific journal under the same title as each chapter respectively. A. Ahmed will be first author, K.A. Hickey will be second author, and S.L. Barker will be third author. Appendix A of this thesis is currently in press in the Geological Society of Nevada 2010 symposium proceedings, due to be published in November, 2010.

TABLE OF CONTENTS

ABSTRACT ii
PREFACE iii
TABLE OF CONTENTS iv
LIST OF TABLES viii
LIST OF FIGURES i
LIST OF TERMS/ ABBREVIATIONS iii
ACKNOWLEDGEMENTS iv
DEDICATION v
CHAPTER 1 – PROJECT OVERVIEW 1
1.1 RATIONALE FOR STUDY 1
1.2 OVERVIEW OF CARLIN TYPE GOLD SYSTEMS 2
1.2.1 Carlin-type gold deposits 2
1.2.2 Tectonic framework 4
1.3 THESIS OBJECTIVE 7
1.4 THESIS ORGANIZATION 7
1.5 SUMMARY 9
1.5 REFERENCES 10
CHAPTER 2- CLAY MINERALS AND LOW TEMPERATURE PROCESSES 14
2.1 INTRODUCTION 14
2.2 CLAY EQUILIBRIA 14
2.3 ILLITE THERMOMETRY 17
2.4 ILLITE POLYTYPISM 18
2.5 ILLITE CRYSTALLINITY 18
2.6 CLAY TEXTURES AND CLAY MORPHOLOGY 20
2.7 CHEMICAL COMPOSITION OF ILLITE 20
2.8 SUMMARY 24
2.9 REFERENCES 25
CHAPTER 3 – BEYOND THE CONFINES OF THE ORE BODY: SURFACE MAPPING OF LOW TEMPERATURE HYDROTHERMAL FLUID ABOVE MAJOR ORE BODIES USING CLAY ALTERATION 28
3.1 INTRODUCTION 28

3.2 GEOLOGICAL SETTING OF CARLIN-GOLD DEPOSITS 32
3.3 CHARACTERISTICS OF CARLIN GOLD DEPOSITS 36
3.3.1 Clay alteration in Carlin-type systems 37
3.4 THERMAL SIGNATURE OF HYDROTHERMAL FLUID FLOW 37
3.5 ANALYTICAL TECHNIQUES 42
3.5.1 Near and Short Wave Infrared Analysis (Terraspec©) 42
3.5.2 X-ray diffraction 43
3.5.3 Scanning Electron Microscope (SEM) 44
3.5.4 Electron Microprobe Analysis 44
3.5.5 Stable Isotope Analysis 45
3.6 SAMPLES 45
3.7 RESULTS 46
3.7.1 Morphology and textural relationships of clays 46
3.7.2 Spatial distribution of clays -Leeville 50
3.7.3 Distribution of clays - Shoshone Range Field Area 56
3.7.4 Comparing the use of XRD vs. Terraspec in the identification of clay minerals 60
3.7.5. Calculated temperature of illite formation 63
3.7.6. Oxygen and Hydrogen Stable Isotope data 64
3.8 INTERPRETATIONS/ DISCUSSION 68
3.8.1 Clay mineral zonation patterns around hydrothermal fluid conduits 68
3.8.2 Illite crystallinity halos 70
3.8.3 Crystal morphology 71
3.8.4 The Origin of Clay Minerals 71
3.8.5 Challenges in using the K + $\boldsymbol{Fe - Mg}$ thermometer 72
3.8.6 Clay morphology, crystallinity , and composition as a function of reaction progress 73
3.9 IMPLICATIONS 75
3.9.1 The ability of analytical tools to identify alteration related to Carlin-Au mineralization 75
3.9.2 Hydrothermal flow on a regional scale 77
3.9.3 The pathway of exhausted fluids in Carlin-type systems 78
3.10 CONCLUSIONS 78
3.11 REFERENCES 80
CHAPTER 4 – SHEDDING LIGHT ON THE ABYSS: LATERAL FLUID FLOW UNDERNEATH AND INTO CARLIN-TYPE GOLD DEPOSITS 89

4.1 INTRODUCTION 89
4.2 GEOLOGICAL SETTING OF THE PIPELINE DEPOSIT 90
4.2.1 Carlin-type Au-Mineralization 92
4.2.2 Previous isotope studies of the Pipeline Deposit 93
4.3 FAULT RELATED FLUID FLOW IN CARLIN SYSTEMS AND THE ABYSS FAULT 93
4.4 METHODS and ANALYTICAL TECHNIQUES 97
4.4.1 Background $\delta^{18}O$, $\delta^{13}C$, Au and trace element values for marine carbonate rocks 99
4.5 RESULTS 101
4.5.1 $\delta^{18}O$ and $\delta^{13}C$ values of rocks 101
4.5.2 $\delta^{18}O$ and $\delta^{13}C$ values of veins 110
4.5.3 Gold and trace element concentrations near the Abyss fault 114
4.6 DISCUSSION 117
4.6.1 Origin of the $\delta^{18}O$ depletion in veins 120
4.7 IMPLICATIONS 122
4.8 CONCLUSION 124
4.9 REFERENCES 125
CHAPTER 5 –CONCLUSIONS 130
5.1 FLUID FLOW INTO CARLIN-TYPE GOLD DEPOSITS 130
5.2 FLUID PATHWAYS OUT OF CARLIN-TYPE GOLD DEPOSITS 130
5.3 ESTABLISHING VECTORS TOWARD CARLIN-TYPE ORE 133
5.4 RECOMMENDATIONS FOR FUTURE WORK 133
5.5 REFERENCES 135
APPENDIX A: THE ELDER CREEK DEPOSIT: An Upper Plate Expression of an Auriferous Carlin-type hydrothermal system 136
INTRODUCTION 136
REGIONAL GEOLOGICAL SETTING 136
GEOLOGICAL SETTING OF THE ELDER CREEK MINE 140
Clay mineralogy 144
Lithogeochemistry 147
METHODOLOGY 147
RESULTS 149
Clay mineralogy 149
Lithogeochemistry 155

INTERPRETATIONS 157
Physiochemical nature of fluid 157
Fluid flow pathways 157
DISCUSSION 161
Deposit classification 163
CONCLUSIONS 164
REFERENCES 165
APPENDIX B– APATITE FISSION TRACK THERMOCHRONOLOGY DATA 168
APPENDIX C – SAMPLE INFORMATION 173
APPENDIX D – X-RAY DIFFRACTION PATTERNS 181
APPENDIX E – MICROPROBE DATA 187
APPENDIX F - ISOTOPIC VARIATION BETWEEN LITHOLOGICAL FORMATIONS 197

LIST OF TABLES

Table 2.1	Calibration chart for FWHM values	19
Table 2.2	Regression line equations and correlation factors for K+[Fe-Mg] thermometer	22
Table 3.1	XRD data for the Leeville study area	53
Table 3.2	Calibrated FWHM values for the Leeville study area	55
Table 3.3	XRD data for the Shoshone Range study area	57
Table 3.4	Calibrated FWHM values for the Shoshone Range study area	59
Table 3.5	XRD vs. Terraspec accuracy	61
Table 3.6	Averaged illite formation temperatures	64
Table 3.7	Stable isotope data	65
Table 4.1	Trace element geochemistry analytical procedures and detection limits	99
Table 4.2	Stable isotope data and geochemistry for background samples from Lone Mtn	100
Table 4.3	$\delta^{18}O$, $\delta^{13}C$, and trace element geochemistry data	102
Table A1	Geochemical data comparison between Elder Creek and Carlin-type deposit	162
Table B1	Thermochronology data of the Northern Carlin trend	168
Table B2	Thermochronology data of the Shoshone Range	170
Table C1	Sample information	173
Table E1	Illite microprobe compositional data	187

LIST OF FIGURES

Fig. 1.1	Location of Carlin-type gold deposits in the western United States……..	3
Fig. 1.2	Major deformation events affecting the western margin of North America……	5
Fig. 2.1	Clay stability phase diagrams……..	15
Fig. 2.2	End member morphologies of illite……	21
Fig. 2.3	The derivation of the K +[Fe-Mg] thermometer……	23
Fig. 3.1	The distal extent and degree of alteration around ore deposits……	29
Fig. 3.2	Regional geology map of north-eastern Nevada……..	32
Fig. 3.3	Geological map and cross section of the Leeville study area……	33
Fig. 3.4	Simplified tectono-stratigraphic column of the RMT system……..	34
Fig. 3.5	Potential fluid evolution pathways……	38
Fig. 3.6	Apatite fission track ages across the Northern Carlin trend……	40
Fig. 3.7	Apatite fission track ages across the Shoshone Range……	41
Fig. 3.8	Sample types……	47
Fig. 3.9	Sample location map from the Leeville study area……..	48
Fig. 3.10	Scanning electron microphotographs showing the morphology of clay minerals……	49
Fig. 3.11	Scanning electron microphotographs showing mineral-mineral relationships……..	51
Fig. 3.12	XRD, Terraspec, FWHM, and microprobe data from across the Leeville area……	52
Fig. 3.13	XRD, Terraspec, and FWHM data from across the Shoshone Range ……	58
Fig. 3.14	Causes for discrepancies between XRD and Terraspec data……	62
Fig. 3.15	Graph of average potassium content of illite and average oxide totals……..	66
Fig. 3.16	Stable isotope data from this study along with data from other Carlin-type deposits……	67
Fig. 3.17	Zones of hydrothermal alteration identified in the Leeville study area……..	69
Fig. 3.18	Trends in illite compositional data from previous studies……..	74
Fig. 4.1	Regional map of northeastern Nevada with inset of the Pipeline deposit……..	91
Fig. 4.2	Cross section A-A^1 through the Abyss fault……	95
Fig. 4.3	Photographs of core above, at and below the Abyss fault……..	96
Fig. 4.4	Drill hole and cross-section location map……	98
Fig. 4.5	$\delta^{18}O$ and $\delta^{13}C$ data……	109
Fig. 4.6	Cross sections through the Pipeline deposit show $\delta^{18}O$ depletion zones……..	111
Fig. 4.7	$\delta^{18}O$ values relative to the Abyss fault……	112

Fig. 4.8 $\delta^{13}C$ values relative to the Abyss fault..... 113
Fig. 4.9 Trace element geochemistry concentrations relative to the Abyss fault..... 115
Fig. 4.10 Potential fluid pathways into the Pipeline ore deposit..... 121
Fig. A1 Regional Geology map of northeastern Nevada..... 138
Fig. A2 Simplified stratigraphic column of lower Palaeozoic rocks..... 139
Fig. A3 Geology of the Elder Creek deposit..... 141
Fig. A4 Photograph of sample 456..... 142
Fig. A5 Field photographs of strongly argillized zones..... 143
Fig. A6 Fluid evolution pathways..... 145
Fig. A7 Phyllosilicate phase diagrams..... 146
Fig. A8 Sample location map..... 148
Fig. A9 Two XRD standards..... 150
Fig. A10 X-ray diffraction patterns..... 152
Fig. A11 Hydrothermal illite textures..... 153
Fig. A12 Illite crystallinity vs. peak position graph..... 154
Fig. A13 Gold ordered trace element diagrams..... 156
Fig. A14 Geochemical halos..... 158
Fig. A15 Stability field clay phase diagram..... 160
Fig. F1 Stable isotope value variation with lithology..... 197

LIST OF TERMS/ ABBREVIATIONS

a_x: activity

CIS: crystallinity index standard (a standardized Kubler Index)

FWHM: Full width at half the maximum value (at given 2Θ location of an x-ray diffraction pattern)

I-S: illite-smectite interlayered clay

Lower plate: Lower Paleozoic shelf and slop carbonate rocks that form the footwall to the Roberts Mountains Thrust fault and are the typically hosts for the Carlin-type gold mineralization

PASW: Predictive Analytics Software (an IBM product)

PIMA: Portable Infrared Mineral Analyzer

RC: Reverse circulation (drill hole)

RMT : Roberts Mountains Thrust Fault

VPDB: Versus Peedee Belminite (international standard for carbon isotopes)

VSMOW: Versus Standard Mean Ocean Water (international standard for oxygen isotopes)

Upper Plate: Lower Paleozoic shallow marine and basinal siliciclastic sediments that form the hangingwall to the Roberts Mountains Thrust fault, and can form thick sequences of cover on top of Carlin-type gold systems.

δ = ratio of the heavy isotope (^{13}C or ^{18}O) vs. the light isotope (^{12}C or ^{16}O)

‰ : per mil (stable isotope measurement relative to an international standard)

ACKNOWLEDGEMENTS

This MSc. thesis is part of a larger project coordinated by Dr. Kenneth Hickey, associate professor, University of British Columbia, Mineral Deposit Research Unit entitled *'Thermal and geochemical footprints of low-temperature sedimentary rock-hosted hydrothermal Au-systems: Identifying far-field vectors toward ore'*. My sincere thanks to those companies and organizations that provided financial support for this project: Barrick Gold Corporation, Newmont Mining Corporation, and Teck Limited with matching funds provided by a Collaborative Research and Development grant from the Natural Sciences and Engineering Research Council. A special thanks to Kevin Creel, Bob Leonardson, Nancy Richter, and Joe Becker for providing support at the Cortez mine. Thank you to the Society of Economic Geologists for providing financial support through scholarships and conference funding.

My sincere thanks to Dr. Kenneth Hickey for his continuing support and mentorship. I will fondly remember luring Ken into the office for some quality thesis review time with the help of a either a chocolate bar or biscuit, or both. As busy as he may have been, he always made the time to meet and provide constructive criticism; a truly brilliant man. I thank my committee members Dr. Greg Dipple, Dr. Dominique Weis, and Dr. Shaun Barker for their interest and guidance. I appreciated their feedback during committee meetings and their commitment to keeping my work within the scope of a Master's project. I am especially grateful for the constant support of Dr. Barker who will be happy never to have to edit anything else I write. I could not have completed any SEM, XRD, or microprobe work without the help of Mati Raudsepp, Edith Czech, Jenny Lai, and Elisabetta Pani. For my work with isotopes, I thank Janet Gabites for sample preparation and data reduction.

I am indebted to my fellow lab-mates Moira Cruickshanks, Will Lepore, and Jeremy Vaughan who provided countless hours of discussion, both thesis related and otherwise. Thanks to good friends Jean Francois Blanchette Guertin, Jaime Poblete, Santiago Vaca, Bram Van Straaten, Esther Bordet, and Tatiana Alva for much needed evening distractions. To Bram and the rest of the 'orphanage', thank you for welcoming me into my second home. A shout out to my best friends Devon and Christa for providing a link to a world unrelated to geology. Last and far from least, I will be forever indebted to Shawn Hood whose patience and support was and is never ending.

And of course to my family. To both my parents for giving me a desire to never stop learning and for inspiring me to pursue higher education. To my mama for always understanding that in times of despair, it is comforting to hear that you're right, even when you're not, and for feeling and experiencing my troubles as much or more than I did. To my Abbu for always providing the extra push, motivation and support to keep me on the right track. And to my special Xantha, who ever since we were young has been a role model for her sense of adventure, and her lack of fear for new experiences and new challenges.

DEDICATION

To Mutti, Abbi, and Gogo (+/- Snooks)

To Shawny

CHAPTER 1 – PROJECT OVERVIEW

1.1 RATIONALE FOR STUDY

Exploration for new economic mineral resources in mature mineral terranes has become increasingly difficult and deposits currently exposed at surface have either been discovered or categorized as sub-economic (Kelley et al., 2006). Recent research has highlighted the importance of discovering new exploration methods and improving on existing exploration methods that look beyond the obvious limits of mineralization to the distal expression of mineralizing systems (Adams and Putnam, 1992; Arehart and Donelick, 2006; Kelley et al., 2006). This task is complicated in the context of low temperature hydrothermal systems (<300°C) where conventional alteration or mineral mapping is difficult to employ. Low temperature systems such as active geothermal systems (Simmons and Browne, 2000; Yang et al., 2001), and Carlin-type gold deposits (Cline et al., 2005) have a tendency to exhibit more subtle alteration halos around ore deposits than their high temperature counterparts such as porphyry deposits (Rose, 1970). This is primarily a function of differences in both thermal and chemical gradients between mineralizing fluid and host rock (Reed, 1982, 1997). Low temperature hydrothermal systems intruding the shallow crust tend to lack large thermal and chemical gradients between hot rock (~50°C at 2km given a geothermal gradient of 25°C/km) and low temperature (~200°C) rock or surface water buffered fluid. Furthermore, the alteration minerals produced from low temperature fluid-rock interactions are generally fine grained phyllosilicate minerals which are difficult to both identify and analyze, and may not represent equilibrium assemblages (Essene and Peacor, 1995). Identifying subtle expressions of hydrothermal alteration around low temperature mineral deposits may provide robust vectors toward mineralization at depth. These expressions provide insights into to the nature and extent of alteration in low temperature systems that help to further existing models for mineralizing processes.

This MSc. thesis is part of a larger project coordinated by Dr. Kenneth Hickey, University of British Columbia, Earth and Ocean Sciences Department, Mineral Deposit Research Unit entitled *'Thermal and geochemical footprints of low-temperature sedimentary rock-hosted hydrothermal Au-systems: Identifying far-field vectors toward ore'*. The project is sponsored by Barrick Gold Corporation, Newmont Mining Corporation, and Teck Limited with matching funds provided by a Collaborative Research and Development grant from the Natural Sciences and Engineering Research Council. The project combines a well-constrained geological understanding of the paleogeographic, tectonic and magmatic environment of gold deposition using a range of thermochronometers, and lithogeochemical,

isotopic and mineralogical tracers to delineate the location and scale of low temperature hydrothermal fluid circulation that resulted in Carlin-type gold deposition, as well as identifying where these deposits are manifested under cover.

1.2 OVERVIEW OF CARLIN TYPE GOLD SYSTEMS

1.2.1 Carlin-type gold deposits

The world-class Carlin-type gold deposits of northeastern Nevada provide 9% of the world's gold production (Cline et al., 2005; Price et al., 2008). The majority of deposits occur along three structural lineaments shown in Figure 1.1: the Carlin trend, the Battle Mountain Eureka trend, and the Getchell trend. The majority of gold is 'invisible', hosted within arsenian-rich pyrite, although the oxidized portion of deposits can contain free gold (Barker et al., 2009; Bettles, 2002). Gold is disseminated and occurs predominantly within lower Paleozoic silty carbonate shelf and slope rocks (Cline et al., 2005). Gold precipitated via sulfidation where a low temperature, slightly acidic fluid reacted with ferrous-carbonate host rocks (Cline and Hofstra, 2000; Lubben, 2004). Many Carlin-type deposits are covered by thick sequences of Paleozoic outer shelf and basin siliciclastic rocks which are largely devoid of mineralization (Cline et al., 2005).

The namesake for Carlin-type gold deposits, the 'Carlin deposit' is located along the Northern Carlin trend, north-eastern Nevada. Subsequent to the discovery of the Carlin gold depoist in the 1960's, a number of other deposits of similar style were discovered in the area (Cline and Hofstra, 2000). Since this type of deposit had not been documented anywhere else, a new classification of hydrothermal ore-deposits was created and termed 'Carlin-type'. Carlin-type gold deposits are typically restricted to the shallow crust (1-4km below surface). The source of fluid and metals is strongly debated. Fluid inclusion and mineral thermometry data indicate that mineralizing fluid forming Carlin deposits in northeastern Nevada was: low temperature (180-240°C), slightly acidic (pH ~4), low-salinity (~2–3 wt% NaCl equivalent), aqueous fluids that contained CO_2 (<4 mol %), and CH_4 (<0.4 mol %), and sufficient H_2S (10^{-1}–10^{-2} m) to transport Au and other bisulfide-complexed metals (Cline and Hofstra, 2000; Lubben, 2004). No fluid inclusion, mineralogical, or textural evidence exists to indicate fluid boiling or immiscibility. Alteration associated with Carlin-type mineralization is subtle and includes: pre-ore

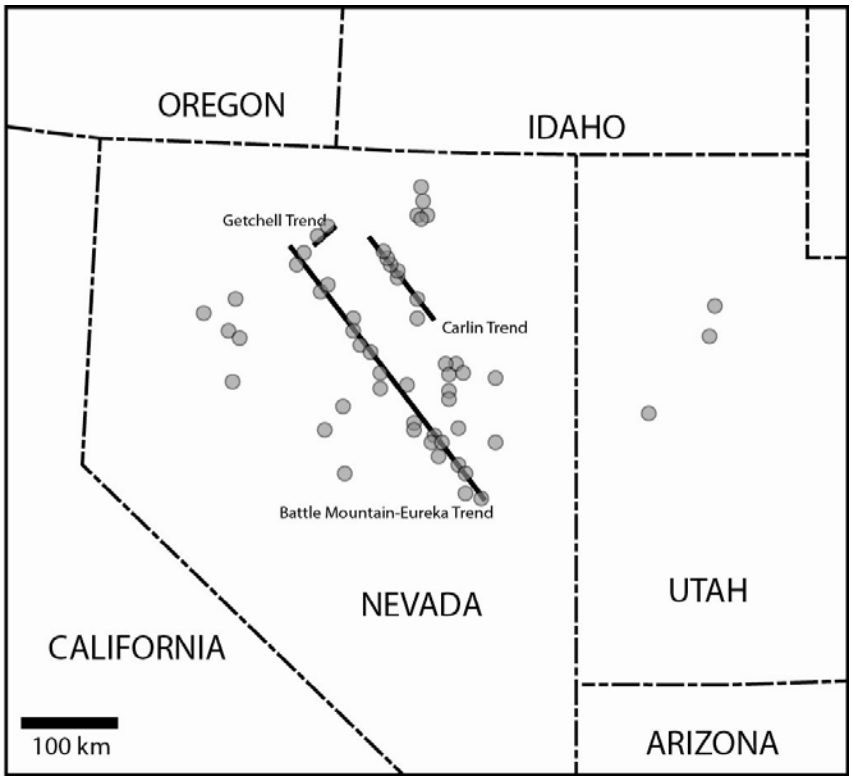

Fig.1.1. (Modified from Hofstra et al., 1999) Dots show locations of Carlin-type gold deposits in the western United States. Deposits occur principally along three structural lineaments: the Battle Mountain – Eureka trend, the Carlin trend, and the Getchell trend. The alignment of Carlin-type deposits reflects major basement fault fabrics which were established during Neoproterozoic rifting (Roberts, 1966; Tosdal et al., 2000).

decalcification, argillization, sulfidation and local silicification. Clay minerals observed in the argillic alteration assemblage include illite, dickite, and kaolinite (Ilchik, 1990; Clode et al., 1997; Folger et al., 1998; Hofstra et al., 1999; Cline and Hofstra, 2000; Cail and Cline, 2001). Thermochronology based estimates of bedrock exhumation suggest that the Carlin-type Au-deposits likely formed over a paleodepth range of <1-4 km (Cline et al., 2005).

δD_{H2O} values measured on hypogene kaolinite, illite and fluid inclusions from a wide-range of Carlin deposits suggest evidence of meteoric water with very low δD_{H2O} values of < -110 ‰ (Hofstra, 1999). Geochemical data and mineral stability also suggest a highly exchanged meteoric source fluid (Ilchik and Barton, 1997). Stable isotope data from fluid inclusions and clay minerals of the the Getchell, Twin Creeks, and Deep Star deposits, however, indicate the additional presence of deeply sourced metamorphic or magmatic fluid (Hofstra et al., 1999; Heitt et al., 2003; Cline et al., 2005). A spatial association between some Carlin-type deposits and Eocene intrusive centers has also led to the interpretation that Carlin-type deposits are distal portions of magmatic hydrothermal systems (Radtke et al., 1980; Arehart et al., 1993).

Gold is typically hosted within Siluro-Devonian miogeoclinal carbonate rocks that form the footwall to the Roberts Mountains Thrust (RMT) (the “lower plate”). The structurally overlying “upper plate” is dominated by Ordovician-Mississippian siliciclastic eugeoclinal rocks (Roberts, 1966). The upper plate is not known to host any major Carlin-type Au deposits although mineralization does occur locally immediately above the RMT in several of the lower plate-hosted deposits. The lack of Carlin-type deposits in the upper plate is thought to reflect the less reactive nature of the siliciclastic rocks that dominate the Roberts Mountains allochthon (Cline et al., 2005).

1.2.2 Tectonic framework

Figure 1.2 presents a timeline of deformation events leading to the formation of Carlin-type gold deposits in Nevada. The western margin of continental North America records a history of prolonged episodic rifting and basin subsidence from the Neoproterozoic to Paleozoic as the proto-Pacific oceanic basin opened following the breakup of Rodinia to form the paleo-continent Laurentia (Powell et al., 1993; Wingate and Giddings, 2000; Lund, 2008). Geochronologic data indicate the presence of two main rifting events beginning in the Cryogenian and accelerated in the Ediacaran to Cambrian (Stewart,

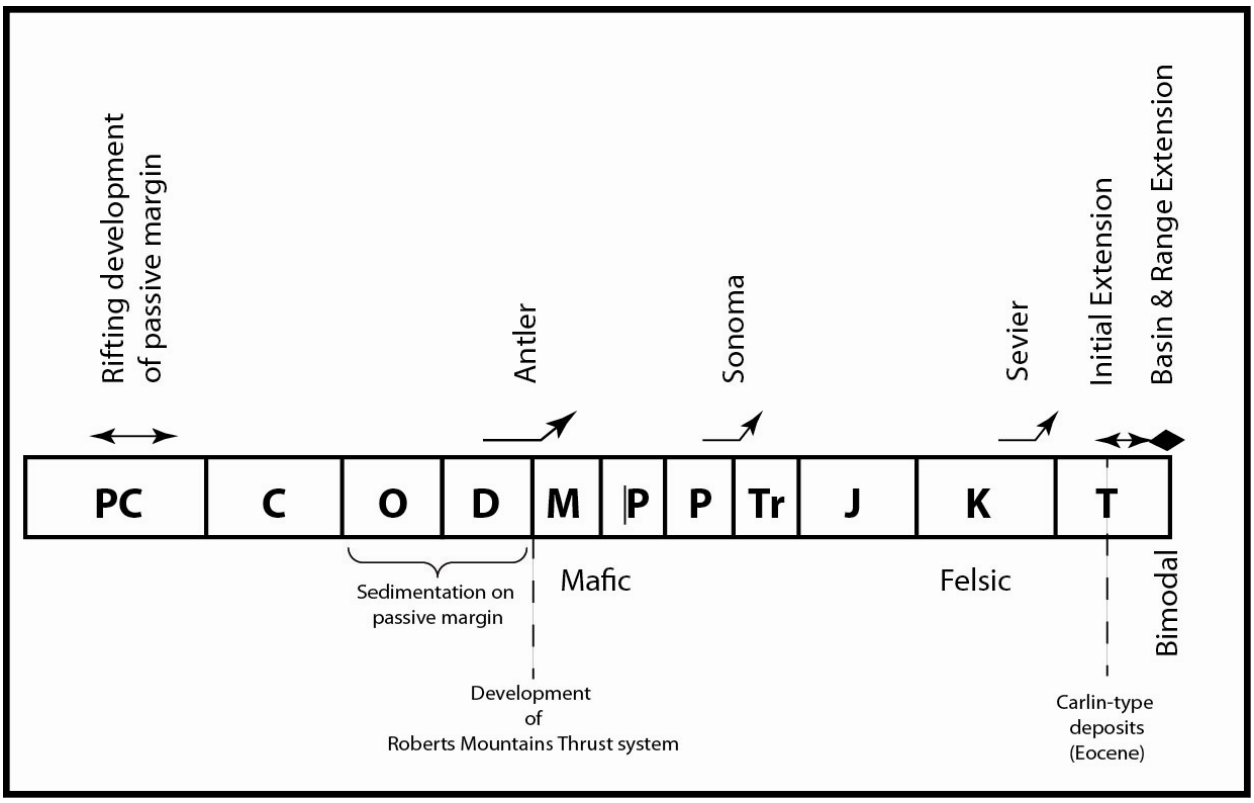

Fig. 1.2. (Modified from Hofstra et al., 1999) Timeline showing the major deformation events affecting the western margin of continental North America. PC = pre-Cambrian C= Cambrian O = Ordovician D= Devonian M = Mississippian IP = Pensylvannian P = Permian Tr = Triassic J= Jurassic K= Cretaceous T = Tertiary.

1972; Thompson et al., 1987; Ross, 1991; Colpron et al., 2002). The earlier rifting event corresponds to the deposition of coarse, partly glaciogenic diamictite and mafic volcanic rocks of the Windermere Supergroup on top of an intercontinental rift margin in British Columbia (Ross, 1991; Colpron et al., 2002). Later rifting in the Neoproterozoic is interpreted to indicate continental breakup and establishment of a passive margin along the western margin of Laurentia (Colpron et al., 2002). Neoproterozoic and Early Cambrian clastic rocks across central Nevada are dominated by quartzite with interstratified argillite and phyllite, and were deposited in a westward-thickening sedimentary wedge over structurally complex, thinned Paleoproterozoic to Neoproterozoic crystalline basement (Poole et al., 1992). During the Early- Middle Devonian, basins formed in the shelf and outer shelf regions of the passive margin, probably as a result of reactivation of Neoproterozoic rift structures in the underlying crystalline basement (Stewart, 1972; Morrow and Sandberg, 2008). Following Neoproterozoic rifting and initial sedimentation, miogeoclinal and eugeoclinal sequence sediments were deposited on top of Cambrian clastic rocks, along the western margin of continental North America (Burchfiel and Davis, 1972). Interbedded carbonate and shale, and silty carbonate were deposited along the shelf and slope, with basinal and shallow marine siliciclastic sediments deposited further west (Burchfiel and Davis, 1972; Morrow and Sandberg, 2008).

Subsequent to deposition, the Paleozoic passive margin sequence was subject to multiple episodes of contractional deformation occurring from middle Mississppian to Early Permian (Cashman et al., 2008). During the Late Devonian – Early Mississippian Antler orogeny, lower Paleozoic basin and slope rocks (locally termed ‘upper plate’) were thrust eastward over coeval shelf-margin and outer-shelf rocks (lower plate) forming the RMT system (Johnson and Pendergast, 1981; Poole et al., 1992). Lower plate carbonate rocks are the typical host for gold mineralization in Carlin-type gold deposits. Upper plate rocks were eventually overlain by Mississippian to Permian shelf deposits; the ‘overlap sequence’ described by Roberts et al., (1958). The Late Mississippian to Middle Pennsylvanian Humboldt orogeny resulted in uplift and later subsidence of the overlap sequences. Rocks of the Golconda allochthon were thrust eastward over upper plate and overlap sequence rocks during the Late Permian and Early Triassic Sonoma orogeny (Miller, 1984). Starting in the Late Triassic and continuing through to the Tertiary, the western margin of North America became the site of semi-continuous east-directed subduction (Speed et al., 1988) leading to the development of the Cordilleran orogenic belt. Further west, subduction was marked by episodes of thin-skinned contractional deformation with accompanying extensional faulting and magmatism.

Two periods of extension affected Northeastern Nevada during the Cenozoic. Extension commenced in the late Paleogene with the onset of regional magmatism (Wernicke et al., 1987; Christiansen et al., 1992; Sonder and Jones, 1999). The spatial and temporal overlap of Carlin-type deposits with the onset of Cenozoic volcanism and extension suggests a fundamental link between these phenomena (Hofstra et al., 1999; Cline et al., 2005). Rb/Sr dating of the syn-ore mineral galkhaite indicates a mineralization age of 38-40 Myr (Tretbar et al., 2000; Arehart et al., 2003; Cline et al., 2005). Subsequent to Carlin-type gold deposition, heterogeneous extension of the Great Basin, accompanied by magmatism continued into the Oligocene and ended with the mid Miocene development of the Basin and Range province and the Northern Nevada Rift; a series of north-northwest-striking mafic dikes and high angle normal faults, basaltic volcanic flow units related to the dikes and epithermal, volcanic-hosted mineral deposits (Wernicke et al., 1987; Zoback et al., 1994).

1.3 THESIS OBJECTIVE

The goal of this thesis is to investigate and answer two scientific questions: *Question 1:* Can we identify fluid flow patterns into and out of low temperature hydrothermal systems by means of thermal and/ or chemical alteration halos, and if so how is fluid flow manifested in host rocks? *Question 2:* What set of tools and analytical techniques may provide vectors toward regions of hydrothermal flow most likely to have precipitated economic grades of mineralization? These two questions are answered with two complimentary studies: (i) by identifying a thermal or chemical alteration halo in upper plate siliciclastic rocks resulting from interaction with exhausted Carlin-type hydrothermal fluid (ii) by investigating alteration within and above a major fault underlying a giant Carlin-type deposit to identify large scale fluid flow pathways. The results contained in this thesis further the understanding of fluid rock interaction in Carlin-type environments and provide information on the practical application of tools and analytical techniques related to identifying low temperature hydrothermal alteration.

1.4 THESIS ORGANIZATION

This thesis is arranged in four chapters. Chapter 1 introduced the concepts outlined in this study by presenting a literature review of Carlin-type gold systems, and the alteration associated with low temperature hydrothermal systems. Chapter 2 provides background information on low temperature clay thermometers. Chapters 3 and 4 are written as stand-alone manuscripts to be submitted to an international scientific journal for publication, and adhere to the formatting protocol of *Economic Geology*.

Chapter 3 presents a study that tested for the presence of clay alteration phases above regions of known mineralization. A regional study of the Shoshone Range and a deposit scale study of the Leeville deposit (both in northeastern Nevada) investigated the relationship between argillization at surface in upper plate siliciclastic rocks, and argillization typically associated with Carlin-type Au mineralization at depth. The identification of a hydrothermal clay mineral assemblage at surface may provide insight into the way in which fluid was exhausted following mineralization of Carlin-type deposits. Identifying zones of surface exhaust provides a direct link to ore deposits at depth. Detailed results of this study include clay mineral zonation patterns, illite formation temperatures, illite crystallinity, textural and morphological analyses of clays, and O and H stable isotope analyses of clay minerals. Results from this chapter indicate that extensive zones of hydrothermal clay alteration at surface are spatially associated to Carlin-type gold deposits at depth. The chapter concludes with a critical analysis of the results achieved using two different analytical techniques, x-ray diffraction and near and short wave spectroscopy, to identify clay minerals.

Chapter 4 of this thesis extends the work of Arehart and Donelick (2006) and Rye (1995) who studied the stable isotopic depletion signature above and within the giant Pipeline gold deposit, northeastern Nevada. This chapter focuses on defining and identifying fluid pathways leading into Carli-type gold systems by studying the Abyss fault; a large thrust structure that separates gold mineralized lower plate on top of largely unmineralized upper plate below the Pipeline deposit. Results are presented from a C and O stable isotope study on carbonate rocks within the hangingwall of the fault to determine whether the Abyss fault acted as a fluid conduit, or whether it played a passive role during mineralization of the giant deposit. Those results indicate that ore-forming fluid flow did occur along the Abyss fault however the fault was not the main conduit for fluid forming the Pipeline gold deposit. Furthermore, fluid pathways within the Pipeline deposit were dominantly lateral, not vertical.

A case study is presented in Appendix A of this thesis of the Elder Creek deposit; a small, sediment hosted disseminated gold deposit in the upper plate siliciclastic rocks of the Shoshone Range. Information is used from chapters 2, 3, and 4 to discuss the potential for Carlin-type gold mineralization in allochthonous siliciclastic rocks (upper plate). Characteristics of the Elder Creek deposit are considered relative to known characteristics of Carlin-type gold deposits including trace-element geochemistry, clay alteration, temperature, and ore mineral assemblages. The study of the Elder Creek deposit has been accepted by the Geological Society of Nevada for publication in the 2010 GSN Symposium proceedings.

Although chapters 3 and 4 focus on different aspects of the same scientific questions outlined in section 1.3, each chapter has been prepared as a stand-alone paper resulting in some inevitable repetition and overlap between the chapters.

1.5 SUMMARY

Exploration for low temperature hydrothermal ore systems can be hindered by a lack of visible alteration. Carlin-type deposits are examples of low temperature hydrothermal systems exhibiting subtle alteration associated with mineralization. In this thesis, we discuss the presence of both a thermal and chemical alteration below, within, above and outboard from large low temperature hydrothermal systems by studying variations in low temperature clay mineral assemblages in siliciclastic rocks and oxygen and carbon isotope depletion in carbonate rocks. In addition, we investigate the role of largescale faults in the process of mineralization to place constraints on pathways for ore forming fluids.

1.5 REFERENCES

Adams, S.S., and Putnam, B.R., III, 1992, Application of mineral deposit models in exploration: a case study of sediment-hosted gold deposits, Great Basin, Western United States: Geological Society, London, Special Publications, v. 63, p. 1-23.

Arehart, G., and Donelick, R., 2006, Thermal and isotopic profiling of the Pipeline hydrothermal system: Application to exploration for Carlin-type gold deposits: Journal of Geochemical exploration, v. 91, p. 27-40.

Arehart, G., Chakurian, A., Tretbar, D., Christensen, J., McInnes, B., and Donelick, R., 2003, Evaluation of radioisotope dating of Carlin-type deposits in the Great Basin, western North America, and implications for deposit genesis: Economic Geology, v. 98, p. 235-248.

Arehart, G., Eldridge, C., Chryssoulis, S., and Kesler, S., 1993, Ion microprobe determination of sulfur isotope variations in iron sulfides from the Post/Betze sediment-hosted disseminated gold deposit, Nevada, USA: Geochimica et Cosmochimica Acta, v. 57, p. 1505-1519.

Barker, S., Hickey, K., Cline, J., Dipple, G., Kilburn, M., Vaughan, J., and Longo, A., 2009, Uncloaking Invisible Gold: Use of NanoSIMS to Evaluate Gold, Trace Elements, and Sulfur Isotopes in Pyrite from Carlin-Type Gold Deposits: Economic Geology, v. 104, p. 897-904.

Bettles, K. 2002, Exploration and geology, 1962–2002 at the Goldstrike property, Carlin Trend, Nevada: Economic Geology Special Publication 9, p. 275–298.

Burchfiel, B., and Davis, G., 1972, Structural framework and evolution of the southern part of the Cordilleran orogen, western United States: American Journal of Science, v. 272, p. 97-118.

Cail, T., and Cline, J., 2001, Alteration associated with gold deposition at the Getchell Carlin-type gold deposit, north-central Nevada: Economic Geology, v. 96, p. 1343-1359.

Cashman, P., Trexler, J., Snyder, W., Davydov, V., and Taylor, W., 2008, Late Paleozoic deformation in central and southern Nevada: GSA Field Guides, v. 11, p. 21-43.

Christiansen, R., Yeats, R., Graham, S., Niem, W., Niem, A., and Snavely, P., 1992, Post-Laramide geology of the US Cordilleran region: The Cordilleran Orogen: Conterminous US G-3, Geological Society of America, Boulder, Colorado, p. 261–406.

Cline, J., and Hofstra, A., 2000, Ore-fluid evolution at the Getchell Carlin-type gold deposit, Nevada, USA: European Journal of Mineralogy, v. 12, p. 195-212.

Cline, J., Hofstra, A., Muntean, J., Tosdal, R., and Hickey, K., 2005, Carlin-type gold deposits in Nevada: Critical geologic characteristics and viable models: Economic Geology, 100th Anniversary Volume, p. 451-484.

Clode, C., Grusing, S., Heitt, D., and Johnston, I., 1997, The relationship of structure, alteration, and stratigraphy to formation of the Deep Star gold deposit: Eureka County, Nevada: Society of Economic Geologists Guidebook Series, v. 28, p. 239–256.

Colpron, M., Logan, J., and Mortensen, J., 2002, U-Pb zircon age constraint for late Neoproterozoic rifting and initiation of the lower Paleozoic passive margin of western Laurentia: Canadian Journal of Earth Sciences, v. 39, p. 133-143.

Essene, E., and Peacor, D., 1995, Clay mineral thermometry-a critical perspective: Clays and Clay Minerals, v. 43, p. 540-553.

Folger, H., Hofstra, A., Eberl, D., and Snee, L., 1998, Importance of clay characterization to interpretation of 40 Ar/39 Ar dates of illite from Carlin-type gold deposits: Insights from Jerritt Canyon: Contributions to the Gold Metallogeny of Northern Nevada, ed. Tosdal, RM, USGS Open File Rept, p. 98–338.

Heitt, D., Dunbar, W., Thompson, T., and Jackson, R., 2003, Geology and geochemistry of the Deep Star gold deposit: Carlin trend, Nevada: Economic Geology, v. 98, p. 1107-1135.

Hofstra, A., Snee, L., Rye, R., Folger, H., Phinisey, J., Loranger, R., Dahl, A., Naeser, C., Stein, H., and Lewchuk, M., 1999, Age constraints on Jerritt Canyon and other carlin-type gold deposits in the Western United States; relationship to mid-Tertiary extension and magmatism: Economic Geology, v. 94, p. 769-802.

Ilchik, R., and Barton, M., 1997, An amagmatic origin of Carlin-type gold deposits: Economic Geology, v. 92, p. 269-288.

Ilchik, R., 1990, Geology and geochemistry of the Vantage gold deposits: Alligator Ridge-Bald Mountain mining district, Nevada: Economic Geology, v. 85, p. 50–75.

Kelley, D., Kelley, K., Coker, W., Caughlin, B., and Doherty, M., 2006, Beyond the obvious limits of ore deposits: the use of mineralogical, geochemical, and biological features for the remote detection of mineralization: Economic Geology, v. 101, p. 729-752.

Johnson, J., and Pendergast, A., 1981, Timing and mode of emplacement of the Roberts Mountains allochthon: Antler orogeny: Geological Society of America Bulletin, v. 92, p. 648-658.

Lubben, J., 2004, Quartz as clues to paragenesis and fluid properties at the Betze-Post deposit, northern Carlin trend, Nevada: Unpublished M.Sc. thesis, Las Vegas, University of Nevada, p. 155.

Lund, K., 2008, Geometry of the Neoproterozoic and Paleozoic rift margin of western Laurentia: Implications for mineral deposit settings: Geosphere, v. 4, p. 429-444.

Miller, E., Holdsworth, B., Whiteford, W., and Rodgers, D., 1984, Stratigraphy and structure of the Schoonover sequence, northeastern Nevada: Implications for Paleozoic plate-margin tectonics: Bulletin of the Geological Society of America, v. 95, p. 1063-1076.

Poole, F., Stewart, J., Palmer, A., Sandberg, C., Madrid, C., Ross Jr, R., Hintze, L., Miller, M., and Wrucke, C., 1992, Latest Precambrian to latest Devonian time; development of a continental margin: The Cordilleran Orogen: Conterminous US, p. 9–54.

Powell, C., Li, Z., McElhinny, M., Meert, J., and Park, J., 1993, Paleomagnetic constraints on timing of the Neoproterozoic breakup of Rodinia and the Cambrian formation of Gondwana: Geology, v. 21, p. 889-892.

Price, J.G. et al., 2008, The Nevada Minerals Industry 2007: Nevada Bureau of Mines and Geology Special Publication MI-2007.

Reed, M., 1982, Calculation of multicomponent chemical equilibria and reaction processes in systems involving minerals, gases and an aqueous phase: Geochimica et Cosmochimica Acta, v. 46, p. 513-528.

—, 1997, Hydrothermal alteration and its relationship to ore fluid composition: Geochemistry of hydrothermal ore deposits, p. 303–365.

Roberts, R., 1966, Metallogenic provinces and mineral belts in Nevada: Nevada Bureau of Mines, Rept, v. 13, p. 47-72.

Roberts, R., Hotz, P., Gilluly, J., and Ferguson, H., 1958, Paleozoic rocks of north-central Nevada: Am: Assoc. Petroleum Geologists Bull, v. 42, p. 2813-2857.

Rose, A., 1970, Zonal relations of wallrock alteration and sulfide distribution at porphyry copper deposits: Economic Geology, v. 65, p. 920-936.

Ross, G., 1991, Tectonic setting of the Windermere Supergroup revisited: Geology, v. 19, p. 1125-1128.

Rye, R., 1995, A model for the formation of carbonate-hosted disseminated gold deposits based on geologic, fluid inclusion, geochemical, and stable isotope studies of the Carlin and Cortez deposits, Nevada: Nevada: US Geological Survey Bulletin, v. 1646, p. 35–42.

Simmons, S., and Browne, P., 2000, Hydrothermal minerals and precious metals in the Broadlands-Ohaaki geothermal system: Implications for understanding low-sulfidation epithermal environments: Economic Geology, v. 95, p. 971-999.

Sonder, L., and Jones, C., 1999, Western United States extension: How the west was widened: Annual Review of Earth and Planetary Sciences, v. 27, p. 417-462.

Speed, R., Elison, M.W., and Heck, F.R., 1988, Phanerozoic tectonic evolution of the Great Basin, *in* Ernst., W.G., ed., Metamorphism and crustal evolution of the western United States, Volume 7: New Jersey, Prentice Hall.

Stewart, J., 1972, Initial deposits in the Cordilleran geosyncline: Evidence of a late Precambrian (< 850 my) continental separation: Geological Society of America Bulletin, v. 83, p. 1345-1360.

Thompson, B., Mercier, E., and Roots, C., 1987, Extension and its influence on Canadian Cordilleran passive-margin evolution: Geological Society London Special Publications, v. 28, p. 409-417.

Tretbar, D., Arehart, G., and Christensen, J., 2000, Dating gold deposition in a Carlin-type gold deposit using Rb/Sr methods on the mineral galkhaite: Geology, v. 28, p. 947-950.

Warr, L., 1996, Standardized clay mineral crystallinity data from the very low-grade metamorphic facies rocks of southern New Zealand: European Journal of Mineralogy, v. 8, p. 115-127.

Wernicke, B., England, P., Sonder, L., and Christiansen, R., 1987, Tectonomagmatic evolution of Cenozoic extension in the North American Cordillera: Geological Society London Special Publications, v. 28, p. 203-221.

Wingate, M., and Giddings, J., 2000, Age and palaeomagnetism of the Mundine Well dyke swarm, Western Australia: implications for an Australia-Laurentia connection at 755 Ma: Precambrian Research, v. 100, p. 335-357.

Yang, K., Browne, P., Huntington, J., and Walshe, J., 2001, Characterising the hydrothermal alteration of the Broadlands-Ohaaki geothermal system, New Zealand, using short-wave infrared spectroscopy: Journal of Volcanology and Geothermal Research, v. 106, p. 53-65.

Zoback, M., McKee, E., Blakely, R., and Thompson, G., 1994, The northern Nevada rift: Regional tectono-magmatic relations and middle Miocene stress direction: Geological Society of America Bulletin, v. 106, p. 371-382.

CHAPTER 2- CLAY MINERALS AND LOW TEMPERATURE PROCESSES

2.1 INTRODUCTION

The purpose of this chapter is to provide background on clay minerals, and their use as indicators of hydrothermal alteration based on different characteristics. The techniques described in this chapter are applied to the surface exploration for Carlin-type gold systems in Chapter 3. As will be shown in this chapter, clay mineral zonation patterns observed around hydrothermal systems can reflect gradients in temperature, fluid composition (e.g., acidity), and reaction progress. Clay mineral assemblages have been used as proxies for temperature and fluid composition based on observations that show that clay minerals predictably and repeatedly undergo the same sequence of transformations with increasing grade of diagenesis, metamorphism, and changes in temperature and fluid composition (Essene and Peacor, 1995; Simmons and Browne, 2000). Observations relating changes in clay minerals to temperature are based on both empirical calibrations as observed from natural clay-bearing systems (Rose, 1970; Simmons and Browne, 2000; Battaglia, 2004) and experimental observations (Whitney and Northrop, 1988; Yates and Rosenberg, 1997; Bauer et al., 2000).

2.2 CLAY EQUILIBRIA

Figure 2.1 illustrates the different temperatures and fluid compositions at which illite, kaolinite, and smectite are stable resolved from solution equilibration experiments conducted from 100-250°C (Yates and Rosenberg, 1997). As temperature increases, water in the interlayer site of smectite is replaced by potassium. The loss of interstitial water causes the crystal structure of smectite to become more ordered resulting in the reaction smectite ➔ illite-smectite interlayered clay (I-S) ➔ illite ➔ muscovite (Lanson and Champion, 1991; Lanson et al., 1998). Well ordered end-member illite and muscovite contain no expandable phases (H_2O, H_3O^+) (Yates and Rosenberg, 1997). At 200-250°C pure, end-member illite, lacking any expandable phases (no H_2O in the interlayers) appears at low $a_{H_4SiO_4}$ values and smectite disappears. The smectite field, which occurs at higher $a_{H_4SiO_4}$ values than illite is replaced by I-S. Above 200°C, and at high a_{K+}/a_{H+} ratios K-feldspar and illite are stable relative to kaolinite.

The equilibrium experiments of Yates and Rosenburg (1997), and modeling by others (Varadachari, 2006) highlight the wide ranges in temperature and fluid composition at which certain clay minerals are

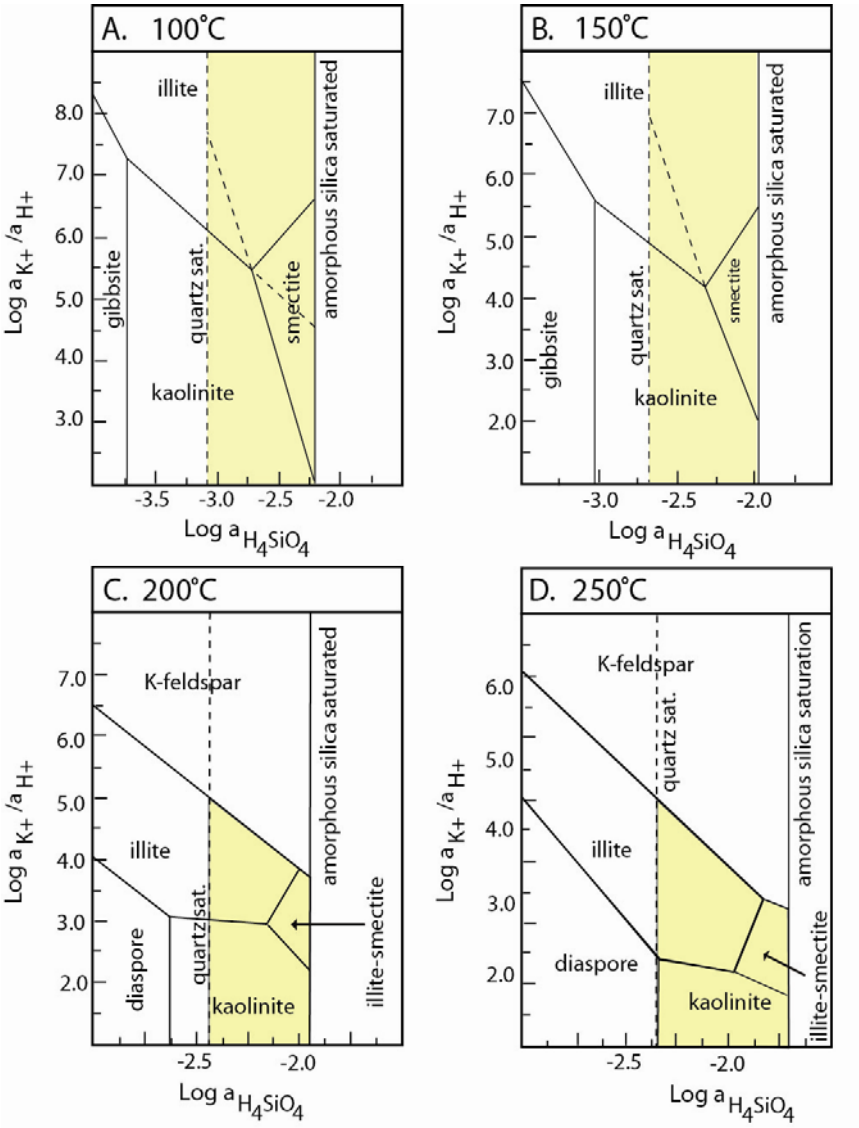

Fig. 2.1. (after Yates and Rosenberg, 1997): Isothermal, isobaric phase diagrams derived from solution equilibration experiments by Yates and Rosenberg (1997) showing the stability fields of illite, illite-smectite and smectite in the simple system K_2O-Al_2O_3-SiO_2-H_2O at 100°C, 150°C, 200°C and 250°C. Natural muscovite/ illite, kaolinite, and quartz or amorphous silica samples were equilibrated in a 2M KCL/HCl solution. Phase boundaries are indicated by solid lines. The Carlin-fluid field (highlighted in yellow) is based on data from previous studies which indicate that mineralizing fluid: (i) is 180-240°C (ii) precipitates quartz, but not amorphous silica as part of the decarbonitization, argillization, silicification and sulfidation alteration sequence(Cline and Hofstra, 2000; Hofstra and Cline, 2000; Lubben, 2004) (iii) does not typically precipitate k-spar/ adularia. Adularia has been identified only at the Twin Creeks deposit, Nevada (Simon et al., 1999; Stenger et al., 1998). As temperature increases, expandable phases in the illite-smectite interlayered clay structure decrease and the overall product tends more toward illite. At 200°C pure, end-member illite appears with no expandable phases; smectite is no longer stable. The smectite field is replaced by illite-smectite interlayered clay. In the range of temperatures associated with ore deposition in Carlin deposits, smectite is not stable, but illite, illite-smectite interlayered clay, and kaolinite are stable depending on fluid composition. These equilibrium experiments indicate that illite and kaolinite can form in a hydrothermal environment within accepted ranges for both fluid temperature and silica content.

stable, and subsequently the different environments in which they form. Smectite is generally not present in rocks at temperatures above 160-200°C (Reyes, 1990; Essene and Peacor, 1995; Yates and Rosenburg, 1995). Kaolinite can occur in low temperature supergene/ diagenetic environments, but also in higher temperature hydrothermal environments in equilibrium with illite (Yates and Rosenberg, 1997). Illite can form from smectite in the following prograde temperature reaction during early diagenesis or from hydrothermal alteration (Iuoup et al., 1988):

$$\text{smectite} + K^+ \rightarrow \text{illite} + H_2O \quad \textbf{(eqn. 2.2.1)}$$

In hydrothermal systems, illite can form via the retrograde alteration of muscovite (Yates and Rosenberg, 1997):

$$\text{muscovite} + H^+ + \text{silica} \rightarrow \text{illite} + K^+ + H_20 \quad \textbf{(eqn. 2.2.2)}$$

Illite can form directly from K-feldspar under diagenetic conditions (2.2.3a) (Moore and Reynolds, 1997) from the initial weathering of igneous rocks (2.2.3b) (Meunier, 1977), and in the presence of an acidic fluid, either surface derived or hydrothermal (2.2.3c) (Faure, 1998) as follows:

$$\text{K-feldspar} + \text{smectite} \rightarrow \text{illite} + \text{chlorite} + \text{quartz} \quad \textbf{(eqn. 2.2.3a)}$$

$$\text{K-feldspar} \rightarrow (\text{illite}) + \text{smectite} + \text{kaolinite} \quad \textbf{(eqn. 2.2.3b)}$$

$$\text{K-feldspar} + H_2O + H^+ \rightarrow \text{illite} + K^+ + \text{amorphous silica} \quad \textbf{(eqn. 2.2.3c)}$$

Equations 2.2.1 and 2.2.2 are favoured for the formation of illite in sedimentary rocks due to the abundance of sedimentary smectite and muscovite in primary sedimentary rock types. In equation 2.3.3b, weathering processes cause K-feldspar to decay initially to illite, but due to the metastability of illite with respect to a low temperature weathering environment, illite quickly reacts to form smectite + kaolinite (Meunier, 1977). Smectite forms from the low temperature (near surface) alteration of aluminosilicate minerals or from shallow diagenesis in sedimentary basin environments.

Inherent problems are associated with studying clay mineral assemblages outside of the laboratory: (i) equilibrium of low temperature clay mineral assemblages may be kinetically inhibited (Essene and Peacor, 1995). There is a risk that low temperature systems never reach equilibrium given that equilibrium is typically attained at elevated temperatures (Essene and Peacor, 1995). Many researchers

assume that the reproducibility of a reaction, such as the smectite ➔ illite reaction, signifies equilibrium conditions. Essene and Peacor (1995) suggest that reproducibility does not necessarily represent equilibrium and that many reactions in nature can be reproducible without representing equilibrium including: the maturation of hydrocarbons during diagenesis, or the precipitation of magnesian calcite or aragonite from seawater. Changes in clay minerals including grain size and composition, may be a function of kinetic factors such as time and fluid-rock ratio, not temperature; (ii) certain aluminosilicate poor lithologies are not favourable to argillization i.e. quartzite, chert, limestone etc. Siliciclastic sediments with low aluminosilicate content may exhibit little to no argillic alteration, specifically no illite alteration unless K^+ is added to the system; (iii) relationships between minerals are difficult to determine due to the fine grained nature of clay minerals. Determining pre-existing minerals from which clay minerals grew is made difficult due to a lack of discerning characteristics between some low temperature clays such as illite and muscovite; and (iv) the origin of clay minerals as products of hypogene, supergene, or diagenetic processes is often difficult to determine due to the wide range of temperatures at which most clays are stable.

2.3 ILLITE THERMOMETRY

Despite the uncertainty regarding equilibrium clay processes, a number of techniques are available to estimate formation temperatures of clay minerals. Clay thermometry techniques provide consistent information on the relationship between crystallinity, morphology, chemical composition, and formation temperature. As a result, these techniques serve as tools for determining temperature of formation, for differentiating between generations of argillization and for distinguishing between supergene and hypogene clay development. Many techniques involved in the characterization of clay minerals are laborious and time consuming (clay separation of different clay size fraction, TEM, SEM, microprobe) and have not found use in the realm of mineral exploration. The advent of rapid analysis tools such as PIMA (portable infrared mineral analyzer) or Terraspec© to identify clay assemblages in the field, has seen the revival of clay thermometry in the context of exploration. One goal of this paper is to determine whether tools such as the PIMA or Terraspec can provide the accuracy necessary to identify potential ore target zones based on clay mineral assemblages. This is accomplished by comparing Terraspec data to data collected by x-ray diffraction.

2.4 ILLITE POLYTYPISM

There are three main illite polytypes: $1M_d$, 1M, and $2M_1$ (Meunier and Velde, 2004). The transition from the $1M_d$ to 1M to $2M_1$ polytype is generally thought to represent a progressive increase in temperature, pressure, reaction time, and/or fluid-rock ratio (Baronnet, 1980; Lonker et al., 1990; Srondon et al., 2001). Low temperature or early stage diagenetic illite was typically thought to occur as the $1M_d$ polytype while $2M_1$ illite represented higher temperature hydrothermal environments or late-stage diagenesis. Continued study of the transition between polytypes suggests that the thermal stability fields of each polytype are poorly defined and that growth mechanisms and kinetics of polytypic transformations play a key role in polytype determination (Baronnet, 1980). Furthermore, illite polytypes have been observed coexisting in the same environment. In the Broadlands Ohaaki geothermal system, 1M and 2M illite co-exist on the nanometer scale (Lonker et al., 1990). Owing to the poorly constrained nature of illite polytypism and the questionable relevance of distinguishing between them, polytypes were not identified in this study.

2.5 ILLITE CRYSTALLINITY

As temperature increases and the crystal structure of illite becomes more ordered, the crystallite or grain particle size of illite increases (Kubler, 1967; Ji and Browne, 2000). The crystallinity of illite can be measured from x-ray diffraction patterns by measuring the full width at half the maximum (FWHM) value of the 10Å (001) illite peak measured in $\Delta°2\theta$. Low FWHM values have been correlated to poorly crystallized illite formed at low temperatures, while high FWHM values correspond to crystalline illite formed at higher temperatures (Kubler, 1967; Warr, 1996). The Kubler index uses measured FWHM crystallinity values to infer temperature in diagenetic and low grade metamorphic environments (Kubler, 1967). According to the Kubler Index, the diagenesis/ anchizone boundary corresponds to temperature values of ~200°C (Frey et al., 1987) and to an FWHM value of 0.42 $\Delta°2\theta$, and the anchizone/epizone boundary corresponds to a temperature of ~300°C and to an FWHM value of 0.25 $\Delta°2\theta$. Kubler (1967) selected these limits on the basis of certain mineralogical changes. The lower anchizone limit coincides with the upper-grade limit of the existence of liquid hydrocarbons, the dickite to pyrophyllite transformation, and finally the loss of interlayer water and the conversion of I-S to pure illite. The upper anchizone limit is associated with the appearance of greenschist facies minerals such as chlorotoid (Kubler, 1967; Kubler and Jaboyedoff, 2000).

Since its initial development, the Kubler index has been standardized to ensure precision between measurements made on different diffractometers. The crystallinity illite standard (CIS) scale, used in this study, provides standards used to calibrate individual diffractometers and correct for differences that exist between different machines, and different clay separation techniques (Warr, 1996). The crystallinity results of this study were calibrated to the standardized scale (the crystallinity index standard, CIS) of Warr (1996) by measuring the same six sets of pelitic rock powder standards used by Warr (1996). Once calibrated to the set of standards, the Kubler index can be applied to the standardized experimental FWHM values. Table 2.1 shows the FWHM values of six clay-separated standards (Warr, 1996) which were used to calibrate the CIS scale for this study. Each standard sample contained illite with a different FWHM value, as determined by Warr (1996).

Table 2.1. Calibration chart showing FWHM values for six standards (Warr, 1996) vs. measured FWHM values calculated in this study for the same standards

Standard Sample ID	FWHM values (Warr, 1996) (Δ°2θ)	FWHM Values (This study) (Δ°2θ)
SW-1	0.63	0.28
SW-2	0.47	0.27
SW-3	0.46	0.23
SW4-4	0.38	0.22
SW5	0.36	0.15
SW6-1	0.25	0.12

A linear regression was calculated using IBM's statistical software package *Predictive Analytics Software* (*PASW) v.18.0*, between the FWHM values measured on the x-ray diffractometer used for this study and the values determined by Warr (1996) (Eqn. 2.2.4). All statistical calculations in this study were performed using *PASW v. 18.0*. The regression was then applied to all FWHM values for samples used in this study.

$$y = 1.794x + 0.041 \qquad \text{Eqn. 2.2.4}$$
$$R = 0.89$$

Where x= FWHM value measured in this study

y = standard value from Warr (1996)

2.6 CLAY TEXTURES AND CLAY MORPHOLOGY

Previous studies indicate that two end-member morphologies of illite exist (Figure 2.2); each representing a different environment of formation (Hancock and Taylor, 1978; Peaver, 1999; Meunier and Velde, 2004; Schleicher et al., 2006). Hexagonal illite is the stable crystal shape of illite and has been empirically observed to form under hydrothermal conditions (Inoue et al., 1988). “Hairy illite” is the metastable crystal shape and is typically observed in the pore-space of sedimentary rocks likely resulting from unconstrained growth in large pore-spaces during diagenetic processes (Peaver, 1999; Schleicher et al., 2006). Meunier and Velde (2004) attribute changes in morphology to temperature. As temperature increases, the crystal shape of illite changes from elongated one-dimensional 'hairy' crystals to more rigid hexagonal laths which increase in width progressively. Bauer et al. (2000) attribute the change between morphologies to reaction progress whereby initial stages of growth result in hairy illite and late stages of growth exhibit hexagonal illite.

However, departures from these end-member morphologies have also been observed. Hancock and Taylor (1978) identified sheeted stacks of illite, typical of hexagonal illite but lacking sharp boundaries. They concluded this was a classic replacement texture. As temperature increased along with depth, a higher temperature mineral (illite) pseudomorphed a pre-existing lower temperature mineral (kaolinite) no longer stable at those temperatures (Hancock and Taylor, 1978). Hancock (1978) describes four different variations of the hexagonal morphology representing progressive stages of diagenesis and therefore increasing temperature: (i) tangential rims where large flakes appear to be formed by a coalescence of much smaller bladed crystals (ii) radial rims where illite flakes protrude radially from grain margins, typically as overgrowths of tangential rims (iii) illite mesh-work where interlocking illite crystals extend far out into porespace (iv) dense homogenous illite whereby illite occurs as large, thick, randomly oriented flakes which are often curves and may result from recrystallization of detrital illite. Studies show that absolute temperature cannot be determined using illite morphology but relative temperatures can be established using variations in both texture and morphology.

2.7 CHEMICAL COMPOSITION OF ILLITE

Modern geothermal environments that are currently precipitating phyllosilicate minerals (Broadlands Ohaaki, Salton Sea, Los Azufres, and Coso) provide robust empirical observations on the positive relationship between temperature and clay mineralogy (Simmons and Browne, 2000; Battaglia,

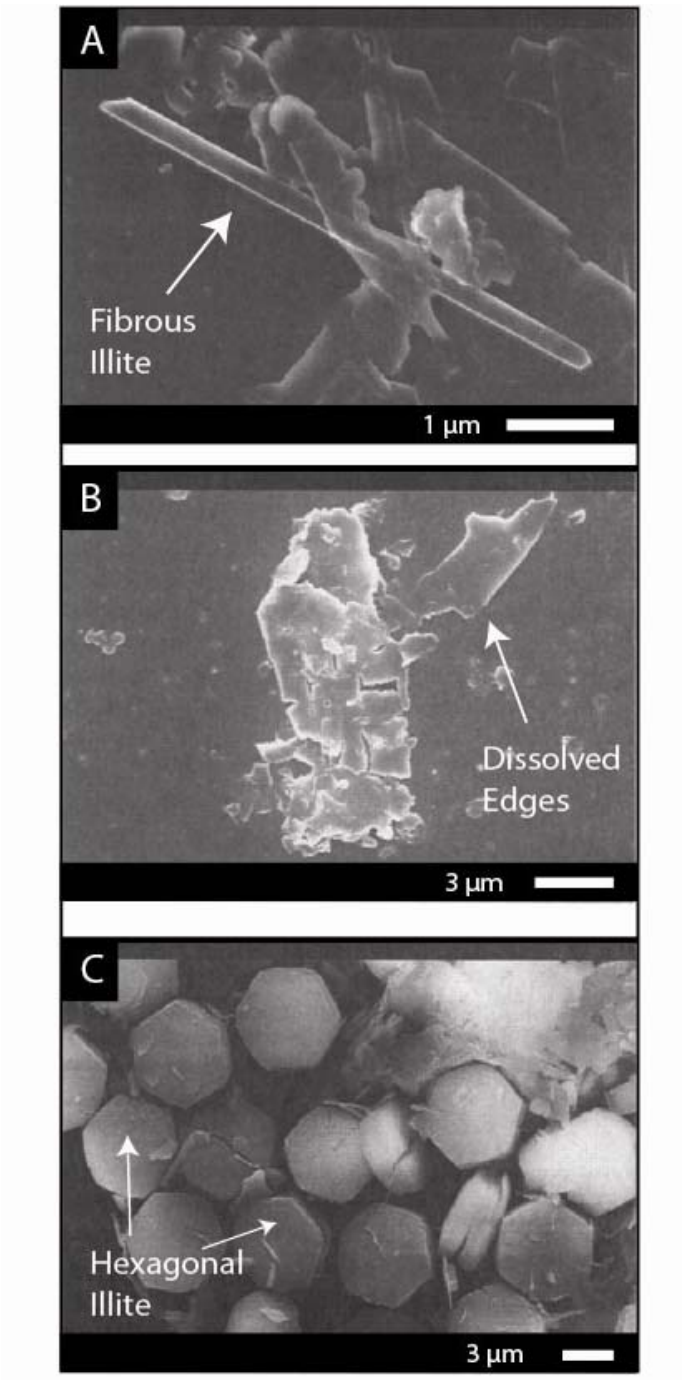

Fig. 2.2. (Modified from Bauer et al., 2000) SEM photographs of synthesis products of micas. A. After 30 days the first lath-shaped "hairy" illite crystals can be observed B. After 210 days the XRD pattern indicates only lath-shaped mica-illite C. After 28 months perfect hexagonal mica-illite crystals can be observed. They are all approximately the same size.

2004). Changes in the chemical composition of illite have been shown to correlate with changes in temperature (Cathelineau, 1988; Battaglia, 2004). As temperature increases, and the crystal structure of illite becomes more ordered, larger cations like Fe and Mg are removed from the interlayer site and replaced by available K (Battaglia, 2004). Therefore, high temperature illite is more potassic than low temperature illite as observed in a compilation of data from the Los Azufres, Salton Sea, and Coso geothermal fields by Cathelineau (1988). However, numerous problems exist with the data of Cathelineau (1988) and are outlined by Battaglia (2004): (i) the relationship between K and temperature is consistent within one geothermal field but absolute temperatures vary between geothermal fields, and (ii) the linear regression lines for data from each geothermal field are not parallel. The data for Coso and Los Azufres geothermal fields are convergent at a K value near 1 (measured in cations), while the regression line for Salton Sea does not converge. The lack of convergence of Salton Sea data is attributed to a lack of elemental Ca in the illite samples analyzed. Hence, [K] alone is not an accurate or consistent proxy for temperature. Based on this previous work completed by Cathelineau (1988), Battaglia (2004) developed a cation-interdependent formula $K{+}|Fe-Mg|$ which appears to be a more robust indicator of temperature.

Figure 2.3 shows data from five geothermal fields around the world which exhibit a linear trend between increases in cation content ($K{+}|Fe-Mg|$) and increases in surrounding temperature. Regression lines are shown in Table 2.2. The best fit linear regression line through illite compositional data acquired by Battaglia (2004) for all five geothermal fields yields a correlation factor of R = 0.84 between temperature and $K{+}|Fe-Mg|$ giving equation (2.2.5):

$$y = 267.95x + 31.46 \qquad \textbf{(Eqn. 2.2.5)}$$

Where $x = K{+}|Fe-Mg|$

Table 2.2. Regression line equations and correlation factors (R) corresponding to data graphed in Figure 6.

	Regression Line Equation	Average Error (%) *	R
Broadlands Ohaaki	$y = 113.19x + 182.59$	5.71	0.72
Coso	$y = 196.47x + 64.00$	10.96	0.97
Salton Sea	$y = 247.68x + 56.36$	4.04	0.96
Los Azufres	$y = 337.93x - 36.57$	7.96	0.79
Aluto Langano	$y = 328.85x - 1.17$	6.73	0.84

*= Measure of average difference between calculated temperatures based on the regression line from all data, and measured temperatures from geothermal well.

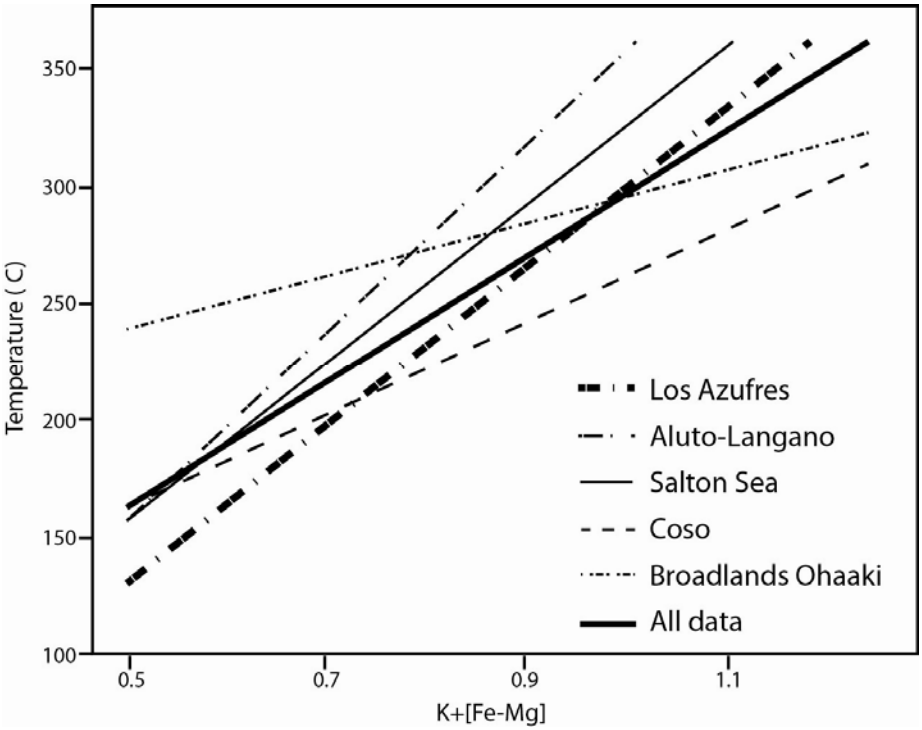

Fig. 2.3. Graph plotting microprobe composition data $K+|Fe-Mg|$ (measured as cations) from five geothermal fields against measured temperatures of those samples presented in Battaglia (2004). Linear regression lines were calculated using *PASW*. A regression line including data from all five geothermal fields is superimposed on individual data groups.

An average error of 7% on the final temperature value was calculated based on the difference between temperature values calculated using the regression line equation, and temperature measured directly from the geothermal well.

2.8 SUMMARY

Variations in the texture, morphology, crystallinity, and composition of clay minerals with temperature can provide information on the temperature at which the minerals formed. There is, however, the possibility that variations in the characteristics of low temperature clay minerals are not in fact solely a function of temperature but instead represent reaction progress (Essene and Peacor, 1995). Temperature is important in order to constrain the origin of clay minerals as either products of hydrothermal alteration or otherwise. In the following chapter, the analytical techniques described in this chapter are applied to clay minerals in sedimentary rocks that occur stratigraphically above and outboard of Carlin-type gold systems to determine whether clay alteration at surface is related to Carlin-type gold mineralization at depth.

2.9 REFERENCES

Baronnet, A., 1980, Polytypism in micas: a survey with emphasis on the crystal growth aspect: Current topics in materials science, v. 5, p. 447-548.

Battaglia, S., 2004, Variations in the chemical composition of illite from five geothermal fields: a possible geothermometer: Clay Minerals, v. 39, p. 501-510.

Bauer, A., Velde, B., and Gaupp, R., 2000, Experimental constraints on illite crystal morphology: Clay Minerals, v. 35, p. 587-597.

Cathelineau, M., 1988, Cation site occupancy in chlorites and illites as function of temperature: Clay Minerals, v. 23, p. 471-485.

Cline, J., and Hofstra, A., 2000, Ore-fluid evolution at the Getchell Carlin-type gold deposit, Nevada, USA: European Journal of Mineralogy, v. 12, p. 195-212.

Essene, E., and Peacor, D., 1995, Clay mineral thermometry-a critical perspective: Clays and Clay Minerals, v. 43, p. 540-553.

Faure, G., 1998, Principles and applications of geochemistry: a comprehensive textbook for geology students: Upper Saddle Riber, New Jersey, Prentice Hall, 600 p.

Frey, M., 1987, Very low-grade metamorphism of clastic sedimentary rocks: Low temperature metamorphism, p. 9–58.

Hancock, N., 1978, Possible causes of Rotliegend sandstone diagenesis in northern West Germany: Journal of the Geological Society, v. 135, p. 35-40.

Hancock, N., and Taylor, A., 1978, Clay mineral diagenesis and oil migration in the Middle Jurassic Brent Sand Formation: Journal of the Geological Society of London, v. 135, p. 69–72.

Hofstra, A., and Cline, J., 2000, Characteristics and models for Carlin-type gold deposits, Chapter 5: in Hagemann, S. G. and Brown, PE, eds., Gold in 2000: Reviews in Economic Geology, v. 13, p. 163-220.

Iuoup, A., 1988, Mechanism of illite formation during smectite-to-illite conversion in a hydrothermal system: American Mineralogist, v. 73, p. 1325-1334.

Ji, J., and Browne, P., 2000, Relationship between illite crystallinity and temperature in active geothermal systems of New Zealand: Clays and Clay Minerals, v. 48, p. 139-144.

Kubler, B., 1967, La cristallinite de l'illite et les zones tout-a-fait superieures du metamorphisme., *in* Schaer, J.P., ed., Colloque sur les etages tectoniques: Baconniere, Neuchatel, p. 105-122.

Kübler, B., and Jaboyedoff, M., 2000, Illite crystallinity: CONCISE REVIEW PAPER: Comptes Rendus de l'Académie des Sciences-Series IIA-Earth and Planetary Science, v. 331, p. 75-89

Lanson, B., and Champion, D., 1991, The I/S-to-illite reaction in the late stage diagenesis: American Journal of Science, v. 291, p. 473-506.

Lanson, B., Velde, B., and Meunier, A., 1998, Late-stage diagenesis of illitic clay minerals as seen by decomposition of X-ray diffraction patterns: Contrasted behaviors of sedimentary basins with different burial histories: Clays and Clay Minerals, v. 46, p. 69-78.

Lonker, S., FitzGerald, J., Hedenquist, J., and Walshe, J., 1990, Mineral-fluid interactions in the Broadlands-Ohaaki geothermal system, New Zealand: American Journal of Science, v. 290, p. 995-1068.

Lubben, J., 2004, Quartz as clues to paragenesis and fluid properties at the Betze-Post deposit, northern Carlin trend, Nevada: Unpublished M.Sc. thesis, Las Vegas, Universitty of Nevada, p. 155.

Meunier, A., 1977, Les mechanismes de l'alteration des granites et le role des microsystemes: tude des arenes du massif granatique de Parthenay (Deux-Se vres): PhD. Thesis, 248 p.

Meunier, A., and Velde, B., 2004, Illite: origins, evolution, and metamorphism: Poitier, France, Springer Verlag, 286 p.

Moore, D., and Reynolds Jr, R., 1997, X-ray diffraction and the identification and analysis of clay minerals, 378 p, Oxford University Press, New York.

Peaver, D., 1999, Illite and hydrocarbon exploration: Proceedings of the National Academy of Sciences, v. 96, p. 3440-3446.

Reyes, A., 1990, Petrology of Philippine geothermal systems and the application of alteration mineralogy to their assessment: Journal of Volcanology and Geothermal Research, v. 43, p. 279-309.

Rose, A., 1970, Zonal relations of wallrock alteration and sulfide distribution at porphyry copper deposits: Economic Geology, v. 65, p. 920-936.

Schleicher, A., Warr, L., Kober, B., Laverret, E., and Clauer, N., 2006, Episodic mineralization of hydrothermal illite in the Soultz-sous-Forêts granite (Upper Rhine Graben, France): Contributions to Mineralogy and Petrology, v. 152, p. 349-364.

Simon, G., Kesler, S., and Chryssoulis, S., 1999, Geochemistry and textures of gold-bearing arsenian pyrite, Twin Creeks, Nevada; implications for deposition of gold in Carlin-type deposits: Economic Geology, v. 94, p. 405-422.

Simmons, S., and Browne, P., 2000, Hydrothermal minerals and precious metals in the Broadlands-Ohaaki geothermal system: Implications for understanding low-sulfidation epithermal environments: Economic Geology, v. 95, p. 971-999.

Srodon, J., Drits, V., McCarty, D., Hsieh, J., and Eberl, D., 2001, Quantitative X-ray diffraction analysis of clay-bearing rocks from random preparations: Clays and Clay Minerals, v. 49, p. 514-528.

Stenger, D., Kesler, S., Peltonen, D., and Tapper, C., 1998, Deposition of gold in carlin-type deposits; the role of sulfidation and decarbonation at Twin Creeks, Nevada: Economic Geology, v. 93, p. 201-215.

Varadachari, C., 2006, Fuzzy phase diagrams of clay minerals: Clays and Clay Minerals, v. 54, p. 616-625.

Warr, L., 1996, Standardized clay mineral crystallinity data from the very low-grade metamorphic facies rocks of southern New Zealand: European Journal of Mineralogy, v. 8, p. 115-127.

Whitney, G., and Northrop, H., 1988, Experimental investigation of smectite-to-illite reaction--dual reaction mechanisms and oxygen-isotope systematics: American Mineralogist, v. 73, p. 77-90.

Yates, D., and Rosenberg, P., 1997, Formation and stability of endmember illite: II. Solid equilibration experiments at 100 to 250 C and Pv, soln: Geochimica et Cosmochimica Acta, v. 61, p. 3135-3144.

CHAPTER 3 – BEYOND THE CONFINES OF THE ORE BODY: SURFACE MAPPING OF LOW TEMPERATURE HYDROTHERMAL FLUID ABOVE MAJOR ORE BODIES USING CLAY ALTERATION

3.1 INTRODUCTION

The passage of hydrothermal fluid through the Earth's crust is invariably accompanied by mineral alteration (Giggenbach, 1981, 1984; Reed, 1997). The degree to which mineral assemblages change is a function of multiple factors: temperature, pressure, time, fluid chemistry, initial rock composition and fluid-rock ratio (Reed, 1997). Alteration associated with mineral deposits commonly extends outboard from the ore body providing robust vectors toward the core of those deposits (Figure 3.1). In alteration halos around low temperature hydrothermal systems, gradients in temperature and chemical composition between mineralizing hydrothermal fluid and host rock can be small. With increasing distance from the core of the hydrothermal system, thermal and chemical gradients between hydrothermal fluid and country rock decrease until a point where no gradient exists between fluid and rock. The distal expression of low temperature hydrothermal systems may be dominated by mineral assemblages also resulting from near surface processes including weathering, shallow diagenesis, and other overprinting hydrothermal events. Tools that identify subtle variations between low temperature minerals which in turn help distinguish between different generations of minerals are required to assess the extent of hydrothermal alteration, and to use that alteration to vector in toward mineralization at depth (Adams and Putnam, 1992; Kelley et al., 2006). However, the use of low temperature minerals to investigate geological problems has been criticized due to the inability of most low temperature assemblages to reach equilibrium causing nanoscale variations in composition (Essene and Peacor, 1995, 1996). Under disequilibrium conditions, properties such as crystallinity, crystal morphology, or composition might represent reaction progress rather than spatial variation in temperature (Essene and Peacor, 1995).

Clay minerals form a large component of low temperature alteration assemblages and have been documented in different settings including: geothermal systems (Simmons and Browne, 2000; Yang et al., 2001), epithermal deposits (White and Hedenquist, 1995), the distal extents of porphyry deposits (Rose, 1970; Tosdal, 2009; Sillitoe, 2010), and diagenetic environments (Meunier and Velde, 2004). Geothermal systems provide current information on low temperature systematics including clay

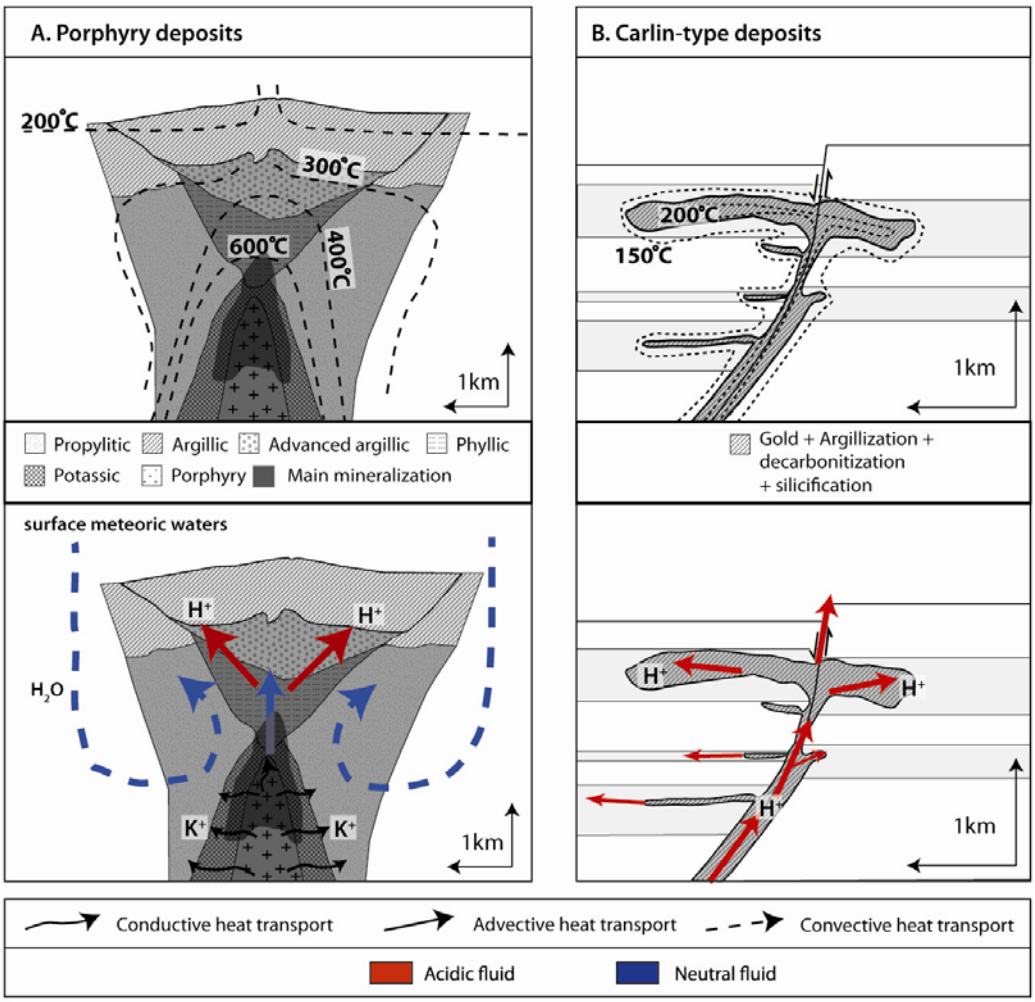

Fig. 3.1. The distal extent and degree of alteration around ore deposits is a direct function of thermal and chemical gradients between country rock and hydrothermal fluid. A. Black dashed lines represent steady state thermal contours resulting in mineral alteration. Porphyry type settings exhibit large thermal and chemical gradients. Initially, hot (>700°C) magma intrudes cold (<200°C) country rock. Hot magmatic fluid alters country rock immediately around the magma body via conduction. Convection cells of circulating pore fluid are generated at the sides of the intrusion. Heat is carried from the intrusion by advection as fluid travels through fractures forming networks of veins. As magmatic fluid travels upward and decreases in temperature, acids dissociate and the fluid becomes acidic. The lower temperature acidic fluid interacts with country rock to produce argillic alteration. As the pluton cools, cold, near-neutral surface meteoric water is drawn into the core of the system resulting in the hydrolysis of minerals and propyltic alteration which may overprint other stages of alteration. Visible alteration in a porphyry system can extend kilometers away from mineralization, with distal alteration assemblages containing minerals significantly different to unaltered host rock assemblages i.e. sericite ± illite ± kaolinite B. In low temperature systems such as the Carlin-type Au systems, there may be little temperature gradient between the incoming fluid (200°C) and the shallow crust (~75°C), resulting in the subtle mineral alteration assemblage illite ± dickite ± kaolinite at the core of the system. Fluid flow is focused along permeable pathways whereby heat is carried primarily by advection. Chemical gradients in low temperature systems may be large, as shown here whereby acidic fluid causes the decarbonatization of permeable carbonate horizons. Visible alteration however is often subtle and may extend as little as a few metres away from mineralized fluid pathways. Distal to the core of the hydothermal system, there may be no difference between the hydrothermal mineral assemblage and the unaltered host rock mineral assemblage (Modified from Sillitoe, 2010; Tosdal et al., 2009; Reed, 1997).

mineral reaction kinetics and timescales of fluid flow. Clay minerals have been used to map out networks of fluid flow pathways in geothermal systems by identifying zonation patterns of clay minerals around upwelling regions of hydrothermal fluid (Simmons and Browne, 2000). Illite, a high temperature clay mineral, occurs within and proximal to fluid conduits. Smectite, a low temperature clay mineral, occurs most distal to fluid pathways with illite-smectite interlayered clay (I-S) between (Simmons and Browne, 2000). Clay mineral mapping can also be used to determine relative proximity to mineralization (Figure 3.1) (Rose, 1970; Seedorf et al., 2005; Sillitoe, 2010). In the idealized alteration model of a porphyry deposit (Rose, 1970, Tosdal et al., 2009), the phyllic assemblage consisting of quartz-sericite (muscovite)-pyrite occurs most proximal to the magmatic heat source where temperature is highest. Argillic alteration assemblages consisting of illite ± kaolinite indicate progressive acidification of the fluid, decreasing temperature with distance from the core of the system, and possibly interaction with surface derived waters (Tosdal et al., 2009).

Another method to trace fluid flow is by the advection of heat. Because heat is transported by an infiltrating fluid at a rate greater than all but the most incompatible of geochemical tracers, transient heating associated with hydrothermal flow is quite likely to be one of the most distally developed expressions of a hydrothermal mineral deposit (Bickle and McKenzie, 1987). Because heat is not only transported by the fluid itself, but also diffuses rapidly outward from fluid flow pathways, the volume of rock affected by the thermal energy of a hydrothermal system will be significantly larger than that recorded by mineralogical alteration and isotopic resetting. The thermal footprint of low temperature systems can be identified using low temperature thermochronology including apatite fission tracks and U-Th/He in apatite and zircon (Chakurian et al., 2003; Cline et al., 2005; McInnes et al., 2005; Arehart and Donelick, 2006; Kelley et al., 2006; Hickey et al., unpublished data).

The Carlin deposits of northern Nevada are one of the world's major sources of gold (Teal and Jackson, 2002; Price et al., 2007). Carlin-type gold deposits are an example of low temperature (180-240°C) hydrothermal systems that exhibit subtle alteration associated with mineralization, making them a difficult target for exploration. In this study, we investigate the ability of low temperature analytical methods to identify hydrothermal alteration manifested distal to the core of Carlin-type gold mineralization by characterizing clay mineral assemblages with respect to paleo-formation temperature, chemistry, crystallinity and morphology. We also provide insight into a combination of analytical techniques that exhibit the highest potential to deliver reliable and robust exploration vectors for low temperature hydrothermal ore deposits in the subsurface.

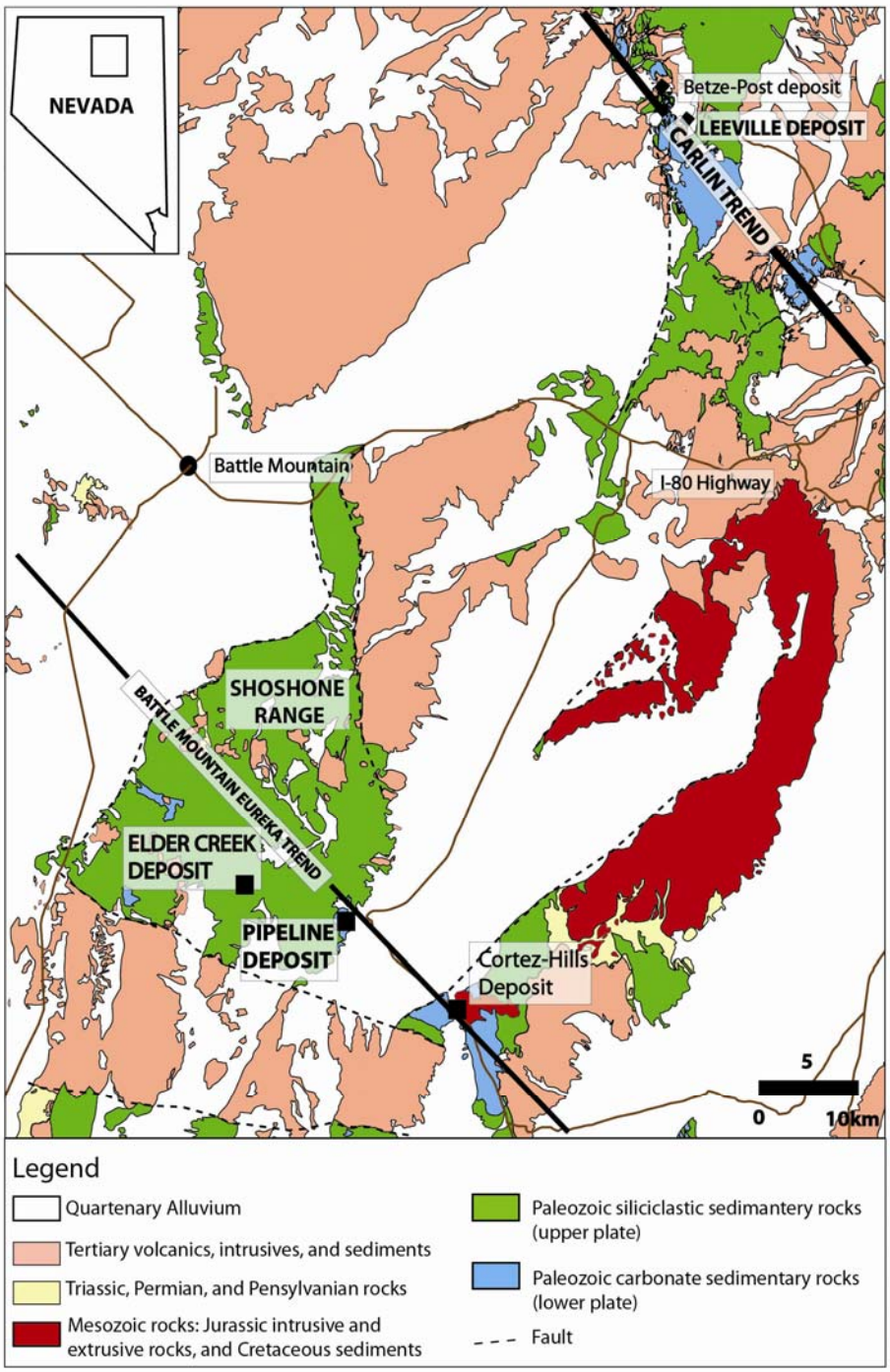

Fig. 3.2. Regional geology map of northeastern Nevada showing location of significant Carlin-type mineral deposits including those discussed in this paper.

Apatite fission track thermochronology data spanning across northeastern Nevada highlighted potential regions of hydrothermal flow around existing Carlin-type deposits. Based on AFT data, two study areas (Figure 3.2), were chosen with the intent of (i) identifying zones of hydrothermal clay alteration using currently available clay thermometers and (ii) establishing whether hydrothermal alteration at surface exhibited a genetic link to Carlin-type ore deposits at depth. The Leeville deposit, (Figure 3.3) is located along the northern Carlin trend, south of the Tuscarora Mountains and is hosted in lower plate rocks immediately beneath the RMT with a few hundred metres of upper plate material preserved above. In this field area, upper plate material was sampled above mineralization to determine whether Carlin-deposit forming fluid had exhausted through the upper plate to surface. The second field area chosen for this study was the Shoshone Range, host to a number of Carlin-type gold deposits that form the Battle Mountain Eureka mineral belt. The giant Pipeline deposit, located at the southeastern end of the Shoshone Range was a starting point for sample collection in an area of known Carlin-style mineralization in lower plate carbonate rocks. From the Pipeline deposit, a northwest trending transect was sampled to determine the aerial extent of alteration in upper plate rocks outboard from a site of known mineralization.

3.2 GEOLOGICAL SETTING OF CARLIN-GOLD DEPOSITS

During the period from Cambrian - Devonian, passive margin miogeoclinal and eugeoclinal sequences were deposited along the rifted margin of western North America (Morrow and Sandberg, 2008). Multiple episodes of compression from Devonian to Cretaceous led to eastward directed thrusting of miogeoclinal rocks on top of eugeoclinal rocks. In northeastern Nevada, there is one main thrust sheet, the Roberts Mountain allochthon (locally termed ‘upper plate’) which has the Roberts Mountain Thrust (RMT) fault at the base. Footwall rocks (‘lower plate’) consist of shelf and slope silty carbonate rocks and are the main host for Carlin-type gold mineralization. The upper plate lacks any major Carlin-type Au deposits although mineralization does occur locally immediately above the RMT in several of the lower plate-hosted deposits.

A tectono-stratigraphic column of lower Paleozoic rocks is presented in Figure 3.4. In most areas, thick sequences of upper plate siliciclastic rocks cover lower plate carbonate rocks, however post-Antler orogeny tectonism and erosion have exposed geologic windows into the lower plate as exhibited at Goat Peak (north-western Shoshone Range), and at the Pipeline deposit locality (south-western Shoshone Range) (Kelson et al., 2008). Structurally, both the upper and lower plates are imbricately thrusted with tight, upright to westward-inclined folds caused by the eastward transport of material

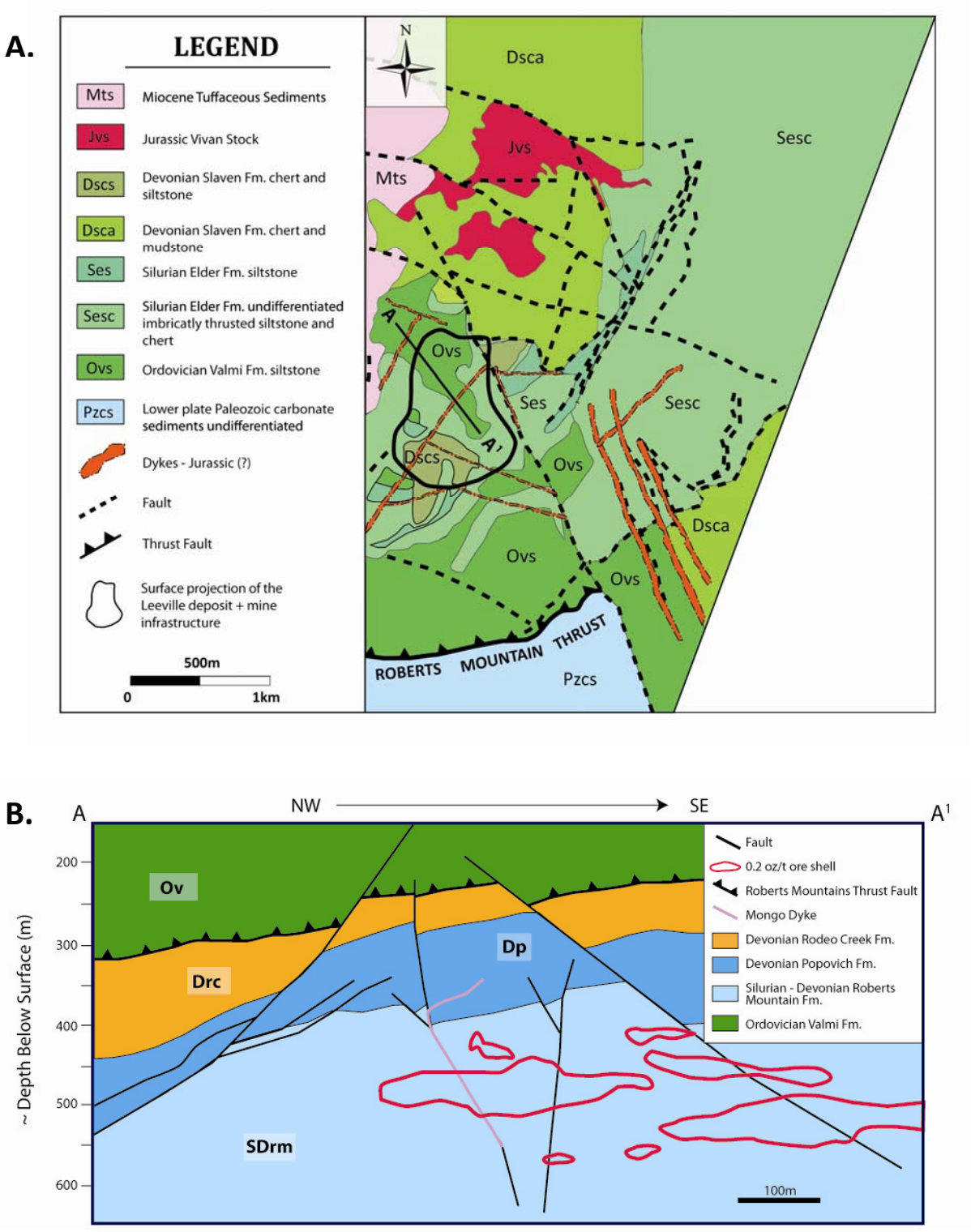

Fig. 3.3. A. Geological map of the Leeville deposit study area. The Roberts Mountain Thrust fault separates Lower Paleozoic upper plate siliciclastic rocks to the North from Lower Paleozoic lower plate carbonate rocks in the South. B. Cross section A –A^1 through the Leeville deposit shows the presence of at least 250m of upper plate siliciclastic rock cover above the main ore zones of the Leeville deposit.

Fig. 3.4. (modified from Bettels et al., 2002 *in* Emsbo et al., 2003) Simplified tectono-stratigraphic column showing lower Paleozoic rocks of the RMT system. Variation in formation names between the Battle Mountain – Eureka trend (left) and Carlin trend (right) are shown. During the Mississippian Antler Orogeny, lower Paleozoic siliciclastic sediments (upper plate) were thrust eastward overtop of lower Paleozoic carbonate sediments (lower plate). Carlin-type gold deposits are typically hosted in lower plate rocks.

during orogenic events dating from the Devonian to late Cretaceous (Noble and Finney, 1999). Subsequent deformation includes broad open folding accompanied by oblique-slip faulting, Mesozoic to Cenozoic low angle faulting, and high angle normal faulting associated with Basin and Range extension (Winterer, 1968; Cluer et al., 1997).

The lower plate of the RMT can be subdivided into four main units (Emsbo et al., 2003). The Devonian Horse Canyon Formation/Rodeo Creek Formation is a calcareous siltstone, mudstone and chert with local occurrences of sandstone and mudstone. The Devonian Wenban Formation/ Popovich Formation is composed of laminated calcareous to dolomitic siltstones, micritic limestone, and thick bioclasitc debris flows. The Silurian Roberts Mountain Formation is dominated by laminated dolomitic and calcareous, and calcareous mudstone and calcareous siltstone. The Ordovician Hanson Creek Formation is a sandy dolomite. The overlying upper plate comprises dominantly siliciclastic units with the rare occurrence of thin carbonate lenses. The Ordovician Valmi/ Vinini Formation is composed of several thousand meters of chert, quartz arenite, argillite, slate, and greenstone (Roberts, 1951). The Silurian Elder Formation is a set of interbedded shale, siltstone, chert, and feldspathic and calcareous sandstone. The Devonian Slaven Formation is a mixture of highly contorted and broken, black, nodular chert with some carbonaceous shale partings.

Paleozoic rocks are intruded by Mesozoic and Cenozoic intrusive rocks (Ressel and Henry, 2006). Igneous rocks of the Shoshone Range include Eocene-Pliocene intermediate to felsic intrusions with basalt, andesite and rhyolite flows and tuffs. Eocene intrusions were emplaced along a west-northwest trend and have been identified both proximal and distal to economic gold mineralization (Gilluly and Gates, 1965; Stager, 1977; Kelson et al., 2005). The Gold Acres stock is a Cretaceous quartz monzonitic pluton located at the southeastern edge of the Shoshone Range proximal to the Pipeline deposit (Mortensen et al., 2000). A thorough compilation of data on the igneous rocks of the Carlin trend by Arehart et al. (2004) and Ressel and Henry (2006) suggest three periods of magmatism in the Northern Carlin trend: Jurassic, Cretaceous, and Eocene. Jurassic intrusions consist of the Goldstrike laccolith and related sills and mostly northwest-striking lamprophyre and rhyolite dikes ~158 Ma (Ressel and Henry, 2006). The Vivian sill exposed at surface and the Little Boulder Basin stock located at depth in the Leeville area have been interpreted as south-eastern extensions of the Goldstrike laccolith (Ressel and Henry, 2006). Cretaceous magmatism is characterized by one occurrence ~4km south of the Leeville deposit. Concordant Pb/U ages of two zircon fractions demonstrate intrusion at 112.4 +/- 0.6 Ma (Mortensen et al., 2000).

3.3 CHARACTERISTICS OF CARLIN GOLD DEPOSITS

Carlin gold deposits are restricted to a small geographic area in northeastern Nevada. The Carlin, Battle Mountain-Eureka, and Getchell Trends describe three regional lineaments along which the majority of Carlin-deposits are focused, including those described in this study (Figure 3.2). The alignment of Carlin-type deposits is thought to reflect major crustal faults established during Neoproterozoic rifting (Roberts, 1966; Tosdal et al., 2000). Lower plate Paleozoic carbonate shelf rocks are the favourable hosts for Carlin gold mineralization (e.g., Cortez Hills, Pipeline, Carlin, Goldstrike, Leeville, and Jerritt Canyon). This has been attributed to the reactivity of carbonate sediments with acidic gold-bearing fluid resulting in mass loss and increased permeability, providing robust pathways for Au-bearing fluid (Cline et al., 2005). Conversely, upper plate rocks are largely devoid of gold mineralization likely due to a lack of reactivity with these same gold bearing fluids. Upper plate rocks of the RMT are however host to base and precious metal deposits including Miocene Au-Ag epithermal deposits, Eocene porphyry deposits, and a limited number of Carlin-type gold deposits i.e. Alligator Ridge (Nutt and Hofstra, 2003), Emigrant (Newmont Mining Company, unpublished data), and Mike (Norby and Orobona, 2002). The Elder Creek deposit, considered in this study, is a small gold deposit located in the Central Shoshone Range. Gold is hosted predominantly in quartzite clast breccia of the Valmi Formation and also within pyrite-rich argillite and shale of the Elder Formation (Ahmed et al., 2010).

Fluid inclusion and mineral thermometry data indicate that mineralizing fluid forming Carlin deposits in north-eastern Nevada were: low temperature (180-240°C), slightly acidic (pH ~4), low-salinity (~2–3 wt% NaCl equivalent) aqueous fluids that contained CO_2 (<4 mol %) and CH_4 (<0.4 mol %), and sufficient H_2S (10^{-1}–10^{-2} mol/kg) to transport Au and other bisulfide-complexed metals (Cline and Hofstra, 2000; Hofstra and Cline, 2000; Lubben, 2004). Stable isotope analyses have provided insight into the source of mineralizing fluid in Carlin-type deposit settings. δD_{H2O} values measured on ore-stage kaolinite and fluid inclusions from a wide-range of Carlin deposits suggest evidence of meteoric water with very low δD_{H2O} values of < -110‰ (Hofstra et al., 1999). Similar data from the Getchell, Twin Creeks, and Deep Star deposits indicate the additional presence of deeply sourced metamorphic or magmatic fluid (Hofstra, 1999; Heitt et al., 2003; Cline et al., 2005). Clay samples from Carlin-deposits appear to form along a mixing line between Eocene-age meteoric water and magmatic or metamorphic fluid.

3.3.1 Clay alteration in Carlin-type systems

The following characteristics are known of alteration in Carlin-type settings: (i) quartz is precipitated as part of the silicification alteration sequence, but not amorphous silica (Bakkan and Einaudi, 1986; Cline and Hofstra, 2000; Cline, 2001; Ye et al., 2003), and (ii) K-feldspar has not been observed in Carlin type systems except for the presence of adularia at the Twin Creeks deposit (Stenger et al., 1998; Simon et al., 1999). According to clay equilibria (Figure 2.1), constraints on temperature (180-240°C), fluid chemistry (pH~4), and observed mineralogy indicate that smectite is not stable, but illite, I-S, and kaolinite are stable depending on variations in fluid chemistry. Illite and kaolinite can form from the same hydrothermal event within a confined range of fluid temperature and silica content. For kaolinite and illite to form from the same fluid, without forming K-feldspar, log a_{K+}/a_{H+} values are estimated to be in the range of 2.0-5.0 (Yates and Rosenberg, 1997).

Similar to patterns observed in geothermal systems, clay zonation has been observed in lower plate carbonate rocks around ore shoots of the Getchell deposit, a Carlin-type gold deposit located in North Central Nevada (Cail and Cline, 2001). Illite was shown to occur in higher volume % with ore, and proximal to ore whereas smectite occurred distal to ore. Both 1M and $2M_1$ polytypes have been observed spatially associated with mineralization in Carlin type environments (Carlin, Kuehn and Rose, 1992; Betze-Post, Arehart et al., 1993b; Deep Star, Heitt et al., 2003).

The absence of major Carlin-type gold deposits in the upper plate suggests that ore fluids responsible for mineralization of the lower plate must have followed one of three fluid evolution pathways shown in Figure 3.5. Either exhausted fluid did not transgress the upper plate and all fluid was exhausted laterally along the RMT, or exhausted fluid transgressed the upper plate and reacted with siliciclastic rocks forming an alteration halo above lower plate gold mineralization. Upper plate rocks contain little to no carbonate, precluding the potential for observing decalcification. Silicification of upper plate rocks would be a challenge to identify given the high silica content of upper plate lithologies. The stage of alteration with the most potential to be observed in upper plate rocks is argillization: illite ± dickite ± kaolinite due to the presence of pre-existing aluminosilicate minerals in some lower Paleozoic sedimentary lithologies.

3.4 THERMAL SIGNATURE OF HYDROTHERMAL FLUID FLOW

AFT has conventionally been applied to a number of geological problems (Gallaghar et al., 1998): (i) resolving the thermal history of sedimentary basins; (ii) investigating the provenance of rocks; (iii)

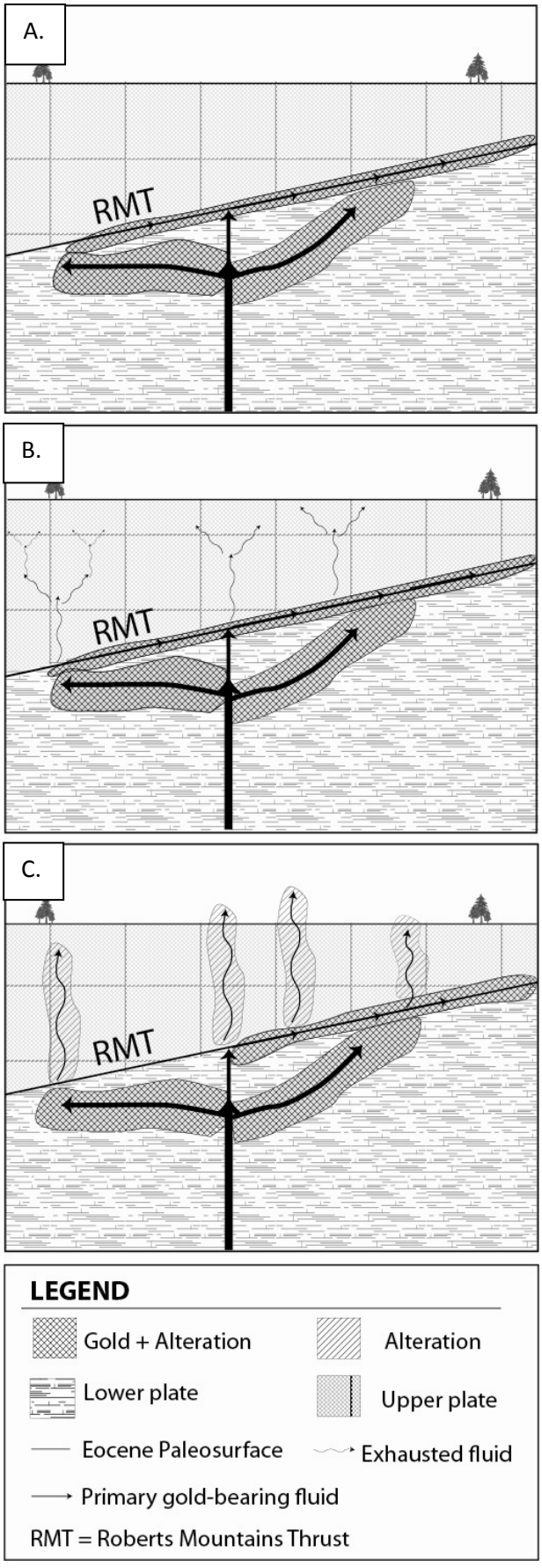

Fig. 3.5. The absence of major gold deposits in the upper plate suggests that ore fluids responsible for mineralization of lower plate carbonate rocks must have followed one of three fluid evolution pathways: A. following gold mineralization of the lower plate, fluid was dominantly rock buffered but still contained a small amount of gold. Fluid flowed upward to the RMT, exploiting pre-existing fault and fracture networks, precipitating gold along the fluid flow-path. Fluid was exhausted laterally along the RMT to surface. The upper plate was largely impermeable to exhausted ore fluids and behaved as an aquitard. This scenario supports observed mineralization of rocks along the RMT. In the scenario described, upper plate siliciclastic rocks would exhibit no signs of alteration due to a lack of interaction with the exhausted Carlin-fluid B. mineralizing fluid was dominantly rock buffered but still contained a small amount of gold. Fluid flowed upward through a network of small-scale fractures becoming increasingly rock-buffered along the flow path. Upon reaching the RMT the fluid precipitated a small amount of gold. Fluid was exhausted laterally along the RMT and also through faults and fractures in upper plate siliciclastic rocks. The upper plate exhibits no signs of Carlin-type alteration because the fluid was completely rock buffered by the time it encountered the upper plate C. largely unbuffered mineralizing fluid was partially exhausted laterally along the RMT and the remainder transgressed upper plate siliciclastic rocks. Sustained fluid-rock interaction between siliciclastic upper plate rocks and partially rock buffered Carlin-type fluid produced a thermal and chemical signature in upper plate rocks.

studying the deformation history of orogenic belts, and (iv) interpreting the conductive heating history around magmatic intrusions. Recent studies show that fission track analysis can also be used to identify regional and deposit scale patterns of hydrothermal fluid flow (Chakurian et al., 2003; Hickey, 2003; McInnes et al., 2005; Arehart and Donelick, 2006; Hickey et al., 2010). The maximum 180-240°C ore-stage fluids responsible for Carlin-type mineralization have the capacity to reset the AFT thermochronometer system on timescales of 10^4-10^6 years (Hickey et al., 2010). Mapping the extent of thermal resetting may assist in delineating the far-field extent of Carlin hydrothermal systems at distances beyond any wall rock type alteration.

Chakurian et al. (2003), Hickey (2003), and Cline et al. (2005) have used AFT data to examine the regional thermal history of the northern Carlin Trend. Results from thermochronological studies of the Northern Carlin trend (Figure 3.6) indicate that areas of Carlin-type mineralization are spatially coincident with pooled AFT ages ranging from 50-25 Ma. All thermochronological data used in this study is included in Appendix B. Areas of young AFT ages lie within large scale regions of Cretaceous or older AFT ages reflecting the pre-mineralization regional cooling history. The thermal effects of the Carlin-hydrothermal system were superimposed on the older regional pattern. Young apatite fission track ages correspond to episodes of transient reheating. Advective heating by circulating hydrothermal fluids appears to be the primary cause of thermal resetting, shown by the heterogeneous nature of fission track ages in the region. This is evidenced by the lack of major reheating in unaltered portions of large Jurassic stocks (i.e., Goldstrike, and Vivian stocks), and total thermal resetting of highly altered, mineralized material in the same stocks. A strongly argillized, mineralized dyke from within the Leeville deposit is partially reset to 44.5 ± 3.0 Ma.

New apatite fission track data of samples from the Shoshone Range are presented along with published data from Arehart and Donelick (2006) in Appendix B. Figure 3.7 shows a map of the Shoshone Range on which results from a geophysical magnetics survey has been superimposed along with pooled apatite fission track ages. The central part of Shoshone range exhibits a mixed population of ages ranging from 20.3-77.4 Ma. A single sample from the western margin of the range exhibits an older age of 108.2 Ma. The older age may represent the western margin of hydrothermal resetting. The southeastern Shoshone Range exhibits dominantly Eocene ages, likely related to the same hydrothermal event responsible for gold mineralization of the Pipeline deposit (Arehart and Donelick, 2006). Younger ages within the Pipeline pit and on the margins of the deposit are likely a result of late Miocene extension and uplift. The northwest Shoshone Range exhibits dominantly young Miocene ages which can be explained two ways: (i) The magnetic high observed in the northwestern Shoshone Range in

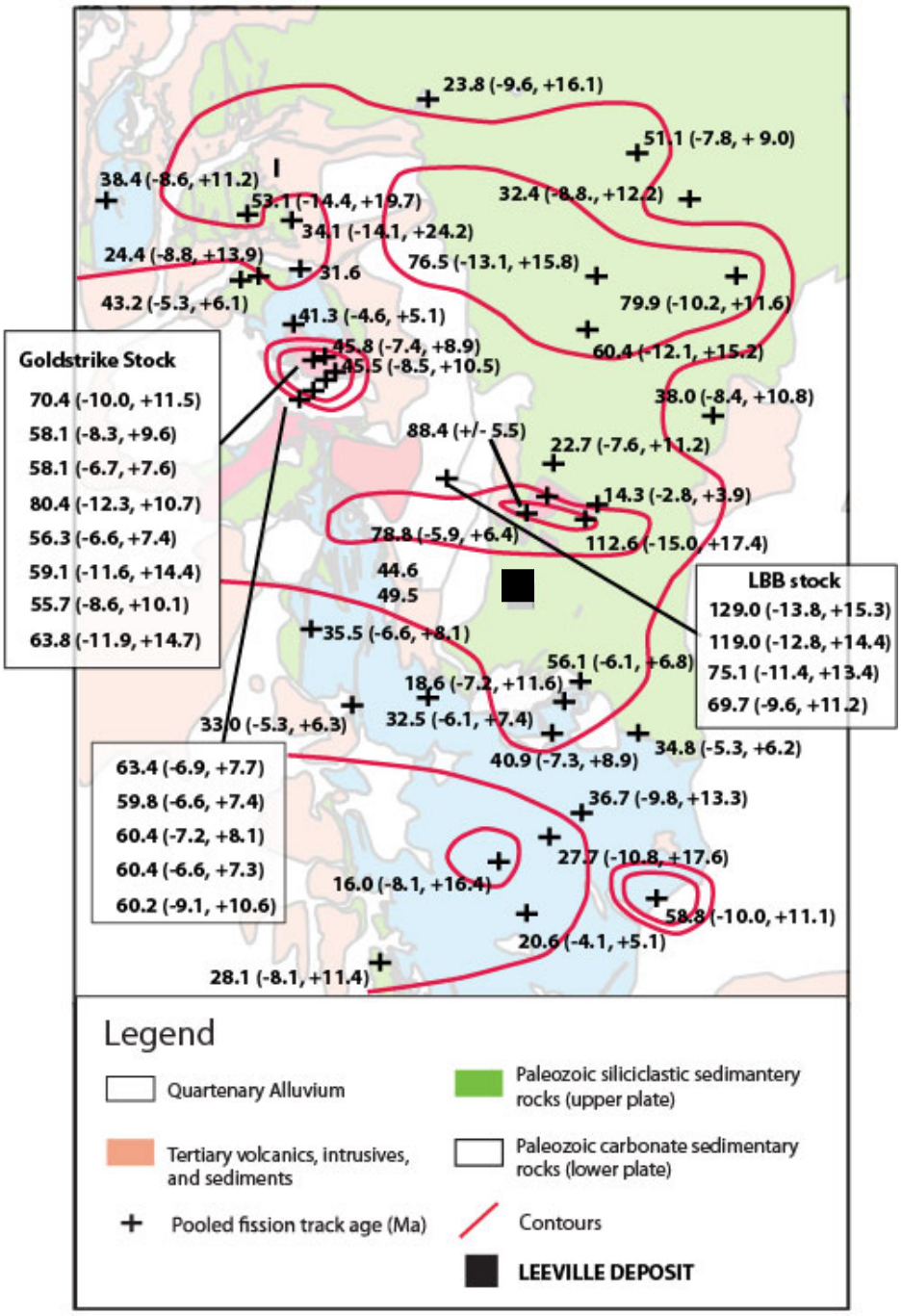

Fig. 3.6. Compilation of apatite fission track ages across the Northern Carlin Trend (Chakurian et al., 2003; Cline et al., 2005; Hickey et al., 2010). A zone of pervasive annealing preserves evidence for an episode of rapid cooling from > 100°C at ~40 Ma., with localized annealing of fission tracks as late as ~20 Ma. The zone of annealing is broadly parallel to the Carlin trend and becomes more heterogeneously distributed and less pervasive farther to the northwest, toward the Post-Betze-Screamer and Meikle deposits (Hickey et al., 2003b). Dyke samples from within the Leeville deposit are totally reset to 44.6 and 49.5 Ma. The Vivian stock is reset to 88.4 Ma, an age that likely represents exhumation (Hickey et al., 2003).

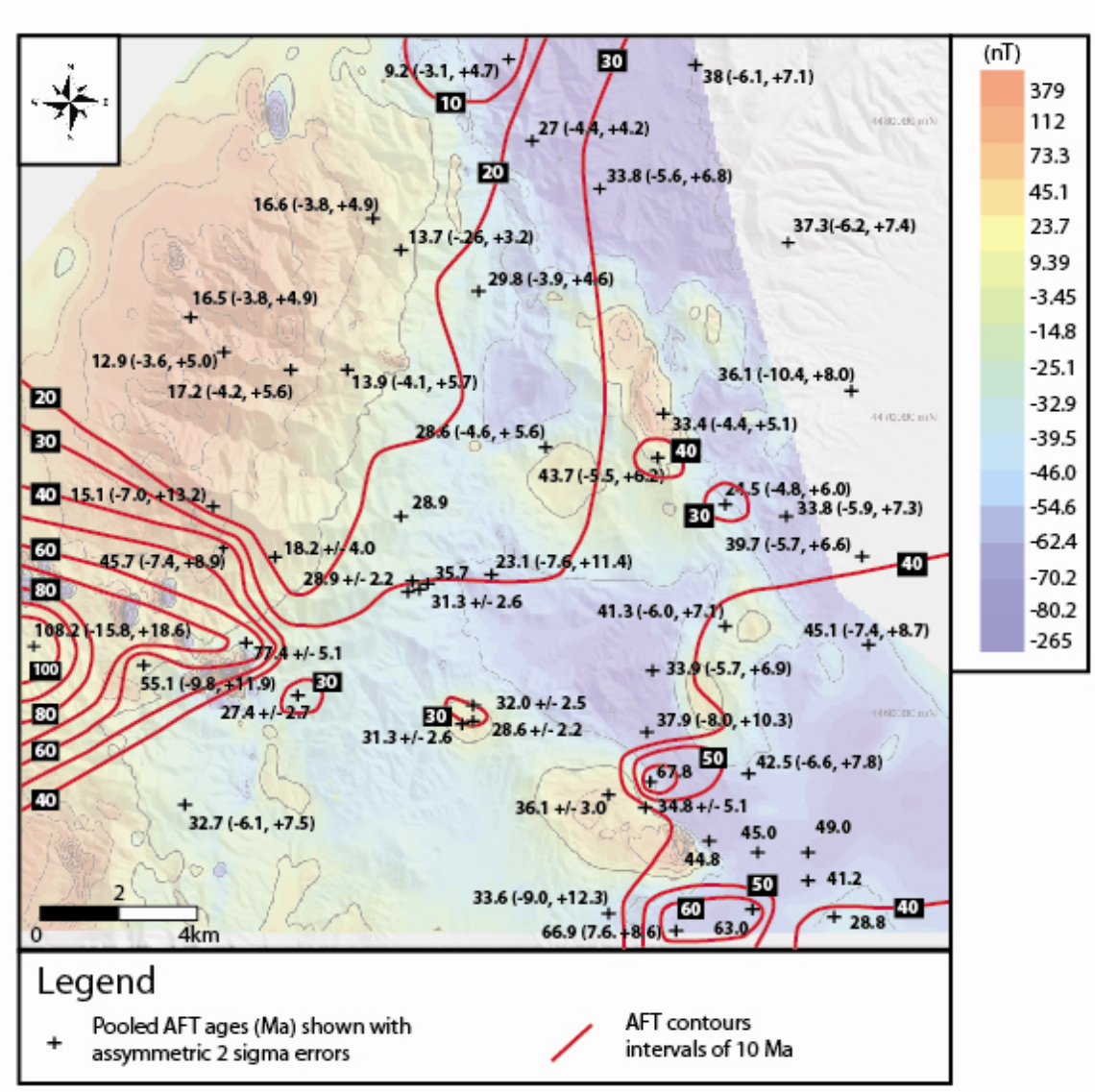

Fig. 3.7. Compilation of apatite fission track pooled ages across the Shoshone Range plotted on a reduced to pole magnetics map with a DBM (database management) overlay. The image was provided by Placer Dome Inc. The northwestern Shoshone Range is dominated by younger ages representative of either Miocene magmatism and related Au-Ag mineralization, or extensive exhumation during the Miocene. The southeastern portion of the Shoshone Range, the location of the Pipeline and Gold Acres deposits is reset to ages between 36-47Ma, coincident to Eocene Carlin-type gold mineralization. The rest of the Shoshone range exhibits ages of mixed populations. A group of older AFT ages (108.2, 77.4, and 55.1 Ma) occur at the far western margin of the Shoshone Range.

Figure 3.7 is a large buried intrusion of Miocene age. Conductive heating and hydrothermal fluid flow associated with the intrusion thermally reset fission track ages in that region. Dissipation of heat outboard from the intrusion resulted in a mixed population of ages in the central Shoshone Range, or (ii) The Miocene was a period of major uplift and exhumation of the northwestern Shoshone Range. A study of the regional topography of the area shows a N-S trending fault along the length of the central Shoshone Range which may have caused significant uplift of the upthrown block, resulting in a 'younging' of AFT ages across the fault from SE to NW . Caetano Tuff, dated at 32.3 Ma (Naeser and Mckee, 1970), has been identified at the eastern and western margins of the Shoshone Range and suggests that Miocene exhumation would have to have been restricted to only the northwestern region of the Shoshone Range.

3.5 ANALYTICAL TECHNIQUES

A number of techniques were employed to measure the variation in clay type, illite crystallinity, illite morphology, and illite composition across the Leeville and Shoshone Range areas. Two different methods were applied to identify clay minerals: the Terraspec analytical spectral device and x-ray diffraction. These two methods were chosen to compare the accuracy of rapid analysis mineral identification tools such as the Terraspec© and PIMA© to the more conventional and standardized technique of x-ray diffraction. A review of the techniques used in this study is presented in Chapter 2.

3.5.1 Near and Short Wave Infrared Analysis (Terraspec©)

The Terraspec analytical spectral device (ASD) uses near and shortwave infrared technology to measure the vibrational energy between bonds in a mineral. The Terraspec and similar tools such as the PIMA have been used as a rapid analysis technique to indentify alteration mineralogy in a variety of ore deposit settings (Uranium deposits: Zhang et al., 2001; Pb-Zn-Ag deposit: Sun et al., 2001, Geothermal systems: Yang et al., 2001).

In this study, ~2.5cm^3 blocks of each sample were analyzed using the Terraspec© analytical spectral device. Multiple readings were taken of each sample and the nature of the material being analyzed (fracture, matrix, vein) recorded. Smear mounted samples of whole rock and clay separated fractions were analyzed with the Terraspec©, however this type of sample preparation yielded nearly aspectral results, the reasons for which are unknown. The reflectance spectra collected using the

Terraspec were interpreted both manually and with the aid of the interpretive software *The Spectral Geologist*© (Merry et al., 1999).

3.5.2 X-ray diffraction

Clay minerals were identified using x-ray diffraction in both whole rock samples and clay separates. Clay separation was performed on whole rock samples, according to the methods outlined by Moore and Reynolds (1997) to obtain the <2 μm fraction, the accepted maximum particle size for clay minerals based on a spherical volume diameter (Johns et al., 1954). 50-100g of sample was disaggregated in a Blendtec© blender with 200ml of distilled water for a period of time between 0.5-1 minute. Higher silica content required longer periods of disaggregation. Following initial disaggregation, the solution was probed with a 500 watt ultrasonic probe for a time between 2 minutes and 10 minutes depending on silica content. The fines from this solution were then decanted into 50ml test tubes. The test tubes were placed in a centrifuge at 2000rpm for 2 minutes. The test tubes were removed and the fines decanted, probed by the ultrasonic device and distributed into new test tubes. The solute remaining at the bottom of the test tube was categorized as the coarse fraction (>25μ). The second round of centrifugation lasted for 5 minutes. The solute remaining from this run was termed the moderate fraction (5-25μ). Following separation of the moderate fraction, the fines were decanted, probed, and centrifuged for 1-2 hrs or until the water remaining ran clear. The remaining solute was termed the fine fraction (<2-5μ). If after 2 hrs the remaining water was still cloudy, the solution was left to settle by gravity. The solute remaining following settling was termed the ultra fine fraction and contained an average grain size of 1μ. Grain sizes were determined by scanning electron microprobe imaging of powdered clay-separated grain mounts using the ruler application.

Air-dried smear mounts were prepared for each fraction of all clay separated samples. 1-2 grams of clay-separated material was mixed with ethanol by mortar and pestle. The resulting paste was placed onto a glass slide according to the methods of Moore and Reynolds (1997). Smear mounts were analyzed by a Bruker D500 and Bruker D8 diffractometer for angles between 0 and 80° 2θ for 18 minutes. Following initial XRD analyses, samples were saturated with glycol to determine the presence of smectite. Samples were placed in a petri dish with a small amount of glycol and set in an oven set at 60°C for 5hrs. The resulting diffraction patterns were then analyzed using the interpretation software EVA©. The location and FWHM of the 001 smectite, illite, and kaolinite peaks were measured. I-S was distinguished from discrete illite and smectite phases by characteristic differences in their respective diffraction patterns. I-S was present if one or more of the following criteria were met: a significant

decrease in the FWHM value of illite following glycolation due to a loss of interstitial water during heating, joint 001 illite and smectite diffraction peaks with no separation between peaks, and/or asymmetry of the 001 illite and smectite peaks (Meunier and Velde, 2004).

X-ray diffraction peak intensity has been directly correlated to abundance and is a method by which to estimate relative quantities of minerals (Alexander and Klug, 1948; Pierce and Siegel, 1969; Ouhadi and Yong, 2003). Relative abundances of illite, smectite, and kaolinite were calculated using the area measured underneath the 001 diffraction peak of each mineral in the <2 μm clay fraction. The amount of I-S was not calculated due to presence of overlapping peaks between IS, illite, and smectite. Calculation of relative peak areas for the quantification of minerals has been used by many researchers however this method has been shown to underestimate certain minerals while overestimating others (Ouhadi and Yong, 2003). We do not suggest that these values are perfectly accurate, but provide information on relative abundances of minerals. In a subset of samples, relative abundances calculated using peak areas were compared to modal abundances estimated by thin sections and were determined to be in agreement. In the majority of samples analyzed in this study, one mineral occurs in much greater abundance than other minerals in the same sample. Accordingly, any error associated with quantitative calculation using peak areas is unlikely to affect the category into which each clay assemblage is placed.

3.5.3 Scanning Electron Microscope (SEM)

Scanning electron microscopy (SEM) was used to characterize the morphology of illite in this study. Additionally, SEM was used to identify the existence of paragenetic relationships between clay minerals. Polished thin sections were analyzed using backscattered electron imaging and smear mounted samples, and randomly oriented powder mounts were analyzed using secondary electron imaging. A 15kv 10μ beam was used. Energy dispersive spectra (EDS) and chemical element maps were analyzed to determine the bulk chemical composition of minerals.

3.5.4 Electron Microprobe Analysis

Mineral analyses of illite were obtained by wavelength dispersive x-ray analysis on a Cameca SX-50 Scanning Electron Microprobe with 4 vertical wavelength-dispersion x-ray spectrometers and a fully-integrated SAMx energy-dispersion X-ray spectrometer. The following parameters were used: an accelerating voltage of 15kV, a beam current of 10nA, and a beam diameter of 10μ. 20-50 points were

probed from each sample depending on the abundance of illite. Two types of illite textures were probed: tight knit aggregates of illite and long euhedral laths of illite. Tight knit aggregates of illite consisted of dozens of grains of illite woven together into 10-100 μm wide masses. Multiple probe points were collected from within each aggregate and from the same grains. Only one type of texture occurred in each sample. Some illite could not be probed because the aggregates were too small (less than the spot size of the beam), or the texture of the illite surface was too rough and would cause inconsistencies in the compositional results. Illite compositions were carefully checked for evidence of any contamination from grains of other minerals inadvertently included in the broad microprobe beam. Initial statistical analyses were conducted on all data points. Specific points were later rejected if the data did not satisfy the following criteria: 85.0% < oxide total < 100% determined by a lack of interlayer H_2O in pure end-member illite and oxide totals used in other studies (Gaudette et al., 1966; Hunziker et al., 1986), and K:Al:Si:Mg:Na:Ca similar to the structural formulae outlined by Gaudette et al. (1966) and Meunier and Velde (2004) where K-values are ~0.8 (cations).

3.5.5 Stable Isotope Analysis

Nine samples (~20mg each) of clay separated (<2μ) material were analyzed at the Queen's Facility for Isotope Research at Queen's University in Kingston, Ontario for oxygen and hydrogen stable isotope analysis using GasBench II, EA, and TC/EA technology and a DELTA^{plus}XP Stable Isotope Ratio Mass Spectrometer. The purpose of these analyses was to help constrain the origin of clay minerals in this study. Along with chemical composition, the oxygen isotope signature of clay minerals can provide information on the origin of water from which the clay formed. Fractionation factors calculated for the distribution of $^{18}O/^{16}O$ and D/H between kaolinite-water, illite-water, and smectite-water are a function of source fluid temperature; the effects of pressure are less than analytical uncertainty (Taylor, 1974; Gilg and Sheppard, 1996; Hoefs, 2009). Fractionation decreases as temperature increases (Gilg and Sheppard, 1996; Taylor, 1974). As such, supergene clay minerals can be distinguished from hypogene clay minerals by observing a relative enrichment or depletion in $\delta^{18}O$ and δD.

3.6 SAMPLES

The samples collected in this study are largely restricted to siliciclastic sedimentary rocks of the lower Paleozoic Roberts Mountain Allochthon (upper plate). A small subset of samples was taken from lower Paleozoic carbonate rocks (lower plate) in and around the Pipeline and Gold Acres pits, and Goat

window. The rationale for sample collection in this study was to identify variation in clay species over a broad spatial extent while sampling a diverse range in primary rock types both proximal and distal to hydrothermal centres. Over 450 samples were collected for Terraspec analysis and a subset of 73 samples was selected for x-ray diffraction analysis. Not all samples collected for Terraspec analysis could be analyzed using x-ray diffraction due to difficulty in processing quartz-rich samples for clay separation. As such, sample density is low in the area between the Pipeline deposit and the Elder Creek deposit owing to the low clay content and the presence of abundant quartzite and chert. Samples represent a broad range of primary rock types with varying percentages of total clay content (Figure 3.8). Clay minerals occur in the pore-space and matrix of sedimentary rocks (S), as thin (<20cm) clay seams (CS) occurring parallel to sedimentary bedding, as alteration products of feldspar and muscovite in intrusive rocks (I), as matrix material in breccia (BX), as a thin veneer along fault surfaces and in fault gouge (FG). Brackets denote the abbreviation used in subsequent tables. Samples collected with low percentages of total clay were mostly confined to aluminosilicate poor, quartzose sedimentary rocks including quartzite, chert, and mudstone. Samples were not taken directly above the Leeville property owing to the presence of mine infrastructure; however two samples were collected from mineralized dykes within the Leeville deposit. A list of all samples collected providing location, and lithology is included in Appendix C. A map of samples locations from the Leeville deposit is shown in Figure 3.9.

3.7 RESULTS

3.7.1 Morphology and textural relationships of clays

Scanning electron microphotographs of the clay minerals in this study are shown in Figure 3.10. In all samples imaged of both sedimentary and non-sedimentary protolith, illite, illite-smectite and smectite form stacks of ‘pseudo-hexagonal’ shaped crystals. The terms ‘hexagonal’ and ‘hairy’ were defined in section 2.2. The term ‘pseudo’ is employed here to denote a lack of definite hexagonal grain boundaries (Schleicher et al., 2006; Hancock, 1978; Hancock and Taylor, 1978). Crystal boundaries are

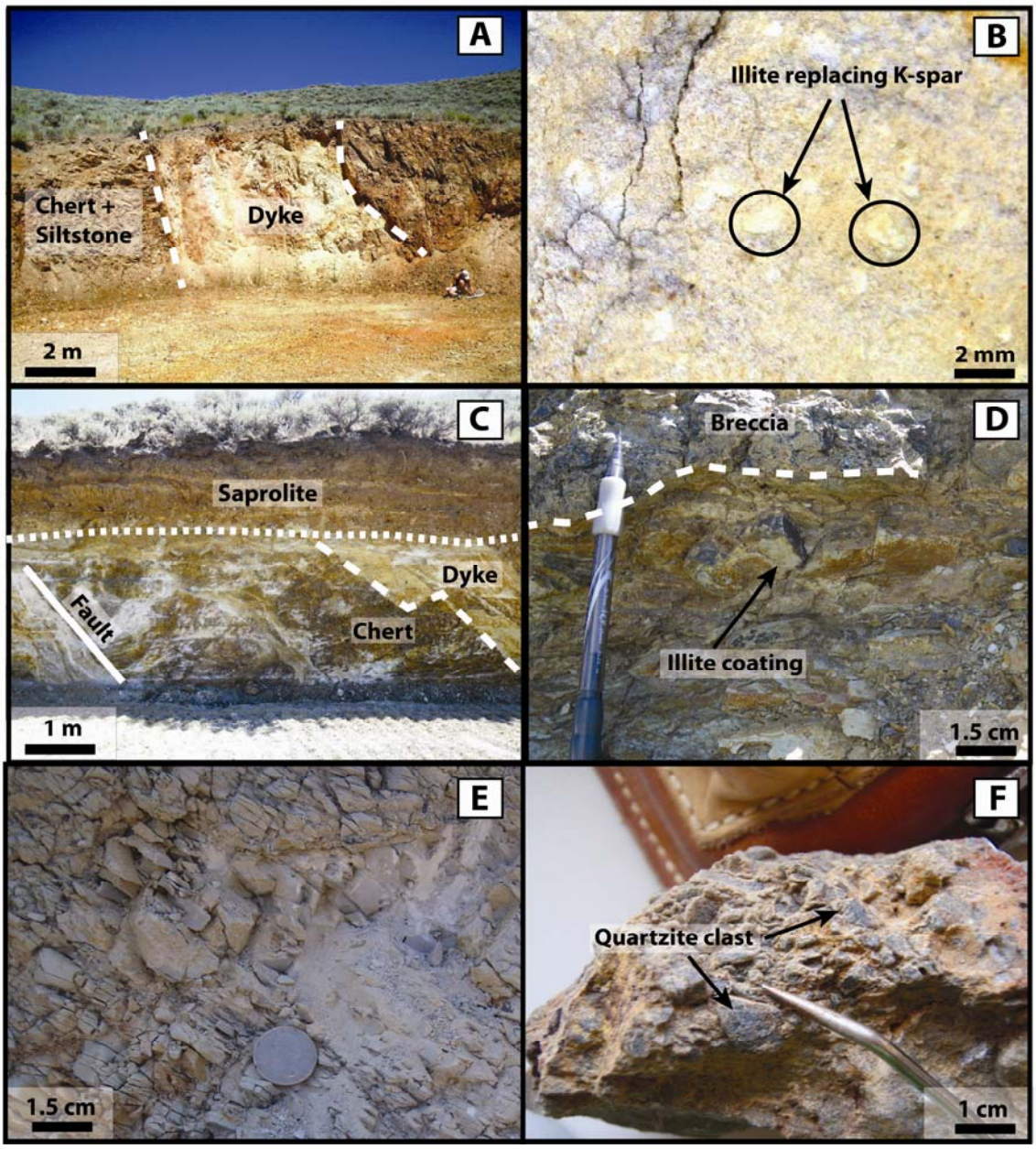

Fig. 3.8. Samples were collected from zones of strong argillization and from phyllosilicate-bearing rocks representing a wide range of lithologies. A. Strong kaolinite and illite altered dyke at the southeast end of the Leeville property B. Magnified photograph of the same argillized intrusion from A. Illite and smectite are replacing k-feldspar phenocrysts and intrusive matrix material C. Argillized fault gouge (white, left) adjacent to a strongly illite and smectite altered dyke (right) with relatively unaltered chert immediately adjacent to the dyke D. Mudstone clast breccia (top) with illite matrix from the North end of the Leeville property. Illite occurs as a thin veneer coating the bottom of intact mudstone beds (bottom) E. Illite-bearing siltstone from the Elder Creek deposit, Shoshone Range F. Quartzite clast breccia with illite and quartz matrix from the Elder Creek deposit, Shoshone Range.

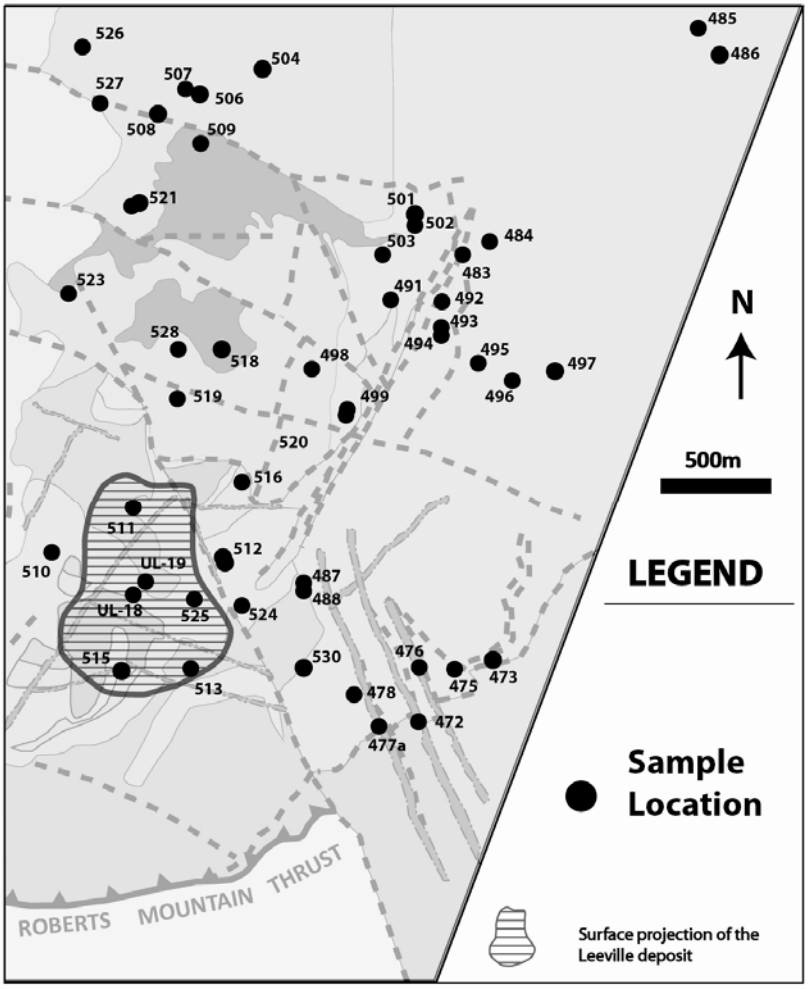

Fig. 3.9. Sample location map for the Leeville study area.

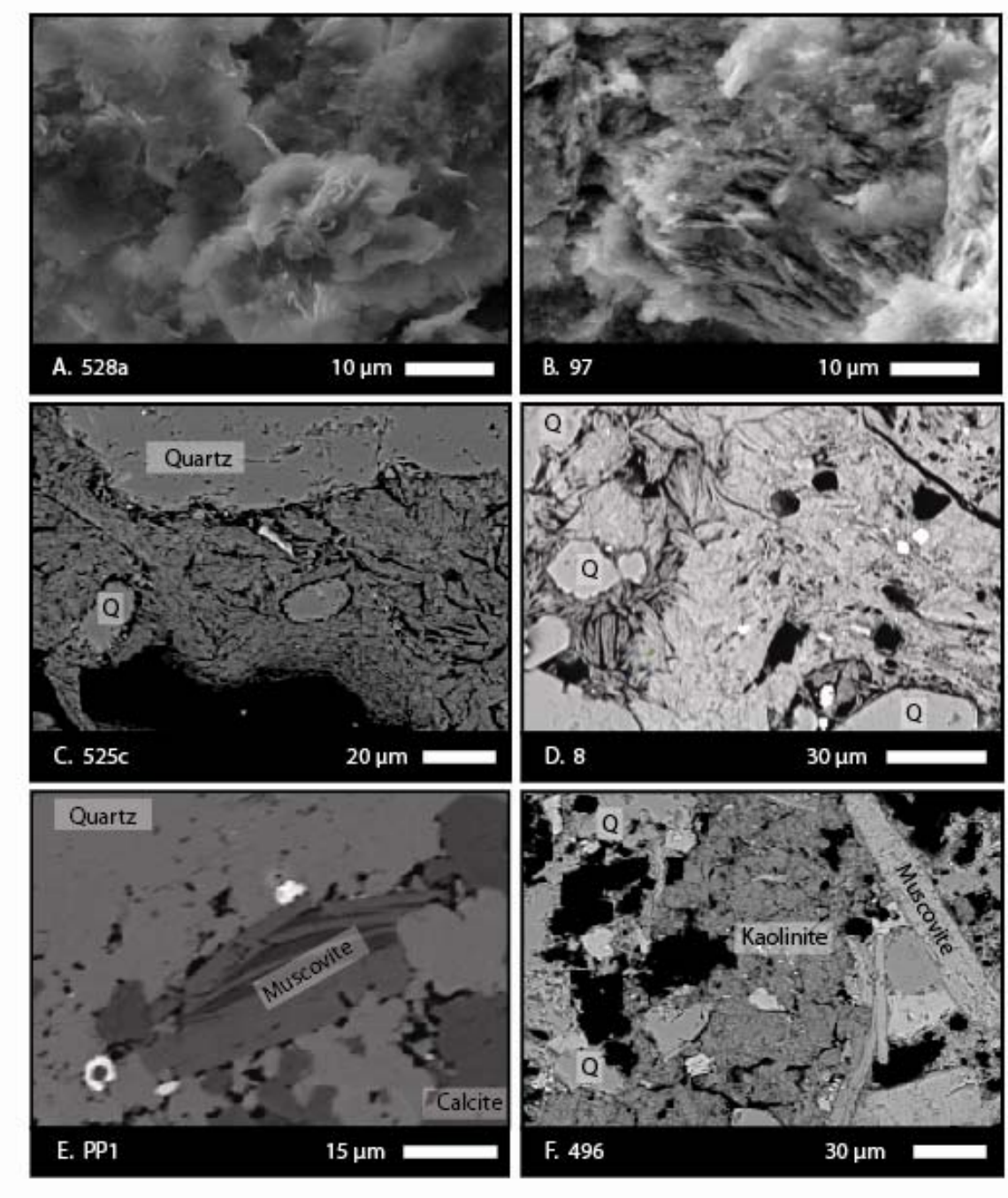

Fig. 3.10. Scanning electron microscope images showing the morphology of clay minerals. A-B. Randomly oriented powder grain mounts of the <2µ size fraction of illite. A. The crystal shape of illite is pseudo-hexagonal with rough crystal edges. All the illite analyzed in this study is of the same morphology. B. Illite crystals are not randomly oriented but occur as stacks of pseudo-hexagonal illite grains. C-F Back scatter images C. Illite occurs as tightly knit aggregates of illite booklets. D. The tightness of each aggregate appears to be related to the amount of space available for growth of the illite crystals. On the left side of the photograph, illite crystals are not as tightly spaced as on the right hand side. E. Muscovite occurs as long euhedral laths with one good cleavage. F. Kaolinite occurs in a similar texture to illite, in tightly knit aggregates of crystals. The morphology of kaolinite crystals could not be resolved from SEM imaging.

ragged and uneven similar to the pseudomorphing replacement texture described by Hancock and Taylor (1978) and possibly akin to the dissolved edges observed between end-member growth stages by Bauer et al. (2000). Needle-shaped or 'hairy' illite were not observed in any of the samples in this study. The pseudo-hexagonal shape of illite may represent the middle stage of a reaction from 'hairy illite' to hexagonal illite (Bauer et al., 2000) or single stage illite formation at temperatures on the higher end of illite stability (Meunier and Velde, 2004).

In both sedimentary and igneous rocks, muscovite occurred as elongate euhedral laths with visible unidirectional cleavage. Muscovite was differentiated from illite and smectite by shape and size. Furthermore, muscovite, often partially replaced by illite, exhibited higher potassium contents in energy dispersive spectra (EDS) than illite and smectite. For the purposes of this study, muscovitic illite is defined as very crystalline illite replacing euhedral muscovite laths visible in thin section and SEM. The term 'Illite' is restricted to samples containing tightly knit aggregates of illite. The fine grained nature of kaolinite inhibited the imaging of its crystal shape. Illite, smectite and kaolinite occur in spatially distinct, tightly knit fibrous aggregates set between quartz, feldspar, and muscovite crystals in both igneous and sedimentary rocks. Aggregates of illite, smectite, and kaolinite were similar to the dense homogeneous texture observed by Hancock (1978) indicative of the latest stage of growth formation in the context of diagenesis.

Paragenetic relationships between illite and kaolinite were difficult to determine based on SEM imaging (Figure 3.11). X-ray element mapping of potassium helped to distinguish between illite and kaolinite in samples containing both minerals. Illite can occur without kaolinite. Kaolinite can also occur without illite. Illite and kaolinite are observed texturally intergrown as fine grained aggregates, and occur simultaneously replacing laths of euhedral muscovite. The spatial occurrence of illite and kaolinite together does not necessarily indicate the synchronous growth of the two minerals. Synchronous growth of illite and kaolinite is however, indicative of specific temperatures and fluid chemistry (Figure 2.1).

3.7.2 Spatial distribution of clays -Leeville

X-ray diffraction pattern data for samples from the Leeville area are outlined in Table 3.1, which includes calculated relative abundances of illite, kaolinite, and smectite in the <2 μm clay fraction. Estimates of total undifferentiated clay content in each sample are given in Appendix C. Figure 3.12a

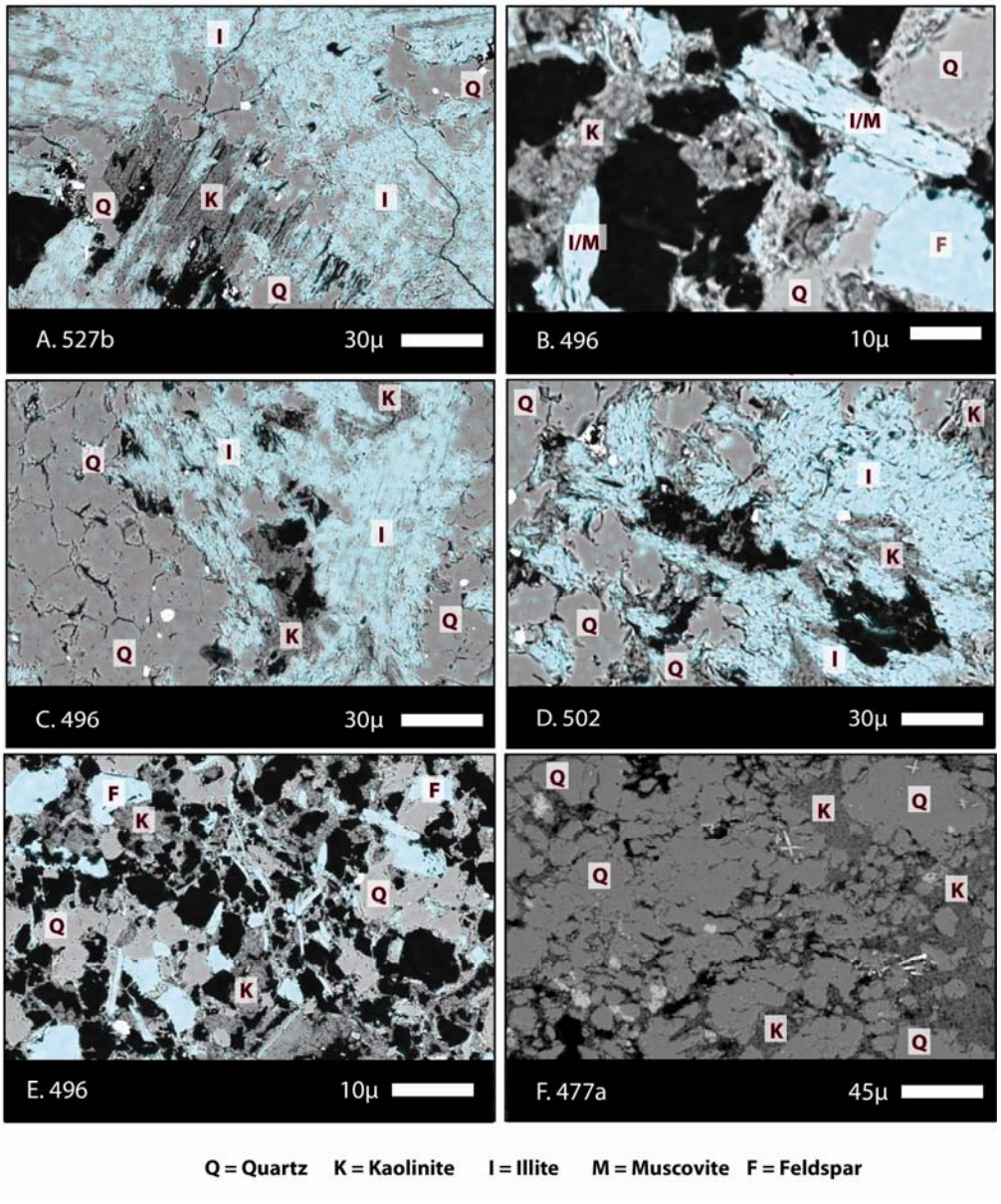

Fig. 3.11. Scanning electron microscope (SEM) back-scatter images with x-ray element maps for potassium overlain, illustrating the complex textural relationship between illite and kaolinite. The timing of growth for these minerals could not be determined by SEM imaging. Illite, muscovite and k-feldspar are highlighted in blue, while kaolinite (potassium deficient aluminosilicate) and quartz are grey. A. Intergrown kaolinite and illite partially replacing muscovite lath in strongly argillized intrusive rock. Illite also occurs as fine grained aggregates between quartz grains. B. Fine grained aggregates of kaolinite between long euhedral laths of muscovite in an arkosic sandstone. Energy dispersive spectrometry data indicate a low potassium content of muscovite in this sample as compared to other muscovite samples indicating the potential of a partial replacement by illite C. Intergrown fine grained aggregates of kaolinite and illite in the same lithology as B. Illite appears to be the dominant mineral replacing a broken euhedral lath of muscovite. D. Illite and kaolinite are intergrown as fine grained aggregates in a strongly fractured and oxidized quartzite sample. E. Arkosic sandstone sample containing kaolinite feldspar and muscovite, and lacking illite. F. Patchily hematized clay fault gouge containing quartz and kaolinite, lacking illite.

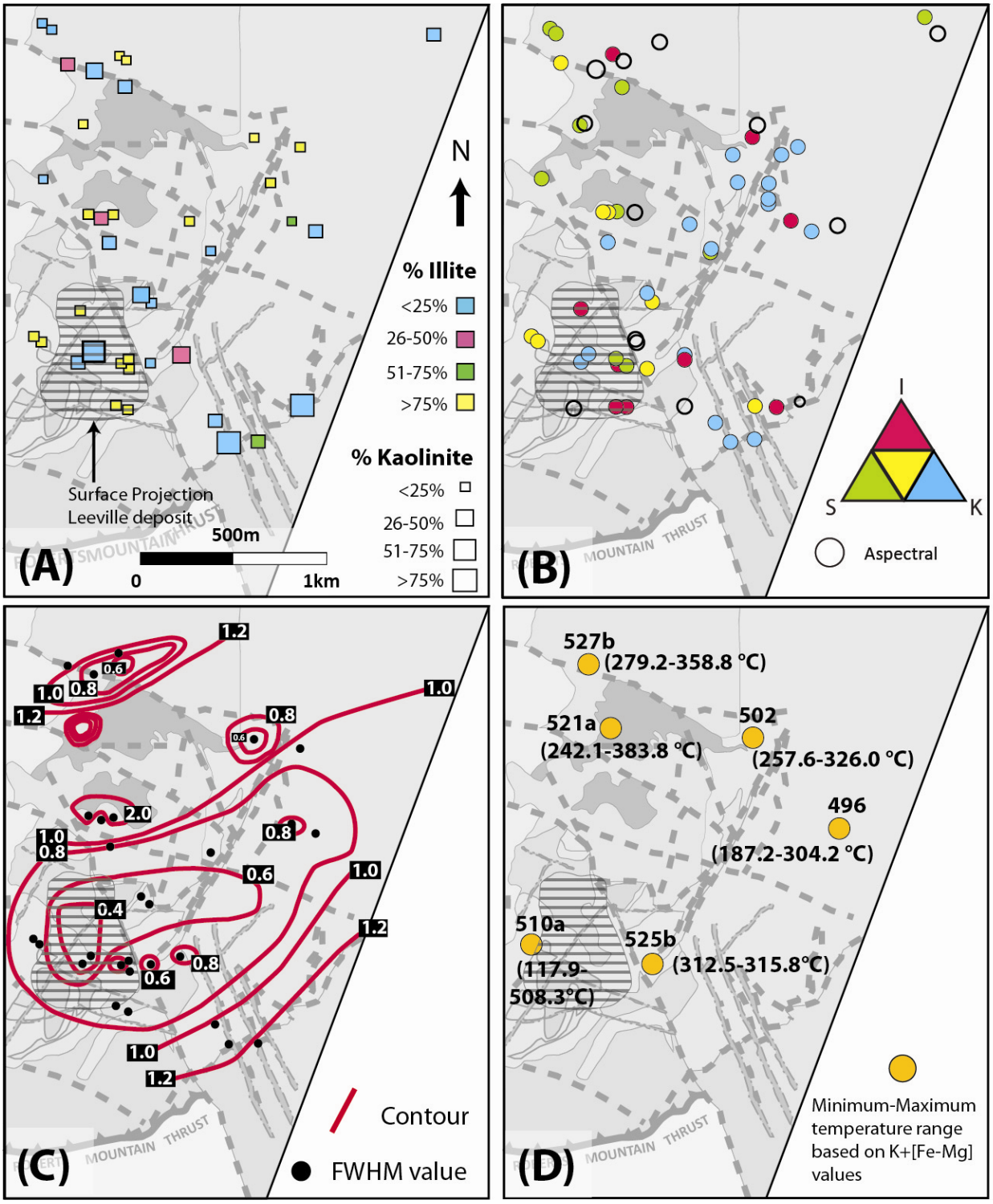

Fig. 3.12. Maps showing the distribution of A. clay minerals identified by XRD diffraction data B. Clay minerals identified by Terraspec data C. Contoured Full Width Half the Maximum values ($\Delta°2\theta$), D. Illite formation temperatures calculated from electron microprobe data.

Table 3.1. XRD data from the <2 µm clay fraction and whole rock samples from the Leeville field area. n=39

Sample	Rock Type	I ■	K ▲	S ◊	I-S +	Illite Peak (2θ)	Illite Peak* (2θ)	Illite FWHM (Δ°2θ)	Illite FWHM *(Δ°2θ)	ΔFWHM Illite (Δ°2θ)	Smectite Peak (2θ)	Smectite Peak* (2θ)	Smectite FWHM (Δ°2θ)	Smectite FWHM* (Δ°2θ)	Kaolinite Peak (2θ)	Kaolinite Peak* (2θ)	% I	%K	% S
472	I	■	▲			10.109	9.968	0.667	0.603	0.064	-	-	-	-	7.146	7.149	57.6	42.4	0.0
473	I	■	▲			10.003	9.924	0.228	0.245	0.017	-	-	-	-	7.109	7.104	12.4	87.6	0.0
477a	FG	■	▲	◊		10.107	9.975	0.568	0.497	0.071	19.658	18.856	0.978	0.648	7.164	7.169	1.5	92.4	6.1
478	I	■	▲	◊		10.189	9.987	0.584	0.514	0.07	14.98	16.788	1.324	0.913	7.16	7.165	9.8	31.8	58.4
484	I	■	▲			10.091	9.971	0.498	0.51	-0.012	-	-	-	-	7.154	7.147	81.1	18.9	0.0
486a×	S	■				10.039		0.494			-	-	-	-	-	-	100	0.0	0.0
487	CS	■	▲			10.012	9.989	0.502	0.48	0.022	-	-	-	-	7.202	7.209	41.2	58.8	0.0
492	BX	■	▲	◊		10.005	9.995	0.266	0.265	0.001	-	-	-	-	7.157	7.167	98.1	0.9	1.0
495	S	■	▲			10.04	9.998	0.455	0.452	0.003	-	-	-	-	7.142	7.145	74.2	25.8	0.0
496	S	■	▲	◊		9.986	9.972	0.344	0.352	-0.008	14.783	16.982	1.322	0.861	7.166	7.164	3.1	32.4	64.5
498×	I	■	▲			9.968	9.934	0.247	0.255	-0.008	-	-	-	-	7.140	7.117	21.2	78.8	0.0
499	I	■	▲	◊	+	9.999	10.01	0.398	0.338	0.06	14.299	16.625	1.128	1.101	7.167	7.155	4.3	25.1	70.6
502	BX	■				9.923	9.919	0.214	0.217	-0.07	-	-	-	-	-	-	100.0	0.0	0.0
506	S	■				9.97	0.951	0.247	0.213	0.034	-	-	-	-	-	-	100.0	0.0	0.0
507	CS	■				10.079	9.944	0.574	0.445	0.129	-	-	-	-	-	-	100.0	0.0	0.0
508	I	■		◊	+	10.045	10.013	0.322	0.324	-0.002	16.521	16.023	1.077	1.824	-	-	10.1	63.9	26.0
509¥	I		▲	◊		-	-	-	-	-	14.225	16.334	-	-	-	-	5.6	28.4	66.0
510a	FG	■	▲	◊		10.062	10.013	0.389	0.352	0.037	14.376	16.521	1.041	1.089	7.165	7.172	62.6	7.2	30.2
510c	CS	■	▲	◊		10.093	10.047	0.394	0.365	0.029	14.792	17.142	2.517	1.151	7.176		56.3	9.9	33.8
511c	FG	■		◊		9.888	9.935	0.143	0.231	-0.108	15.007	16.785	-	-	-	-	9.4	0.0	90.6
513b	FG	■	▲			10.042	9.989	0.406	0.403	0.003	-	-	-	-	7.157	7.156	92.6	7.5	0.0
513c	FG	■	▲			10.06	10.026	0.38	0.359	0.021	-	-	-	-	7.211	7.156	77.5	22.5	0.0
516b	CS	■	▲	◊		10	9.98	0.283	0.271	0.012	12.486	16.625	1.063	1.479	7.172	7.159	17.0	52.0	31.0
516d	FG	■	▲	◊		9.989	9.999	0.238	0.235	0.003	12.427	16.729	1.107	1.348	7.169	7.169	2.2	6.6	91.2
519	S	■	▲	◊		10.113	10.003	0.426	0.458	-0.032	14.454	16.842	1.123	0.59	7.159	7.168	1.5	48.9	49.6
521a	BX	■		◊		10.037	10.01	0.303	0.293	0.01	-	-	-	-	-	-	99.1		0.9
523	I		▲			-	-	-	-	-	13.888	16.749	1.144	0.448	7.152	7.158	0.0	0.6	99.4
524	FG	■	▲	◊	+	10.023	9.909	0.246	0.355	-0.109	14.245	16.521	0.976	1.464	7.169	7.116	18.0	14.4	67.6
525a-1	FG	■				10.079	10.007	0.437	0.421	0.016	-	-	-	-	-	-	100.0	0.0	0.0
525a-2	FG	■	▲			10.064	9.996	0.419	0.421	-0.002	-	-	-	-	7.152	7.155	88.8	11.2	0.0
525b	FG	■				10.056	9.994	0.405	0.392	0.013	-	-	-	-	-	-	100.0	0.0	0.0
526a	I			◊	+	-	-	-	-	-	14.684	16.637	0.731	0.5	-	-	0.0	0.2	99.8
526b	I		▲	◊		-	-	-	-	-	14.895	16.685	0.994	0.819	7.21	-	0.0	0.1	99.9
527	FG	■	▲	◊		10.037	9.927	0.616	0.578	0.038	14.613	16.625	1.774	1.345	7.171	7.142	29.9	30.7	39.4
528a	CS	■	▲	◊	+	10.075	9.916	1.231	0.788	0.443	15.384	17.052	1.439	1.158	7.176	7.176	83.6	4.9	11.5
528c	S	■	▲	◊	+	10.113	9.998	1.121	0.999	0.122	16.521	17.162	1.91	1.577	7.194	0.724	27.1	36.5	36.5
528d	I	■		◊		10.087	9.945	0.549	0.532	0.017	14.694	16.625	1.001	0.898	-	-	83.0	0.0	17.0
UL-18	I	■	▲	◊		10.056	10.022	0.143	0.153	-0.01	14.228	16.893	0.159	0.329	7.165	7.149	5.4	89.4	5.2
UL-19	I	■	▲	◊	+	10.005	10.002	0.167	0.154	0.013	14.144	16.811	0.193	0.474	7.133	7.133	8.5	49.6	42.0

I = illite, I-S=illite-smectite, S=smectite, K=kaolinite × = whole rock XRD analysis

* = glycolated ¥ = contains chlorite, no FWHM values calculated for smectite

Rock type: I = intrusive, S= sedimentary, CS= clay seam, FG = fault gouge, BX = breccia

shows the distribution of clay minerals identified from x-ray diffraction patterns of the fine fraction (<2μm) across the map area. Most samples contained all three of the dominant clay types: illite, kaolinite, and smectite in varying amounts. No obvious correlation became evident between lithology and associated clay mineralogy although smectite does appear most abundant in altered intrusive samples, including those from in and around the Vivian sill: 499, 509, 523, 526, and 527. Dyke samples UL-18 and UL-19 from within the Leeville underground deposit containing elevated gold values (0.094ppm and 0.005ppm respectively) contained abundant kaolinite with smectite and illite. Sample UL-19 contains significantly more smectite and I-S, and less gold than sample UL-18. Illite dominated samples were present within close proximity to the surface projection of the Leeville deposit. Sample 525, on the edge of the projected deposit only comprised illite. Samples 510 and 513 contained abundant illite with lesser amounts of kaolinite, and smectite. Sample 528 contained more illite than smectite.

Figure 3.12b shows the distribution of clay minerals identified from Terraspec reflectance spectra of whole rock samples. Smectite dominates the northwestern part of the Leeville study area. Some illite occurs above the surface projection of the Leeville deposit. The most prominent trend outlined by Terraspec data is a SW-NE trending region of kaolinite dominated samples starting at the Leeville deposit. This trend in kaolinite correlates to the illite trend observed in the same samples using x-ray diffraction. Many samples returned aspectral data characterized by a reflectance spectrum with no identifiable absorption peaks. Comparison of results from the Terraspec data and the XRD indicate that the majority of samples analyzed by the Terraspec produced reflectance spectra indicative of a different clay assemblage than that returned by XRD. Terraspec data returned numerous false positives when in fact illite occurs only in discrete areas. Inconsistency between XRD and Terraspec data are discussed in detail below.

FWHM values of illite in samples from the Leeville area, calibrated to the CIS scale are shown in Table 3.2. Results indicate that FWHM values are dominantly above the accepted value of 0.42°2θ for the boundary between diagenesis and low grade anchizonal metamorphism. This boundary coincides with a temperature of ~200°C (Kisch, 1990) which is within the temperature range measured from fluid inclusions paragenetically related to Carlin-type Au-mineralization (Hofstra and Cline, 2000; Cline et al., 2005). Two samples within close proximity to the surface projection of the Leeville deposit show lower FWHM values indicative of increased crystallinity and higher temperature than surrounding samples. Contouring of FWHM values across the Leeville deposit, shown in Figure 3.12c, an extensive zone of high crystallinity illite; above and outboard of the surface projection of the Leeville deposit. Contoured

Table. 3.2. FWHM values of illite from clay separated samples collected from the vicinity of the Leeville deposit calibrated to the CIS-scale. Samples lacking illite are not included in this table.

Sample ID	Rock Type	Experimental FWHM Value (Δ°2θ)	Calibrated FWHM Value (Δ°2θ)	Inferred T (°C)*
472	I	0.67	1.24	Diagenetic
477a	I	0.57	1.06	Diagenetic
478	FG	0.58	1.08	Diagenetic
484	I	0.5	0.94	Diagenetic
486	S	0.49	0.92	Diagenetic
487	CS	0.5	0.94	Diagenetic
492	BX	0.27	0.53	Diagenetic
495	S	0.46	0.87	Diagenetic
496	S	0.34	0.65	Diagenetic
499	I	0.4	0.76	Diagenetic
502	BX	0.21	0.42	Diagenetic - Anchizonal
506	S	0.25	0.49	Diagenetic
507	CS	0.57	1.06	Diagenetic
508	I	0.32	0.62	Diagenetic
510a	FG	0.39	0.74	Diagenetic
510c	CS	0.39	0.74	Diagenetic
511c	FG	0.14	0.29	Epizonal
513b	FG	0.41	0.78	Diagenetic
513c	FG	0.38	0.72	Diagenetic
516b	CS	0.28	0.54	Diagenetic - Anchizonal
516d	FG	0.24	0.47	Diagenetic - Anchizonal
519	S	0.43	0.81	Diagenetic
521a	BX	0.3	0.58	Diagenetic - Anchizonal
524	FG	0.25	0.49	Diagenetic - Anchizonal
525a-1	FG	0.44	0.83	Diagenetic
525a-2	FG	0.42	0.79	Diagenetic
525b	FG	0.41	0.78	Diagenetic
527	FG	0.62	1.15	Diagenetic
528a	CS	1.23	2.25	Diagenetic
528c	S	1.12	2.05	Diagenetic
528d	I	0.55	1.03	Diagenetic
UL-18	I	0.14	0.29	Epizonal
UL-19	I	0.15	0.31	Epizonal

n=33

Rock type: I = intrusive, S= sedimentary, CS= clay seam, FG = fault gouge, BX = breccia

FWHM values increase away from the Leeville deposit, with small zones of crystalline illite proximal to faults and other permeable pathways.

3.7.3 Distribution of clays - Shoshone Range Field Area

XRD pattern data for samples from the Shoshone Range field area are outlined in Table 3.3, Appendix D. The distribution of clays identified using XRD is shown in Figure 3.13a. Abundant quartz content and lack of aluminosilicate minerals in this area restricted the samples analyzed by XRD. There are two main sites of argillization along this transect, both of which are known occurrences of gold; the giant Carlin Au Pipeline deposit and the Elder Creek gold deposit. Samples from the Pipeline and Gold Acres deposits contained illite and some sedimentary muscovite. At the Elder Creek deposit, illite was identified in the matrix of gold-hosting quartzite clast breccia, in strongly altered siltstone, and in dyke material. To the north of the Elder Creek deposit, unaltered siltstone contained no illite, only smectite and kaolinite. Unaltered siltstone and argillite from west of the Pipeline deposit contained illite-smectite, smectite and kaolinite. The assemblage contained by samples 134 and 123 appears to be the background clay content of most upper plate rocks.

Calibrated FWHM values from the Shoshone Range study area are presented in Table 3.4, Figure 3.13b and indicate a range of metamorphic grades. Samples from the Gold Acres deposit exhibited the lowest FWHM values indicative of the highest crystallinity illite. Within the Elder Creek deposit FWHM values vary between 0.45-0.94 $\Delta°2\theta$. Illite occurring within the main zone of mineralization at Elder Creek is less crystalline than illite from the Pipeline and Gold Acres deposits. Just outside the main zone of mineralization, one sample contains poorly crystalline illite with an FWHM value of 1.12 $\Delta°2\theta$, however, ~1km northwest of the main zone of mineralization, sample 230 (quartzite clast breccias) exhibits highly crystalline illite with an FWHM value of 0.45 $\Delta°2\theta$.

Over 300 samples were collected from the Shoshone Range field area for Terraspec© analysis. The data from these analyses are shown in Figure 3.13c. Of these 300 samples over ¼ returned aspectral reflectance data. Another ¼ of the samples contained a lack of measurable clay, whereby quartz or carbonate minerals dominated the spectrum. The final ½ yielded a combination of muscovite, illite,

Table. 3.3. XRD data of <2μm fraction and whole rock samples from the Shoshone Range. n=35

Sample	Rock Type	I ■	K▲	S ●	I-S ○	001 Illite Peak	001 Illite Peak*	Illite 001 FWHM	Illite 001 FWHM *	ΔFWHM Illite	001 Smectite Peak	001 Smectite Peak*	Smectite 001 FWHM	Smectite 001 FWHM*	Kaolinite 001 Peak	Kaolinite 001 Peak*	% I	%K	% S
8	**BX**	■				10.152	10.059	0.47	0.487	-0.017	-	-	-	-	-	-	100.0	0.0	0.0
10	**BX**	■				10.018	10.055	0.447	0.423	0.024	-	-	-	-	-	-	100.0	0.0	0.0
12	**S**	■				10.118	10.052	0.476	0.472	0.004	-	-	-	-	-	-	100.0	0.0	0.0
62	**S**	■			○	10.206	10.003	0.359	0.295	0.064	-	-	-	-	-	-	100.0	0.0	0.0
64	**S**	■	▲	●		10.214	10.009	0.309	0.301	0.008	14.943	17.242	0.996	0.678	7.202	7.180	45.1	45.7	9.0
76	**S**	■	▲			10.083	10.036	0.44	0.458	-0.018	14.300	-	-	-	7.207	7.188	60.6	39.4	0.0
82	**S**	■	▲	●		10.147	10.047	0.422	0.451	-0.029	15.082	17.212	0.927	0.681	7.194	7.186	11.0	18.6	70.4
83	**S**	■	▲	●		10.021	9.969	0.344	0.365	-0.021	14.229	14.181	0.151	0.134	7.095	7.085	54.5	33.1	11.0
84	**S**	■				10.149	10.110	0.44	0.414	0.026	-	-	-	-	-	-	100.0	0.0	0.0
97	**S**	■	▲			10.221	10.103	0.653	0.61	0.043	-	-	-	-	-	-	97.4	2.6	0.0
99	**S**	■				10.101	10.017	0.498	0.473	0.025	-	-	-	-	-	-	100.0	0.0	0.0
100	**S**	■				10.116	10.095	0.438	0.422	0.016	-	-	-	-	-	-	100.0	0.0	0.0
103	**S**	■	▲			10.104	10.120	0.455	0.488	-0.033	-	-	-	-	7.179	7.197	94.0	6.0	0.0
123	**S**	■	▲	●	○	10.135	10.050	0.636	0.517	0.119	14.467	15.439	0.367	1.155	7.194	7.184	36.7	15.5	47.7
134**	**S**	■	▲	●		10.118	10.078	-	-	-	14.256	17.253	1.616	1.368	7.210	7.208	4.0	18.9	77.3
230	**S**	■	▲			10.059	10.040	0.23	0.214	0.016	-	-	-	-	7.191	7.191	90.7	9.3	0.0
260	**S**	■	▲			10.050	10.049	0.218	0.209	0.009	-	-	-	-	7.184	7.194	76.8	23.2	0.0
264[x]	**S**		▲			-	-	-	-	-	-	-	-	-	7.159	7.146	0.0	100.0	0.0
268[x]	**S**	■	▲			10.105	10.061	0.22	0.216	0.004	-	-	-	-	7.199	7.186	46.8	53.2	0.0
274[x]	**S**		▲		○	-	-	-	-	-	-	-	-	-	7.125	7.178	0.0	100.0	0.0
280	**S**	■				10.077	10.052	0.322	0.317	0.005	-	-	-	-	-	-	100.0	0.0	0.0
285[x]	**S**	■				10.014	9.958	0.258	0.268	-0.01	-	-	-	-	-	-	100.0	0.0	0.0
292[x]	**S**					-	-	-	-	-	-	-	-	-	-	-	-	-	-
303[x]	**S**	■				10.069	9.909	0.204	0.207	-0.003	-	-	-	-	-	-	100.0	0.0	0.0
400	**S**	■				9.922	9.999	0.351	0.353	-0.002	-	-	-	-	-	-	100.0	0.0	0.0
401	**S**	■				9.975	9.922	0.452	0.352	0.100	-	-	-	-	-	-	100.0	0.0	0.0
404	**S**	■				10.019	10.015	0.488	0.403	0.085	-	-	-	-	-	-	100.0	0.0	0.0
406	**S**	■				9.979	9.827	0.372	0.379	-0.007	-	-	-	-	-	-	100.0	0.0	0.0
408	**S**	■				10.017	9.989	0.471	0.410	0.061	-	-	-	-	-	-	100.0	0.0	0.0
413	**S**	■				10.023	9.976	0.417	0.409	0.008	-	-	-	-	-	-	100.0	0.0	0.0
432	**S**	■				10.030	9.974	0.456	0.396	0.060	-	-	-	-	-	-	100.0	0.0	0.0
437	**I?**	■				9.975	9.945	0.229	0.227	0.002	-	-	-	-	-	-	100.0	0.0	0.0
444	**S**	■	▲			10.030	9.982	0.44	0.463	-0.019	-	-	-	-	7.162	7.141	50.5	49.5	0.0
PP1	**S**	■	▲			10.078	10.066	0.255	0.256	-0.001	-	-	-	-	7.182	7.181	93.2	6.8	0.0
E-S**	**S**	■	▲	●	○	10.087	10.061	-	-	-	14.553	16.837	1.36	1.3569	7.192	7.182	1.5	58.5	40.0

*=glycolated [x]= whole rock, not clay separated **= quantity of illite too small to measure FWHM value

I = illite, K=kaolinite, S=smecite, I-S=illite-smectite

Rock type: I = intrusive, S= sedimentary, CS= clay seam, FG = fault gouge, BX = breccia

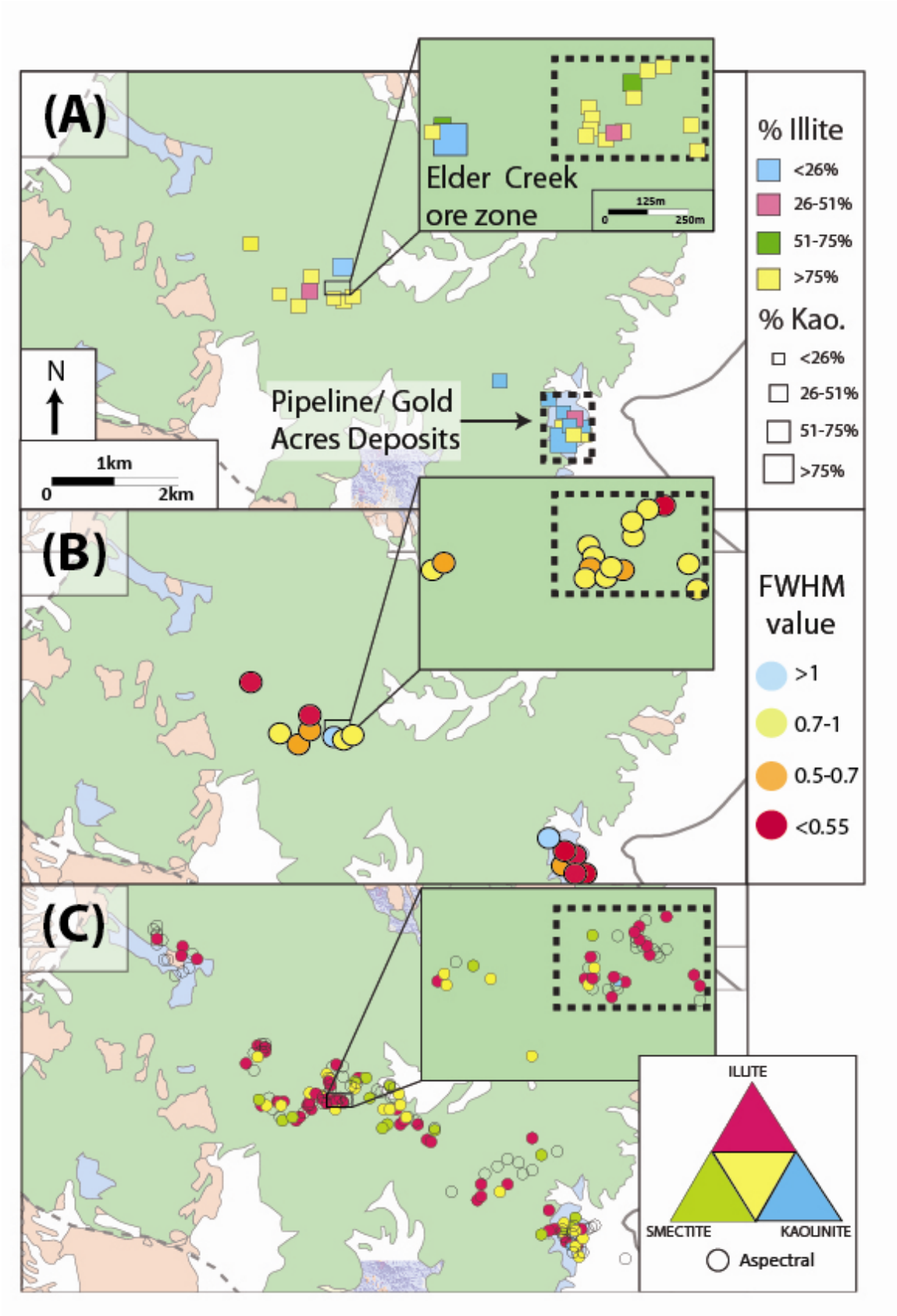

Fig. 3.13. Maps showing the distribution of A. XRD data B. FWHM values C. Terraspec data

Table. 3.4. FWHM values for clay separated samples from the Shoshone Range area calibrated to the CIS-scale

Sample ID	Rock Type	Experimental Value (Δ°2θ)	Calibrated Value (Δ°2θ)	Inferred Temperature zone
8	BX	0.47	0.88	Diagenetic
10	BX	0.45	0.85	Diagenetic
12	S	0.48	0.90	Diagenetic
62	S	0.36	0.69	Diagenetic
64	S	0.31	0.60	Diagenetic
76	S	0.44	0.83	Diagenetic
83	S	0.34	0.65	Diagenetic
84	S	0.44	0.83	Diagenetic
97	S	0.65	1.21	Diagenetic
99	S	0.5	0.94	Diagenetic
100	S	0.44	0.83	Diagenetic
103	S	0.46	0.87	Diagenetic
123	S	0.64	1.19	Diagenetic
230	S	0.23	0.45	Diagenetic-Anchizonal
260	S	0.22	0.44	Diagenetic-Anchizonal
268	S	0.22	0.44	Diagenetic-Anchizonal
280	S	0.32	0.62	Diagenetic
285	S	0.26	0.51	Diagenetic-Anchizonal
303	S	0.20	0.41	Diagenetic-Anchizonal
400	S	0.35	0.67	Diagenetic
401	S	0.45	0.85	Diagenetic
404	S	0.50	0.94	Diagenetic
406	S	0.37	0.71	Diagenetic
408	S	0.47	0.89	Diagenetic
413	S	0.42	0.79	Diagenetic
432	S	0.46	0.86	Diagenetic
437	I?	0.23	0.45	Diagenetic-Anchizonal
444	S	0.44	0.83	Diagenetic
PP1	S	0.26	0.51	Diagenetic

n=29

Rock type: I = intrusive, S= sedimentary, CS= clay seam, FG = fault gouge, BX = breccia

kaolinite, and smectite. Samples identified as containing abundant illite in XRD were also typically identified as containing illite. Kaolinite was not as prevalent as in the Leeville field area; no kaolinit-dominated samples were identified in the Shoshone Range. Muscovite was identified by the Terraspec in both the Pipeline and Gold Acres properties. The same discrepancy present at the Leeville field area between XRD and Terraspec© data was also present in the Shoshone Range study area.

3.7.4 Comparing the use of XRD vs. Terraspec in the identification of clay minerals

Table 3.5 compares mineral assemblages identified using the Terraspec with those identified using XRD. Of 76 samples analyzed using both x-ray diffraction and the Terraspec, only 35% of samples show agreement between the two methods. Three factors contribute to the discrepancy between XRD and Terraspec data (Figure 3.14): (i) colour intensity, (ii) crystal size, and (iii) poly mineralic samples.

(i) Dark samples including silty limestone, carbonaceous material, and strongly oxidized material do not reflect back enough light to be detected by the Terraspec. The result is an 'aspectral' reflectance pattern (Figure 3.14a); one that contains no obvious absorption peaks and that cannot be interpreted;

(ii) Terraspec analysis of the <2 μ clay fraction also resulted in aspectral reflectance patterns (Figure 3.14b). Following clay separation, x-ray diffraction peaks for illite, kaolinite, smectite and illite-smectite were better defined; however the peak locations did not change. The majority of quartz was removed from the sample and therefore quartz peaks did not interfere with the peaks of clay minerals. In the same samples analyzed by the Terraspec, absorption peaks at 1400nm, 1900nm, 2200nm were either absent or too small to interpret. Powdered whole rock smear mounts, and smear mounts of the coarse clay separated fraction (>10 μm) exhibited strong reflectance spectra indicating that the smear mount technique was not the cause of the aspectral data.

(iii) A. Samples containing illite in much greater quantities than kaolinite (identified using XRD) exhibited peaks characteristic of only illite (Figure 3.14c). In reflectance spectra where illite is dominant but kaolinite is present, the 1400nm and 2200nm absorption peaks should become asymmetrical and skewed to higher wavelengths. This phenomenon is due to appearance of poorly formed 'doublet' peaks characteristic of

Table. 3.5. Comparison between minerals identified using XRD and those identified using Terraspec. Samples identified as containing illite-smectite interlayered clay by XRD were considered correct if the sample was identified as containing illite and smectite by Terraspec. All Terraspec data represent whole rock samples, while XRD data contains both whole rock and clay separated samples. n= 76

	XRD DATA				TERRASPEC DATA			Match
Sample	I ■	K▲	S ●	I-S ○	I ■	K▲	S ●	Y/N
8	■				■			Y
10	■				A			N
12	■	▲			■		●	N
14		▲	●	○	■		●	Y
62	■				■			Y
64	■				■			Y
76	■	▲	●		■		●	N
82		▲			■	▲		N
83	■	▲	●		■	▲		N
84	■				■			Y
97	■	▲			■			N
99	■				■			Y
100	■				■			Y
103	■	▲			A			N
123		▲		○			●	N
134	■	▲	●		■			N
230	■	▲			■			N
260	■	▲			A			N
280	■				A			N
307	■	▲			■			N
E-S		▲	●	○	■			N
264		▲				▲		Y
268	■	▲				▲		N
274		▲		○		▲	●	N
285	■	▲				▲	●	N
292	C					▲	●	N
303	■				■			Y
400	■				■			Y
401	■				■			Y
404	■				■			Y
406	■				■			Y
408	■				■			Y
413	■				■			Y
432	■				■			Y
437	■				■	▲		Y
444	■	▲				▲		N
472	■	▲	●			▲		N
473*	■	▲			A			N

	XRD DATA				TERRASPEC DATA			Match
Sample	I ■	K▲	S ●	I-S ○	I ■	K▲	S ●	Y/N
477a	■	▲	●			▲		N
478	■	▲	●		■	▲		N
484	■	▲			■	▲		Y
486*				○	■ (?)			?
487	■	▲	●		■	▲		N
492	■	▲	●			▲		N
496	■	▲	●		■	▲	●	Y
498*	■	▲			■	▲		Y
502					■			Y
506					A			N
507	■				■			Y
508	■		●	○	A			N
509‡		▲	●				●	N
510a	■	▲	●			▲	●	N
510b*					■			N
510c	■	▲	●			▲	●	N
511c	■	▲	●		■			N
513a*	■				■			Y
513b	■	▲			■			N
513c	■	▲			■			N
516b	■	▲	●	○	■	▲	●	Y
516d	■	▲	●		■	▲	●	Y
519	■	▲	●			▲		N
521a	■	▲	●				●	N
523	■	▲	●				●	N
524a	■	▲	●	○	■	▲	●	N
525a-1	■						● (?)	N
525a-2	■	▲					● (?)	N
525b	■				●			Y
526a			●				●	Y
526b		▲	●				●	N
526d	■	▲	●				●	N
527b	■	▲	●		■	▲	●	Y
528a	■	▲	●	○		▲	●	N
528c	■	▲	●	○		▲	●	N
528d	■		●				●	N
UL-18	■	▲	●			▲		N
UL-19	■	▲	●	○		▲		N

*=whole rock XRD analysis, A = aspectral, C= carbon

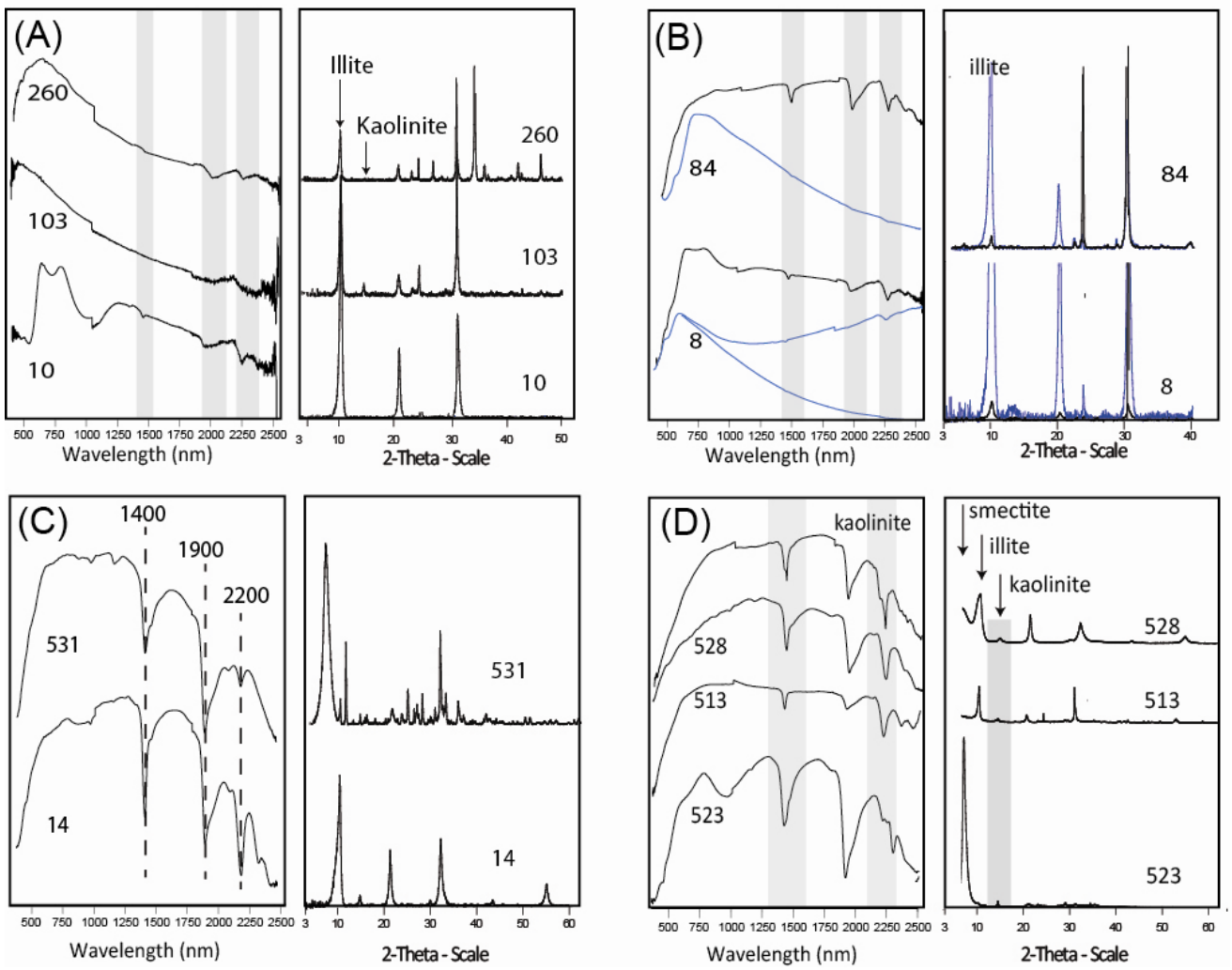

Fig. 3.14. Comparison between Terraspec data (left) and XRD data (right) indicate that the Terraspec does not produce data indicative of the correct mineral assemblage in four situations. A. Apsectral reflectance patterns are produced when the colour of a sample is dark, B. Aspectral reflectance patterns are produced when the crystal size of a sample is < 2μ, C. Illite-smectite interlayered clay produces the same pattern as mixes of discrete illite and smectite phases, D. Small amounts of kaolinite are not detected by the Terraspec.

kaolinite. Skewed, asymmetrical peaks were not observed in these samples. Conversely, large proportions of kaolinite in a sample can make the identification of less abundant clay minerals difficult. The assemblage kaolinite + illite + smectite cannot be differentiated from kaolinite + smectite. Additionally pure kaolinite can often be confused with kaolinite + minor illite.

B. Illite-smectite interlayered clay can cannot be distinguished from mixes of discrete illite and smectite phases (Figure 3.14d). The reflectance spectrum of smectite is similar to that of illite but does not contain absorption features at 2340 or 2440nm. Additionally, the ratio between the 1900nm absorption peak for water and the 2200nm absorption peak for the Al-OH group provides a key difference between illite and smectite. Interstitial water in the structure of smectite causes the 1900nm water peak to be deeper than the 2200nm Al-OH peak. As crystallinity of the phyllosilicate minerals increase from smectite to illite-smectite to illite to muscovite, this 1900nm water peak becomes shallower.

C. Variations in the 2200nm peak position of illite between shorter wavelengths (Fe/Mg rich) and higher wavelengths (potassium rich) represent compositional end-members of illite/muscovite. Where illite occurs with other minerals, such as kaolinite, shifts in the 2200nm peak position may not be a function illite composition, but instead represent interference by other mineral reflectance patterns.

3.7.5. Calculated temperature of illite formation

Averaged illite compositional data from the Leeville area and the Shoshone Range are shown in Table 3.6, including $K+|Fe-Mg|$ and temperature values calculated according to equation 2.3.4 with an average error of 7% on the final temperature. Final temperatures represent averages of multiple microprobe data points for each sample of which oxide totals were >85.0%. Raw data for all samples used in this study are included in Appendix E. Average $K+|Fe-Mg|$ values lie between 0.43 and 1.20. Average calculated temperatures fall between 234.2°C and 354.2°C, and are plotted spatially in Figure 3.12d. The temperature ranges calculated for illite formation are wide; all samples except for 8 exhibit ranges > 100°C.Samples from the Elder Creek deposit are not plotted spatially but sample locations are provided in Appendix C.

Table 3.6. Average temperatures calculated from illite microprobe compositional data using regression lines calculated in Table 2.1.

Sample	Location	Rock Type	Min	Max	Average K+[Fe-Mg]	Calculated T (°C) using regression lines from Fig. 7 Amedo Langano	Los Azufres	Salton Sea	Coso	Broadlands Ohaaki	Average T
8	Shoshone	S	0.63	0.89	0.76	247.7	219.1	243.8	212.7	268.2	234.2
97	Shoshone	S	0.82	0.94	0.88	286.8	259.4	273.3	236.1	281.7	266.2
PP1	Shoshone	S	0.94	1.40	1.20	394.9	370.4	354.6	300.6	318.9	354.2
496	Leeville	S	0.58	1.02	0.84	273.5	245.7	263.2	228.1	277.1	255.3
502	Leeville	BX	0.84	1.10	0.95	311.6	284.8	291.9	250.9	290.2	286.4
510a	Leeville	FG	0.32	1.78	0.94	308.85	282.02	289.86	249.22	289.29	284.1
527	Leeville	FG	0.92	1.22	1.04	342.2	316.3	315.0	269.1	300.8	311.3
525b	Leeville	FG	1.05	1.06	1.05	345.7	319.8	317.6	271.2	302.0	314.1
521a	Leeville	BX	0.78	1.31	1.16	379.5	354.6	343.1	291.5	313.6	341.7

n = 9

Muscovitic illite, previous defined based on imaging of clays in this study as illite-replacing euhedral muscovite laths, returned higher oxide totals on average (>~90%), and average potassium values >0.83 (cations) than illite. Tightly knit aggregates of illite returned lower oxide totals (70-92%). The relationship between illite-type, average potassium content, and average oxide totals is shown in Figure 3.15. Low oxide totals correspond to low average potassium contents. As oxide total increases, the potassium content of illite/muscovitic illite becomes more variable. Oxide totals beneath ~82% show a linear relationship between oxide total and potassium content. Temperature associated with oxide totals beneath ~87.5% may not provide a valid estimate of cation content. No correlation is apparent between primary rock types hosting illite and calculated temperatures of illite formation.

3.7.6. Oxygen and Hydrogen Stable Isotope data

The isotopic composition of water in equilibrium with clay minerals from this study is shown with similar data from other Carlin-type deposits compiled by Cline et al. (2005) in Figure 3.16. Table 3.7 provides $\delta^{18}O$ and δD isotope data for kaolinite, illite, and smectite mineral separates. The fractionation factors (α) for kaolinite-H_2O, illite-H_2O, and smectite-H_2O calculated by Gilg and Sheppard (1996) and Yeh (1980) were used. Temperatures were chosen for fractionation factor calculation based on temperatures chosen in other stable isotope studies on Carlin deposits for direct comparison (Yates and Rosenburg, 1997

Table 3.7. Calculated values for H_2O in equilibrium with $\delta^{18}O$ and δD stable isotope data for clay minerals collected in this study.

Sample	Rock type	Mineral assemblage	T(°C)	α Mineral-H_2O Hydrogen **	α Mineral-H_2O Oxygen *	$\delta D_{(VSMOW)}$ Mineral	$\delta^{18}O_{(VSMOW)}$ Mineral	$\delta D_{(VSMOW)}$ H_2O	$\delta^{18}O_{(VSMOW)}$ H_2O
477a	I	kaolinite	200	-20	5	-157	2.2	-136.71	-2.8
484	I	illite-kaolinite	200	-10	5.5	-71	16.7	-60.68	11.2
495	S	illite-kaolinite	200	-10	5.5	-116	12.1	-105.71	6.6
510c	CS	illite-smectite-kaolinite	150	-15	10	-96	14.0	-81.08	4.0
516b	CS	illite	200	-1	6	-134	10.8	-132.65	4.8
525a	CG	illite	200	-1	6	-133	8.1	-131.93	2.1
526a	I	smectite	50	-25	21	-103	13.8	-77.59	-7.2
8	BX	illite	200	-1	6	-122	13.1	-121.00	7.1

*After Gilg and Sheppard (1996)

* After Gilg and Sheppard (1996); Yeh, 1980

α Fractionation factor

Hofstra et al., 1999). Above temperatures of ~150°C, fractionation factors converge near 0. Hence, variation in formation temperature (± 50°C) is not critical to determining fractionation factors. In the case of poly-mineral clay separates, a weighted average fractionation factor was determined based on relative modal assemblages calculated from x-ray diffraction patterns.

Smectite exhibits light δD_{H2O} and $\delta^{18}O_{H2O}$ values and plots proximal to the meteoric water line. As such, the samples containing illite>smectite>kaolinite may have a lighter $\delta^{18}O$ signature caused by a mixed mineral signature and the presence of supergene smectite. Low δD_{H2O} and high $\delta^{18}O_{H2O}$ values of pure kaolinite separate suggest a mixed origin fluid forming kaolinite, with a dominating Eocene meteoric signature (as defined by Hofstra et al., 1999). Pure illite separates exhibit consistently low δD_{H2O} values and heavy $\delta^{18}O_{H2O}$ values. These values are consistent with those measured in the majority of Carlin deposits which show δD_{H2O} values between -160 and -120 (Hofstra et al., 1999).

Sample 484 containing illite>kaolinite and sample 510 containing illite> smectite> kaolinite exhibit anomalous light δD_{H2O} values indicative of a deeply sourced fluid. This could be explained by the mixing of magmatic/ metamorphic fluid, with Jurassic-aged meteoric water forming clays that predate Carlin-

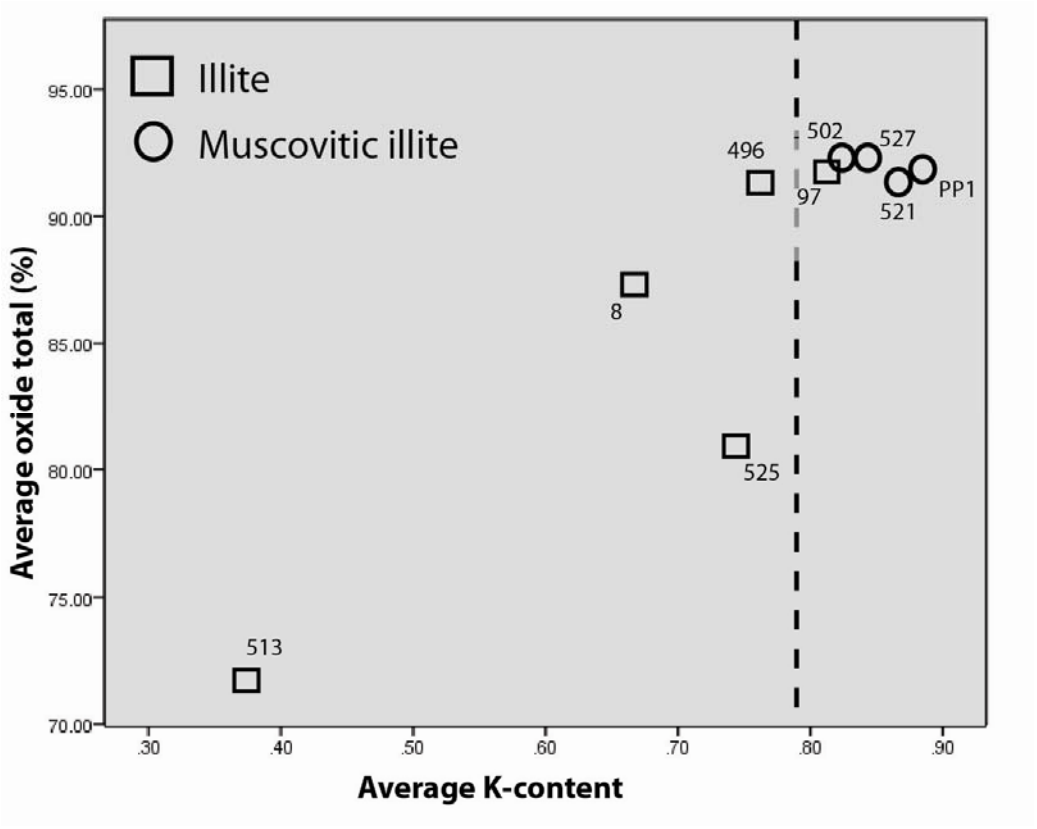

Fig. 3.15. Correlation graph between the average potassium content of all illite samples analyzed by electron microprobe, and the average total of all oxides in those samples.

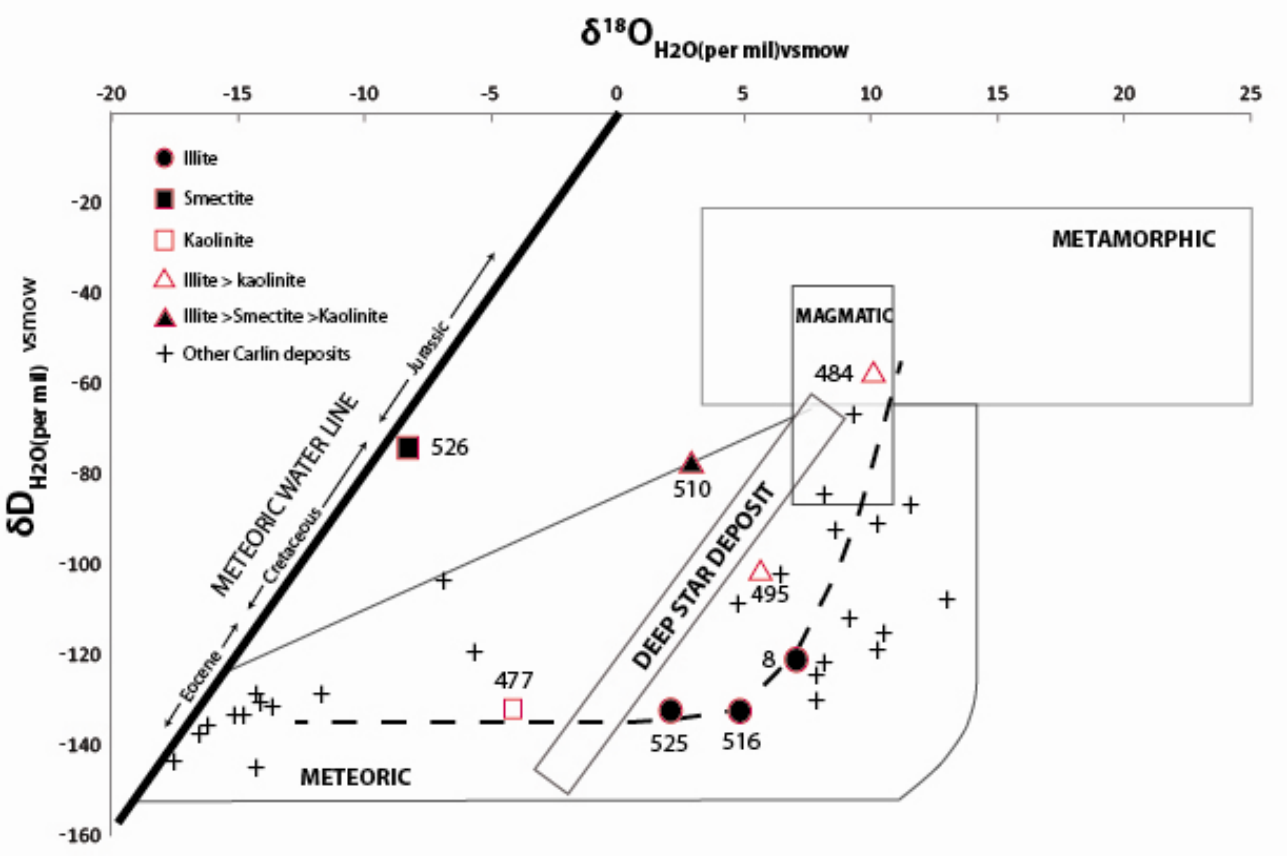

Fig. 3.16. $\delta^{18}O$ and δD values for H_2O in equilibrium with clay minerals in this study, plotted with stable isotope mineral data from other Carlin deposits, including the Deep Star deposit (Hofstra et al., 1999; Heitt et al., 2003; Kuehn, 1989). Eocene, Cretaceous, and Jurassic meteoric water lines (accounting for Paleo-latitudes), and metamorphic, magmatic and meteoric water fields are taken from Hofstra et al., (1999). The dashed line represents the trend observed in the data from this study, excluding the pure smectite sample which plots on the meteoric line and is interpreted to be a secondary alteration effect.

type mineralizaiton. Conversely, these samples may represent an end-member to the mid-Tertiary mixing line between magmatic/ metamorphic and meteoric reservoirs. Samples from the Deep Star deposit containing mica>smectite>kaolinite and mica>kaolinite> smectite also fall within the magmatic field indicating these clays may have a relationship to Carlin-type fluid (Cline et al., 2005).

3.8 INTERPRETATIONS/ DISCUSSION

A compilation of clay zonation patterns, illite crystallinity data, and stable isotope analyses highlight four zones of hydrothermal alteration in the Leeville study area (Figure 3.17). These zones correlate well with fault zones, dykes, and known hydrothermal ore deposits. The following section discusses the ability of different analytical techniques to assess the presence of hydrothermal alteration which may represent upwelling of exhausted fluid following Carlin-type gold deposition in underlying lower plate carbonate rocks.

3.8.1 Clay mineral zonation patterns around hydrothermal fluid conduits

Areas that have experienced hydrothermal fluid flow can be detected using patterns in clay mineral zonation. Zones 1, 2, 3, 4 outlined in Figure 3.17 correlate with an abundance of illite and a lack of smectite. However, samples UL-18 and UL-19 from within the Leeville deposit exhibit only a small amount of illite and abundant kaolinite and smectite. The abundance of smectite and kaolinite in these two samples may be indicative of late supergene alteration overprinting hypogene alteration. Another possibility is that kaolinite is part of the hypogene alteration assemblage responsible for mineralization of the Leeville deposit. Kaolinite is stable in a wide range of thermal and chemical environments making it a both supergene and hypogene alteration mineral.

The link between kaolinite and a hypogene hydrothermal alteration assemblage is challenging to establish because of the difficulties in identifying a paragenetic relationship between kaolinite and illite. Samples were imaged by SEM and observed to be intergrown, but no relative timing was evident. In previous studies, the term ‘intergrown’ has been used to describe the relationship of clay minerals to ore in Carlin-type gold deposits with the implication that the two minerals formed simulatenously (Nutt and Hofstra, 2003; Cail and Cline, 2001). There is no way to determine if two clay minerals formed at the same time from an intergrown texture. Presumed ore-stage clay minerals have been dated in a number of Carlin-type deposits without ever producing an Eocene age. This could be a result of mixed age populations or it could represent the lack of syn-ore argillization (Chakurian et al., 2003). Without

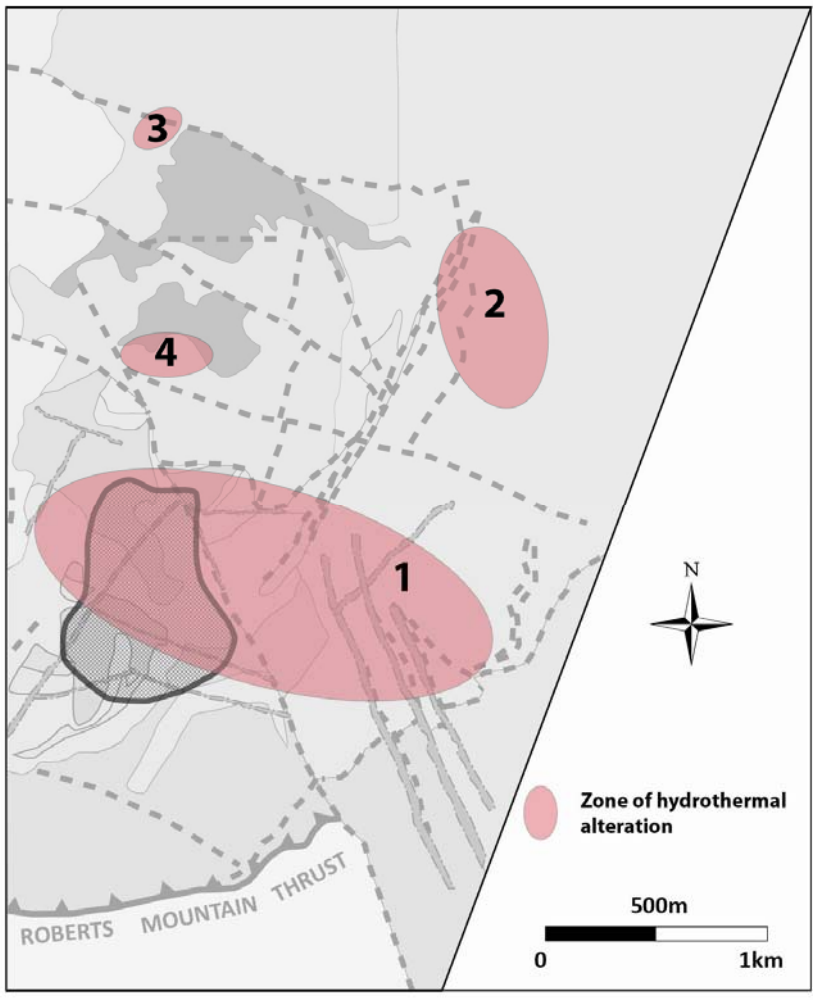

Fig. 3.17. Four zones of hydrothermal alteration can be identified in the Leeville study area based on clay zonation patterns, the distribution of highly crystalline illite, and stable isotope analyses of clay minerals.

absolute dates on clay mineral formation, the most accurate description of this relationship is a spatial association between clay minerals and ore. At present, the most robust mineral indicator of hydrothermal alteration is illite.

Dickite was not identified in samples from either the Leeville or the Shoshone Range areas. Clay equilibria suggest that dickite is metastable relative to kaolinite up to temperatures of 350°C (Zotov et al., 1998). The presence of kaolinite and the lack of dickite indicates that hydrothermal activity in both areas is likely to have occurred below 350°C, which is consistent with illite thermometry data included in this study. Kaolinite and smectite are more abundant in the Leeville area than in the Shoshone area. In the first stages of weathering, feldspar alters to illite + smectite + kaolinite, though illite is soon replaced by expandable lower temperature phases (Meunier and Velde, 2004). The lack of aluminosilicate material in the sedimentary rocks limited the degree of argillization in upper plate rocks of the Shoshone Range. Thick packages of quartzite and chert dominate the surface geology of the Shoshone Range, whereas in the Leeville deposit there is abundant feldspathic siltstone, breccia, and intrusive material.

3.8.2 Illite crystallinity halos

Zones 1-4 (Figure 3.17) in the Leeville study area correspond to areas containing highly crystalline illite, with the most extensive zone of high crystallinity focused proximal to the Leeville deposit (Figure 3.12c). Low FWHM values, or highly crystalline illite forms a large ~1.5km diameter halo above and east of the deposit. The occurrence of illite in igneous rock types indicates that illite is not a product of diagenesis, but of hydrothermal alteration. The shape and location of the halo may indicate where ore-forming fluid was exhausted following gold mineralization of the Leeville deposit. The dyke swarm at the southeastern edge of the Leeville property forms an extension of zone 1 highly crystalline illite. At this location, highly crystalline illite may be a product of hydrothermal activity associated with base metal mineralization hosted by some dykes. Several smaller zones of crystalline illite occur distal to the surface projection of the Leeville deposit, dominantly within or adjacent to fault zones. Zone 2 occurs at the junction of multiple faults. The relationship between faulting and highly crystalline illite suggests that fluid flow was localized along faults. However not all faults exhibit crystalline illite, as shown by the abundance of smectite and kaolinite proximal to many mapped faults. North of the Leeville deposit in zone 4, highly crystalline illite is juxtaposed against poorly crystalline illite within the same faulted zone of intrusive and sedimentary rock. Inconsistent crystallinity data on the outcrop scale indicates that fluid responsible for hydrothermal clay alteration was focused along centimetre or metre-wide pathways. Where fault zones occur in sedimentary units, alteration is restricted to the fault surfaces and does not

extend into the wall rock. Centimetre wide zones of clay gouge mark zones of fluid flow. Outside fault zones, the only sedimentary rocks observed to contain illite were breccias.

3.8.3 Crystal morphology

Illite crystals are pseudo- hexagonal in shape, indicative of a hydrothermal origin, rather than diagenetic (Peaver, 1999; Schleicher et al., 2006). The absence of a perfectly hexagonal grain shape to these crystals may be caused by: (i) growth of a new phase of fibrous illite along pre-existing cores of hexagonal illite (Macchi, 1987); (ii) the preferential removal or dissolution of illite along grain boundaries. Ragged and pitted grain boundaries have been observed as a result of the dissolution of other minerals: chromite (Leblanc, 1980), kaolinite (Hancock and Taylor, 1978), or (iii) a transitional crystal shape between end-member hexagonal and 'hairy' morphologies (Meunier and Velde, 2004). The tight knit aggregates, and curved shape of some illite crystals observed in this study may represent recrystallization of detrital illite (Hancock and Taylor, 1978). No empirical studies have shown a consistent relationship between temperature and morphology, therefore crystal morphology is useful only as a relative thermometer not an absolute indicator of temperature.

3.8.4 The Origin of Clay Minerals

Stable isotope analyses of hydrogen and oxygen can identify the source of water in equilibrium with clay minerals as meteoric, magmatic, or metamorphic water (Taylor, 1974). Figure 3.16 shows the isotope values for water in equilibrium with samples obtained in this study along with values obtained from Carlin deposits in other studies. Carlin type deposits typically exhibit depleted δD_{H_2O} values indicative of water largely meteoric in origin (Hofstra et al., 1999). Water in equilibrium with pure illite and kaolinite samples from this study resulted in similarly depleted δD_{H_2O} values. Mixed illite-kaolinite and illite-smectite-kaolinite samples from this study show higher δD_{H_2O} values than pure illite samples. High δD_{H_2O} values were also obtained from the Getchell deposit ranging from -153 to 44 ‰ (Groff, 1996; Cline and Hofstra, 2000) indicative of a magmatic/metamorphic fluid source. Given that smectite likely formed from secondary weathering processes, either illite or kaolinite, or both minerals must have formed from a magmatic/ metamorphic fluid dominated environment.

High $\delta^{18}O_{H_2O}$ values of illite and kaolinite minerals from this study follow a water-rock exchange curve between Eocene meteoric water and shaley limestone rocks of the lower plate similar to the pattern observed in other Carlin-type deposits (Hofstra et al., 1999). This may indicate that fluid forming

illite and kaolinite was buffered by rocks of the lower plate prior to alteration of the upper plate and supports a model whereby Carlin-type fluid is exhausted through upper plate rock following mineralization of lower plate rocks. Mixed clay samples appear to have formed along a mixing line between exchanged meteoric fluid and magmatic or deeply sourced fluid. Variation in the isotopic composition of different samples may reflect different proportions of fluid mixing or fluid-rock interaction (Cline et al., 2005.) Smectite exhibits light δD_{H2O} and $\delta^{18}O_{H2O}$ values and plots proximal to the meteoric water line and is interpreted to have formed by secondary alteration processes. Samples containing illite>smectite>kaolinite may have a lighter $\delta^{18}O$ signature caused by a mixed mineral signature and the presence of supergene smectite. Without smectite contaminating the sample, it is possible that illite and kaolinite would plot in the same region as pure illite and kaolinite samples.

3.8.5 Challenges in using the K + $|Fe - Mg|$ thermometer

The K + $|Fe - Mg|$ thermometer was used to calculate illite formation temperatures however it does not appear to be applicable where a composition-temperature calibration cannot be obtained. Three main challenges contributed to the failure of the K + $|Fe - Mg|$ thermometer in this study: (i) technical problems associated with sample preparation and data collection (ii) compositional heterogeneity within the illite mineral structure (iii) a poor fit to the initial data used to calibrate the K + $|Fe - Mg|$ thermometer (Battaglia, 2004).

(i) Clay minerals are extremely soft, and rocks containing abundant clay are typically not cohesive. Multiple stages of epoxy impregnation was often not sufficient to create material strong enough to withstand the diamond drill saw used to cut thin section-size blocks, limiting the number of samples that could be analyzed using the microprobe. Furthermore, during the polishing process, clay material was often preferentially removed from the thin section over harder minerals like quartz and calcite leaving voids where clay mineral occurred. Where illite was present, the surface texture of the mineral was rough. Smooth surfaces are required to ensure that the electron microprobe beam is analyzing homogenous material. Analyses of rough surfaces may account for low oxide totals observed in many samples in this study, and for large variation in the composition of microprobe points within the same sample.

(ii) TEM studies of illite have shown that compositional variation in clay minerals occurs on the micrometre scale (Essene and Peacor, 1995). Compositions of a given clay layer are

generally variable from packet to packet, and therefore any bulk chemical analyses of these minerals, including microprobe measurements, may represent averages over the intergrowths (Essene and Peacor, 1995).

The relationship between temperature and cation content is different in each geothermal field studied by Battaglia (2004), suggesting that the thermometer may be accurate on a deposit scale but not between deposits. Figure 3.18 shows that two distinct data sets are discernable between the five geothermal fields. Los Azufres, Aluto-Langano, and Salton Sea geothermal fields exhibit an overall steeper temperature gradient with increased K + $|Fe - Mg|$ values as compared to the Coso and Broadlands Ohaaki data. No evident pattern exists in the geographical location or host rock between geothermal fields to explain the bimodality of the data. One possible explanation is variation in the availability of potassium and to a lesser degree magnesium and iron, between deposits (Ji and Browne, 2000). Host rock lithologies do vary between deposits from volcanic to sedimentary rocks. Potassium leached from wall rock may have an effect on the composition of illite formed.

3.8.6 Clay morphology, crystallinity , and composition as a function of reaction progress

Three thermometers were employed in this study to estimate the formation temperature of illite with the intention of relating the calculated temperature to either a Carlin or non Carlin temperature range. A useful geothermometer requires that phases are chemically and structurally homogeneous with well described structures and compositions (Essene and Peacor, 1995). Low temperature clay minerals are not typically homogenous, either structurally, or chemically. The lack of structural and chemical constraint on low temperature minerals suggests that currently used clay thermometers including illite crystallinity and the smectite➔illite reaction are not useful because they are not based on equilibrium reactions. Essene and Peacor (1995) suggest that low temperature mineral reactions are best represented by reaction progress or Ostwaldian steps whereby a system in a state of metastable equilibrium will proceed via steps toward a state which has a minimum free energy (Ostwald, 1897; Van Santen, 1983). Changes in the morphology of illite have also been attributed to reaction progress, whereby initial growth stages produce needle-shaped or 'hairy' illite and final growth stages produce hexagonal illite (Bauer et al., 2000). The pseudo-hexagonal crystal shape of illite observed in this study may represent an intermediate stage between primary and final growth stages.

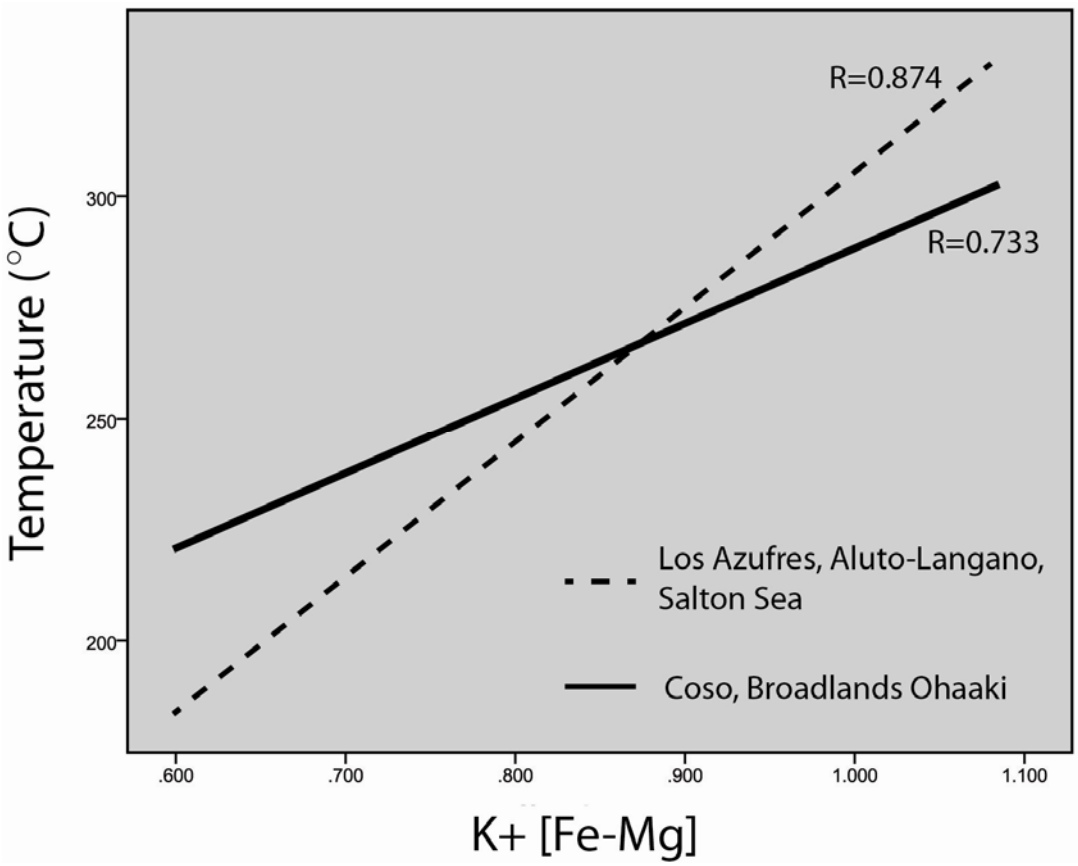

Fig. 3.18. Illite compositional data reported by Battaglia (2004) can be divided into two separate data sets. K + $|Fe - Mg|$ values are recorded in cations. The regression lines for these data sets are shown here. Los Azufres, Aluto-Langano, and Salton Sea geothermal fields exhibit a steeper overall temperature gradient that Coso and Broadlands Ohaaki.

One of the main factors affecting the consistency of clay thermometers is their low temperature nature. Most metamorphic thermometers occur at relatively high temperatures due to the necessity of an approach to equilibrium, which is operative only at elevated temperatures due to the rate of reactions (Essene and Peacor, 1995). Clay equilibria experiments at temperatures comparable to Carlin-type systems (~200°C) have shown the transformation between smectite ➔ illite-smectite ➔ illite ➔ muscovite ➔ k-feldspar can occur within timescales on the order of days (Yates and Rosenburg, 1997) or years (Bauer et al., 2000). Thermochronological evidence suggests hydrothermal fluid flow associated with Carlin-type systems proceeded for thousands of years; sufficient time for clay mineral assemblages to approach equilibrium (Hickey et al., 2010). Although empirical and experimental evidence provides a strong case against the significance of kinetic factors in low temperature environments, we must acknowledge that the clay mineral reactions observed in this study may represent reaction progress not absolute changes in temperature.

3.9 IMPLICATIONS

3.9.1 The ability of analytical tools to identify alteration related to Carlin-Au mineralization

A number of methods to constrain the origin of clay minerals, as either hydrothermal or non-hydrothermal, have been proposed in this study with varying success: (i) illite zonation patterns and illite crystallinity (ii) cation compositional variation within illite (iii) paragenetic relationships by scanning electron petrography (iv) morphology of illite crystals (v) stable isotope analysis of oxygen and hydrogen in clay minerals. The temperature of Carlin-type ore deposits is coincident with temperatures achieved during late diagenesis therefore, textures, morphologies, stable isotope compositions, cation compositions, and crystallinity values indicative of Carlin-type alteration may simply represent detrital clay resulting from late stage diagenesis (<200°C). Spatial relationships between high and low temperature clay minerals can outlines zones of high temperature alteration, however no relationship to Carlin-type mineralization can be established. Stable isotope analysis is the only method available that provides information on the origin of water forming minerals analyzed, and the range of isotope values observed in Carlin-type deposits is highly variable. Of the five techniques applied in this paper, the presence of illite and the crystallinity of illite appear to be the most robust indicator of hydrothermal atleration. Illite crystallinity, combined with stable isotope data exhibits potential to both identify clay minerals and determine their origin. These two methods strongly suggest that illite occurring above the

Leeville deposit was formed by a fluid of mixed meteoric and magmatic/metamorphic origin, consistent with previous studies on clay alteration associated with Carlin-type systems however no paragenetic relationship between ore and clay minerals can corroborate such an interpretation.

While the use of rapid-analysis tools such as the Terraspec has proven successful in many environments (Hauff, 1991; Huston et al., 1999; Blevings, 2008; Goetz, 2009), this study shows that certain mineral assemblages tend to obscure the positive identification of all clay minerals in a sample. In the context of exploration for Carlin-type deposits, inaccurate identification of clay mineralogy may create a 'false positive'; i.e., an area exhibits reflectance patterns indicative of Carlin-type clay minerals where those minerals are not in fact present. Inaccurate identification may also result in a 'false negative' whereby a prospective area is overlooked due to the absence of typical Carlin-type clay minerals.

Terraspec data from the Leeville deposit indicated that kaolinite occurred ubiquitously across the field area. XRD data presented a different scenario whereby illite dominated the same areas previously identified as kaolinite-dominated by the Terraspec. In this case, the lack of a pattern in the Terraspec data would have resulted in either the targeting of the entire field area or the failure to identify any one area that appeared different than another. The same problems arose in the interpretation of Terraspec data from the Shoshone Range. According to the Terraspec, illite occurred across the entire field area making the identification of specific targets impossible. XRD results from the same area indicate that illite is focused in two areas corresponding to two known gold deposits: the Pipeline/ Gold Acres deposit and the Elder Creek gold deposit. The darker colour of samples from the Shoshone range (typically medium to dark grey) resulted in more aspectral samples than in the Leeville study area. Carlin-type gold mineralization is often spatially, if not genetically, associated with zones of carbon alteration. Finally, samples within these carbonaceous zones could not be analyzed by the Terraspec due to the low reflectivity of carbonaceous samples.

Infrared techniques may be successful in low temperature hydrothermal systems exhibiting very strong surface argillization where the clay minerals being analyzed are abundant, and the clay assemblage is dominated by a single mineral. These prerequisites are not often observed in the field, or in low temperature systems that exhibit subtle alteration. The Terraspec has difficulty in interpreting spectra of complex multi- clay mineral assemblages which are typical of Carlin-type deposits. Complex clay mineral assemblages are more accurately interpreted using x-ray diffraction.

3.9.2 Hydrothermal flow on a regional scale

Regional thermochronology studies presented in this paper show that nearly the entire Shoshone Range is thermally reset. In certain areas, such as the region surrounding the Elder Creek deposit, apatite fission tracks (AFT) are reset where no high temperature clay alteration exists. The discrepancy between apatite fission tracks and clay alteration suggests:

(i) The smectite ➔ illite reaction is a kinetic process whereby fluid-rock ratio and time are key factors in determining whether or not illite is formed. Areas where fission tracks are reset but there is no evidence of illite may be indicative of insufficient fluid-rock interaction or insufficient interaction time to transform smectite to illite;

(ii) (ii) Apatite fission track resetting is also kinetic process whereby track resetting is a function of temperature, fluid-rock interaction and interaction time. Fission track resetting may occur at lower fluid-rock ratios and shorter timescales than the smectite ➔ illite conversion, creating a thermal halo around upwelling zones of hydrothermal fluid;

(iii) (iii) Apatite fission track ages from the Shoshone Range may represent the partial resetting of fission tracks by a series of young hydrothermal events including the Miocene Northern Nevada Rift and related precious metal deposits (Zoback et al., 1994; Leavitt et al., 2000;), Eocene magmatic activity in the Northern and Central Shoshone Range (Kelson et al., 2008), and Eocene hydrothermal fluid flow resulting in gold mineralization at the Pipeline Deposit (Arehart and Donelick, 2006). The core of hydrothermal systems; i.e., Pipeline/ Gold Acres deposits, Elder Creek deposit, and epithermal deposits of the Northern Shoshone may exhibit total fission track resetting while the regions peripheral to the main hydrothermal core experience only sufficient heat or fluid: rock interaction to partially reset fission tracks.

(iv) AFT resetting of the Shoshone Range is not a function of hydrothermal fluid flow, but of exhumation and represents variable uplift between ~70-25 Mya (observed fission track ages in the Shoshone Range). Given a geothermal gradient of 30°C/km (Hickey, 2003), a minimum of ~3.5km of uplift and erosion would have had to occur. Restoration of the Eocene landscape at the time of Au-mineralization using thermal modelling of AFT data, and assuming a geothermal gradient of 30°C/my, suggest that ~500-1500m of erosion has occurred since the mid Eocene (42Ma) (Hickey, 2003). In order for exhumation to account

for young fission track ages in the Shoshone Range, the rate of exhumation would have to triple.

3.9.3 The pathway of exhausted fluids in Carlin-type systems

Three scenarios were presented to describe potential outflow zones of fluid exhausted from the core of Carlin-type hydrothermal systems. If hydrothermal alteration zone 1 (above the Leeville deposit, Figure 3.17) in fact represents alteration caused by exhausted fluid from the Leeville deposit, then following ore deposition in lower plate carbonate material, exhausted fluid (still containing some gold) travelled upward and upon meeting the Roberts Mountain thrust fault (RMT) precipitated some gold. A portion of fluid continued laterally along the RMT, and the remaining fluid transgressed the upper plate through faults and other permeable pathways like zones of brecciation. The surface expression of this fluid is the occurrence of abundant illite ± kaolinite along fault surfaces, as the matrix in hydrothermal breccias, and as pervasive alteration of some dykes. This is similar to scenario 3 from Figure 3.5.

3.10 CONCLUSIONS

Sedimentary and intrusive rocks of northeastern Nevada have experienced multiple episodes of hydrothermal and magmatic activity. In addition, sedimentary rocks have undergone diagenesis. As a result clay minerals are a common component of upper plate rocks of the Roberts Mountains Thrust (RMT). Consequently, we were unable to establish a paragenetic relationship between clay minerals and Carlin-type gold mineralization due to the widespread occurrence of clays in both mineralized and unmineralized environments, and the absence of significant differences in the characteristics of hydrothermal and non-hydrothermal clay minerals. In summary:

1. Abundant highly crystalline illite with a mixed magmatic/metamorphic- meteoric water stable isotope signature is indicative of hydrothermal alteration. Hydrothermal alteration was identified around the Leeville, Pipeline, Gold Acres, and Elder Creek deposits, which are known occurrences of Carlin-type gold mineralization. Similar styles of alteration were identified around faults, fractures, and zones of brecciation indicating that upwelling hydrothermal fluid transgressed upper plate siliciclastic rocks through focused permeable pathways.

2. The fine grained nature of most clay minerals inhibits simple petrographic imaging, textural analysis, and identification of mineral-mineral relationships. Mineral heterogeneity on the micron scale and poor sample preparation may result in invalid compositional analyses. Kinetic factors such as fluid-rock ratio, and time may have more of an effect than temperature on determining crystallinity, composition, and mineral assemblages. In turn changes in clay characteristics may not represent equilibrium processes.

3. Reflectance data produced by the Terraspec is flawed under four circumstances (i) a sample is too dark and produces an aspectral reflectance pattern, (ii) the grain size of the sample is too small (<2 μm), and (iii) a sample contains multiple minerals. These three situations are commonly encountered in Carlin-type environments resulting in the potential for misinterpretation of data, the identification of fictional targets, or the exclusion of potential targets.

3.11 REFERENCES

Adams, S.S., and Putnam, B.R., III, 1992, Application of mineral deposit models in exploration: a case study of sediment-hosted gold deposits, Great Basin, Western United States: Geological Society, London, Special Publications, v. 63, p. 1-23.

Ahmed, A., Hickey., K., and Barker, .S., 2010, The Upper Plate Expression of an Auriferous Carlin-type Hydrothermal System: Geological Symposium of Nevada Proceedings.

Alexander, L., and Klug, H.P., 1948, Basic aspects of x-ray absorption in quantitative diffraction analysis of powder mixtures: Analytical Chemistry, v. 20, p. 886-889.

Amouric, M., and Baronnet, A., 1983, Effect of early nucleation conditions on synthetic muscovite polytypism as seen by high resolution transmission electron microscopy: Physics and Chemistry of Minerals, v. 9, p. 146-159.

Arehart, G., Eldridge, C., Chryssoulis, S., and Kesler, S., 1993, Ion microprobe determination of sulfur isotope variations in iron sulfides from the Post/Betze sediment-hosted disseminated gold deposit, Nevada, USA: Geochimica et Cosmochimica Acta, v. 57, p. 1505-1519.

Arehart, G., and Donelick, R., 2006, Thermal and isotopic profiling of the Pipeline hydrothermal system: Application to exploration for Carlin-type gold deposits: Journal of Geochemical exploration, v. 91, p. 27-40.

Arkai, P., Merriman, R., Roberts, B., Peacor, D., and Toth, M., 1996, Crystallinity, crystallite size and lattice strain of illite-muscovite and chlorite; comparison of XRD and TEM data for diagenetic to epizonal pelites: European Journal of Mineralogy, v. 8, p. 1119-1137.

Bakken, B., and Einaudi, M., 1986, Spatial and temporal relation between wall rock alteration and gold mineralization, main pit, Carlin gold mine, Nevada, USA, Volume 86, p. 388–403.

Barker, S., Hickey, K., Cline, J., Dipple, G., Kilburn, M., Vaughan, J., and Longo, A., 2009, Uncloaking Invisible Gold: Use of Nanosims to Evaluate Gold, Trace Elements, and Sulfur Isotopes in pyrite from Carlin-Type Gold Deposits: Economic Geology, v. 104, p. 897-904.

Baronnet, A., 1980, Polytypism in micas: a survey with emphasis on the crystal growth aspect: Current topics in materials science, v. 5, p. 447-548.

Battaglia, S., 2004, Variations in the chemical composition of illite from five geothermal fields: a possible geothermometer: Clay Minerals, v. 39, p. 501-510.

Bauer, A., Velde, B., and Gaupp, R., 2000, Experimental constraints on illite crystal morphology: Clay Minerals, v. 35, p. 587-597.

Bickle, M.J., and McKenzie, D., 1987, The transport of heat and matter by fluids during metamorphism: Contributions to Mineralogy and Petrology, v.95, p.384-392.

Blenkinsop, T., 1988, Definition of low-grade metamorphic zones using illite crystallinity: Journal of Metamorphic Geology, v. 6, p. 623-628.

Blevings, S., Vancouver, B., Kennedy, L., and Hickey, K., 2008, Controls on Copper and Gold Mineralization along the Contact between the Coast Plutonic Complex and the Southeast Coast Belt, Taseko Lakes Region, Southwestern British Columbia (NTS 092O/04): Geoscience BC Report, p. 21-33.

Cail, T., and Cline, J., 2001, Alteration associated with gold deposition at the Getchell Carlin-type gold deposit, north-central Nevada: Economic Geology, v. 96, p. 1343-1359.

Chakurian, A., Arehart, G., Donelick, R., Zhang, X., and Reiners, P., 2003, Timing constraints of gold mineralization along the Carlin trend utilizing apatite fission-track, 40Ar/39Ar, and apatite (U-Th)/He methods: Economic Geology, v. 98, p. 1159-1171.

Cline, J., and Hofstra, A., 2000, Ore-fluid evolution at the Getchell Carlin-type gold deposit, Nevada, USA: European Journal of Mineralogy, v. 12, p. 195-212.

Cline, J., 2001, Timing of gold and arsenic sulfide mineral deposition at the Getchell Carlin-type gold deposit, north-central Nevada: Economic Geology, v. 96, p. 75-89.

Cline, J., Hofstra, A., Muntean, J., Tosdal, R., and Hickey, K., 2005, Carlin-type gold deposits in Nevada: Critical geologic characteristics and viable models: Economic Geology, 100th Anniversary Volume, p. 451-484.

Clode, C., Grusing, S., Heitt, D., and Johnston, I., 1997, The relationship of structure, alteration, and stratigraphy to formation of the Deep Star gold deposit: Eureka County, Nevada: Society of Economic Geologists Guidebook Series, v. 28, p. 239–256.

Cluer, J., Cellura, B., Keith, S., Finney, S., and Bellert, S., 1997, Stratigraphy and structure of the Bell Creek nappe (Antler orogen), Ren property, northern Carlin trend, Nevada: The RMT, Elko and Eureka counties, Nevada: Nevada Petroleum Society, p. 41–54.

Emsbo, P., Hofstra, A.H., Lauha, E.A., Griffin, G.L., and Hutchinson, R.W., 2003, Origin of High-Grade Gold Ore, Source of Ore Fluid Components, and Genesis of the Meikle and Neighboring Carlin-Type Deposits, Northern Carlin Trend, Nevada: Economic Geology, v. 98, p. 1069-1105.

Essene, E., and Peacor, D., 1995, Clay mineral thermometry-a critical perspective: Clays and Clay Minerals, v. 43, p. 540-553.

Faure, G., 1998, Principles and applications of geochemistry: a comprehensive textbook for geology students: Upper Saddle Riber, New Jersey, Prentice Hall, 600 p.

Folger, H., Hofstra, A., Eberl, D., and Snee, L., 1998, Importance of clay characterization to interpretation of 40 Ar/39 Ar dates of illite from Carlin-type gold deposits: Insights from Jerritt Canyon: Contributions to the Gold Metallogeny of Northern Nevada, ed. Tosdal, RM, USGS Open File Rept, p. 98–338.

Frey, M., 1987, Very low-grade metamorphism of clastic sedimentary rocks: Low temperature metamorphism, p. 9–58.

Gallagher, K., Brown, R., and Johnson, C., 1998, Fission track analysis and its applications to geological problems: Annual Review of Earth and Planetary Sciences, v. 26, p. 519-572.

Gaudette, H., Eades, J., and Grim, R., 1966, The nature of illite: Clays and Clay Minerals, v. 13, p. 35-48.

Giggenbach, W., 1981, Geothermal mineral equilibria: Geochimica et Cosmochimica Acta, v. 45, p. 393-410.

- 1984, Mass transfer in hydrothermal alteration systems--A conceptual approach: Geochimica et Cosmochimica Acta, v. 48, p. 2693-2711.

Gilg, H., and Sheppard, S., 1996, Hydrogen isotope fractionation between kaolinite and water revisited: Geochimica et Cosmochimica Acta, v. 60, p. 529-533.

Gilluly, J., and Gates, O., 1965, Tectonic and igneous geology of the northern Shoshone Range, Nevada, US Gov. Print. Off.

Gleadow, A., and Fitzgerald, P., 1987, Uplift history and structure of the Transantarctic Mountains: new evidence from fission track dating of basement apatites in the Dry Valleys area, southern Victoria Land: Earth and Planetary Science Letters, v. 82, p. 1-14.

Goetz, A., Curtiss, B., and Shiley, D., 2009, Rapid gangue mineral concentration measurement over conveyors by NIR reflectance spectroscopy: Minerals Engineering, v. 22, p. 490-499.

Groff, J., 1996, 40Ar-39Ar geochronology of gold mineralization and origin of aurifereous fluids for the Getchell and Twin Creeks mines, Humboldt County, Nevada, Ph. D. Thesis, New Mexico Institute of Mining and Technology, Socorro, New Mexico, 291 p.

Hancock, N., 1978, Possible causes of Rotliegend sandstone diagenesis in northern West Germany: Journal of the Geological Society, v. 135, p. 35-40.

Hancock, N., and Taylor, A., 1978, Clay mineral diagenesis and oil migration in the Middle Jurassic Brent Sand Formation: Journal of the Geological Society of London, v. 135, p. 69–72.

Hauff, P., Kruse, F., and Madrid, R., 1991, Defining gold ore zones using illite polytypes, The Society, p. 239-247.

Heitt, D., Dunbar, W., Thompson, T., and Jackson, R., 2003, Geology and geochemistry of the Deep Star gold deposit: Carlin trend, Nevada: Economic Geology, v. 98, p. 1107-1135.

Hickey, K., 2003, Restoration of the Eocene Landscape in the Carlin-Jerritt Canyon Mining District: Constraining Depth of Mineralization for Carlin-type Au-deposits using Low-Temperature Apatite Thermochronology. Geological Society of America, v. 35, p. 358.

Hickey, K., Haynes, S., Tosdal, R., and Mortensen, J., 2003, Cretaceous-Paleogene denudation, volcanism and faulting in the Carlin-Jerritt Canyon mining district, northeastern Nevada: Implications for the paleogeographic and tectonic environment of Carlin-type gold deposits: Mineral exploration and sustainable development: Rotterdam Millpress, p. 685–688.

Hoefs, J., 2009, Stable isotope geochemistry, Springer Verlag, Germany, 285p.

Hofstra, A., and Cline, J., 2000, Characteristics and models for Carlin-type gold deposits, Chapter 5: in Hagemann, S. G. and Brown, PE, eds., Gold in 2000: Reviews in Economic Geology, v. 13, p. 163-220.

Hofstra, A., Snee, L., Rye, R., Folger, H., Phinisey, J., Loranger, R., Dahl, A., Naeser, C., Stein, H., and Lewchuk, M., 1999, Age constraints on Jerritt Canyon and other carlin-type gold deposits in the Western United States; relationship to mid-Tertiary extension and magmatism: Economic Geology, v. 94, p. 769-802.

Hunziker, J., Frey, M., Clauer, N., Dallmeyer, R., Friedrichsen, H., Flehmig, W., Hochstrasser, K., Roggwiler, P., and Schwander, H., 1986, The evolution of illite to muscovite: mineralogical and isotopic data from the Glarus Alps, Switzerland: Contributions to Mineralogy and Petrology, v. 92, p. 157-180.

Huston, D., Kamprad, J., and Brauhart, C., Definition of high-temperature alteration zones with PIMA: an example from the Panorama VHMS district, central Pilbara Craton: Geology, v. 93, p. 292-303.

Ilchik, R., 1990, Geology and geochemistry of the Vantage gold deposits: Alligator Ridge-Bald Mountain mining district, Nevada: Economic Geology, v. 85, p. 50–75.

Iuoup, A., 1988, Mechanism of illite formation during smectite-to-illite conversion in a hydrothermal system: American Mineralogist, v. 73, p. 1325-1334.

Ji, J., and Browne, P., 2000, Relationship between illite crystallinity and temperature in active geothermal systems of New Zealand: Clays and Clay Minerals, v. 48, p. 139-144.

Johns, W., Grim, R., and Bradley, W., 1954, Quantitative estimations of clay minerals by diffraction methods: J. sediment. Petrol, v. 24, p. 241–251.

Kelley, D., Kelley, K., Coker, W., Caughlin, B., and Doherty, M., 2006, Beyond the obvious limits of ore deposits: the use of mineralogical, geochemical, and biological features for the remote detection of mineralization: Economic Geology, v. 101, p. 729-752.

Kelson, C., Crowe, D., and Stein, H., 2005, Geochronology and geochemistry o£ the Hilltop, Lewis, and Bullion mining districts and surrounding area, Battle Mountain-Eureka trend, Nevada, Geological Society of Nevada, p. 25.

—, 2008, Geochemical and Geochronological Constraints on Mineralization within the Hilltop, Lewis, and Bullion Mining Districts, Battle Mountain-Eureka Trend, Nevada: Economic Geology, v. 103, p. 1483-1506.

Kisch, H., 1990, Calibration of the anchizone: a critical comparison of illite'crystallinity'scales used for definition: Journal of Metamorphic Geology, v. 8, p. 31-46.

Kubler, B., 1967, La cristallinite de l'illite et les zones tout-a-fait superieures du metamorphisme., *in* Schaer, J.P., ed., Colloque sur les etages tectoniques: Baconniere, Neuchatel, p. 105-122.

Kübler, B., and Jaboyedoff, M., 2000, Illite crystallinity: CONCISE REVIEW PAPER: Comptes Rendus de l'Académie des Sciences-Series IIA-Earth and Planetary Science, v. 331, p. 75-89

Kuehn, C., and Rose, A., 1992, Geology and geochemistry of wall-rock alteration at the Carlin gold deposit, Nevada: Economic Geology, v. 87, p. 1697-1721.

Lanson, B., Velde, B., and Meunier, A., 1998, Late-stage diagenesis of illitic clay minerals as seen by decomposition of X-ray diffraction patterns: Contrasted behaviors of sedimentary basins with different burial histories: Clays and Clay Minerals, v. 46, p. 69-78.

Leavitt, E., Goldstrand, P., Schmidt, K., Wallace, A., Spell, T., and Arehart, G., 2000, Geochronology of the Midas gold-silver deposit and its relationship to volcanism and mineralization along the northern Nevada rift: Volcanic History, Structure, and Mineral Deposits of the North-Central Northern Nevada Rift, Field Trip Guidebook, v. 8, p. 157–162.

Leblanc, M., 1980, Chromite growth, dissolution and deformation from a morphological view point: SEM investigations: Mineralium Deposita, v. 15, p. 201-210.

Lonker, S., FitzGerald, J., Hedenquist, J., and Walshe, J., 1990, Mineral-fluid interactions in the Broadlands-Ohaaki geothermal system, New Zealand: American Journal of Science, v. 290, p. 995-1068.

Lubben, J., 2004, Quartz as clues to paragenesis and fluid properties at the Betze-Post deposit, northern Carlin trend, Nevada: Unpublished M.Sc. thesis, Las Vegas, Universitty of Nevada, p. 155.

Macchi, L., 1987, A review of sandstone illite cements and aspects of their significance to hydrocarbon exploration and development: Geological Journal, v. 22, p. 333-345.

McInnes, B., Evans, N., Fu, F., and Garwin, S., 2005, Application of thermochronology to hydrothermal ore deposits: Reviews in mineralogy and geochemistry, v. 58, p. 467-498.

Merry, N., Pontual, S., and Gamson, P., 1999, The Spectral Geologist" TSG" v 2.0 user manual: AusSpecInternational Pty. Ltd, Commonwealth Scientific and Industrial Research Organisation (CSIRO), Australia.

Meunier, A., 1977, Les mecanismes de l'alteration des granites et le role des microsystemes: etude des arenes du massif granatique de Parthenay (Deux-Se vres), PhD. Thesis, 258p.

Meunier, A., and Velde, B., 2004, Illite: origins, evolution, and metamorphism: Poitier, France, Springer Verlag, 286 p.

Moore, D., and Reynolds Jr, R., 1997, X-ray diffraction and the identification and analysis of clay minerals, Oxford University Press, New York, 378 p.

Morrow, J., and Sandberg, C., 2008, Evolution of Devonian carbonate-shelf margin: Nevada: Geology, v. 4, p. 445-458.

Mortensen, J., Thompson, J., and Tosdal, R., 2000, U-Pb age constraints on magmatism and mineralization in the northern Great Basin, Nevada: Geology and ore deposits, p. 419–438.

Naeser, C., and Mckee, E., 1970, Fission-track and K-Ar ages of Tertiary ash-flow tuffs, north-central Nevada: Geological Society of America Bulletin, v. 81, p. 3375-3384.

Noble, P., and Finney, S., 1999, Recognition of fine-scale imbricate thrusts in lower Paleozoic orogenic belts—An example from the Roberts Mountains allochthon, Nevada: Geology, v. 27, p. 543.

Norby, J., and Orobona, M., 2002, Geology and mineral systems of the Mike deposit: Gold Deposits of the Carlin Trend, p. 143–167.

Nutt, C., and Hofstra, A., 2003, Alligator Ridge district, east-central Nevada: Carlin-type gold mineralization at shallow depths: Economic Geology, v. 98, p. 1225-1241.

Ostwald, W., 1897, Studies of the formation and transformation of solid substances: phys. Chem, v. 22, p. 289.

Ouhadi, V., and Yong, R., 2003, Impact of clay microstructure and mass absorption coefficient on the quantitative mineral identification by XRD analysis: Applied Clay Science, v. 23, p. 141-148.

Pevear, D., 1999, Illite and hydrocarbon exploration: Proceedings of the National Academy of Sciences, v. 96, p. 3440-3446.

Pierce, J., and Siegel, F., 1969, Quantification in clay mineral studies of sediments and sedimentary rocks: Journal of Sedimentary Petrology, v. 39, p. 187-193.

Price, J.G., Muntean, J.L., Davis, D.A., and Hess, R.H., 2007, The Nevada mineral industry-2007: Nevada Bureau of Mines and Geology, v. Special Publication, p. 178.

Reed, M., 1982, Calculation of multicomponent chemical equilibria and reaction processes in systems involving minerals, gases and an aqueous phase: Geochimica et Cosmochimica Acta, v. 46, p. 513-528.

—, 1997, Hydrothermal alteration and its relationship to ore fluid composition: Geochemistry of hydrothermal ore deposits, p. 303–365.

Reiners, P., and Brandon, M., 2006, Using thermochronology to understand orogenic erosion: Annual Review Earth and Planetary Sciences, v. 34, p. 419-466.

Ressel, M., and Henry, C., 2006, Igneous geology of the Carlin trend: Nevada: Development of the Eocene plutonic complex and significance for Carlin-type gold deposits: Economic Geology and the Bulletin of the Society of Economic Geologists, v. 101, p. 347-383.

Reyes, A., 1990, Petrology of Philippine geothermal systems and the application of alteration mineralogy to their assessment: Journal of Volcanology and Geothermal Research, v. 43, p. 279-309.

Roberts, R., 1951, Geology of the Antler Peak quadrangle, Nevada: US Geol: Survey Geol. Quad. Map GQ-10.

—, 1966, Metallogenic provinces and mineral belts in Nevada: Nevada Bureau of Mines, Rept, v. 13, p. 47-72.

Rose, A., 1970, Zonal relations of wallrock alteration and sulfide distribution at porphyry copper deposits: Economic Geology, v. 65, p. 920-936.

Schleicher, A., Warr, L., Kober, B., Laverret, E., and Clauer, N., 2006, Episodic mineralization of hydrothermal illite in the Soultz-sous-Forêts granite (Upper Rhine Graben, France): Contributions to Mineralogy and Petrology, v. 152, p. 349-364.

Seedorff, E., Dilles, J., Proffett Jr, J., Einaudi, M., Zurcher, L., Stavast, W., Johnson, D., and Barton, M., 2005, Porphyry deposits: Characteristics and origin of hypogene features: Economic Geology, v. 100, p. 251–298.

Sillitoe, R., 2010, Porphyry copper systems: Economic Geology, v. 105, p. 3-41.

Simon, G., Kesler, S., and Chryssoulis, S., 1999, Geochemistry and textures of gold-bearing arsenian pyrite, Twin Creeks, Nevada; implications for deposition of gold in Carlin-type deposits: Economic Geology, v. 94, p. 405-421.

Simmons, S., and Browne, P., 2000, Hydrothermal minerals and precious metals in the Broadlands-Ohaaki geothermal system: Implications for understanding low-sulfidation epithermal environments: Economic Geology, v. 95, p. 971-999.

Srodon, J., Drits, V., McCarty, D., Hsieh, J., and Eberl, D., 2001, Quantitative X-ray diffraction analysis of clay-bearing rocks from random preparations: Clays and Clay Minerals, v. 49, p. 514-528.

Stager, H., 1977, Geology and Mineral Deposits of Lander County, Nevada, Part II Geology: Bulletin, v. 88.

Stenger, D., Kesler, S., Peltonen, D., and Tapper, C., 1998, Deposition of gold in carlin-type deposits; the role of sulfidation and decarbonation at Twin Creeks, Nevada: Economic Geology, v. 93, p. 201-215.

Sun, Y., Seccombe, P., and Yang, K., 2001, Application of short-wave infrared spectroscopy to define alteration zones associated with the Elura zinc-lead-silver deposit, NSW, Australia: Journal of Geochemical exploration, v. 73, p. 11-26.

Taylor, H.P., 1974, The Application of Oxygen and Hydrogen Isotope Studies to Problems of Hydrothermal Alteration and Ore Deposition: Economic Geology, v. 69, p. 843-883.

Teal, L., and Jackson, M., 2002, Geologic overview of the Carlin trend gold deposits: Gold deposits of the Carlin trend: Nevada Bureau of Mines and Geology Bulletin, v. 111, 204 p.

Tosdal, R., Dilles, J., and Cooke, D., 2009, From source to sinks in auriferous magmatic-hydrothermal porphyry and epithermal deposits: Elements, v. 5, p. 289-295.

Tosdal, R., Wooden, J., and Kistler, R., 2000, Inheritance of Nevadan mineral belts from Neoproterozoic continental breakup: Geology and ore deposits, p. 15–18.

van de Kamp, P., 2008, Smectite-illite-muscovite transformations, quartz dissolution, and silica release in shales: Clays and Clay Minerals, v. 56, p. 66-81.

Van Santen, R., 1984, The Ostwald step rule: The Journal of Physical Chemistry, v. 88, p. 5768-5769.

Varadachari, C., 2006, Fuzzy phase diagrams of clay minerals: Clays and Clay Minerals, v. 54, p. 616-625.

Warr, L., 1996, Standardized clay mineral crystallinity data from the very low-grade metamorphic facies rocks of southern New Zealand: European Journal of Mineralogy, v. 8, p. 115-127.

Wernicke, B., England, P., Sonder, L., and Christiansen, R., 1987, Tectonomagmatic evolution of Cenozoic extension in the North American Cordillera: Geological Society London Special Publications, v. 28, p. 203-221.

White, N., and Hedenquist, J., 1995, Epithermal gold deposits: styles, characteristics and exploration: Society of Economic Geologists Newsletter, v. 23, p. 9–13.

Whitney, G., and Northrop, H., 1988, Experimental investigation of smectite-to-illite reaction--dual reaction mechanisms and oxygen-isotope systematics: American Mineralogist, v. 73, p. 77-90.

Winterer, E., 1968, Tectonic Erosion in the Roberts Mountains, Nevada: The Journal of Geology, p. 347-357.

Yang, K., Browne, P., Huntington, J., and Walshe, J., 2001, Characterising the hydrothermal alteration of the Broadlands-Ohaaki geothermal system, New Zealand, using short-wave infrared spectroscopy: Journal of Volcanology and Geothermal Research, v. 106, p. 53-65.

Yates, D., and Rosenberg, P., 1997, Formation and stability of endmember illite: II. Solid equilibration experiments at 100 to 250 C and Pv, soln: Geochimica et Cosmochimica Acta, v. 61, p. 3135-3144.

Ye, Z., Kesler, S., Essene, E., Zohar, P., and Borhauer, J., 2003, Relation of Carlin-type gold mineralization to lithology, structure and alteration: Screamer zone, Betze-Post deposit, Nevada: Mineralium Deposita, v. 38, p. 22-38.

Yeh, H., 1980, Ratios and late-stage dehydration of shales during burial: Geochimica et Cosmochimica Acta, v. 44, p. 341-352.

Zhang, G., Wasyliuk, K., and Pan, Y., 2001, The characterization and quantitative analysis of clay minerals in the Athabasca Basin, Saskatchewan: application of shortwave infrared reflectance spectroscopy: Canadian Mineralogist, v. 39, p. 1347-1363.

Zoback, M., McKee, E., Blakely, R., and Thompson, G., 1994, The northern Nevada rift: Regional tectono-magmatic relations and middle Miocene stress direction: Geological Society of America Bulletin, v. 106, p. 371-382.

CHAPTER 4 – SHEDDING LIGHT ON THE ABYSS: LATERAL FLUID FLOW UNDERNEATH AND INTO CARLIN-TYPE GOLD DEPOSITS

4.1 INTRODUCTION

Hydrothermal ore deposits form when metals are precipitated from a hydrothermal fluid following some physiochemical change; i.e., acid neutralization, oxidation, decreasing temperature and/or pressure (Barnes, 1997). Ore-forming fluids are generally thought to enter hydrothermal mineral deposits via major fault structures, tapping some fluid reservoir at depth underneath the deposit. The presence of faults and cracks in country rock can provide higher permeability pathways for hydrothermal fluid, in otherwise low permeability wall rock (Jiang et al., 1997; Oliver and Bons, 2001). Conversely, faults can act as barriers to fluid flow by the development of fine clay-rich gouge and/or the precipitation of hydrothermal cementation minerals (Sibson, 1992; Caine et al., 1996).

In the shallow crust, fluid flow responsible for the formation of many hydrothermal ore deposits is generally thought to occur in a dominantly vertical direction controlled by high angle fault structures, with fluids driven largely by buoyancy changes caused by thermal anomalies at depth i.e. skarn (Sillitoe and Bonham, 1990), epithermal (John et al., 2003), VMS (Schardt et al., 2005). Such a model implies that ore fluids well up directly underneath the deposit. The role of lateral fluid flow in the formation of hydrothermal ore deposits is generally thought to be small, and is most commonly observed within basin-hosted stratabound ore deposits such as Mississippi Valley Type deposits (Garven and Freeze, 1984), where gravity and gradients in topography drive fluid flow. Computer simulations suggest that in order for lateral flow to dominate, horizontal permeability must be on the order of one hundred times greater than vertical permeability (Rosenberg et al., 1993; Dickson et al., 1995; Fisher and Becker, 1995). Extensive lateral flow has been documented in some deposit settings up to 8km from the source of fluid at the giant Bingham porphyry deposit (Sillitoe and Bonham, 1990), and up to 3km from its magmatic source in skarn deposits (Meinert, 1987).

Stable isotope analyses of carbon and oxygen provide a means by which to map fluid flow-rock interaction and determine fluid flow pathways. In a fluid buffered system, such as Carlin-type gold systems, the exchange of oxygen isotopes between country rock and relatively ^{18}O depleted meteoric-hydrothermal fluid can lower the $\delta^{18}O$ values of country rocks from 'background' (unaltered) values to lower (Taylor and Epstein, 1963; Criss and Taylor, 1986; Singleton and Criss, 2002). The overall lowering of $\delta^{18}O$ values is termed 'depletion'. For example, calcium carbonate dissolved as a hydrothermal fluid may reprecipitate with a different oxygen and carbon isotope signature than prior to dissolution according to the following equilibrium reaction:

$$CaC^{18}O^{16}O^{16}O + H_2(^{16}O) \Leftrightarrow CaC^{16}O^{16}O^{18}O + H_2(^{18}O) \quad \textbf{(eqn. 4.1)}$$

The newly formed hydrothermal mineral is typically strongly depleted with respect to the heavy oxygen isotope compared to its sedimentary predecessor. High fluxes of meteoric fluids and high fluid rock ratios will lower $\delta^{18}O$ values of rocks. Carbon isotope values of the newly precipitated mineral depend on the origin of carbon in the fluid: either organic or deeply sourced (magmatic or metamorphic). Measurable stable isotope shifts between unaltered and altered rock may occur where there is no other evidence of hydrothermal alteration such as gold or other trace element anomalies (Taylor, 1974; Criss and Taylor, 1986; Singleton and Criss, 2002; Arehart and Donelick, 2006).

Oxygen isotopes have been used to delineate hydrothermal fluid flow pathways in the Comstock Lode epithermal mining district, where faults focusing ore-forming fluid are defined by long belts of depleted $\delta^{18}O$ values (Criss et al., 2000; Singleton and Criss, 2002; 2004). Stable isotope analyses have also been used to identify isotope depletion halos around ore bodies in order to vector toward the core of ore-systems (Taylor et al., 1974; Cathles, 1993; Paradis et al., 1993; Naito et al., 1995; Stenger et al., 1998; Arehart and Donelick, 2006). This paper presents a study that uses carbon and oxygen stable isotopes in conjunction with a pre-existing trace element database to investigate pathways taken by ore-forming fluids into the Pipeline deposit, a giant Carlin-type sediment hosted disseminated gold deposit located in north-eastern Nevada (Figure 1). In particular, there is a large, shallow-lying thrust fault beneath the ore deposit that we investigated as a major feeder zone for mineralization. The results of this study suggest that ore-forming fluid flow into the Pipeline deposit was dominantly lateral and occurred along major pre-existing thrust faults.

4.2 GEOLOGICAL SETTING OF THE PIPELINE DEPOSIT

The world class Carlin-type gold deposits of north-eastern Nevada provide nearly one tenth of the world's annual gold production (Cline et al., 2005; Price et al., 2007). The majority of gold is disseminated and occurs in silty carbonate rock forming the footwall (lower plate) of the Roberts Mountain thrust system (Cline et al., 2005). Hangingwall siliciclastic rocks (upper plate) are not known to host any major gold deposits however gold does occur locally at the Roberts Mountains Thrust (RMT). The giant Pipeline gold deposit is located at the south-eastern corner of the Shoshone Range in north-eastern Nevada, approximately 70km southeast of the town of Battle Mountain (Figure 4.1). The Pipeline deposit is located in a tectonic window through the RMT fault that exposes lower plate carbonate rocks at surface. Bedrock is covered by 14-100m of Quaternary alluvium (Foo et al., 1996).

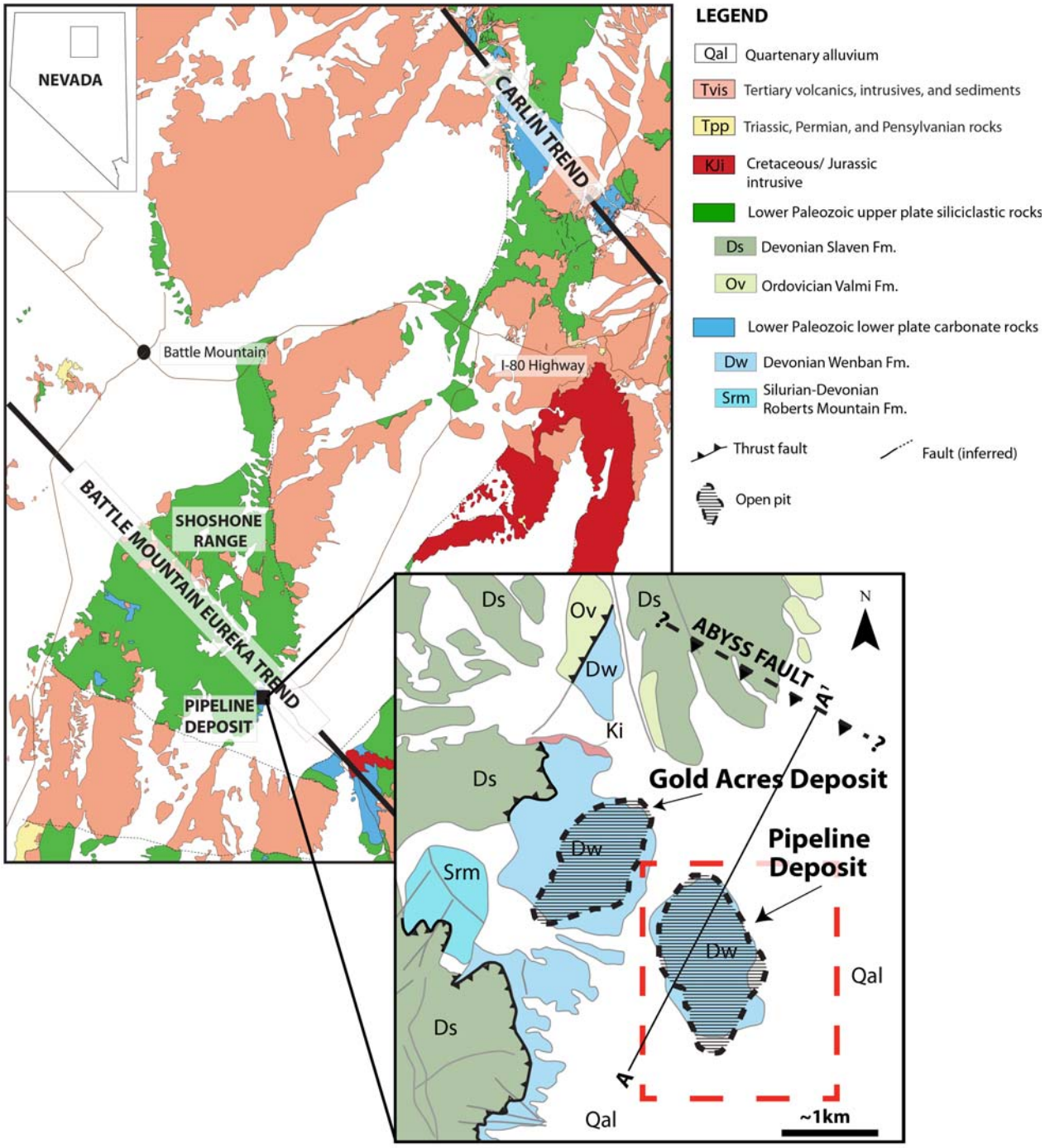

Fig. 4.1. Regional geology map of north-eastern Nevada showing the location of the Pipeline gold deposit at the south-eastern corner of the Shoshone Range. (Inset) Simplified geology map of the Pipeline gold deposit and surrounding area. The Pipeline deposit is located in a tectonic window through the upper plate that exposes lower plate at surface. A- A^1 is the location of geological cross-section shown in Figure 4.2. Dashed red square represents location of Figure 4.4.

At the Pipeline deposit, lower plate carbonate rocks can be subdivided into four main units (Emsbo et al., 2003). The Devonian Horse Canyon Formation is a calcareous siltstone, mudstone and chert with local occurrences of sandstone and mudstone. The Devonian Wenban Formation is composed of laminated calcareous and dolomitic siltstones, micritic limestone, and thick bioclasitc debris flows. The Silurian Roberts Mountain Formation is dominated by laminated dolostone, calcareous mudstone and calcareous siltstone. The Ordovician Hanson Creek Formation is dominantly a sandy dolostone. The overlying upper plate comprises siliciclastic units with the rare occurrence of thin carbonate lenses. In the region of the Pipeline deposit, the volumetrically most extensive of the upper plate clastic sediment packages is the Ordovician Valmi Formation composed of several thousand meters of chert, quartz arenite, argillite, slate, and greenstone (Roberts, 1966). The Silurian Elder Formation is a set of interbedded shale, siltstone, chert, and feldspathic and calcareous sandstone. The Devonian Slaven Formation is a mixture of highly contorted and broken, black, nodular chert with some carbonaceous shale partings.

4.2.1 Carlin-type Au-Mineralization

Carlin-type deposits are sediment hosted disseminated gold deposits that are largely restricted to north-eastern Nevada. Most of the gold is disseminated in deposits within silty carbonate host rocks that were decarbonatized during hydrothermal alteration (Cline et al., 2005). Gold occurs almost exclusively as auriferous, trace-element rich pyrite rims (Barker et al., 2009). Fluid inclusions in ore-stage minerals from a number of Carlin-type gold deposits have provided constraints on the temperature and composition of ore-forming fluids in Carlin systems. Fluids were between 180-240°C, slightly acidic (pH ~4), reduced, and low salinity and contain little CO_2 and CH_4. Previous studies have shown a correlation between elevated concentrations of As, Sb, Hg, Tl, and Te with increasing gold concentration in Carlin-type gold deposits (Emsbo et al., 2003; Barker et al., 2009; Almeida et al., 2010). On the nanoscale, gold-rich pyrite rims from the Banshee and Turquoise ridge deposits exhibit elevated concentrations of this trace element assemblage when compared to rims where gold is absent (Barker et al., 2009). Stable isotope analyses of ore-stage minerals to determine the source of ore-forming fluid indicate that fluids were dominated by meteoric water; however some deposits exhibit a distinctly magmatic/ metamorphic isotope signature.

In the Pipeline deposit, economic gold grades are largely restricted to the Wenban and Roberts Mountains Formations with lower grades contained in the Ordovician Hanson Creek and Devonian Horse

Canyon Formations. Gold grade is controlled by two main factors: (i) higher inherent permeability of has made them preferred hosts for mineralization whereas massive limestone, dolostone and marble are not, and (ii) secondary permeability in zones of brecciation and faulting, specifically duplex thrust fault structures. Host rocks exhibit a local addition of organic carbon typically associated with faults and fractures, however, no genetic relationship has been established between carbon alteration and gold mineralization. No igneous rocks occur within the Pipeline deposit proper, although the Gold Acres stock, a Cretaceous quartz monzonite pluton, is located less than one km from the western edge of the Pipeline deposit (Mortenson et al., 2000). The stock is associated with poly metallic skarn mineralization of the Gold Acres deposit, adjacent to the Pipeline deposit. Lower plate limestone and limey-siltstone of the Pipeline deposit are locally contact metamorphosed evidenced by the occurrence of marble and tremolite crystals.

4.2.2 Previous isotope studies of the Pipeline Deposit

Previous work analyzing light stable isotopes in carbonate minerals was carried out by Arehart and Donelick (2006), and Rye (1985) who identified a $\delta^{18}O$ isotopic depletion halo in carbonate rocks around the Pipeline gold deposit. These studies identified a characteristic depletion trend from unaltered rocks to altered rocks. Unaltered rocks exhibited $\delta^{18}O$-enriched isotope signatures with $\delta^{18}O$ values of ~23 ‰. Altered carbonate rocks exhibited more $\delta^{18}O$ depleted values of ~11 ‰. A generally positive relationship between carbon and oxygen depletion is apparent from the data of previous studies (Arehart and Donelick, 2006). Carbon isotope data is more erratic and exhibits less variation than oxygen isotope data. $\delta^{13}C$ values vary from -5.5 – 0.4 ‰. The general lowering of $\delta^{13}C$ values from typical marine carbonate values (~0.0 ‰) may reflect some conversion of organic carbon to carbonate and subsequent exchange with rock carbonate. Because the amount of organic carbon is relatively minor in comparison to the amount of rock carbonate carbon, the changes in rock carbon isotopes is generally fairly minimal (Arehart and Donelick, 2006). Data published by Arehart and Donelick (2006) has been incorporated into this study.

4.3 FAULT RELATED FLUID FLOW IN CARLIN SYSTEMS AND THE ABYSS FAULT

Many studies have highlighted the importance of large fault structures to fluid flow in Carlin type deposits (Radtke et al., 1980; Kuehn and Rose, 1992; Ressel et al., 2000). On the regional scale, Carlin-type deposits occur along NE-SW trending lineaments including the Carlin and Battle Mountain-Eureka

mineral belts. The alignment of Carlin-type deposits is thought to reflect major basement fault fabrics established during Neoproterozoic rifting (Roberts, 1966; Tosdal et al., 2000). The Roberts Mountain thrust fault, a result of compression during the Antler Orogeny, defines the upper stratigraphical limit to gold mineralization in most Carlin-type gold deposits. On the deposit scale, individual deposits are typically fault controlled; examples include Carlin (Kuehn and Rose, 1992), Getchell (Cline and Hofstra, 2000), and Meikle (Emsbo et al., 2003). The Post-Genesis fault system has been identified as a significant conduit to mineralizing fluid forming a network of Carlin-type deposits in the Northern Carlin trend including the giant Betze-Post deposit (Leonardson and Rahn, 1996). Mineralization in these systems is thought to be a passive process whereby fluids flowed along reactivated older faults. Only in a few cases is there evidence for over-pressuring to supra-lithostatic pressures and development of new fault systems (Kuehn and Rose, 1992; Cline and Hofstra, 2000; Heitt et al., 2003).

No major structures have been identified as feeder zones for ore-forming fluid in the Pipeline deposit. The Pipeline deposit is, however, unique in that it is the only locality identified where lower plate has been thrust over upper plate cross-cutting the RMT. Figure 4.2 presents a schematic section though the Pipeline deposit. The Abyss fault is a major structural feature underlying mineralization at the Pipeline deposit. 3D modeling of the Abyss fault surface indicates that the fault is curvi-planar, dipping variably to the south and southwest and is projected to intersect the surface at the North end of the Pipeline property (Barrick Gold Corporation internal report). Structural mapping of the Pipeline and Gold Acres deposits suggests that the RMT and the Abyss fault are part of a duplex fault/fold culmination similar to the hinterland dipping and antiformal stacked duplexes described by Boyer and Elliott (1982). The RMT represents the roof thrust, and the Abyss represents a younger floor thrust (Leonardson, 2010). Imbricate faults stemming from the Abyss floor thrust may have provided a permeable pathway for mineralizing fluid (Leonardson, 2010). A number of deep drill holes have intersected lower plate silty limestone beneath the Abyss fault. This intersection is thought to represent the footwall expression of the RMT beneath the Abyss fault (Figure 4.2).

Visible alteration at the Abyss fault zone is generally characterized by strong carbon alteration accompanies by decalcification, clay gouge and zones of rubble (Figure 4.3). Abundant calcite veining can occur directly above the fault (within <50m); however, calcite veining is common throughout the

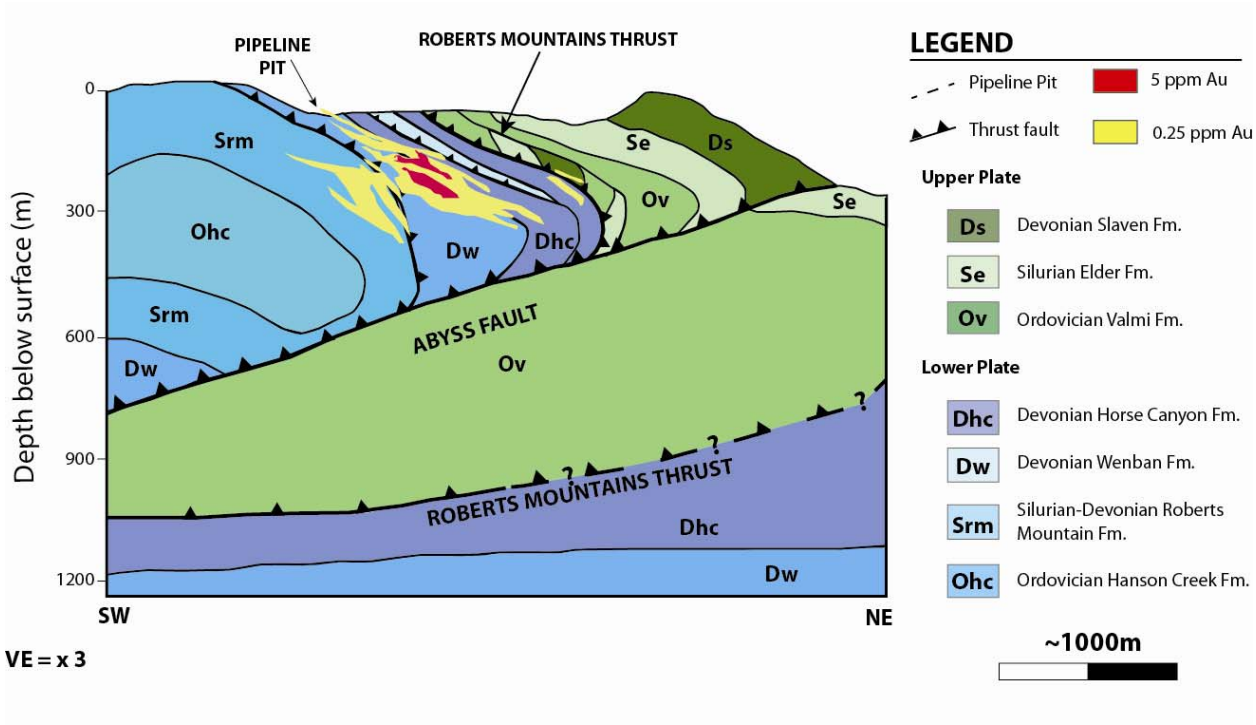

Fig. 4.2. Schematic cross section through the Pipeline deposit (section A-A[1] in Figure 1). The Abyss fault offsets the RMT placing imbricately thrusted lower plate on top of a thick sequence of upper plate. This is a reversal of the tectono-stratigraphic sequence emplaced by the Roberts Mountain thrust.

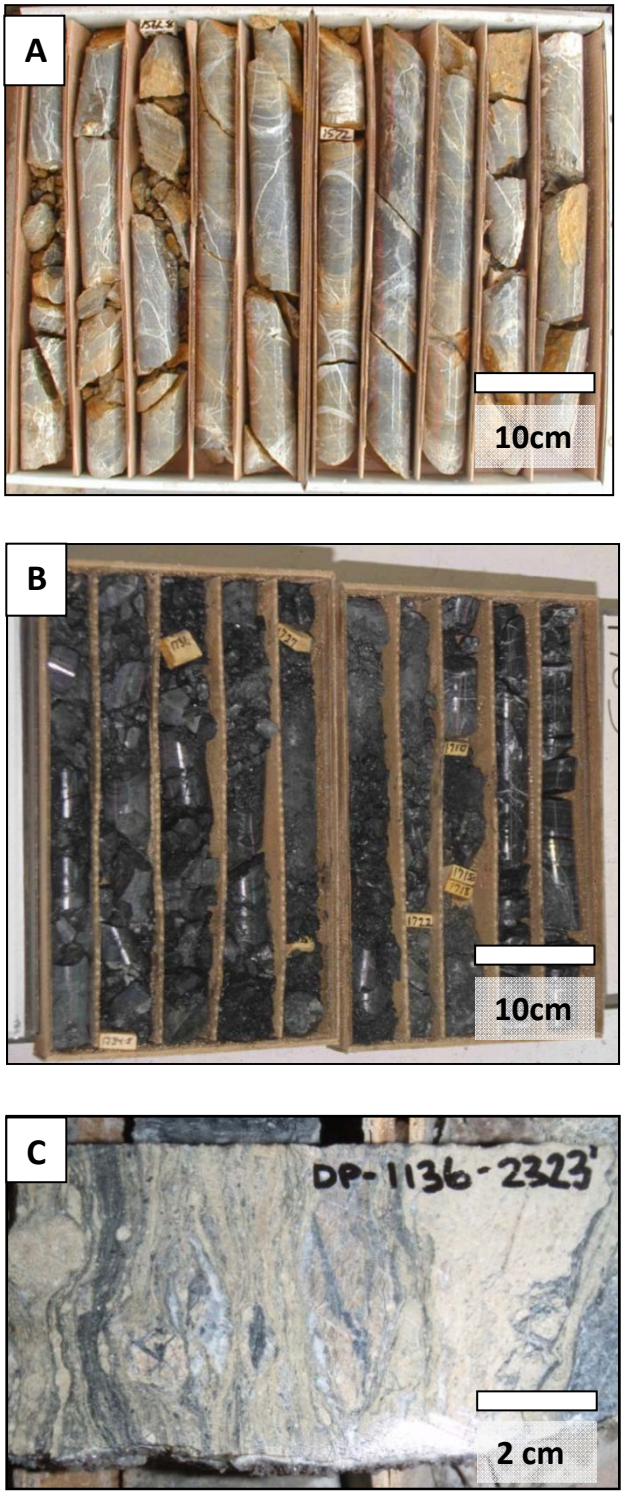

Fig. 4.3. Core photographs of zones above, within, and beneath the Abyss fault. A. Unaltered, unmineralized silty limestone ~65m above the main Abyss fault zone containing abundant calcite veining. B. The Abyss fault zone is characterized by local decalcification typically associated with strong carbon alteration, and zones of rubble and fault gouge. C. The footwall of the Abyss fault is marked by variably ductiley and brittley deformed Ordovician Valmi Fm. greenstone with siltstone, chert, and limestone lenses at greater depth.

deposit. Footwall siliciclastic rocks can be variably deformed proximal to the fault contact. Footwall rocks contain abundant silica veining and little calcite veining. The fault may also lack visible alteration. In such cases, the fault is marked only by a small zone of rubble, and an abrupt transition from carbonate rocks to siliciclastic rocks.

This study aims to determine the role of the Abyss fault in guiding ore-forming fluids into the Pipeline deposit. Significant clay gouge followed by loss of permeability may suggest that the Abyss fault was as a barrier to vertical fluid flow. In such a case, oxygen isotopes values would be undepleted at and above the fault. We would also expect an absence of gold and other associated trace elements at the fault. Conversely, the Abyss fault may have been the main conduit for fluid. Ore-forming fluid flowed along the fault and entered the deposit along secondary faults connected to the Abyss fault. In this case, oxygen isotope depletion would occur pervasively from the Abyss fault upward into the main zone of gold mineralization. Similarly, we would expect Au and other trace element values to be elevated in the same regions. Finally, flow of ore-forming fluids may have occurred along the Abyss fault but is not connected with fluids forming the Pipeline deposit. Oxygen isotopes along the fault would be depleted in this situation and gold and other trace element may be present in elevated concentrations if the fluid was carrying gold.

4.4 METHODS and ANALYTICAL TECHNIQUES

Over 285 carbonate rock and calcite vein samples from the Pipeline open pit, and drill holes through the Abyss Fault from surface (both reverse circulation (RC) chips and drill core) were analyzed for carbon and oxygen stable isotopes. Drill hole locations are shown in Figure 4.4. Samples taken from RC-chip holes represent 3.05m (10ft) composites. Samples for this study were taken at regular intervals starting at the Abyss fault contact between upper plate (footwall) and lower plate (hangingwall). Sample density was highest proximal to the fault with density decreasing with distance from the main fault zone: every 5-10m near the contact, and every 30-40m between 100-300m above the contact. Vein samples were analyzed separately from the rock matrix. Drill core samples were spot micro-drilled to obtain ~2-3g of powdered material. Multiple chips from each RC interval were ground into a fine powder and homogenized using a mortar and pestle. Analyses were completed by the Pacific Centre for Isotopic and Geochemical Research at the University of British Columbia. Weighed samples (between 0.2 to 1.5g) were analyzed using a ThermoFinnigan Delta plus mass spectrometer and gas bench. Sample and standard mineral powders were treated with phosphoric acid in sealed glass exetainers that had been

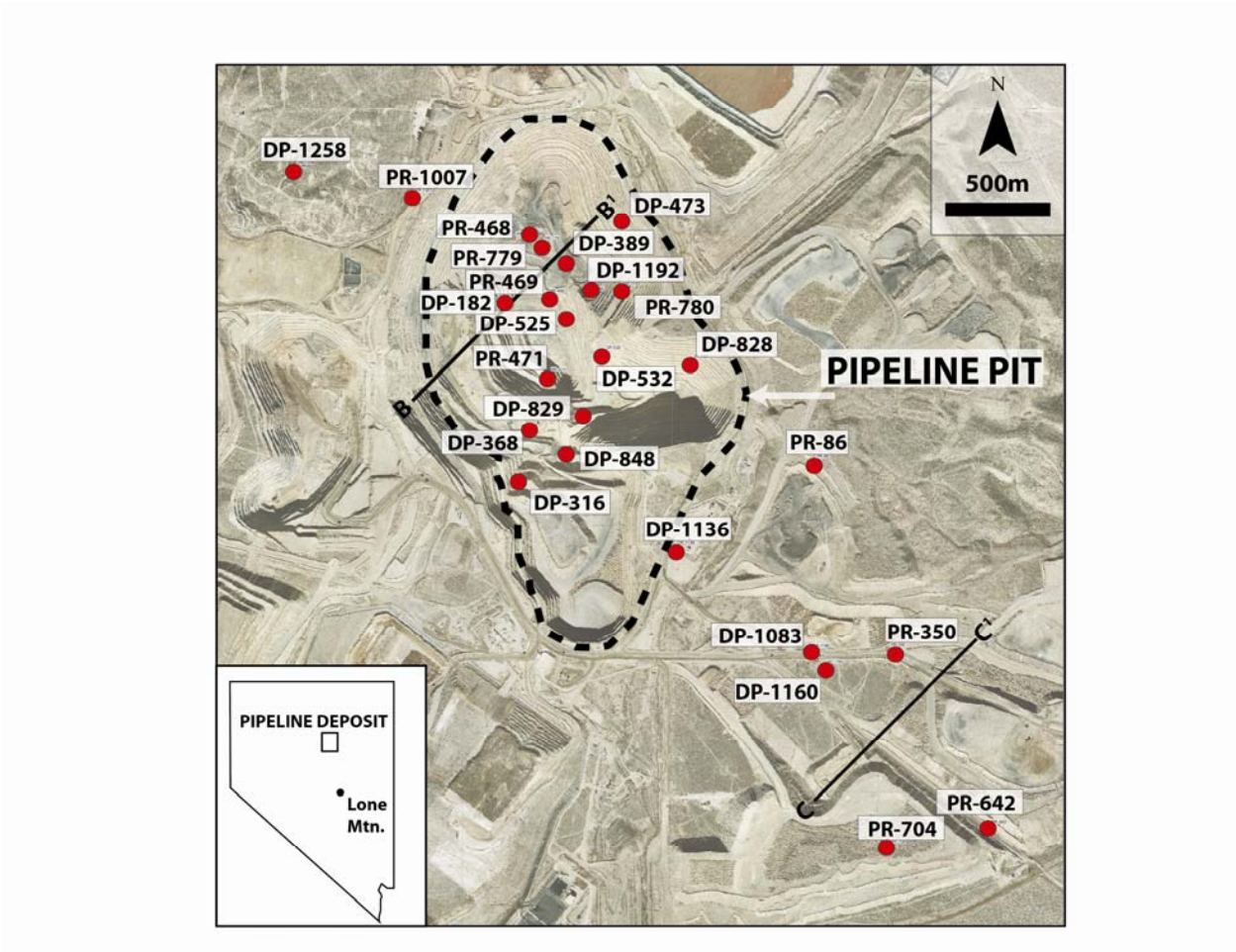

Fig. 4. Location of all drill holes sampled in this study and location of cross sections. The inset map shows the location of Lone Mountain, the type-section for lower plate rocks used as samples for background values for stable isotope analyses in this study.

flushed with helium. The CO_2 produced was introduced into the mass spectrometer in continuous flow mode, using helium as the carrier gas. The gas from the sample was run along with internal reference standards, as well as internationals standards NBS18, NBS19, BN13, BN83-2, H6M, and Merck. Finally, the CO_2 produced was introduced into the mass spectrometer in continuous flow mode. *Laboratory Information Management Software* (http://www.usgs.gov/) was employed to aid in the reduction of data.

Gold assay and multi-element lithogeochemistry values included in this study are courtesy of Barrick Gold Corporation Pipeline deposit database. Each analysis represents a 3.05m (10ft) composite. Reverse circulation chip composites consisted of a random sampling of chips along a 3.05m interval. Drill core composites consisted of small pieces of split core taken at regular intervals from along a 3.05m section. Background samples collected from the Lone Mountain area were analyzed separately from mine samples; however the analytical methods used were the same. Samples were sent to ALS Chemex Laboratory for analyses. Analytical procedures and detection limits for elements analyzed in this study are described in Table 4.1. Standard QA/QC procedures were adhered to. Internal company standards were included every 20 samples, and paired blanks and duplicates every 20 samples between standards.

Table. 4.1. Procedures and detection limits for elements analyzed in this study.

Element	Procedure	Lower – Upper detection limit (ppm)
Au	Fire assay	0.01-100
As	Aqua regia digestion	0.1-10,000
Sb	Aqua regia digestion	0.05-10,000
Hg	Aqua regia digestion	0.01-10,000
Tl	Aqua regia digestion	0.02-10,000
Te	Aqua regia digestion	0.01-500

4.4.1 Background $\delta^{18}O$, $\delta^{13}C$, Au and trace element values for marine carbonate rocks

The Lone Mountain area, central Nevada, is a classic section for unaltered, unmineralized lower plate rock and includes all the formations observed in the Pipeline deposit (Figure 4.4) (Finney et al., 1999). Samples from the Lone Mountain area were collected for stable isotope analyses to better constrain the isotopic range of unaltered lower Paleozoic marine carbonate rocks in Nevada. $\delta^{18}O$ values

are reported relative to VMOW (standard mean ocean water) and $\delta^{13}C$ values are reported relative to VPDB (Peedee Belemnite). $\delta^{18}O$ and $\delta^{13}C$ values for background samples from Lone Mountain are shown in Table 4.2. Background samples show a range in $\delta^{18}O$ values from 24.3 – 27.2 ‰ which is consistent with the range of previously reported global values for Silurian-Devonian marine carbonate (Veizer et al., 1999). In order to ensure that samples are indeed depleted, and to account for any analytical error, for the purposes of this study a sample is considered to be depleted in $\delta^{18}O$ if the value is <20.0 ‰. $\delta^{13}C$ values for unaltered marine carbonates are typically ~ 0 ‰ (Ohmoto and Rye, 1979). $\delta^{13}C$ values in background samples from this study are within the range previously reported for the Lone Mountain area (Finney et al., 1999). A sample is considered to be depleted in $\delta^{13}C$ is values are significantly higher or lower than typical marine carbonate values.

Aside from one sample containing 0.155ppm Au, all other samples from Lone Mountain contain gold concentrations <0.075 ppm. Given the lack of ore-grade gold mineralization, and an apparent lack of extensive interaction with a hydrothermal fluid (as evidenced by stable isotope analyses), the Lone Mountain samples can also provide some insight into background values for Au, As, Sb, Tl, and Te in marine carbonate rocks (Table 4.2). Arsenic values range from below detection limit (<0.1 ppm) to 26 ppm. Antimony concentrations don't exceed 1 ppm. All Tl values are below detection limit, and Te is near or at the detection limit of 0.01 ppm. Previous studies have shown that in ore-grade samples, the concentration of these trace elements can be 2-3 orders of magnitude larger than background values (Stenger et al., 1998; Cline et al., 2005; Almeida et al., 2010).

Table 4.2. Stable isotope data and trace element geochemistry values for unaltered, unmineralized background samples from Lone Mountain, Nevada. Average error on $\delta^{18}O$ = ± 0.6 ‰, $\delta^{13}C$ = ± 0.2‰.

Unit	Rock Type	Easting	Northing	$\delta^{13}C$ (‰)	$\delta^{18}O$ (‰)	Au (ppm)	As (ppm)	Sb (ppm)	Hg (ppm)	Tl (ppm)	Te (ppm)
Hanson Creek Fm.	Limestone	4382291	562116	1.47	25.4	0.003	5	0.32	0.021	<0.5	0.01
Roberts Mountain Fm.	Silty Limestone	4382357	562266	-0.05	26.6	0.073	6	0.77	0.1	<0.5	0.01
Roberts Mountain Fm.	Silty Limestone	4382328	562179	1.24	24.3	0.018	5	0.37	0.038	<0.5	0.01
Lone Mountain	Dolomite	4382630	562539	0.93	24.6	0.155	26	0.73	0.113	<0.5	0.03
Nevada Group	Dolomite	4382957	562844	-0.68	25.5	0.003	<0.1	0.15	0.007	<0.5	0.01
Nevada Group	Limestone	4383087	563024	3.51	26.2	<0.001	4.1	0.42	0.008	<0.5	0.01
Nevada Group	Limestone	4383145	563108	-1.19	27.2	<0.001	0.1	0.09	<0.005	<0.5	0.02

4.5 RESULTS

4.5.1 $\delta^{18}O$ and $\delta^{13}C$ values of rocks

Carbon and oxygen stable isotope data for rock and vein samples analyzed in this study are presented in Table 4.3. A broadly positive relationship exists between $\delta^{18}O$ depletion and $\delta^{13}C$ depletion in the same samples; however, there is far less range in carbon isotope values (Figure 4.5). There was no apparent correlation between stratigraphic formation and stable isotope composition (Appendix F). Samples from different formations are not differentiated in Figure 4.5. Samples of carbonate matrix at and above the Abyss fault ranged from 3 ‰ to 25 ‰, and $\delta^{13}C$ values range from -21.08 to 2.28 ‰. Only four samples exhibit $\delta^{13}C$ values lower than -8 ‰, and may be a result of analytical error. Approximately 40% all of rock samples occur outside of the range associated with background marine carbonate oxygen isotope values, indicating that these samples are depleted in $\delta^{18}O$. Approximately 60% of samples occur outside of the $\delta^{13}C$ range ((-1)-1‰) typically associated with marine carbonates. In particular, two samples located at the Abyss fault contain significantly depleted $\delta^{13}C$ values.

Cross sections through the Pipeline deposit showing oxygen isotope data for rock samples is presented in Figure 4.6, and includes previous analyses completed by Arehart and Donelick (2006) taken from the main ore zone of the Pipeline deposit. Not every drill hole sample intersecting the Abyss fault exhibits stable isotope depletion. Drill holes DP-525, PR-471, and PR-704 exhibit background, undepleted oxygen isotope values at and within close proximity to the Abyss fault (Figure 4.6). The majority of samples, however, within ~100 m of the Abyss fault are significantly more depleted in $\delta^{18}O$ than samples above this depth. Data included from drill holes intersecting the main zone of mineralization indicate pervasive depletion in the region of highest gold concentration. Shallow drill holes, such as DP-1258, that stop before intersecting the Abyss fault exhibit mineralization throughout the span of the drill hole (Table 4.3, Figure 4.6). Stable isotope values of samples from shallow drill holes are largely depleted.

Figures 4.7 and 4.8 illustrate the trend in stable isotope values as a function of depth relative to the Abyss fault. There is an absence of depleted values between 100 m – 800 m above the Abyss fault, with only six samples exhibiting depletion in $\delta^{18}O$. Samples between the Abyss fault zone and 150 m below the Abyss fault vary between depleted and undepleted, but no samples exhibit the same significantly depleted values (<15 ‰) present directly at the Abyss fault. Stable isotope data beneath the Abyss fault is limited due to the lack of carbonate material in upper plate rocks. Approximately 200m

Table 4.3. $\delta^{18}O$ and $\delta^{13}C$ values for rock and vein samples. Average error for $\delta^{18}O$ = ± 0.15‰, $\delta^{13}C$ = ± 0.33 (To Abyss = Distance from the Abyss fault, Fm = Formation, Srm = Silurian Roberts Mountain, Dw =Devonian Wenban, Ohc=Ordovician Hanson Creek, Dhc = Devonian Horse Canyon, Ov = Ordovician Valmi, Se= Silurian Elder, RC= reverse circulation, DH = diamond drill hole)

HOLE ID	Depth (m)	To Abyss (m)	Fm	$\delta^{13}C$ rock (‰)	$\delta^{18}O$ rock (‰)	$\delta^{13}C$ vein (‰)	$\delta^{18}O$ vein (‰)	Au (ppm)	As (ppm)	Sb (ppm)	Tl (ppm)	Te (ppm)	Hg (ppm)
DP-1083	285.8	270.5	Srm	0.59	18.83	-3.19	13.63	0.028					
RC	303.3	253.0	Srm	0.7	19.78	-2.43	10.49	0.028					
	317.3	239.0	Srm	-0.94	20.33	-4.76	13.63	0.028					
	334.1	222.2	Srm	0.17	21.66			0.084					
	334.1	222.2	Srm	0.4	21.32	-2.52	16.82	0.084					
	359.4	196.9	Srm	0.12	21.32	1.02	8.76	0.028					
	382.8	173.5	Srm	-1.26	19.09			0.056					
	391.7	164.6	Srm	-1.38	22.26	-3.44	14.23	0.168					
	394.1	162.2	Srm	0.23	21.04			0.056					
	404.5	151.8	Srm	-1.09	18.95	-5.12	13.21	0.028					
	424.3	132.0	Srm	-0.35	22.5	-3.67	11.66	0.28					
	426.7	129.6	Srm			-5.16	12.17	0.56					
	438.0	118.3	Srm	0.81	23.75			0.112					
	446.8	109.5	Srm	1.39	25.2			0.028					
	446.8	109.5	Srm	0.3	24.36			0.028					
	461.5	94.8	Srm	0.53	22.63			0.056					
	461.5	94.8	Srm	-1.76	21.37			0.056					
	481.6	74.7	Srm	-0.16	20.13	-0.87	20.67	0.028					
	502.0	54.3	Srm	-1.53	19.59	-1.51	10.33	0.028					
	527.0	29.3	Srm		22.9			0.028					
	531.0	25.3	Srm	0.22	21.54			0.056					
	543.5	12.8	Srm	-1.48	14.5			0.028					
	552.3	4.0	Srm	0.35	15.99	-2.25	10.88	0.028					
	555.3	1.0	Srm	-0.84	17.72	-2.23	-0.02	0.112					
	555.7	0.6	Srm	-2.32	15.73	-0.56	13.26	0.112					
DP-1136	641.6	66.1	Srm	-1.08	20.11	-3.51	10.1	0.028					
DH	648.3	59.4	Srm	-1.03	21.09	-3.04	8.5	0.028					
	657.8	49.9	Srm	-15.4	20.62			0.028					
	669.0	38.7	Srm	-1.12	19.72	-2.75	8.8	0.028					
	661.7	46.0	Srm	-0.99	19.68			0.028					
	676.0	31.7	Srm			-3.56	10.19	0.028					
	678.2	29.5	Srm			-0.98	20.32	0.028					
	680.9	26.8	Srm	-1.48	20.96	-0.97	19.66	0.028					
	680.9	26.8	Srm	-0.89	20.44			0.028					
	691.9	15.8	Srm	-1.46	20.4			0.028					
	657.8	49.9	Srm	-0.98	21.2			0.028					
	695.2	12.5	Srm	-0.01	18.83			0.028					
	696.5	11.2	Srm	-1.36	19.91	-3.63	9.86	0.028					
	700.4	7.3	Srm	-1.33	20.21			0.028					
	700.4	7.3	Srm	-1.5	19.2			0.028					
	701.5	6.2	Srm	-1.19	18.97	-0.57	18.92	0.028					
	703.5	4.2	Srm	-1.19	18.63	-1.47	17.97	0.028					
	703.5	4.2	Srm	-1.83	20.07			0.028					
	704.4	3.3	Srm	-1.54	17.92			0.028					
	704.7	3.0	Srm	-2.55	13.9			0.028					
	707.7	0.0	Srm	-2.79	17.66			0.028					
								0					
DP-1160	276.6	247.7		-2.46	14.29	-3.04	9.8	0.056	112	13.2	0.18	0.03	0.75
DH	303.0	221.3		0.45	19.08	-3.49	11.49	0.028	125	9.81	0.28	0.02	0.47

HOLE ID	Depth (m)	To Abyss (m)	Fm	$\delta^{13}C$ rock (‰)	$\delta^{18}O$ rock (‰)	$\delta^{13}C$ vein (‰)	$\delta^{18}O$ vein (‰)	Au (ppm)	As (ppm)	Sb (ppm)	Tl (ppm)	Te (ppm)	Hg (ppm)
DP-1160	332.5	191.8		1.46	24.77			0.028	90	7.75	0.12	0.02	0.62
	368.5	155.8		-0.11	19.85	-3.92	11.87	0.336	152	22.8	1.4	0.04	1.26
	410.3	114.0		1.27	21.98			0.028	33	3.1	0.05	0.01	0.14
	416.1	108.2		0.5	21.85			0.028	46	2.98	0.14	0.02	0.07
	416.1	108.2		1.49	23.39			0.028	46	2.98	0.14	0.02	0.07
	435.3	89.0		0.44	22.98			0.028	33	3.04	0.1	0.02	0.15
	435.3	89.0		0.39	23.83			0.028	33	3.04	0.1	0.02	0.15
	452.6	71.7		0.46	21.69	1.16	23.42	0.028	68	9.87	0.15	0.02	1.33
	467	57.3		1.51	22.5	1.17	23.34	0.028	90	18.5	0.28	0.1	1.43
	481.6	42.7		1.57	21.94	1.4	23.4	0.028	12	1.73	0.08	0.1	0.05
	493.2	31.1		1.26	21.07			0.028	19	1.84	0.08	0.11	0.04
	527	-2.7		-9.28	22.9			0.616	165	12.7	0.06	0.1	1.19
DP-1192	243.8	112.8	Dw	-0.4	22.73			0.028	49	4.12	0.06	0.01	0.56
DH	253	103.6	Dw	0.93	21.53			0.028	48	7.37	0.07	0.01	1.19
	265.2	91.4	Dw	-0.23	21.37			0.028	46	3.83	0.03	0.02	0.24
	274.3	82.3	Dw	-1.49	20.45			0.028	41	4.22	0.08	0.02	0.32
	283.5	73.1	Dw	1.32	24.2			0.028	22	1.69	0.05	0.02	0.13
	292.6	64.0	Dw			0.66	24.16	0.028	21	1.84	0.04	0.02	0.12
	298.7	57.9	Dw	0.81	23.04			0.028	13	1.24	0.04	0.03	0.05
	307.8	48.8	Dw	0.69	23.04			0.028	14	2.52	0.05	0.05	0.04
	313.9	42.7	Dw			0.61	22.01	0.028	18	3.77	0.03	0.02	0.1
	320	36.6	Dw	1.2	21.25			0.028	7	5	0.03	0.02	0.18
	329.2	27.4	Dw	1.35	18.16	-6.49	12.02	0.028	10	11.9	0.04	0.02	0.23
	341.4	15.2	Dw	1.44	18.09			0.028	11	2.64	0.07	0.02	0.23
	347.5	9.1	Dw	0.28	21.86			0.036	39	22.2	0.07	0.02	0.41
	353.6	3.0	Dw	-0.43	19.18			0.076	39	22.2	0.07	0.02	0.41
	706.2	-349.6	Se	-2.94	13.88			0.003	21.5	2.6	0.09	0.04	0.1
DP-1258	0.3	n/a	Dw	-3.067	14.501			0.0056					
DH	7.9	n/a	Dw	-3.68	12.894			0.0056					
	36	n/a	Dw	-3.174	13.73			0.0056					
	66.1	n/a	Dw	-0.085	22.459			0.0056					
	112.8	n/a	Dw	-6.874	14.031			0.0196					
	142.6	n/a	Dw	-4.915	14.64			0.0196					
	187.5	n/a	Srm	-2.145	17.93			0.028					
	294.7	n/a	Srm	-0.852	7.949			0.0448					
	314.6	n/a	Srm	0.834	13.3			0.014					
	383.7	n/a	Srm	-4.352	14.853			0.014					
	400.2	n/a	Ohc	-0.377	20.513			0.042					
	438	n/a	Ohc	-2.954	13.463			0.0028					
	480.4	n/a	Ohc	-3.174	15.225			0.0028					
DP-532	152.1	366.1	Dw	-1.06	20.78	-4.47	11.71	2.856	351	29.6	1.84	0.71	4.71
DH	170.7	347.5	Dw	0.1	20.37	0	12.69	0.168	158	9.59	0.22	0.03	6.83
	189	329.2	Dw	-1.2	19.82			0.448	432	28.9	0.36	0.06	2.75
	223.1	295.1	Dw	-0.72	18.57	-0.44	19.38	0.392	151	5.19	0.36	0.04	0.86
	223.1	295.1	Dw	0.17	19.17			0.392	151	5.19	0.36	0.04	0.86
	838.2	-320.0	Dw	-4.23	16.85			0.028	35.1	2.35	0.15	0.04	0.03
	253	265.2	Dw	0.53	21.9	0.49	15.93	0.028	38	5.17	0.07	0.02	0.17
	294.1	224.1	Dw	0.57	22.22	-1.22	12.44	0.056	30	5.7	0.08	0.1	0.24
	332.2	186.0	Dw	0.25	21.62	-3.46	10.97	0.028	5	4.07	0.06	0.05	0.12
	359.7	158.5	Dw	0.06	22.01			0.028	168	2.91	0.09	0.02	4.39
	390.1	128.1	Dw			-4.66	11.6	0.028	18	7.89	0.04	0.03	0.21
	432.8	85.4	Dw	1.13	21.5			0.028	44	16.25	0.03	0.01	0.3
	448.1	70.1	Dw	-0.37	19.02	-4.13	20.46	0.028	14	4.16	0.02	0.02	0.45

HOLE ID	Depth (m)	To Abyss (m)	Fm	$\delta^{13}C$ rock (‰)	$\delta^{18}O$ rock (‰)	$\delta^{13}C$ vein (‰)	$\delta^{18}O$ vein (‰)	Au (ppm)	As (ppm)	Sb (ppm)	Tl (ppm)	Te (ppm)	Hg (ppm)
DP-532	466.3	51.9	Dw	-0.92	17.43	-0.98	19.03	0.056	32	4.08	0.22	0.09	0.58
DH	481.6	36.6	Dw	-0.14	21.09			0.028	43	2.58	0.16	0.02	0.54
	496.8	21.4	Dw	0.1	21.77			0.028	10	0.44	0.09	0.01	0.15
	512.1	6.1	Dw	0.19	20.16	0.13	18.79	0.028	35	0.45	0.13	0.01	0.36
	521.2	-3.0	Ov	-1.7	13.76			0.476	35	0.45	0.13	0.01	0.36
	524.3	-6.1	Ov		19.45			0.476	134	4.75	0.22	0.07	0.49
	527.3	-9.1	Ov	2.28	19.72			0.084	134	4.75	0.22	0.07	0.49
	838.2	-320.0	Ov	-3.69	17.13			0.028	35.1	2.35	0.15	0.04	0.03
	880.9	-362.7	Ov	-5.44	17.52			0.028	7.7	0.79	0.26	0.01	0.03
	949.5	-431.3	Ov	-3.64	18.1			0.028	6.2	0.6	0.25	0.01	0.01
	949.5	-431.3	Ov	-1.9	19.3			0.028	6.2	0.6	0.25	0.01	0.01
DP-828	332.2	128.0	Srm	-1.78	20.37	-4.23	11.5	0.028					
RC	335.3	124.9	Srm	0.99	23.31			0.028					
	359.7	100.5	Srm	0.92	23.54			0.028					
	405.4	54.8	Srm	0.85	23.27			0.028					
	405.4	54.8	Srm	-0.06	21.08			0.028					
	429.8	30.4	Srm			0.53	13.62	0.028					
	460.2	0.0	Srm	-4.27	15.96			0.028					
	472.4	-12.2	Srm			-3.27	9.26	0.028					
	478.5	-18.3	Srm	-14.04	18.44			0.028					
	478.5	-18.3	Srm	-4.82	14.92			0.028					
DP-829	487.7	112.8	Srm	-3.74	15.29			0.028	11	4.74	0.34	0.02	0.13
RC	493.8	106.7	Srm			-5.94	10.78	0.028	14	11.3	0.2	0.02	0.29
	502.9	97.6	Srm	-2.05	20.2			0.028	2	0.7	0.34	0.01	0.06
	518.2	82.3	Srm	-1.2	21.34			0.028	7	0.8	0.32	0.02	0.07
	533.4	67.1	Srm	-1.44	21.52			0.028	8	1.11	0.36	0.02	0.03
	548.6	51.9	Smr	-1.21	21.16			0.028	7	0.9	0.49	0.02	0.03
	557.8	42.7	Srm	-1.48	21.21			0.028	7	1.42	0.42	0.02	0.04
	570.0	30.5	Srm	-1.36	21.04			0.028	2	1.39	0.35	0.02	0.03
	582.2	18.3	Srm	-1.78	20.66			0.056	8	1.36	0.42	0.03	0.03
	591.3	9.2	Srm	-2.79	18.55			0.028	39	1.63	0.46	0.02	0.04
	594.4	6.1	Srm	-2.52	18.86			0.028	39	1.63	0.46	0.02	0.04
	600.5	0.0	Ov	-3.67	17.56			0.028	171	3.26	0.2	0.04	0.08
	518.2	82.3	Ov	-1.48	21.01			0.028	7	0.8	0.32	0.02	0.07
PR-1007	499.9	85.3	Ohc	-2.92	11.14			0.0196	33	15.55	0.41	0.13	1.14
RC	527.3	57.9	Ohc	-2.91	18.61			0.0028	6	0.32	0.57	0.02	0.02
	539.5	45.7	Srm	-3.13	15.96			0.1064	51	0.82	0.34	0.04	0.03
	545.6	39.6	Srm			-1.28	19.78	0.0028	12	0.81	0.38	0.02	0.03
	557.8	27.4	Srm	-2.55	19.81			0.0028	5	0.98	0.34	0.02	0.02
	570.0	15.2	Srm	-2.63	16.94			0.0028	9	1.66	0.32	0.02	0.03
	579.1	6.1	Srm	-1.48	8.05			0.07	13	3.71	0.32	0.02	0.02
	582.2	3.0	Srm	-1.27	5.57			0.1512	77	7.64	0.15	0.04	0.06
	582.2	3.0	Srm	-1.5	5.54			0.1512	77	7.64	0.15	0.04	0.06
	606.6	-21.4	Ov	-2.74	7.33			0.0168	37	2.63	0.34	0.04	0.03
PR-350	307.8	100.6		-21.08	20.81								
RC	323.1	85.3		-3.81	11.81								
	341.4	67.0		-3.65	13.7			0.028					
	356.6	51.8		-1.88	17.46			0.028					
	368.8	39.6		-3.04	16.38			0.028					
	384.0	24.4		-3.94	13.36			0.028					
	387.1	21.3		-2.5	15.31			0.14					
	393.2	15.2		-1.76	17.61								

HOLE ID	Depth (m)	To Abyss (m)	Fm	$\delta^{13}C$ rock (‰)	$\delta^{18}O$ rock (‰)	$\delta^{13}C$ vein (‰)	$\delta^{18}O$ vein (‰)	Au (ppm)	As (ppm)	Sb (ppm)	Tl (ppm)	Te (ppm)	Hg (ppm)
PR-350	396.2	12.2		0.58	21.44								
RC	405.4	3.0		0.12	19.51								
PR-468	170.7	137.1	Srm	0.32	20.65			0.084	32	1.77	0.32	0.02	0.71
RC	179.8	128.0	Srm	-0.06	20.19			0.084	29	2.26	0.31	0.02	0.77
	192.0	115.8	Srm	-0.83	20.82			0.028	32	1.98	0.29	0.02	0.25
	210.3	97.5	Srm	-0.54	21.29			0.028	28	3.26	0.32	0.02	0.22
	225.6	82.2	Srm	-1.27	19.49			0.056	52	2.47	0.17	0.03	0.71
	246.9	60.9	Srm	-1.5	20.27			0.056	31	4.13	0.1	0.05	0.25
	268.2	39.6	Srm	-1.94	14.94			0.084	32	4.01	0.22	0.04	0.58
	277.4	30.4	Srm	0.64	16.47			0.028	12	1.93	0.1	0.05	0.19
	286.5	21.3	Srm	-2.3	15.32			0.028	16	1.78	0.07	0.02	0.22
	298.7	9.1	Srm	-2.267	14.523			0.028	19	2.38	0.12	0.02	0.18
	301.8	6.0	Srm	-2.44	18			0.028	19	2.38	0.12	0.02	0.18
	304.8	3.0	Srm	-1.23	15.44			0.028	113	5.56	0.17	0.03	0.23
	323.1	-15.3	Ov	-3.75	16.68			0.196	76	6.78	0.27	0.03	0.15
	365.8	-58.0	Ov	-1.52	17.92			0.112	198	7.69	0.11	0.04	0.3
	518.2	-210.4	Ov	-5.062	11.884			0.028	15.4	0.54	0.03	0.01	0.06
	536.4	-228.6	Ov	-1.623	13.607			0.028	7.4	1.78	0.11	0.03	0.13
	545.6	-237.8	Ov	-4.624	13.808			0.028	5	1.56	0.15	0.02	0.11
	563.9	-256.1	Ov	-7.546	14.262			0.028	15.2	2.44	0.21	0.05	0.19
	582.2	-274.4	Ov	-0.44	17.427			0.028	3	0.87	0.1	0.02	0.11
	600.5	-292.7	Ov	-1.615	16.638			0.028	11	0.88	0.07	0.02	0.08
	643.1	-335.3	Ov	-5.34	16.22			0.028	5.1	1.2	0.1	0.03	0.09
	676.7	-368.9	Ov			-5.23	16.8	0.028	6.4	0.69	0.12	0.01	0.12
	691.9	-384.1	Ov	-5.498	16.108			0.028					
	722.4	-414.6	Ov	1.42	18.37			0.028					
	783.3	-475.5	Dhc	-2.78	19.36			0.028					
	841.2	-533.4	Dhc	0.37	22.15			0.028	37.9	3.09	0.17	0.04	0.21
	883.9	-576.1	Dw	-1.89	3.29			0.028					
	887	-579.2	Dw	0.18	22.85			0.028					
	887	-579.2	Dw	0.643	19.163			0.028					
PR-469	243.8	122.0	Srm	-1.02	21.66			0.028	32	4.57	0.16	0.15	0.62
RC	259.1	106.7	Srm	-1.11	21.72			0.028	18	2.26	0.09	0.03	0.29
	277.4	88.4	Srm	-1.43	21.07			0.028	40	2.92	0.12	0.03	0.27
	301.8	64.0	Srm	-0.56	21.28			0.028	14	1.7	0.15	0.03	0.3
	310.9	54.9	Srm	-1.17	14.48			0.028	19	1.72	0.21	0.03	0.21
	320	45.8	Srm			-5.48	10.69	0.028	16	2.4	0.19	0.02	0.22
	329.2	36.6	Srm	-1.02	20.52			0.028	34	11.7	0.16	0.11	0.22
	338.3	27.5	Srm			-5.95	11.58	0.028	25	2.42	0.2	0.04	0.18
	350.5	15.3	Srm	-0.85	21.47			0.028	21	2.31	0.17	0.03	0.2
	362.7	3.1	Srm	-2.28	19.17			0.028	18	1.82	0.16	0.03	0.31
	396.2	-30.4	Ov	2.06	19.11	-1.68	16.47	0.028	14.2	3.73	0.33	0.07	0.1
	411.5	-45.7	Ov	-0.12	19.53			0.028	22.9	3.58	0.26	0.06	0.2
	423.7	-57.9	Ov	-0.34	17.9			0.028	28.3	5.28	0.33	0.06	0.18
	429.8	-64.0	Ov	-0.38	20.26	-1.44	13.71	0.028	81	4.6	0.38	0.08	0.21
	438.9	-73.1	Ov	-1.28	16.77			0.028	63.1	4.29	0.14	0.04	0.16
	442	-76.2	Ov	-1.86	16.7			0.028	54.3	4.76	0.05	0.03	0.08
	451.1	-85.3	Ov	-0.8	16.89			0.028	26.7	6.53	0.59	0.06	0.08
	457.2	-91.4	Ov	-3.36	15.99			0.028	50.3	13.5	1.94	0.08	0.46
	463.3	-97.5	Ov	-2.16	17.34			0.028	75.7	9.45	0.37	0.07	0.18
PR-471	484.6	106.7	Dw	-1.53	16.6			0.028					
RC													
PR-642	335.3	131.0	Dw	-1.91	19.03			0.028					

HOLE ID	Depth (m)	To Abyss (m)	Fm	δ^{13}C rock (‰)	δ^{18}O rock (‰)	δ^{13}C vein (‰)	δ^{18}O vein (‰)	Au (ppm)	As (ppm)	Sb (ppm)	Tl (ppm)	Te (ppm)	Hg (ppm)
PR-642	344.4	121.9	Dw	-0.7	19.62	-4.25	13.63	0.028					
RC	359.7	106.6	Dw	-2.81	18.03	-4.6	12.18	0.028					
	365.8	100.5	Dw			-4.21	13.84	0.028					
	368.8	97.5	Dw	0.58	19.25			0.028					
	381	85.3	Dw	-0.56	17.19	-4.8	13.88	0.028					
	396.2	70.1	Dw			-4.89	14.16	0.028					
PR-704	335.3	131.0	Dw	-0.21	20.93			0.028					
RC	350.5	189.0	Srm	-1.18	18.7			0.042					
	365.8	173.7	Srm	0.44	22.04			0.0364					
	381.0	158.5	Srm			-4.58	13.42	0.0336					
	396.2	143.3	Srm	0.29	19.83			0.028					
	411.5	128.0	Srm	1.22	18.22	0.92	20.88	0.028					
	426.7	112.8	Srm	-0.41	20.35			0.028					
	442.0	97.5	Srm	-0.15	19.4			4.34					
	463.3	76.2	Srm	0.29	18.71	-0.37	15.13	0.1708					
	475.5	64.0	Srm	-0.55	18.86			0.0756					
	490.7	48.8	Srm	-0.55	17.68			0.0336					
	499.9	39.6	Srm	-0.3	17.27			0.042					
	509.0	30.5	Srm	0.25	22.41			0.0308					
	515.1	24.4	Srm	0.91	17.38	0.85	18.32	0.028					
	524.3	15.2	Srm	1.54	24.68			0.0336					
	530.4	9.1	Srm			1.24	21.82	0.0308					
	536.4	3.1	Srm		20.87			0.028					
PR-779	121.9	140.2	Srm	0.24	22.48			0.112					
RC	152.4	109.7	Srm	0.73	24.67			0.028					
	152.4	109.7	Srm	0.27	24.24			0.028					
	164.6	97.5	Srm	-0.46	18.64	-0.34	18.59	0.028					
	198.1	64.0	Srm	1.66	19.9	1.62	21.81	0.028					
	216.4	45.7	Srm	-0.09	21.13			0.028					
	228.6	33.5	Srm	0.52	21.67			0.028					
	240.8	21.3	Srm	-0.54	18.78			0.028					
	249.9	12.2	Srm	-1.52	17.59	-0.3	17.91	0.224					
	253.0	9.1	Srm			-2.14	3.42	0.112					
PR-780	152.4	121.9	Dw	-1.78	14.82			0.042	136	14.45	0.28	0.05	2.88
RC	179.8	94.5	Dw	-1.21	19.99			0.0112	195	18.1	0.32	0.04	1.46
	201.2	73.1	Dw	0.36	19.55			0.0756	83	5.75	0.02	0.03	0.74
	249.9	24.4	Srm	-2	17.9			0.0224	110	39.9	0.11	0.04	1.16
	274.3	0.0	Srm			-11.39	22.17	2.6684	105	10.25	0.07	0.17	0.84
PR-86	298.7	57.9		-0.91	18.88			0.028					
RC	301.8	54.8		-0.54	19.53			0.028					
	310.9	45.7		-0.47	19.82			0.028					
	313.9	42.7				-4.28	9.03	0.028					
	323.1	33.5		-0.53	21.34			0.028					
	338.3	18.3		0.1	11.33			0.028					
	341.4	15.2		-1.56	16.61			0.056					
	353.6	3.0		-2.24	16.71			0.028					
	365.8	-9.2		-7.79	12.9			0.028					
Surface			Srm	-1.844	15.136	E	524528	N	4454902				
Surface			Srm	1.053	16.803	E	524476	N	4454928				
Surface			Srm	-5.055	7.296	E	524476	N	4454927				

HOLE ID	Depth (m)	To Abyss (m)	Fm	$\delta^{13}C$ rock (‰)	$\delta^{18}O$ rock (‰)	$\delta^{13}C$ vein (‰)	$\delta^{18}O$ vein (‰)	Au (ppm)	As (ppm)	Sb (ppm)	Tl (ppm)	Te (ppm)	Hg (ppm)
DP-136	98.5	486.8		-5.4	16.4			0.028					
DH	145.7	439.5		-4.1	16.1	-2.3	13.4	0.168					
	176.1744	409.0		-0.9	14.9	-5.8	16.6	0.028					
	215.7984	369.4		-5	14.2	-5	17.8	0.504					
	234.3912	350.8		-4.9	13.7			1.344					
	240.1824	345.0		-4.1	15.2	-5.3	16.5	1.064					
	259.08	326.1		-4.6	12.9	-5.1	17.1	3.892					
	274.32	310.9		-4.6	13.2	-6.1	16.7	0.028					
	287.4264	297.8		-4.7	12.8			0.028					
	293.5224	291.7		-3.4	13.1	-5.2	16.5	0.028					
	317.2968	267.9		-4.2	12			0.028					
	336.1944	249.0		-2.4	14.5	-3	14.5	0.028					
	362.1024	223.1		-2	16.4	-1.9	17.7	0.308					
	384.9624	200.3		-2.9	13.4	-3.1	18.4	0.028					
	413.9184	171.3		-3.1	13.6			0.252					
DL-182	64.9	520.3		-5.5	13.2	-4.7	16.9	0.056					
DH	86.3	499.0		-3.6	16.1	-5.5	17	0.028					
	132.0	453.2		-1	12.8	-5.2	17.3	0.028					
	137.8	447.4		-6.1	16.8	-3.7	17.9	0.252					
	168.6	416.7		-2	15.6	-5	17.4	0.028					
	197.5	387.7		-4	14.3	-3	17.8	0.028					
	215.8	369.4		0.4	17.9	-0.9	10.4	0.028					
	235.6	349.6		-3.7	13.3	0.3	9.8	0.028					
	252.4	332.8		-2.7	13	-0.4	12.4	0.028					
	269.1	316.1		-5	13.1	-5.4	17.8	0.7					
	278.3	306.9		-2.4	12.8	-5.1	16.5	0.196					
	324.0	261.2		-2.6	16.4	-2	14.7	0.028					
	348.7	236.5		-3.6	14.9	-3.4	17.2	2.492					
	355.4	229.8		-2.2	21.5	-5.8	10.1	12.404					
	381.3	203.9		-2.2	20.9			0.252					
	403.3	182.0		-1.5	20.1			0.028					
DP-268	83.2	660.5		-2.6	14.3	-3.4	18.6	0.336					
DH	92.0496	651.7		-2.5	17.6			1.148					
	186.8424	556.9		-2.3	17.2	-7.1	16.7	0.336					
	197.8152	545.9		-1.3	21.6	-4.1	18.1	0.588					
	219.7608	524.0		-2.8	11.9	-4.1	18.8	1.288					
	222.8088	520.9		-2.7	15.3	-3.1	19.1	1.176					
	232.5624	511.1		-3.8	17.5			1.792					
	233.7816	509.9		-3.7	15.4			1.792					
	240.4872	503.2		-3.5	15.8			1.428					
	245.6688	498.0		-3.2	15.2			1.008					
	252.3744	491.3		-5.5	18.2	-6.6	13.6	0.588					
	384.6576	359.1		-2.2	14	-2.6	15.2	0.952					
	391.668	352.0		-3.8	15.9			0.672					
	433.7304	310.0		-3	10.4	-1	11.6	0.028					
DP-316	55.8	529.4		-2.4	13.4	-5.6	15.9	0.028					
DH	63.4	521.8		-3.4	14.7			0.028					
	67.9704	517.2		-4	14			0.028					
	85.344	499.9		-3	15			0.28					
	85.6488	499.6		-0.9	16.4			1.68					
	88.392	496.8		-2.2	14.6	0.2	26.4	1.68					
	90.8304	494.4		-2.3	16			0.028					
	96.9264	488.3		-2	13	-2	15.9	0.028					

HOLE ID	Depth (m)	To Abyss (m)	Fm	$\delta^{13}C$ rock (‰)	$\delta^{18}O$ rock (‰)	$\delta^{13}C$ vein (‰)	$\delta^{18}O$ vein (‰)	Au (ppm)	As (ppm)	Sb (ppm)	Tl (ppm)	Te (ppm)	Hg (ppm)
DP-316	115.2144	470.0		0	16.2	-4.8	16.5	0.028					
DH	130.4544	454.8		-1.1	11.6	0.6	10.3	0.028					
	139.5984	445.6		-1.7	18.3			0.028					
DP-368	56.4	675.1		-1.1	1.7			0.28					
DH	64.6	666.9		-0.5	12.7	0.6	11.2	0.42					
	66.1	665.4		-2.5	8.6			0.42					
	75.0	656.5		-1.4	15	-2.4	30.1	0.42					
	91.4	640.1		-2.7	11.3	-0.4	10.1	1.092					
	112.8	618.7		-2.4	15.4	-3.7	15.2	0.28					
	0.0	0.0											
DP-389	189.6	572.4		-2.7	21	-6.7	16.1	0.28					
DH	222.2	539.8		-4.5	18.6	-5.5	17.3	1.82					
	229.5	532.5		-1.6	21.2	-2.4	23.9	0.028					
	256.0	506.0		-0.6	15.7	-1	13.8	0.224					
	256.6	505.4		-1	18.1	-3.1	13.7	0.336					
	259.4	502.6		-0.7	16.4	-1.3	23.1	0.252					
	275.2	486.8		-0.3	19.5			0.028					
	289.0	473.0		0.1	21.7			0.196					
DP-473	218.8	543.2		-3.8	20.3			0.028					
DH	256.9	505.1		-4.6	17.1	-5.4	17.2	0.112					
DP-525	215.8	546.2		-0.8	16.5	-1.9	14.2	0.028					
DH	225.9	536.1		-2.4	15.4	-4.7	16.2	0.504					
	227.4	534.6		-1.4	15.7	-0.1	12.3	0.504					
	235.0	527.0		-2.6	19.1			2.632					
	247.8	514.2		-1.2	12.7	0.9	6.3	0.028					
	271.0	491.0		-1.1	16.5	-5.4	17.8	0.028					
	281.3	480.7		-1.3	14.2	-5	17.3	0.42					
	305.7	456.3		-1	20.8	-6.6	16.9	0.028					
	320.6	441.4		-0.9	18.6	-6.1	16.3	0.028					
	340.8	421.2		-1.5	13.6			0.028					
DP-848	337.7	454.8		-4.4	17.3			0.028					
DH	342.0	450.5		-4.1	16			0.028					
	344.1	448.4		-4.3	16.8	-4.5	12.4	0.028					
	359.7	432.8		-3.2	17.2	-3.1	18.2	0.028					
	369.7	422.8		-3.1	17.8			0.028					
	380.7	411.8		-2.6	15.9	-1.2	9.5	0.028					
	385.0	407.5		-2.7	17.5			0.028					
	402.0	390.4		-2.4	17.5			0.028					
	410.3	382.2		-2.5	15.6			0.028					
	415.7	376.7		1.9	11.6			0.028					

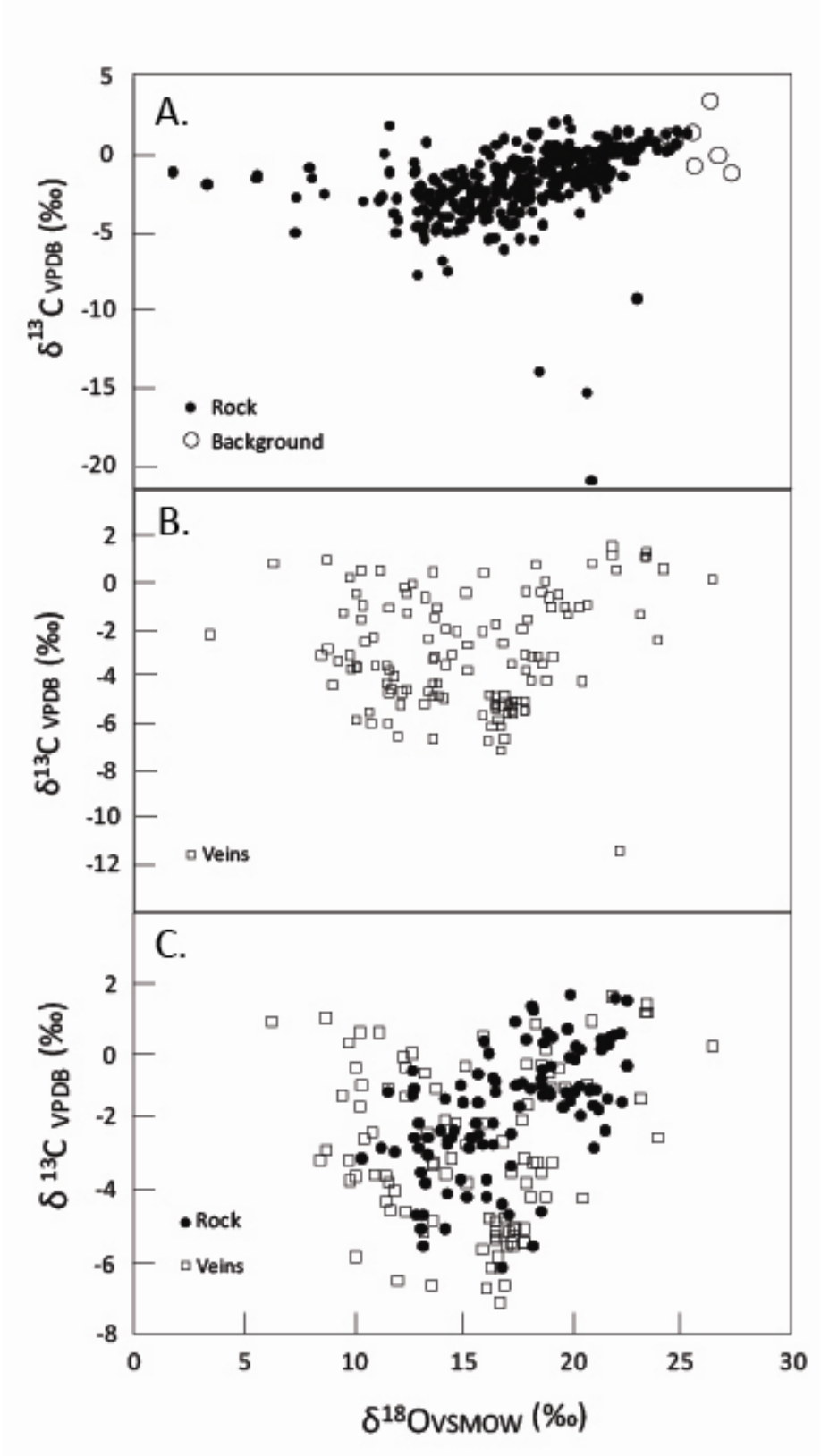

Fig. 4.5. Carbon and oxygen stable isotope values of A. rocks samples (black) compared to stable isotope values of background rock samples collected from Lone Mountain (white). B. Vein samples. C. Samples containing both veins and rock stable isotope values. All graphs include data published by Arehart and Donelick (2006).

below the Abyss fault in drill hole DP-1136, PR-468 and PR-469, the footwall expression of the RMT fault is intersected. There is a progressive change away from the Roberts Mountain Thrust beneath the Abyss fault from depleted values (~12 ‰) to undepleted values (~ 23 ‰).

4.5.2 $\delta^{18}O$ and $\delta^{13}C$ values of veins

Vein samples exhibit a wide range in $\delta^{18}O$ values between -0.02 and 30.1‰ (Figure 4.5). The isotopic composition of vein samples form a general trend from background $\delta^{18}O$ and $\delta^{13}C$ values to strongly depleted $\delta^{18}O$ and $\delta^{13}C$ values (Figure 4.5). Over 85% of vein values are depleted. More vein values are depleted compared to rock values from the same sample. In general, the lower threshold for $\delta^{18}O$ vein values is ~7.5 ‰ with two vein samples below this threshold. This lower threshold is consistent at and above the Abyss fault. The lower limit for rock values is ~3‰ higher than for vein samples at ~10‰. Within the main ore zone of the Pipeline deposit (>300m above the Abyss fault) the majority of veins are depleted with respect to unmineralized unaltered marine limestone with values between ~8-15 ‰. Rock values from within the zone of mineralization are similar to vein values. Underneath the main ore zone and above the Abyss fault, vein values are depleted where rock values from the same sample are undepleted. Of all vein samples analyzed >100m above the Abyss fault, only three vein values are depleted. Proximal to the Abyss fault, variation exists between depleted and undepleted veins, with nearly equal distribution, however rock values in the same samples are largely undepleted. The absence of veins beneath the Abyss fault restricts any observations between the vein and rock values at this depth.

The same pattern in the isotopic distribution of veins is not apparent in $\delta^{13}C$ values of veins. Within the main ore zone, and proximal to the Abyss fault, veins are evenly distributed between typicalmarine values of 0 ‰, and slightly depleted values of -5 ‰. The lower threshold for $\delta^{13}C$ values of veins is ~-7 ‰. Values are nearest to this threshold at the Abyss fault and in the main ore zone of the Pipeline deposit. There is a small increase in $\delta^{13}C$ values of veins between 100-300m above the Abyss fault, where values do not occur below ~-5 ‰. Within 100m of either side of the Abyss fault, both $\delta^{18}O$ and $\delta^{13}C$ vein data can be divided into two groups. Group 1 $\delta^{18}O$ values occur between ~8-15 ‰, and group 2 between 17-25 ‰. Group 1 $\delta^{13}C$ values occur between (-7)-(-3) ‰, and group 2 between (-2)-2 ‰. Vein samples above the 100m mark are evenly distributed in composition.

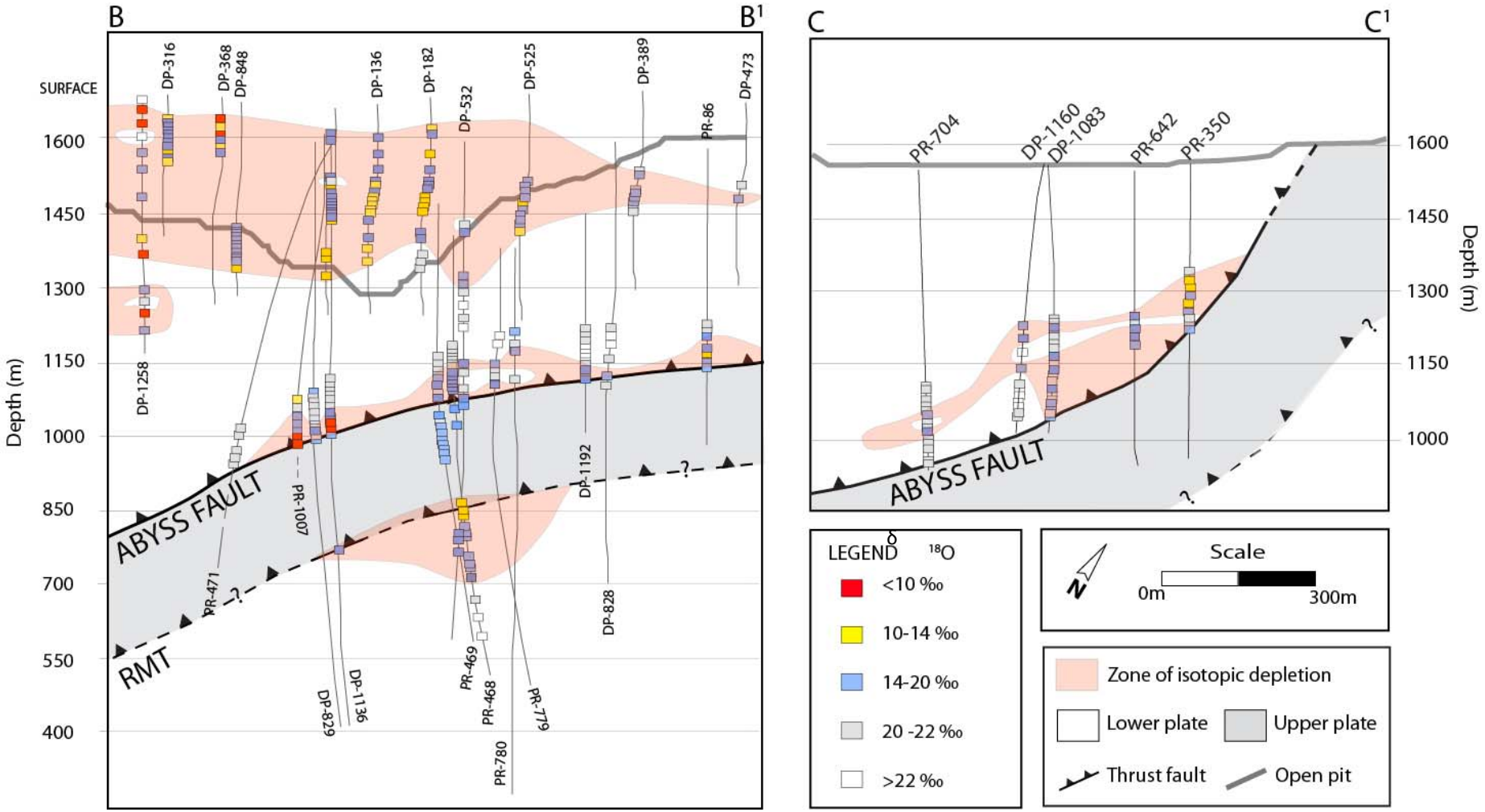

Fig. 4.6. Cross sections through the Pipeline deposit study area showing $\delta^{18}O$ values of rocks. Zones of isotopic resetting (values < 20‰) are shown in red. Samples are variably depleted along the Abyss fault, e.g., DP-1136, DP-532, and PR-1007 exhibit strong depletion at the fault whereas PR-471, PR-704 and DP-1160 exhibit values closer to background, unaltered samples. Samples previously analyzed by Arehart and Donelick from the Pipeline pit are dominantly depleted (<20 ‰).

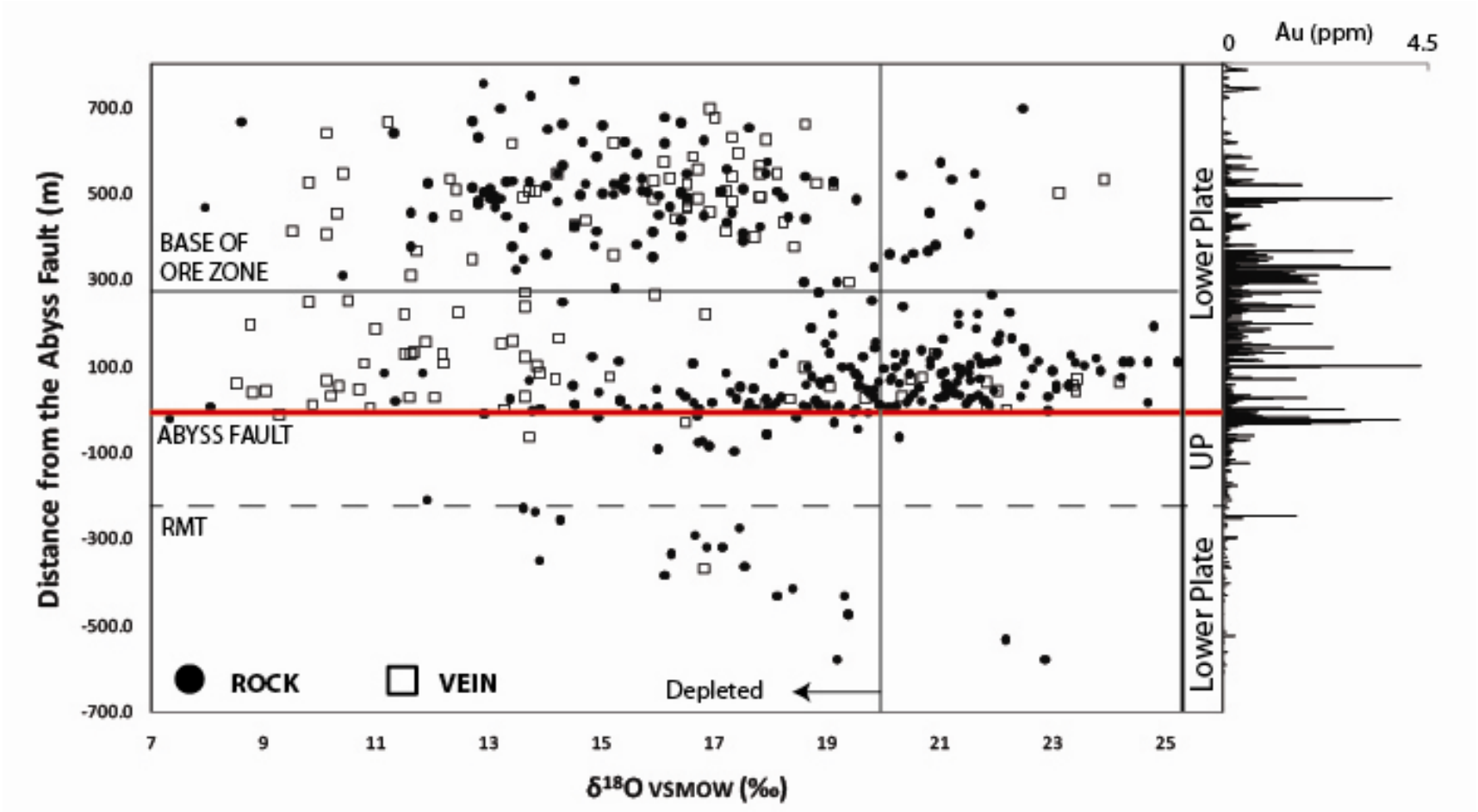

Fig. 4.7. Graph showing the $\delta^{18}O$ composition of carbonate rocks and veins relative to the Abyss fault (located at depth 0m). A moving average graph of gold concentrations (3.05m/ 10ft composites) are shown on the right (n=3828). The base of the main ore zone is shown and represents an average distance from the Abyss fault to known ore. Gold concentrations are highest within the main ore zone. Gold concentrations are also elevated at the Abyss fault and at certain intervals in between the Abyss fault and the main zone of gold mineralization in the Pipeline deposit. The distance between the (RMT) from the Abyss fault is an average depth based on two deep drill holes that intersect the RMT underneath the Abyss fault. Samples proximal to the Abyss fault (+/-100m) vary between depleted and undepleted $\delta^{18}O$ values. Samples at depths >100- 300m above the Abyss fault show dominantly undepleted $\delta^{18}O$ values. Samples at depths >300 m above the Abyss fault exhibit nearly pervasive $\delta^{18}O$ depletion. Samples between the Abyss fault and RMT (beneath the Abyss fault) are dominantly undepleted but become significantly depleted at the RMT. A trend away from depletion is exhibited by samples beneath the RMT. At the Abyss fault, veins samples both depleted and undepleted, however above at distance >100m from the Abyss fault, veins are dominantly depleted.

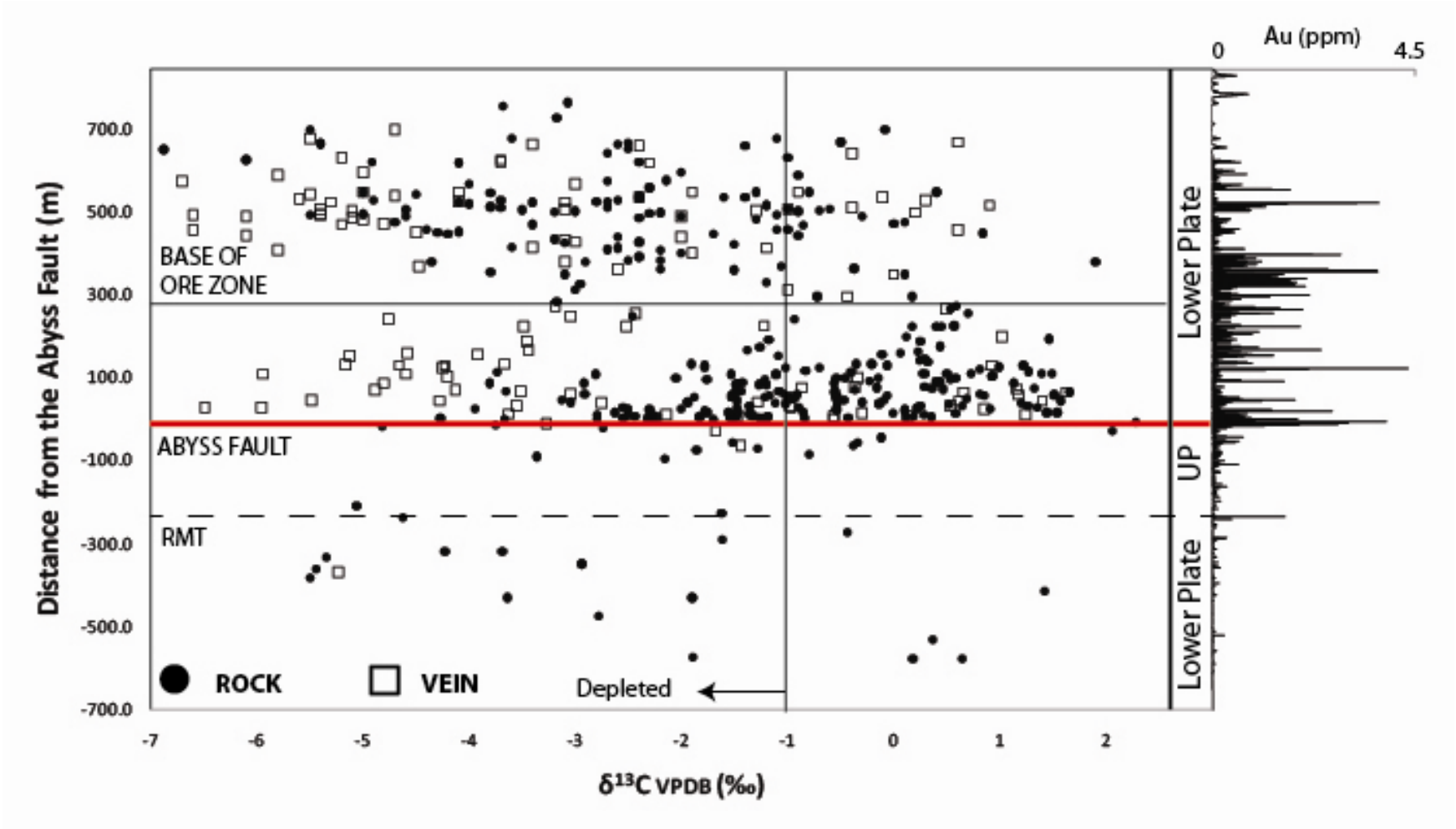

Fig. 4.8. Graph showing the $\delta^{13}C$ composition of carbonate rocks and veins relative to the Abyss fault (located at depth 0m). A three point moving average line graph of gold concentrations (3.05m/ 10ft composites) are shown on the right (n=3825). Patterns similar to those in $\delta^{18}O$ data are observed in $\delta^{13}C$ data, however the range in $\delta^{13}C$ values in smaller. Samples proximal to the Abyss fault (+/-100m) show both depleted and undepleted $\delta^{13}C$ values. Samples at depths >100- 300m above the Abyss fault show less depleted to undepleted $\delta^{13}C$ values. Samples at depths >300 m above the Abyss fault exhibit $\delta^{18}O$ depletion. Samples between the Abyss fault and RMT (beneath the Abyss fault) are dominantly undepleted but become significantly depleted at the RMT. A trend away from depletion is exhibited by samples beneath the RMT. $\delta^{13}C$ values of veins samples do not as obvious a same pattern as observed in $\delta^{18}O$ values of vein samples. Veins are both depleted and undepleted at all depths relative to the Abyss fault.

4.5.3 Gold and trace element concentrations near the Abyss fault

Trace element geochemistry for samples analyzed in this study is presented in Table 4.3, Figure 4.9. Above approximately 600m depth (below surface) the mine database contains only gold analyses; trace elements were not analyzed. Hence, gold values are presented in Table 4.3 where there are no other trace element concentrations. Where present, gold and trace element concentrations represent 3.05 (10ft) composites. This contrasts with stable isotope analyses, which represent either millimeter size drill holes or single chips from a 3.05m (10ft) reverse circulation composite. Due to the small sampling for stable isotopes, isotope depletion may not correlate to gold or trace element concentrations on the single sample scale. Instead, overall trends in the relationship between isotope depletion and trace element geochemistry are important.

Consistently elevated gold concentrations, compared to unaltered samples from Lone Mountain (Table 4.2) occur at and above the Abyss fault. The greatest abundance of high gold values starts at the Abyss fault and continues until approximately 400m above the Abyss fault. Beneath the Abyss fault, gold concentrations are significantly lower than values above the Abyss fault, with a small spike in gold occurring underneath the RMT (below the Abyss fault). All trace element concentrations above the Abyss fault, except for arsenic, are significantly higher than concentrations below the Abyss fault. Immediately above the base of the ore zone, the lower limit of As, Sb, and Tl increases so that few samples exhibit background-level concentrations. Samples below the Abyss fault zone do not carry significant concentrations of Sb or Hg. Immediately beneath the Abyss fault zone, Sb and Hg concentrations exhibit significant increases. Arsenic shows progressive increase in concentration from beneath the RMT (below the Abyss fault) to the Abyss fault. Immediately above the fault zone, arsenic values drop to near background values. Arsenic values remain low with increasing distance from the Abyss fault and exhibit only a small increase proximal to the base of the ore zone. Concentrations of Sb are highest between 100-350m above the Abyss fault, and Hg concentrations are highest from 100-300m above the fault. Arsenic concentrations are elevated beneath the Abyss fault and show a nearly linear increase upward to the Abyss fault zone. Both Tl and Te exhibit less deviation from background

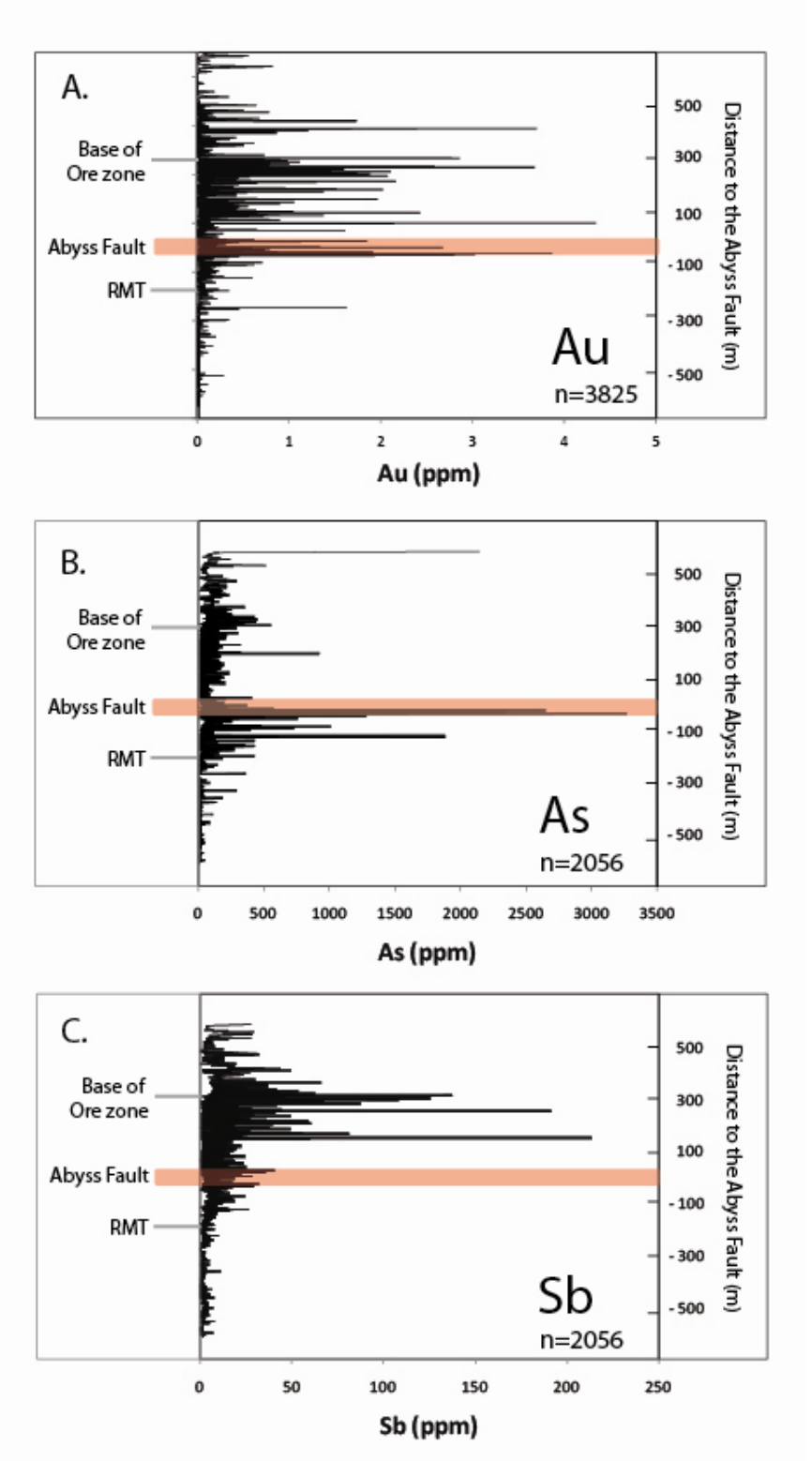
A.
Base of
Ore zone
Abyss Fault
RMT
Au
n=3825
0
1
2
3
4
5
Au (ppm)
500
300
100
-100
-300
-500
Distance to the Abyss Fault (m)
B.
Base of
Ore zone
Abyss Fault
RMT
As
n=2056
0
500
1000
1500
2000
2500
3000
3500
As (ppm)
500
300
100
-100
-300
-500
Distance to the Abyss Fault (m)
C.
Base of
Ore zone
Abyss Fault
RMT
Sb
n=2056
0
50
100
150
200
250
Sb (ppm)
500
300
100
-100
-300
-500
Distance to the Abyss Fault (m)

.

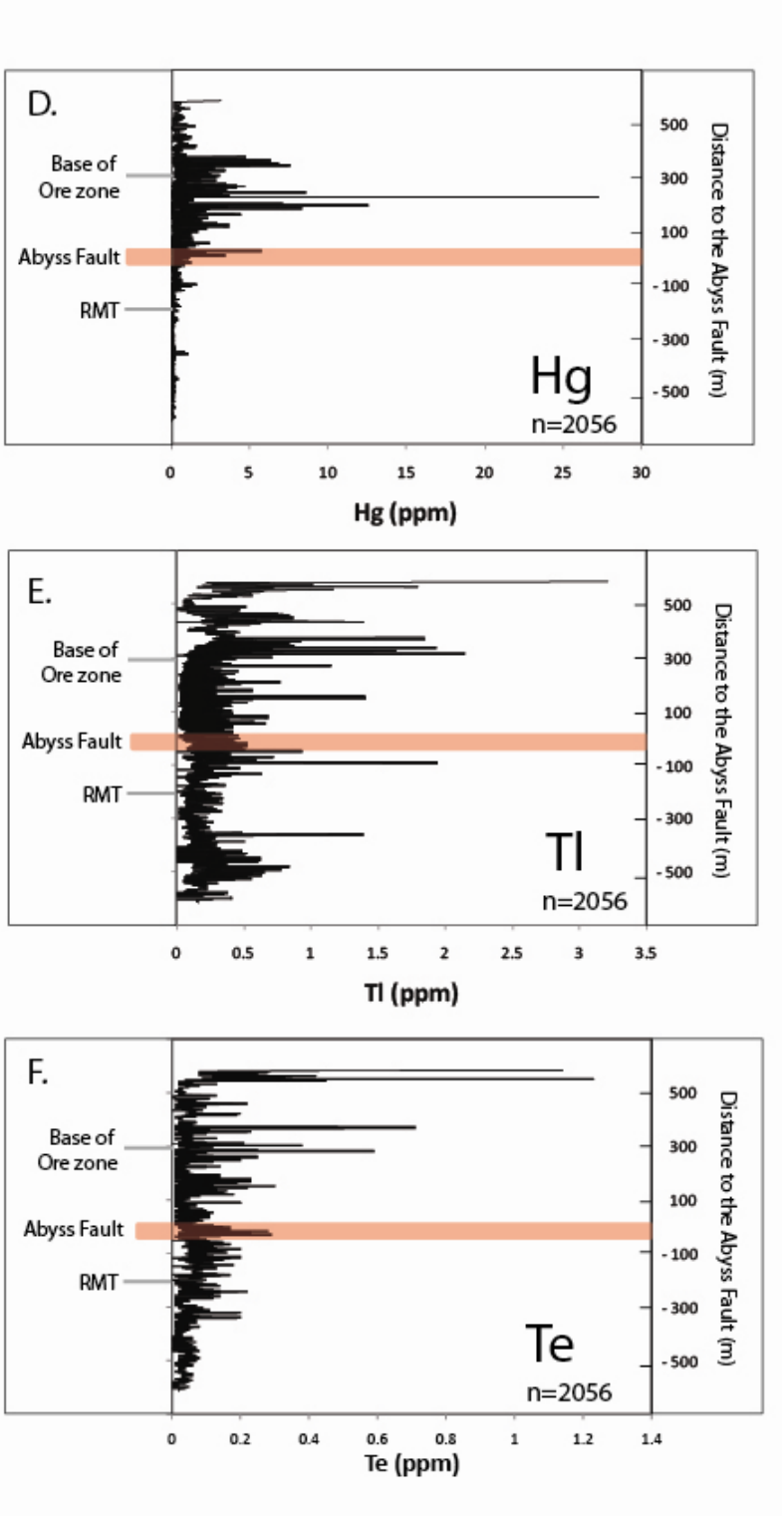

Fig. 4.9. Line graphs of three point moving averages showing concentrations of gold and other trace elements relative to the Abyss Fault. Data is shown only for drill holes where isotope data exists. Note that trace element data at distances >600m above the Abyss fault do not exist. A. Gold B. Arsenic C. Antimony D. Mercury E. Thallium F. Tellurium. The Abyss fault is shown here as a ~75m wide zone (red band) and represents the area at which visible alteration and isotope depletion are observed.

values throughout the section than the Au, As, Sb, or Hg, but exhibit an overall increase in concentration at the distance corresponding to the main Pipeline ore deposit. Te increases almost linearly from beneath the Abyss fault to distances of >500m above the Abyss fault. Concentrations of Tl are most elevated immediately beneath the RMT and Abyss fault, in a region extending from the base of the ore zone to approximately 600m above the Abyss fault.

4.6 DISCUSSION

The absence of a depletion halo or significant concentrations of gold between the Abyss fault zone and the main ore zone indicate that the Abyss fault was not the main conduit for fluid forming the Pipeline deposit. Rocks at the Abyss fault are isotopically depleted in comparison to unaltered, unmineralized samples from the Lone Mountain area. The Abyss fault acted as a conduit for gold-bearing fluid as evidenced by elevated concentrations of gold at the Abyss fault compared to background, unaltered samples from Lone Mountain. Isotopic depletion at the Abyss fault occurs in a region ~50m wide, defining a zone of fluid flow both inside and slightly outside of the main fault plane. Fluid flow above and below the Abyss fault plane is suggestive of a damage zone around the main fault that created secondary permeability and enhanced fluid flow in those areas. The absence of depletion everywhere along the Abyss fault suggests that fluid flow was not pervasive along the main fault or within the damage zone. Undepleted values may represent 'islands' where hydrothermal cementation minerals were precipitated along the fault, inhibiting subsequent fluid flow, as described by Sibson (1992).

Strongly depleted $\delta^{13}C$ values may represent variation in the abundance of organic carbon between samples. Marine limestone typically contain $\delta^{13}C$ values ~0 ‰, with other sources of carbon exhibiting much lower values of carbon i.e. deep seated carbon ~ (-7 ‰), and reduced/ organic carbon < (-15) ‰ (Ohmoto and Rye, 1979; 1997). The majority of samples in this study were not depleted in $\delta^{13}C$ indicating that carbon was locally sourced from marine carbonate rocks. Certain Carlin-type deposits have exhibit spatial association to hydrocarbon reserves (i.e., Alligator Ridge; (Ilchik et al., 1986). Only four rock samples from this study exhibit strong carbon depletion, two of which occur at the Abyss fault. The Abyss fault may have been a conduit for hydrocarbons, the origins of which remain unclear. Oxygen isotope values are not depleted where carbon isotopes are strongly depleted suggesting that the fluid

responsible for oxygen depletion along the Abyss fault was not the same fluid that caused carbon depletion.

Isotopic depletion of oxygen also occurs at the RMT beneath the Abyss fault; however, Au, Sb, Hg, Tl, and Te show no relative enrichment. The presence of minor As, and some isotopic depletion at the RMT indicate that the RMT may have been a conduit for fluid, but either the fluid was depleted in gold, or the fluid was strongly rock buffered and did not react with wall rock. In the Pipeline deposit and other Carlin-type gold systems, the RMT also occurs above the main ore zone (Figure 4.2). The majority of gold mineralization is hosted in the footwall of the RMT, with some gold occurring at and directly below the RMT (above the Abyss fault) likely representing the pooling of gold-bearing fluid underneath the fault. Fluid flow may not have occurred along the RMT, but underneath the RMT and Isotopic depletion at the RMT beneath the Abyss fault signifies the pooling of fluid underneath the RMT.

Between 300-500m above the Abyss fault, there is a large zone of nearly pervasive oxygen isotope depletion. Oxygen isotope depletion in this area corresponds spatially to the main ore zone of the Pipeline deposit. The same zone of depletion also correlates to elevated concentrations of Sb, Tl, and Te, and to a lesser degree, As. Hence, depletion was likely a product of interaction between gold-bearing hydrothermal fluids and carbonate host rock (Rye, 1985; Arehart and Donelick, 2006). The absence of background concentrations of As, Sb, and Tl in the main ore zone indicate pervasive interaction between host rocks and ore-forming fluid.

There is a span of approximately 200m between the Abyss fault zone and the main ore zone where stable isotope values are within the range associated with unaltered background samples. The absence of isotopic depletion in the area (between the Abyss fault and the main ore zone) suggests a lack of extensive hydrothermal fluid flow. However, Au and associated trace elements occur in elevated concentrations in this same region conversely suggesting that ore-forming fluids have passed through those rocks. The lack of a correlation between gold concentration and isotopic depletion in individual samples may be related to differences in the scales of fluid flow, and the extent of fluid-rock interaction resulting in gold precipitation and isotopic depletion.

In Carlin-type systems, gold is submicroscopic in fine-grained Fe-sulfide minerals, primarily pyrite (Cook and Chryssoulis, 1990; Ulrich et al., 1999; Barker et al., 2009). Ore-stage pyrite is believed to form via sulphidation of pre-existing Fe-silicate and Fe-carbonate minerals (Hofstra et al., 1991; Kesler et al., 2003). Bisulphide-complexed metals including gold were adsorbed on and incorporated into precipitating pyrite (Hofstra et al., 1991; Arehart et al., 1993). Fluid flow resulting in the precipitation of

gold may be focused through fractures or vugs, and can occur on a small scale with. The same fluid precipitating gold may not interact with surrounding rock sufficiently to lower the stable isotope signature significantly outside the confines of the fluid flow pathway. The fluid flow pathway may be depleted only on the centimetre scale, and the random isotopic sampling methods used in this study, would not pick up on such small scale depletion. Unlike gold precipitation, large volumes of fluid and high levels of fluid-rock interaction are required in order to form large zone of isotopic depletion.

Although the zone between the Abyss fault and the Pipeline ore zone is largely undepleted, gold and other trace elements occur locally in significant concentrations. The damage zone associated with the Abyss fault may have created enough secondary permeability distal to the main fault plane (>100m above) to allow for the 'leakage' of gold-bearing fluids into hangingwall rocks. The leakage of small amounts of fluid would explain the presence of high gold concentrations above the Abyss fault without significant isotopic depletion in the same area. In the main ore zone of the Pipeline deposit, flow of ore-forming fluid is likely occurring on a much larger scale than isolated gold precipitation events, in surrounding rocks. In this circumstance, isotopic depletion occurs in the same area and on the same spatial scale as high gold concentrations (Figures 4.7 & 4.8).

If we assume a high concentration of gold in the fluid (100ppb), and precipitation of all gold from that fluid (ρ_{fluid} = ~1kg/m^3), over 19 km^3 of ore-forming fluid would be required to form a gold deposit the magnitude of the Pipeline deposit (~10 million oz.). Leakage of 19km^3 of fluid into hangingwall rocks from the Abyss fault without altering the isotopic composition of rocks between the Abyss fault and the main zone of mineralization seems unlikely. Fluid flow occurred at, and along the Abyss fault, not across it, and not directly above it. A lack of connectivity between Abyss fault depletion and depletion associated with the ore deposit provides constraints on the flow path taken by ore-forming fluids into the Pipeline deposit:

(i) Carbon and oxygen isotope depletion does not extend from the Abyss fault into the Pipeline deposit indicating that ore-forming fluids did not flow en mass across the fault up into the Pipeline deposit. This suggests that flow of ore-forming fluids into the Pipeline deposit must have been dominantly lateral (Figure 4.10). Fluid flow occurred along three main lateral paths, disconnected from one another: the main conduit above the Abyss fault that fed the Pipeline deposit, the Abyss fault zone, and potentially along or beneath the RMT. The source of fluid flowing along all three pathways may have been the same. At some point distal to

the deposit, a single flow path may have split into three flow paths, with only the main conduit providing sufficient volumes of gold and fluid to make an economic deposit.

(ii) Lateral fluid flow along the RMT, the Abyss fault, and into the Pipeline deposit may have occurred at different times and may represent different pulses of fluid flow. This may account for the variation in trace element geochemistry observed along each fluid conduit. The main zone of gold mineralization in the Pipeline deposit above the Abyss fault may represent the interaction between a gold-rich fluid and reactive carbonate rock. Fluid flow along the Abyss fault may represent interaction between a slightly gold-depleted fluid and carbonate rock. Finally, low gold concentrations and the absence of the high concentrations of associated trace elements indicates that fluid flowing along the RMT was likely largely depleted in gold and there was insufficient fluid-rock interaction to strongly buffer the fluid and induce the precipitation of auriferous pyrite.

(iii) 3D modelling by Barrick Gold Corp. personnel of drill hole data from the Pipeline deposit indicates that economic gold grade is restricted to shallow depths (>300 m above the Abyss fault). Ore-grade gold mineralization is controlled primarily by imbricate thrust fault structures (Leonardson, 2010). Localized thrust faulting above the Abyss fault may have provided lateral pathways for fluid flow (Figure 4.10). Fluid flow above and perhaps along strike of the Abyss fault, making use of thrust fault duplexes, would explain the absence of high gold grade at distances >300m above the Abyss fault where all rock properties other than secondary permeability are similar to those at shallow depths.

4.6.1 Origin of the $\delta^{18}O$ depletion in veins

Interpreting observed relationships between $\delta^{18}O$ depletion patterns in veins and rocks is challenging in the absence of information on the relative timing of each depletion event. Veins are not typically associated with mineralization in Carlin-type gold deposits (Cline et al., 2005). Although veins do not typically carry gold in these systems, veins may have precipitated from the same fluid as the fluid precipitating gold. Given a fluid temperature of 200°C, the fractionation factor (α) between calcite and water is ~11 ‰ (Bottinga, 1968) indicating that fluid forming depleted veins had a $\delta^{18}O$ value between (-3) - 8 ‰. This range in oxygen isotope values is comparable with typical Carlin fluids which can span (-15) – 10 ‰ (Hofstra et al., 1999; Cline et al., 2005). Veins precipitating from the same ore-forming

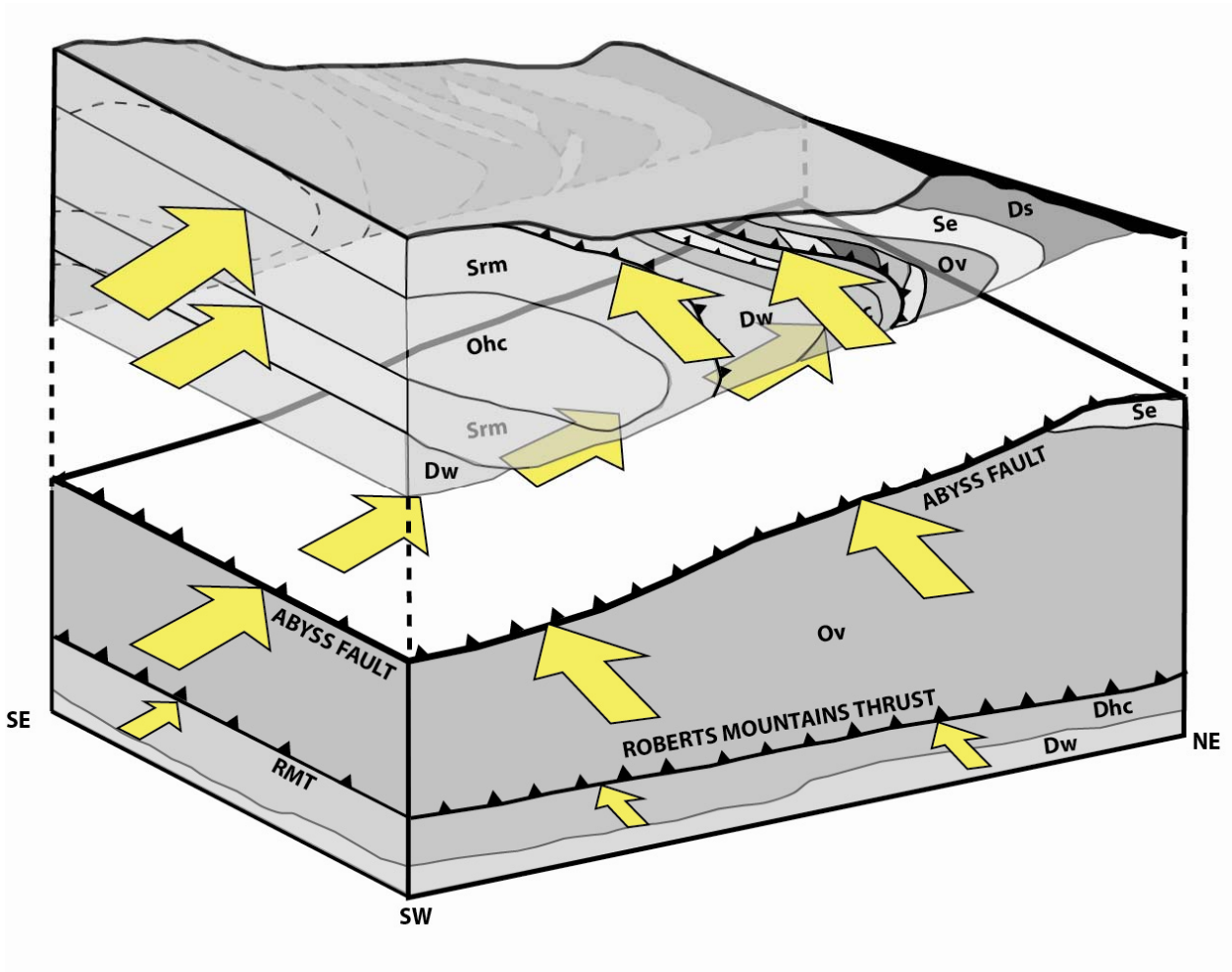

Fig. 4.10. Box model showing potential source directions for fluid flow and fluid flow pathways into the Pipeline deposit. Ore forming fluids did not cross the Abyss fault. Fluid flow was dominantly lateral and likely exploited zones of high secondary permeability including breccias zones and thrust fault duplexes.

fluid would be expected to exhibit overall lower isotope values than rock samples that interacted with the same fluid, due to the direct precipitation of veins from fluid. Rocks do not typically fully exchange all parts with the fluid, resulting in partially exchanged values representing both the rock value and fluid value. Higher degrees of fluid rock interaction result in increased levels of isotopic exchange between fluid and rock. If it is assumed that the main zone of gold mineralization at the Pipeline deposit corresponds to the highest degree of fluid rock interaction, the highest degree of isotopic depletion should also correspond to the same zone. This would explain the more pervasive depletion of rock and vein samples within the main ore zone of the Pipeline deposit. Where fluid rock interaction was low, or fluid flow of ore forming fluids was patchy, vein and rock values will exhibit both depletion and background values, as observed at the Abyss fault. The tendency of vein values toward undepleted values may represent the progressive buffering of ore-forming fluid by host carbonates. Background vein samples would have precipitated from highly rock buffered fluid and represent typical marine carbonate values. This hypothesis is supported by the presence of similar oxygen and carbon depletion thresholds at the Abyss fault and in the main ore zone above.

Equally plausible is that veins precipitated either prior or subsequent to the main Carlin-type gold event, and may be a result of any number of hydrothermal events including circulating magmatic hydrothermal fluid perhaps from the Gold Acres stock, down-welling and circulating meteoric water that was partially exchanged with the wall rock (Arehart and Donelick, 20060, diagenesis (Chilingar and Wolf, 1988), or from one of multiple regional compressional events affecting north-eastern Nevada. If veins were emplaced prior to gold mineralization, ore-forming fluid may have reset the isotopic composition of vein material to lower values. Variation in isotope depletion in veins within and below the main ore zone would then depend on fluid-rock interaction, and the degree to which fluids were buffered by surrounding carbonate rock.

4.7 IMPLICATIONS

Many models describing ore-forming processes are suggestive of dominantly vertical flow of ore forming fluids into an ore deposit, typically along steeply dipping structures (Sibson et al., 1988; John et al., 2003; Schardt et al., 2005). Results from this study show that ore-forming fluids did not enter the

Pipeline gold deposit via some vertical feeder structure, but instead may have traveled some distance laterally before precipitating gold. Perhaps more important is the presence of multiple disconnected lateral fluid conduits parallel to the main fluid conduit. The presence of fluid flow along the RMT, over a kilometer beneath the main ore zone of the Pipeline deposit provides insight into the enormous scale of fluid flow in Carlin-type hydrothermal systems. Not only are vast quantities of fluid required in order to account for the size of giant gold deposits, but flow of ore-forming fluids is occurring on a scale greater than a single flow path. At present, patterns in isotopic depletion have identified three pathways for hydrothermal fluid within and below the main ore zone separated by hundreds of metres. Deeper drilling beneath the footwall expression of the RMT may reveal more fluid pathways. Ultimately, a complete understanding of the scale of fluid flow in these systems is limited by the cost and logistics associated with drilling deep drill holes.

Unless an ore deposit is formed by groundwater flowing along a lateral flow path and driven by a topographic gradient, at some point fluid flow must be vertical. A strong meteoric signature has been observed in the stable isotope analyses of ore-forming minerals in Carlin-type systems (Hofstra et al., 1999; Cline et al., 2005). In order to account for the temperature of Carlin-type fluid (200°C; Lubben, 2004; Hofstra and Cline, 2000; Cline et al., 2005), meteoric water must have circulated with fluid descending and rising along vertical conduits. Therefore, while fluid flow on the deposit scale, entering the Pipeline deposit hydrothermal system may have been dominantly lateral, the extent of lateral fluid flow outside the deposit is unknown.

The interplay between lateral and vertical fluid flow in the formation of hydrothermal ore deposits highlights the importance of permeability. Where fluids are not overpressured, the path a fluid takes appears to be a passive process based on gravity and primary and secondary permeability of that rock. Primary intergranular permeability may be an important factor in determining gold grade on the deposit scale, but is not as important as secondary permeability in determining pathways into the deposit for ore-forming fluid. In order to overcome the effect of buoyancy and the natural tendency for fluids to rise, permeability has to be significantly higher in a lateral direction than in a vertical direction (Rosenberg et al., 1993; Dickson et al., 1995; Fisher and Becker, 1995). Many Carlin-type deposits contain steeply-dipping fault structures that are interpreted to have been feeder zones for ore-forming fluid. No major vertical structure has been identified as a feeder zone at the Pipeline deposit. Thrust faulting of sedimentary packages above the Abyss fault may provided the necessary ground preparation

and sufficient secondary permeability to guide mineralizing fluid to its point of gold precipitation in the Pipeline gold deposit.

Limited exposure of the tops, sides, and bottoms of most ore-forming systems restricts the understanding of fluid flow pathways leading into individual ore deposits (Dilles and Einaudi, 1992). However, a combination of deformation, exhumation, and mining itself can result in the total exposure of an entire mineralizing system; e.g., Yerington porphyry deposit; (Dilles and Einaudi, 1992; Gustafson and Quiroga, 1995; Einaudi et al., 2000). The signature of fluid flow has typically been studied using a combination of visual alteration; i.e., silicification, decalcification, oxidation etc., and trace element geochemistry. Such methods are useful for interpreting controls on metal and trace element precipitation but they do not provide information on where fluids may have traveled prior to precipitating gold. Mapping carbon and oxygen depletion can help to delineate zones of hydrothermal alteration and extensive fluid-rock interaction where trace elements and metals have not precipitated.

4.8 CONCLUSION

Ore-deposit models invoking a single conduit for ore-forming fluids may be simplistic. Depleted oxygen isotope values of carbonate rock samples both within the main ore zone of the Pipeline deposit, and along the underlying Abyss and Roberts Mountains thrust (RMT) faults indicate the presence of three disconnected pathways for hydrothermal fluid flow, with only one flow path feeding ore-forming fluid into the main ore zone of the Pipeline deposit. There is no observable isotopic depletion connecting the main ore zone with depletion of the underlying Abyss and RMT faults, suggesting that fluid along each pathway was dominantly lateral. An abrupt increase in concentration of Au, As, Sb, Hg, Tl, and Te at the Abyss fault, and the absence of elevated concentrations of these elements beneath the Abyss fault indicate that interaction between gold-bearing fluid and reactive carbonate rock was greatest at and above the Abyss fault.

4.9 REFERENCES

de Almeida, C., Olivo, G., Chouinard, A., Weakly, C., and Poirier, G., 2010, Mineral Paragenesis, Alteration, and Geochemistry of the Two Types of Gold Ore and the Host Rocks from the Carlin-Type Deposits in the Southern Part of the Goldstrike Property, Northern Nevada: Implications for Sources of Ore-Forming Elements, Ore Genesis, and Mineral Exploration: Economic Geology, v. 105, p. 971-1004.

Arehart, G., Eldridge, C., Chryssoulis, S., and Kesler, S., 1993, Ion microprobe determination of sulfur isotope variations in iron sulfides from the Post/Betze sediment-hosted disseminated gold deposit, Nevada, USA: Geochimica et Cosmochimica Acta, v. 57, p. 1505-1519.

Arehart, G., and Donelick, R., 2006, Thermal and isotopic profiling of the Pipeline hydrothermal system: Application to exploration for Carlin-type gold deposits: Journal of Geochemical exploration, v. 91, p. 27-40.

Barker, S., Hickey, K., Cline, J., Dipple, G., Kilburn, M., Vaughan, J., and Longo, A., 2009, UNCLOAKING INVISIBLE GOLD: USE OF NANOSIMS TO EVALUATE GOLD, TRACE ELEMENTS, AND SULFUR ISOTOPES IN PYRITE FROM CARLIN-TYPE GOLD DEPOSITS: Economic Geology, v. 104, p. 897-904.

Barnes, H., 1997, Geochemistry of hydrothermal ore deposits, Wiley and Sons, 992 p.

Bottinga, Y., 1968, Calculation of fractionation factors for carbon and oxygen isotopic exchange in the system calcite-carbon dioxide-water: The Journal of Physical Chemistry, v. 72, p. 800-808.

Boyer, S., and Elliott, D., 1982, Thrust systems: AAPG Bulletin, v. 66, p. 1196-1230.

Caine, J., Evans, J., and Forster, C., 1996, Fault zone architecture and permeability structure: Geology, v. 24, p. 1025-1028.

Cathles, L., 1993, Oxygen isotope alteration in the Noranda mining district, Abitibi greenstone belt, Quebec: Economic Geology, v. 88, p. 1483-1511.

Chilingar, G.V., and Wolf, k.H., 1988, Diagenesis, Elsevier, New York, New York, 591 p.

Cline, J., Hofstra, A., Muntean, J., Tosdal, R., and Hickey, K., 2005, Carlin-type gold deposits in Nevada: Critical geologic characteristics and viable models: Economic Geology, 100th Anniversary Volume, p. 451-484.

Cook, N., and Chryssoulis, S., 1990, Concentrations of invisible gold in the common sulfides: Canadian Mineralogist, v. 28, p. 1-16.

Criss and Taylor, 1986. R.E. Criss and H.P. Taylor, Jr. , Meteoric-hydrothermal systems. *Rev. Mineral.* **16** (1986), pp. 373–424.

Criss, R., Singleton, M., and Champion, D., 2000, Three-Dimensional Oxygen Isotope Imaging of Convective Fluid Flow around the Big Bonanza, Comstock Lode Mining District, Nevada: Economic Geology, v. 95, p. 131-142.

Dickson, P., Schultz, A., and Woods, A., 1995, Preliminary modelling of hydrothermal circulation within mid-ocean ridge sulphide structures: Geological Society London Special Publications, v. 87, p. 145-157.

Dilles, J., and Einaudi, M., 1992, Wall-rock alteration and hydrothermal flow paths about the Ann-Mason porphyry copper deposit, Nevada; a 6-km vertical reconstruction: Economic Geology, v. 87, p. 1963-2001.

Einaudi, M., Proffett, J., and Barton, M., 2000, Overview of the Yerington Porphyry Copper District: Magmatic to Nonmagmatic Sources of Hydrothermal Fluids: Their Flow Paths and Alteration Effects on Rocks and Cu-Mo-Fe-Au Ores: Contrasting styles of intrusion-associated hydrothermal systems, p. 55-66.

Emsbo, P., Hofstra, A.H., Lauha, E.A., Griffin, G.L., and Hutchinson, R.W., 2003, Origin of High-Grade Gold Ore, Source of Ore Fluid Components, and Genesis of the Meikle and Neighboring Carlin-Type Deposits, Northern Carlin Trend, Nevada: Economic Geology, v. 98, p. 1069-1105.

Finney, S., Berry, W., Cooper, J., Ripperdan, R., Sweet, W., Jacobson, S., Soufiane, A., Achab, A., and Noble, P., 1999, Late Ordovician mass extinction: a new perspective from stratigraphic sections in central Nevada: Geology, v. 27, p. 215-218.

Fisher, A., and Becker, K., 1995, Correlation between seafloor heat flow and basement relief: observational and numerical examples and implications for upper crustal permeability: J. geophys. Res, v. 100, p. 12641-12657.

Foo, S., Hays Jr, R., McCormack, J., Geologist, C., and Reno, N., 1996, Geology and mineralization of the Pipeline gold deposit, Lander County, Nevada, Geological Society of Nevada, p. 111-121.

Garven, G., and freeze, r.A., Theoretical analysis of the role of groundwater flow in the genesis of stratabound ore deposits: American Journal of Science, v. 284, p.1085-1124.

Gustafson, L., and Quiroga, G., 1995, Patterns of mineralization and alteration below the porphyry copper orebody at El Salvador, Chile: Economic Geology, v. 90, p. 2-16.

Hagemann, S.G., Groves, D.I., Ridley, J.R., Vearncombe, J.R., 1992, The Archean lode gold deposits at Willuna, Western Australia; high-level brittle-style mineralization in a strike-slip regime: Economic Geology, v. 87; p. 1022-1053.

Heitt, D., Dunbar, W., Thompson, T., and Jackson, R., 2003, Geology and geochemistry of the Deep Star gold deposit: Carlin trend, Nevada: Economic Geology, v. 98, p. 1107-1135.

Hofstra, A., Leventhal, J., Northrop, H., Landis, G., Rye, R., Birak, D., and Dahl, A., 1991, Genesis of sediment-hosted disseminated-gold deposits by fluid mixing and sulfidization: Chemical-reaction-path modeling of ore-depositional processes documented in the Jerritt Canyon district, Nevada: Geology, v. 19, p. 36-40.

Hofstra, A., Snee, L., Rye, R., Folger, H., Phinisey, J., Loranger, R., Dahl, A., Naeser, C., Stein, H., and Lewchuk, M., 1999, Age constraints on Jerritt Canyon and other carlin-type gold deposits in the

Western United States; relationship to mid-Tertiary extension and magmatism: Economic Geology, v. 94, p. 769-802.

Hofstra, A., and Cline, J., 2000, Characteristics and models for Carlin-type gold deposits, Chapter 5: in Hagemann, S. G. and Brown, PE, eds., Gold in 2000: Reviews in Economic Geology, v. 13, p. 163-220.

Ilchik, R.P., Brimhall, G.H., Schull, H.W., 1986, Hydrothermal Maturation of Indigenous Oranic Matter at the Alligator Ridge Gold Deposits, Nevada: Economic Geology, v. 81, p.113-130.

Jiang, Z., Oliver, N., Barr, T., Power, W., and Ord, A., 1997, Numerical modeling of fault-controlled fluid flow in the genesis of tin deposits of the Malage ore field, Gejiu mining district, China: Economic Geology, v. 92, p. 228-247.

John, D.A., Hofstra, A.H., Fleck, R.J., Brummer, J.E., Saderholm., E.C., 2003, Geologic Setting and genesis of the Mule Canyon Low-Sulfidation Epithermal Gold-Silver Deposit, North-Central Nevada: Economic Geology, v. 98, p. 425-463.

Johnson, J., and Pendergast, A., 1981, Timing and mode of emplacement of the Roberts Mountains allochthon: Antler orogeny: Geological Society of America Bulletin, v. 92, p. 648-658.

Kesler, S., Fortuna, J., Ye, Z., Alt, J., Core, D., Zohar, P., Borhauer, J., and Chryssoulis, S., 2003, Evaluation of the Role of Sulfidation in Deposition of Gold, Screamer Section of the Betze-Post Carlin-Type Deposit, Nevada: Economic Geology, v. 98, p. 1137-1157.

Kuehn, C., and Rose, A., 1992, Geology and geochemistry of wall-rock alteration at the Carlin gold deposit, Nevada: Economic Geology, v. 87, p. 1697-1721.

Leonardson, R., and Rahn, J., 1996, Geology of the Betze-Post gold deposits, Eureka county, Nevada, Geological Society of Nevada, p. 61-94.

Leonardson, R., 2010, Barrick Gold Acres Structure, Geological Socety of Nevada Symposium 2010, Reno, Nevada.

Lubben, J., 2004, Quartz as clues to paragenesis and fluid properties at the Betze-Post deposit, northern Carlin trend, Nevada: Unpublished M.Sc. thesis, Las Vegas, Universitty of Nevada, p. 155.

Meinert, L.D., 1987, Skarn zonation and fluid evolution in the Groundhog mine, Central mining district, New mexico: Economic Geology, v. 82, p. 523-545.

Mortensen, J., J. Thompson, et al. (2000). "U-Pb age constraints on magmatism and mineralization in the northern Great Basin, Nevada." Geology and ore deposits: 419–438.

Naito, K., Fukahori, Y., Peiming, H., Sakurai, W., Shimazaki, H., and Matsuhisa, Y., 1995, Oxygen and carbon isotope zonations of wall rocks around the Kamioka Pb-Zn skarn deposits, central japan: application to prospecting: Journal of Geochemical Exploration, v. 54, p. 199-211.

Ohmoto, H., and Rye, R., 1979, Isotopes of sulphur and carbon: Geochemistry of Hydrothermal Ore Deposits. 2nd, p. 509–567.

Ohmoto, H., Rye, R., and Barnes, H., 1997, Geochemistry of hydrothermal ore deposits: NY: Wiley, p. 509–567.

Oliver, N., and Bons, P., 2001, Mechanisms of fluid flow and fluid–rock interaction in fossil metamorphic hydrothermal systems inferred from vein–wallrock patterns, geometry and microstructure: Geofluids, v. 1, p. 137-162.

Paradis, S., Taylor, B., Watkinson, D., and Jonasson, I., 1993, Oxygen isotope zonation and alteration in the northern Noranda District, Quebec; evidence for hydrothermal fluid flow: Economic Geology, v. 88, p. 1512-1525.

Poole, F., Stewart, J., Palmer, A., Sandberg, C., Madrid, C., Ross Jr, R., Hintze, L., Miller, M., and Wrucke, C., 1992, Latest Precambrian to latest Devonian time; development of a continental margin: The Cordilleran Orogen: Conterminous US, p. 9–54.

Price, J.G., Muntean, J.L., Davis, D.A., and Hess, R.H., 2007, The Nevada mineral industry-2007: Nevada Bureau of Mines and Geology, v. Special Publication, p. 178.

Radtke, A., Rye, R., and Dickson, F., 1980, Geology and stable isotope studies of the Carlin gold deposit, Nevada: Economic Geology, v. 75, p. 641-672.

Ressel, M., Noble, D., Henry, C., and Trudel, W., 2000, Dike-hosted ores of the Beast deposit and the importance of Eocene magmatism in gold mineralization of the Carlin Trend, Nevada: Economic Geology, v. 95, p. 1417-1444.

Roberts, R., 1966, Metallogenic provinces and mineral belts in Nevada: Nevada Bureau of Mines, Rept, v. 13, p. 47-72.

Rosenberg, N., Spera, F., and Haymon, R., 1993, The relationship between flow and permeability field in seafloor hydrothermal systems: Earth and Planetary Science Letters, v. 116, p. 135-153.

Rye, R., 1985, A model for the formation of carbonate-hosted disseminated gold deposits based on geologic, fluid inclusion, geochemical, and stable isotope studies of the Carlin and Cortez deposits, Nevada: Nevada: US Geological Survey Bulletin, v. 1646, p. 35–42.Schardt, C., Yang, J., Large, R., 2005, Numerical heat and fluid-flow modeling of the Panorama volcanic-hosted massive sulfide district, western Australia, v.100, p. 547-566.

Sibson, R.H., Robert, F., and Poulson, K.H., 1988, High-angle reverse faults, fluid-pressure cycling, and mesothermal gold-quartz deposits: geology, v. 16, p. 551-555.

Sibson, R., 1992, Implications of fault-valve behaviour for rupture nucleation and recurrence: Tectonophysics, v. 211, p. 283-293.

Silberling, N., and Roberts, R., 1962, Pre-Tertiary stratigraphy and structure of northwestern Nevada, Geological Society of America Symposium.

Sillitoe, R.H., and Bonham, H.F., Sediment-hosted gold deposits: Distal products of magmatic-hydrothermal systems: Geology, v.18, p.157-161.

Singleton, M., and Criss, R., 2002, Effects of normal faulting on fluid flow in an ore-producing hydrothermal system, Comstock Lode, Nevada: Journal of Volcanology and Geothermal Research, v. 115, p. 437-450.

Singleton, M., and Criss, R., 2004, Symmetry of flow in the Comstock Lode hydrothermal system: Evidence for longitudinal convective rolls in geologic systems: Journal of Geophysical Research, v. 109, p. 3205-3220.

Stenger, D., Kesler, S., Peltonen, D., and Tapper, C., 1998, Deposition of gold in carlin-type deposits; the role of sulfidation and decarbonation at Twin Creeks, Nevada: Economic Geology, v. 93, p. 201-215.

Taylor, H.P., Jr. and Epstein, S., 1963. O18/O16 ratios in rocks and coexisting minerals of the Skaergaard intrusion. J. Petrol., v. 4, p. 51-74.

Taylor, H.P., 1974, The Application of Oxygen and Hydrogen Isotope Studies to Problems of Hydrothermal Alteration and Ore Deposition: Economic Geology, v. 69, p. 843-883.

Thorman, C.H., Ketner, K.B., Peterson, F. (1990): The Elko orogeny - Late Jurassic orogenesis in the Cordilleran miogeocline. *GSA Abstracts with Programs*, 22, 3, 88.

Tosdal, R., Wooden, J., and Kistler, R., 2000, Inheritance of Nevadan mineral belts from Neoproterozoic continental breakup: Geology and ore deposits, p. 15–18.

Ulrich, T., Günther, D., and Heinrich, C., 1999, Gold concentrations of magmatic brines and the metal budget of porphyry copper deposits: Nature, v. 399, p. 676-679.

Veizer, J., Ala, D., Azmy, K., Bruckschen, P., Buhl, D., Bruhn, F., Carden, G., Diener, A., Ebneth, S., and Godderis, Y., 1999, 87Sr/86Sr,[delta] 13C and [delta] 18O evolution of Phanerozoic seawater: Chemical Geology, v. 161, p. 59-88.

CHAPTER 5 –CONCLUSIONS

The primary objective of this project was to evaluate distal patterns of fluid flow into and out of Carlin type gold deposits. This study highlighted the challenges in establishing distal vectors toward ore in low temperature, fracture and fault controlled hydrothermal systems. The key results and interpretations of this study are summarized below:

5.1 FLUID FLOW INTO CARLIN-TYPE GOLD DEPOSITS

- Depleted oxygen and carbon stable isotope values in lower Palaeozoic carbonate rocks, along with elevated concentrations of Au, As, Sb, hg, Tl, and Te, identified flow of gold-bearing hydrothermal fluid along the Abyss fault zone underneath the Pipeline deposit.

- Fluid flow occurred within the fault zone, but not in between the fault zone and main ore zone of the Pipeline deposit. Furthermore fluid flow did not occur across the fault.

- If the Abyss fault was not the main conduit for ore-forming fluids at the Pipeline deposit, fluid must have entered the Pipeline deposit along dominantly lateral flow paths, likely focused along pre-existing thrust fault duplex structures which were zones of greater permeability than intact host rock.

- Ore-forming fluids in Carlin-type settings may be sourced some lateral distance from the main site of ore deposition, and not directly beneath the deposit.

- The dominance of lateral flow over vertical flow at the Pipeline deposit highlights the importance of low angle structures as primary conduits for ore-forming fluids into hydrothermal ore deposits

5.2 FLUID PATHWAYS OUT OF CARLIN-TYPE GOLD DEPOSITS

- Stable isotope values of clay minerals, the abundance of illite, and the crystallinity of illite, are robust indicators of hydrothermal alteration in Carlin-type systems. The combination of these three tools outlined a number of zones of hydrothermal alteration in both the Shoshone Range

and Leeville study areas. The region above and proximal to the surface projection of the Leeville deposit exhibits multiple zones of hydrothermal fluid upflow resulting in pervasive illitization of upper plate siliciclastic rocks. The Pipeline/ Gold Acres and Elder Creek deposits also contain abundant illite.

- The presence of highly crystalline illite highlights zones of focused fluid upflow, typically along faults and other secondary permeability structures such as breccias. Fluid flow occurs both pervasively and along focused fluid pathways depending on primary rock type. Igneous intrusions are more commonly pervasively altered whereas hydrothermal alteration is restricted to fractures and fault surfaces in more brittle and quartz rich, less argillaceous sedimentary lithologies.

- Certain geothermometers do not provide consistent or reliable information on formation temperature. Although a general relationship exists between increasing formation temperature and increasing $K + |Fe - Mg|$ values, data from five geothermal fields demonstrates that the relationship is not linear and varies between fields (Battaglia, 2004). Hence, the $K + |Fe - Mg|$ thermometer cannot be applied to systems containing illite where temperature cannot be directly measured, and a temperature-composition curve has not been calibrated without accruing a large error. Crystal morphology is similarly not readily applicable to the determination of formation temperatures. No single crystal shape or crystal texture appears related to hydrothermal alteration. Although hexagonal illite is more commonly found in hydrothermal environments, similarly shaped illite has also been observed as a replacement texture of kaolinite during diagenesis, and as a late stage product of growth.

- The Terraspec analytical spectral device does not consistently identify accurate mineral assemblages associated with Carlin-type ore systems when compared to x-ray diffraction. Furthermore, samples containing carbon or abundant oxide material return uninterpretable data. Broad patterns may be apparent in Terraspec data, but the accuracy of those patterns is questionable. X-ray diffraction is the most reliable and accurate tool for the identification of clay minerals.

- Illite zonation, illite crystallinity, and stable isotope analyses are indicators of hydrothermal alteration, but they do not assist in establishing paragenetic relationships between observed

hydrothermal alteration assemblages and ore formation, specifically Carlin-type gold mineralization. Detailed imaging of textural relationships between clay minerals was similarly unable to determine timing relationships. In the absence of absolute age dates, the only relationship that can be inferred between ore-formation and surface hydrothermal alteration is a spatial one.

- Essene and Peacor (1995) criticize the use of low temperature mineral assemblages in providing any information on temperature due to heterogeneities in composition on the nanoscale, and kinetically inhibited equilibrium in low temperature systems. Data collected in this study using established clay thermometers may not represent equilibrium conditions. The potential lack of equilibrium; however, does not diminish the presence of patterns related to illite zonation and illite crystallinity.

- Collecting data from clay minerals is a difficult process. This study has shown that small grain size can limit the amount of data collected using SEM and EM techniques owing to the width of the electron beams. Furthermore, the soft nature of clay minerals makes sample preparation including thin section making extremely difficult.

- Following gold precipitation in the Pipeline deposit, gold-depleted fluids were likely exhausted laterally, at least initially, along the same structures as those that allowed fluid to enter the deposit. Upon intersecting the RMT, fluid may either have exploited the thrust fault as conduit to reach surface, or fluid may have transgressed the upper plate through small scale fault and fractures. Hydrothermal alteration observed at surface in upper plate rocks from the Leeville, Gold Acres and Elder Creek deposits indicates that some low temperature hydrothermal fluid was able to transgress upper plate rocks from depth; however, whether this fluid was of Carlin-type fluid is unknown. Similarities in trace element geochemistry, ore assemblage, and alteration mineralogy suggest that the Elder Creek deposit (Appendix A) may be an example of low temperature (200°C) gold mineralization resulting from the exhaust of Carlin-type ore forming fluid.

5.3 ESTABLISHING VECTORS TOWARD CARLIN-TYPE ORE

- Flow of ore-forming is focused along narrow conduits, and fluid appears generally unbuffered by host rock within the main zones of mineralization and along ore-forming fluid pathways.

- Low fluid rock interaction along focused flow pathways may result in narrow alteration halos around those pathways, making exploration difficult.

- Zones of $\delta^{18}O$ depletion overlap spatially with elevated gold concentrations, but do not form extensive halos around ore bodies.

- Clay mineral mapping at surface can detect zones of hydrothermal fluid upflow which are spatially associated to Carlin-type ore bodies at depth. Zones of abundant highly crystalline illite could potentially be used to infer a hydrothermal system at depth, however these zones would not provide information on source of hydrothermal fluid responsible for alteration.

5.4 RECOMMENDATIONS FOR FUTURE WORK

The results contained in this study indicate that clay mineral mapping of low temperature hydrothermal systems, such as Carlin-type gold deposits, is extremely challenging due to difficulty in (i) sample preparation; (ii) paragenetic studies; (iii) structural and compositional heterogeneities within single minerals, and (iv) the occurrence of clay minerals unrelated to hydrothermal alteration at surface. Many studies have shown that TEM is the ultimate tool to image and understand clay minerals (Lonker et al., 1990; Arkai et al., 1996). TEM allows for the interpretation of micro-scale variations in one clay packet. Applying the clay thermometers used in this study to samples that have been previously classified as homogeneous using TEM may resolve issues raised by Essene and Peacor (1995) regarding compositional and structural heterogeneities in low temperature minerals. TEM however is time consuming and is not a realistic exploration tool.

The main problem with distinguishing between generations of clay is the absence of absolute ages on illite from many of the dykes and intrusions present in the Leeville study area, and elsewhere. Horst Zwingmaan with the *Commonwealth Scientific and Research Organization* has developed a combined age-determination method involving XRD, SEM, and TEM characterization of clay minerals followed by K-Ar and Ar-Ar dating. Complete characterization of the clay prior to obtaining an age may

provide the constraints required for valid dating of clay minerals. This method has been successful in acquiring an Eocene age date from illite in a mineralized dyke sample from the Banshee Deposit, Carlin Trend, Nevada (Jeremy Vaughan, Ph.D. Thesis, unpublished data). The drawback of this technique is length of time required for analyses (~1 year).

In addition to challenges inherent within the structure of clay minerals, the method by which clay mineral data is collected is important. The lack of agreement between clay minerals identified using Terraspec and the same minerals identified using XRD is problematic. The interpretation of reflectance spectra should not be left to interpretive software such as *TSG*©. Extensive training of geologists is necessary to make full use of Terraspec data, and a set of samples should be calibrated to x-ray diffraction patterns in different deposit settings to ensure that the entire mineral assemblage is being detected by the Terraspec.

This study was successful in identifying major flow paths for ore-forming fluids into the Pipeline - deposit using a combination of stable isotope analyses and trace element geochemistry. Differences in the sampling scale for Au and associated trace elements, and stable isotopes can make comparing the two datasets in space difficult. Gold and trace element geochemistry typically represent composites over multiple metres, whereas stable isotope analyses typically represent a much smaller volume of rock or vein material (few mm^3). One method to overcome sampling scale discrepancies is to use the same pulp material prepared by laboratories for geochemical analyses for stable isotope analyses (Vaughan, Ph.D. Thesis, unpublished data). Although depleted stable isotope values may be diluted by larger areas of undepleted material, valid comparisons could be made between the two sets of data over short intervals. Furthermore, recent advances in stable isotope analytical techniques using the 'ISOTOPE ANALYZER' have reduced both the running time and cost of individual analyses while obtaining an error similar to more conventional analytical techniques (Dipple et al., unpublished data). Time and cost reduction make stable isotope analyses a more practical tool for exploration, perhaps more so than down hole trace element geochemistry.

5.5 REFERENCES

Arkai, P., Merriman, R., Roberts, B., Peacor, D., and Toth, M., 1996, Crystallinity, crystallite size and lattice strain of illite-muscovite and chlorite; comparison of XRD and TEM data for diagenetic to epizonal pelites: European Journal of Mineralogy, v. 8, p. 1119-1137.

Battaglia, S., 2004, Variations in the chemical composition of illite from five geothermal fields: a possible geothermometer: Clay Minerals, v. 39, p. 501-510.

Essene, E., and Peacor, D., 1995, Clay mineral thermometry-a critical perspective: Clays and Clay Minerals, v. 43, p. 540-553.

Lonker, S., FitzGerald, J., Hedenquist, J., and Walshe, J., 1990, Mineral-fluid interactions in the Broadlands-Ohaaki geothermal system, New Zealand: American Journal of Science, v. 290, p. 995-1068.

APPENDIX A: THE ELDER CREEK DEPOSIT: An Upper Plate Expression of an Auriferous Carlin-type hydrothermal system

INTRODUCTION

The Carlin deposits of northern Nevada are one of the world's major sources of gold (Teal and Jackson, 2002; Price et al., 2007). Gold deposition is thought to have deposited between ~42 and 36 Ma (Hofstra, et al., 1999; Arehart, et al., 2003, Cline, et al., 2005) and is typically hosted within Siluro-Devonian miogeoclinal carbonate rocks that form the footwall to the Roberts Mountain thrust (the "lower plate") The largest deposits tend to be preferentially concentrated in silty limestone units that extend to ~1000m stratigraphically beneath the thrust (e.g.,, Hofstra and Cline, 2000; Teal and Jackson, 2002). The structurally overlying Roberts Mountains allochthon (the "upper plate") is dominated by Ordovician-Mississippian siliciclastic eugeoclinal rocks (Arehart, 1996, Hofstra and Cline, 2000, Teal and Jackson, 2002). The upper plate is not known to host any major Carlin-type Au deposits although mineralization does occur locally immediately above the RMT in several of the lower plate-hosted deposits. Given the large tonnages and high grades associated with Carlin Au-deposits in Nevada (Cline et al., 2005) it is clear that the hydrothermal systems responsible for these deposits must have involved huge volumes of fluid. Thermochronology based estimates of bedrock exhumation suggest that the Carlin-type Au-deposits likely formed over a paleodepth range of <1-3km (Cline et al., 2005). At these depths, the large hydrothermal systems responsible for the Carlin deposits should have welled-up up to near surface depths, and, in doing so, must almost certainly have passed through upper plate rocks. The lack of Carlin-type deposits in the upper plate is thought to reflect the less reactive nature of the siliciclastic rocks that dominate the Roberts Mountains allochthon (Cline et al., 2005; Nutt and Hofstra, 2003) However, the definition of Carlin-type deposits as being inherently associated with carbonate dominated host-rocks (Hofstra and Cline, 2000) has tended to divert attention away from a conceptual understanding of how the same hydrothermal system might be expressed in siliciclastic upper plate rocks. The likely scenario of upwelling of Carlin hydrothermal fluids into the upper plate invokes two obvious questions; what is the physiochemical manifestation of that hydrothermal system in upper plate rocks, and what is the nature of any Au-deposit that formed as a result.

In this study we assess the possible physiochemical expression of Carlin-type auriferous hydrothermal activity in upper plate rocks of the northern Shoshone Range, northern Nevada. Specifically we studied the Elder Creek deposit, a small upper-plate hosted gold deposit located ~14 km west-northwest of the giant Pipeline Carlin-type Au-deposit (Figure A1). Combining lithogeochemistry and an analysis of clay mineralogy, we suggest that mineralization at the Elder Creek deposit may have genetic roots in a Carlin-type hydrothermal system. Whether it represents the exhaust of a deposit at depth, or the product of a pregnant ore-solution remains to be determined.

REGIONAL GEOLOGICAL SETTING

Recent reviews by Hofstra and Cline (2000) and Cline et al. (2005) have outlined the regional and tectonic setting for the Carlin Au-deposits of northern Nevada. The northern Shoshone Range is part of the greater Battle Mountain-Eureka trend which includes Battle Mountain to the north-west and the

Cortez Mountains to the south-east. Thick sequences of upper plate siliciclastic sediments cover lower plate carbonate sediments, however post-Antler orogeny tectonism and erosion have exposed geologic windows into the lower plate as exhibited at Goat Peak (north-west Shoshone Range), and at the Pipeline deposit (south-west Shoshone Range) (Kelson et al., 2008).

Figure A2 presents a simplified stratigraphic section through the lower and upper plates of the RMT package. Sequence stratigraphy work by Harry Cook (Barrick Gold Corporation-unpublished data) indicate that the lower plate underlying the Shoshone Range is comprised of Ordovician to Devonian shelf-slope facies carbonate sediments including silty limestone, silty micrite, limey-siltstone and mudstone, and dolostone, with a minor contribution of siliciclastic material. Lower plate carbonate sediments of the Shoshone Range are the favorable hosts for Carlin-style Au mineralization (Pipeline, Gold Acres). This has been attributed to the reactivity of carbonate sediments with acidic gold-bearing fluid resulting in volume loss and increased permeability, providing robust pathways for Au-bearing fluid (Cline et al., 2005).

The overlying upper plate is comprised of dominantly siliciclastic units with the rare occurrence of thin carbonate lenses. The volumetrically most extensive of the upper plate clastic sediment packages is the Ordovician Valmi Formation, composed of several thousand meters of chert, quartz arenite, argillite, slate, and greenstone (Roberts, 1951). The Silurian Elder Formation is a set of interbedded shale, siltstone, chert, and feldspathic and calcareous sandstone. The Devonian Slaven Formation is a mixture of highly contorted and broken, black, nodular chert with some carbonaceous shale partings. Gold mineralization at the Elder Creek property is hosted by these upper plate units, in the north-central part of the Shoshone Range. Structurally, the Upper Plate is imbricately thrusted with tight, upright to east-verging folds caused by the eastward transport of material during the Antler orogeny in the late Devonian (Noble and Finney, 1999). These folds have been modified by subsequent deformation that include broad open folding accompanied by oblique-slip faulting, Mesozoic to Cenozoic low angle faulting and high angle normal faulting associated with Basin and Range extension (Winterer, 1968 and Cluer et al., 1997).

Igneous rocks of the Shoshone Range include Eocene-Pliocene intermediate to felsic intrusions with basalt, andesite and rhyolite flows and tuffs. Eocene intrusions were emplaced along a west-northwest trend through the Shoshone range and have been identified both proximal and distal to economic mineralization (Kelson et al., 2005; Stager, 1977; Gilluly and Gates, 1965) Jurassic-Cretaceous intermediate-felsic intrusions have been identified at the south-eastern margins of the Shoshone Range (Pipeline, Cortez Hills) (Barrick Gold Corp- unpublished data).

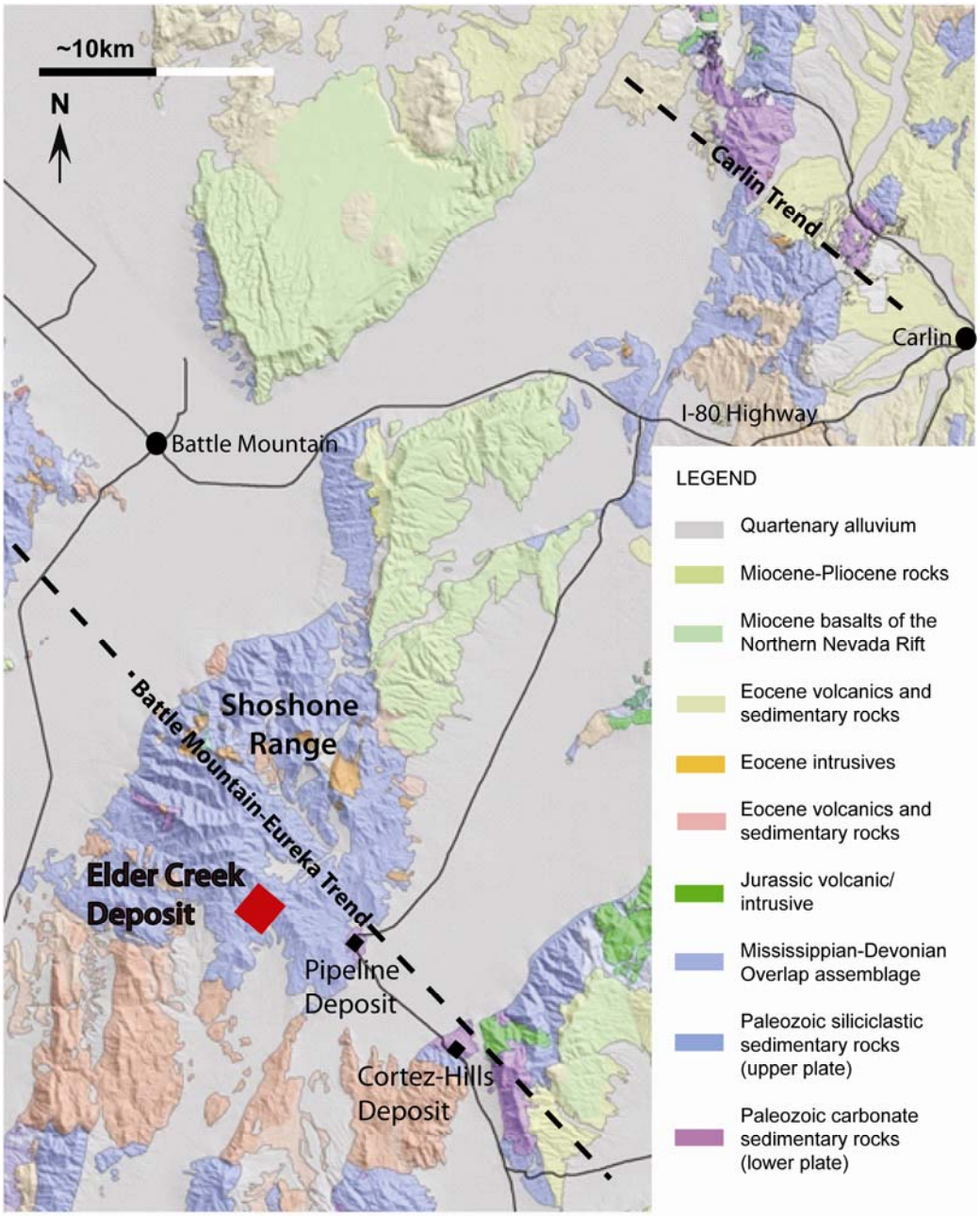

Fig. A1. Regional geology map of north-eastern Nevada. The Elder Creek deposit is located along the Northwest-Southeast trending Battle Mountain- Eureka trend, which crosscuts the Shoshone Range. The geology of the Shoshone range is largely restricted to two rock packages, a lower Paleozoic autochthonous carbonate package (lower plate) and a lower Paleozoic allochthonous siliciclastic package (upper plate). The Pipeline and Cortez-Hills deposits are two giant Carlin-type gold deposits located ~12-14km south-east of the Elder Creek deposit.

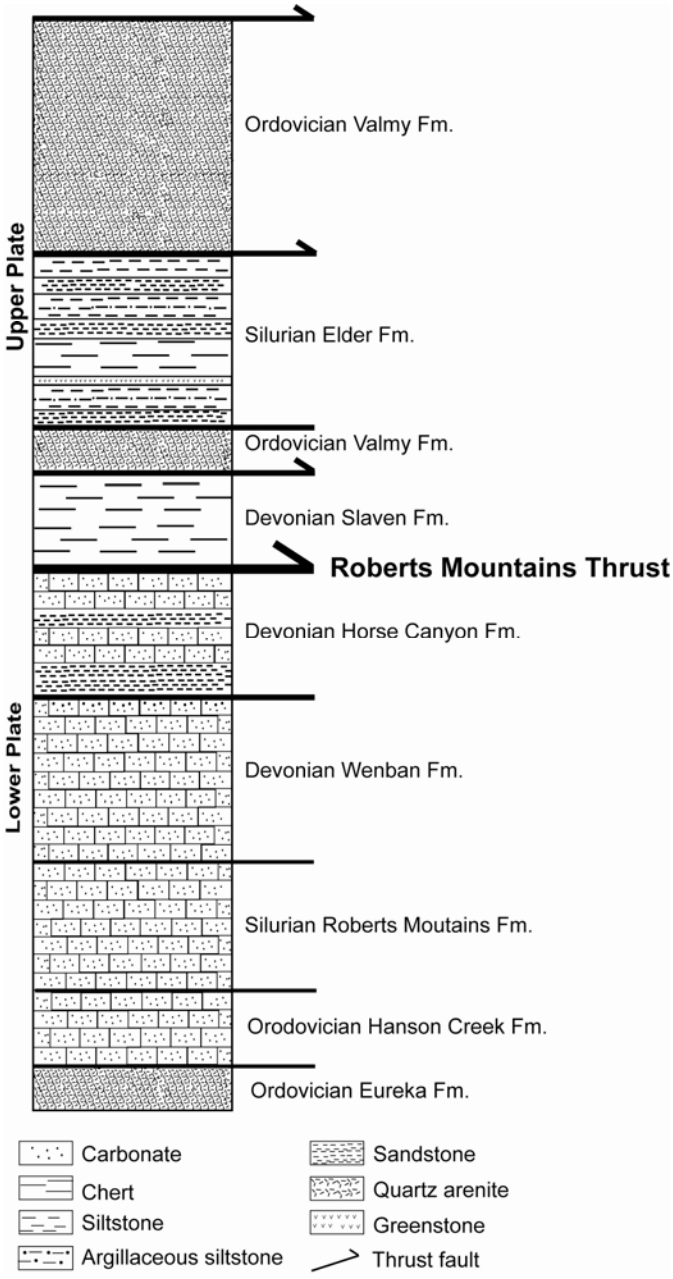

Fig. A2. Post Antler-orogeny tectono-stratigraphic column of lower Paleozoic rocks. Generalized stratigraphy column exhibiting how the RMT fault separates Lower Paleozoic carbonate rocks (lower plate) in the footwall, from Lower Paleozoic siliciclastic rocks (upper plate) in the hangingwall. Mineralization at the Elder Creek deposit occurs in the upper plate. Stratigraphy data taken from: (Chapin, unpublished data; Cline et al., 2005; Noble and Finney, 1999).

GEOLOGICAL SETTING OF THE ELDER CREEK MINE

The Elder Creek deposit was first discovered by Mapco in 1984 as a result of regional geochemical exploration including stream sediment and outcrop sampling (Russell, 2004). A drilling program ensued and gold reserves were estimated to be ~66 000 oz (1.87 tons) at a 0.012 oz/t (0.34g/t) cutoff grade (Heyl, 1991). Mapco began mine production in 1988 and produced over 13 000 tons of ore. Mining ceased in 1990 as a result of challenges in ore processing due to the high carbon content of the ore. Mill City Gold Corporation revived exploration at the Elder Creek deposit in 2003 and 2004. Exploration is currently not underway.

The geology of the four main benches cut into the Elder Creek deposit is shown in Figure A3 along with a southwest-northeast cross-section. The main lithologies mapped at the Elder Creek deposit include thick bedded and ribbon style chert, thinly bedded siltstone and argillite, thickly bedded to massive sandstone, massive quartz arenite ("quartzite"), quartz arenite clast breccia and minor greenstone. Bedding is strongly folded at the mesoscopic scale across the deposit. An east-west trending north-verging syncline and a north-south trending vertical anticline cut the deposit.

The most obvious brittle deformational feature within the Elder Creek deposit is the Carbon fault. This gently southwest dipping structure separates oxidized silty argillite, and siltstone in the hangingwall from carbonaceous argillite in the footwall (Heyl, 1991). Carbon occurs pervasively in the matrix of all sedimentary rock types in the Elder Creek pit, however only the lower two pit benches exhibit zones of high carbon content. A north-south trending zone of brecciation is located in the lowermost benches more at the west end of the deposit. Angular quartz arenite clasts are set within a strongly hematized clay and fine grained angular quartz matrix (Figure A4). Analysis of lithogeochemistry data indicates that this zone is the main host for gold mineralization. Brecciation of both quartz arenite and siltstone also occurs along fault margins.

Sedimentary rocks have been strongly argillized in the vicinity of the Elder Creek deposit. Siltstone beds are bleached and subsequent petrographic analyses indicate abundant clay in the matrix between rounded quartz grains. The matrix material of quartz arenite clast hydrothermal breccia is composed of clay and angular quartz fragments. Unbrecciated quartz contains little (<0.5 percent (%)) clay in the matrix between rounded to subrounded quartz grains. Clay also occurs in the matrix material of cataclasite, and fault gouge. Three ~1m wide zones of intense argillization were identified characterized by extensive bleaching, lack of sedimentary texture, and sharp contacts with neighboring lithologies (Figure A3). Two of these argillized zones crosscut sedimentary bedding, while the last one appears conformable to bedding (Figure A5). The complete replacement of primary mineralogy by clay made lithological identification impossible. Given the extent of argillization, and the crosscutting nature of two of the three argillic zones, we suggest that these zones are highly altered igneous dykes.

Oxidation occurs either as the pervasive alteration of sedimentary matrix minerals, or preferential alteration along fractures, and of brecciated material. The aforementioned strongly argillized siltstone beds are locally oxidized to goethite and jarosite. Fractures within quartz arenite, chert, and siltstone are coated with a thin veneer of hematite. The matrix material of quartz arenite clast breccia is strongly hematized and jarosite forms a thin rim around quartz grains, likely after pyrite.

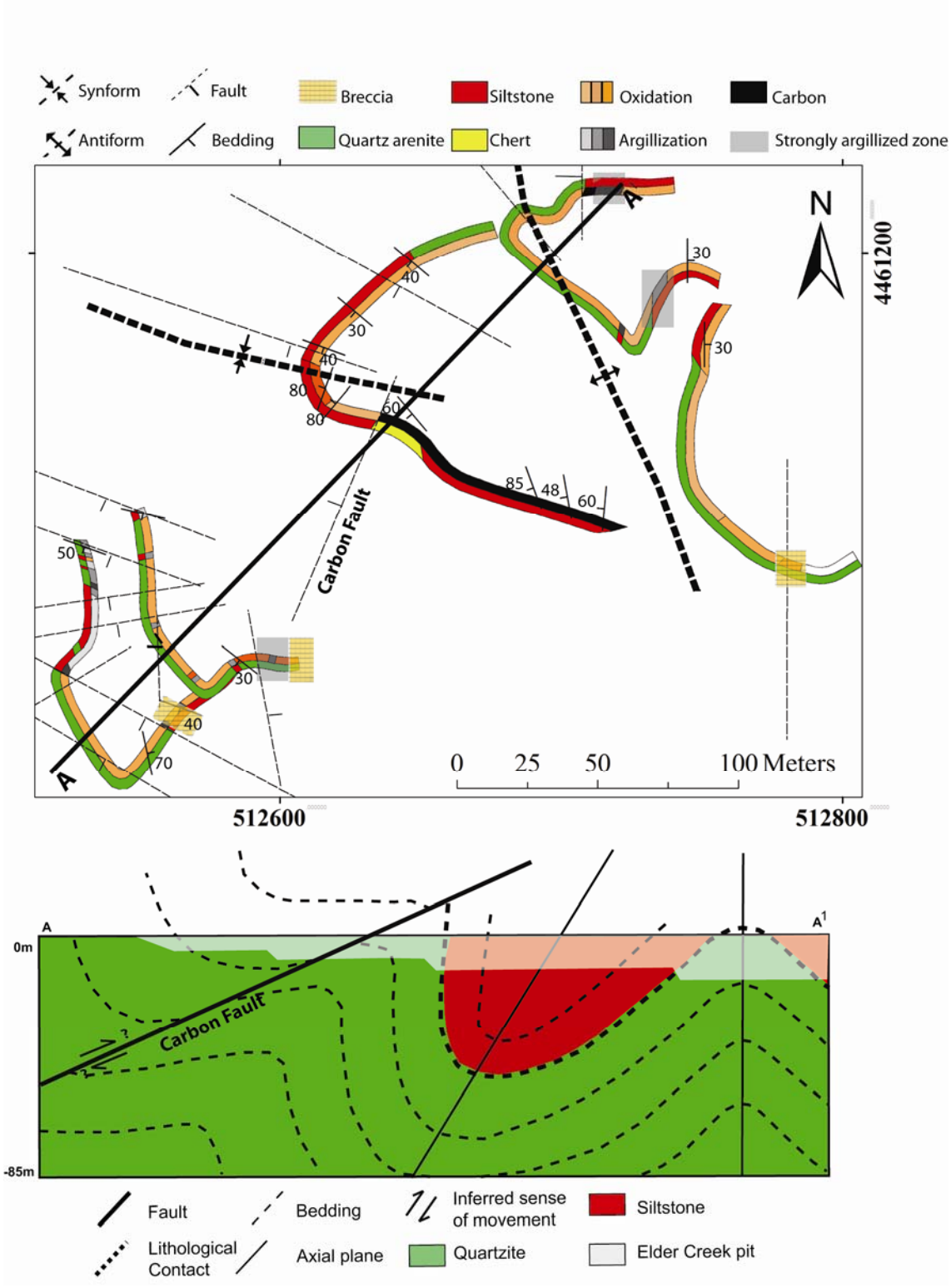

Fig. A3. A) Geology and alteration map of the Elder Creek deposit open pit. Each mapped bench is composed of a strip of lithology (outside) and a strip of alteration (inside). B) Cross section A-A^{1} through the deposit exhibits major structural features including the Carbon fault, an antiform, and a north-east verging synform.

Fig. A4. Hand specimen photograph of sample 456 containing 0.231g/t Au: angular quartzite clasts are set within an oxidized matrix containing illite, jarosite, and very fine grained angular quartz fragments.

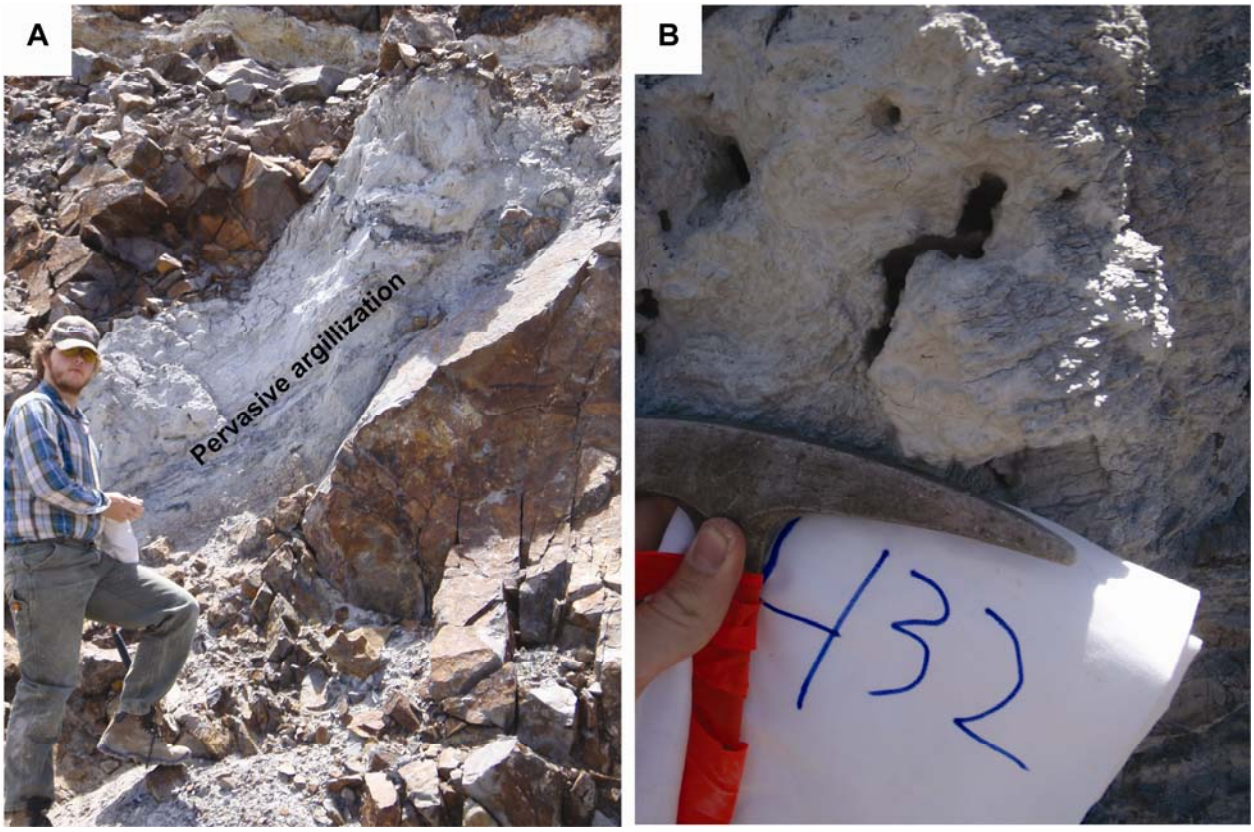

Fig. A5. Field photographs illustrating the occurrence of hydrothermal illite: A) Bleached white, pervasively argillized unit sandwiched between brecciated quartzite and massive quartzite. This unit does not appear sedimentary in nature due to the stark bleached colour, and soft argillic texture. Adjacent massive quartzite gives no indication of whether this unit cross cuts or is parallel to bedding at the outcrop scale. Siltstone ~10 metres south is not parallel to this unit which strikes North and dips East. No other sedimentary unit appears similar to this one B) Magnified image of the same pervasively altered unit. Note the lack of any sedimentary texture at this scale. Three zones exhibiting this type of intense bleaching were mapped in the Elder Creek pits.

RESEARCH APPROACH

Gold mineralization in Carlin-type environments is inherently associated with lower plate carbonate sediments. However, given the large amount of fluid required to form giant deposits (Pipeline), and the typical emplacement of such deposits directly below the RMT, it follows that fluid must have transgressed the upper plate. This study was undertaken to determine the extent to which mineralization at the Elder Creek property represents a Carlin hydrothermal system. Figure A6 illustrates three conceptual paths that Carlin hydrothermal fluid could have taken into the upper plate from the lower plate; each likely to result in a different physiochemical signature of the Carlin hydrothermal system. In the first instance (Fig. 6a), the fluid entering the upper plate and rising to near surface depths in the Eocene is a primary Carlin ore fluid unbuffered by any interaction with lower plate carbonate rocks. Given favorable host rock interaction, or a rapid, internally buffered, change in the physiochemical make-up of the fluid, this fluid could have produced a Au-deposit somewhere between the Eocene surface and the RMT. Ultimately, such a fluid would have deposited gold in the near surface environment owing to inherent cooling and oxidation as it mixed with Eocene groundwater. In the second case (Fig. 6b), the upwelling fluid deposited gold (and other associated trace metals) in lower plate carbonate rocks, prior to rising into the upper plate. This Carlin exhaust fluid, would be expected to have lower concentrations of gold and other trace elements that co-exsolve with Au, but should have maintained most of its heat. In the final case (Fig. 6c) the Carlin fluid also deposited most of its gold below prior to rising into the upper plate. However, on its passage into and through the upper plate it became extremely rock buffered and eventually loses all physiochemical expression in the rocks.

Previous studies suggest that Carlin-style ore fluids were moderately acidic (pH = 4.3 – 4.4), low temperature (180 – 240°C), and low salinity (2-3 wt. percent (%) dissolved NaCl equivalent). Gold occurs typically as submicron particles within trace element rich pyrite and arsenian pyrite, and is deposited along with As, Hg, Sb, Tl +/- Te (Cline et al., 2005; Theodore et al., 2003; Cail and Cline, 2001). Decarbonatization of carbonate host rocks by mineralizing fluid is typically followed by argillization, silicification, and sulfidation. Minerals part of the argillization sequence include illite + kaolinite +/- dickite (Cline et al., 2005; Hofstra and Cline, 2000; Cail and Cline, 2001).

Clay mineralogy

Stability field phase diagrams for phyllosilicate minerals in the system $K_2O + Al_2O_3 + SiO_2 + H_2O$, under isobaric, isothermal conditions from 100-250°C indicate the following (Figure A7): (1) muscovite is not a stable phase in low temperature environments (<250°C) (2) illite is favored by moderate temperature, and nearly neutral to slightly acidic conditions; (3) kaolinite is favored by a range of temperatures from low to moderate, and slightly to very acidic conditions; and (4) smectite and illite-smectite interlayered clays are favored by low temperatures and nearly neutral to slightly acidic conditions (Seedorf et al., 2005; Meunier and Velde, 2004; Yates and Rosenberg, 1997; Montoya and Hemley, 1975).

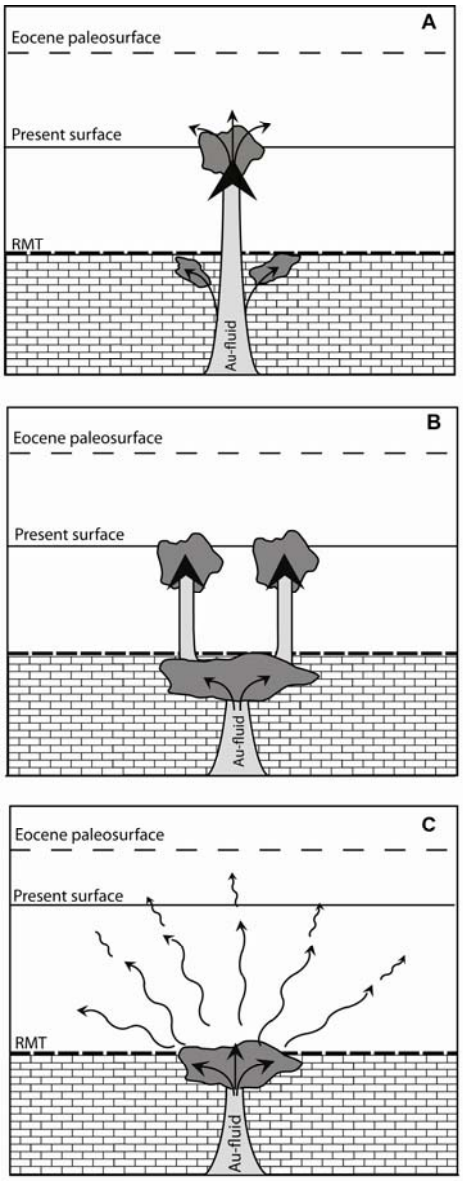

Fig. A6. Three scenarios suggesting three different fluid evolution paths through both the lower and upper plate rocks. A) The first scenario suggests that gold deposits in the upper plate are not a function of exhausted fluids at all. Gold may have precipitated in the lower plate; however, fluid transgressing the upper plate was not rock-buffered. As such, fluid contained enough gold to precipitate a deposit in the upper plate, and enough heat to produce a Carlin-type alteration signature (illite + kaolinite +/-dickite). B) The second scenario proposes that mineralizing fluid did in fact interact with lower plate carbonate rocks, precipitating gold (and associated trace elements As, Hg, Sb, Tl, +/- Te.) Following lower plate mineralization, the fluid still contained gold (albeit at lower concentrations) and was able to precipitate gold and produce the same argillic alteration assemblage in the upper plate. C) The last scenario suggests that mineralizing fluid precipitated all contained gold, and all trace elements in the lower plate and that by the time the fluid reached the upper plate, it was completely rock buffered. We would expect to see little or no evidence of fluid flow in the upper plate.

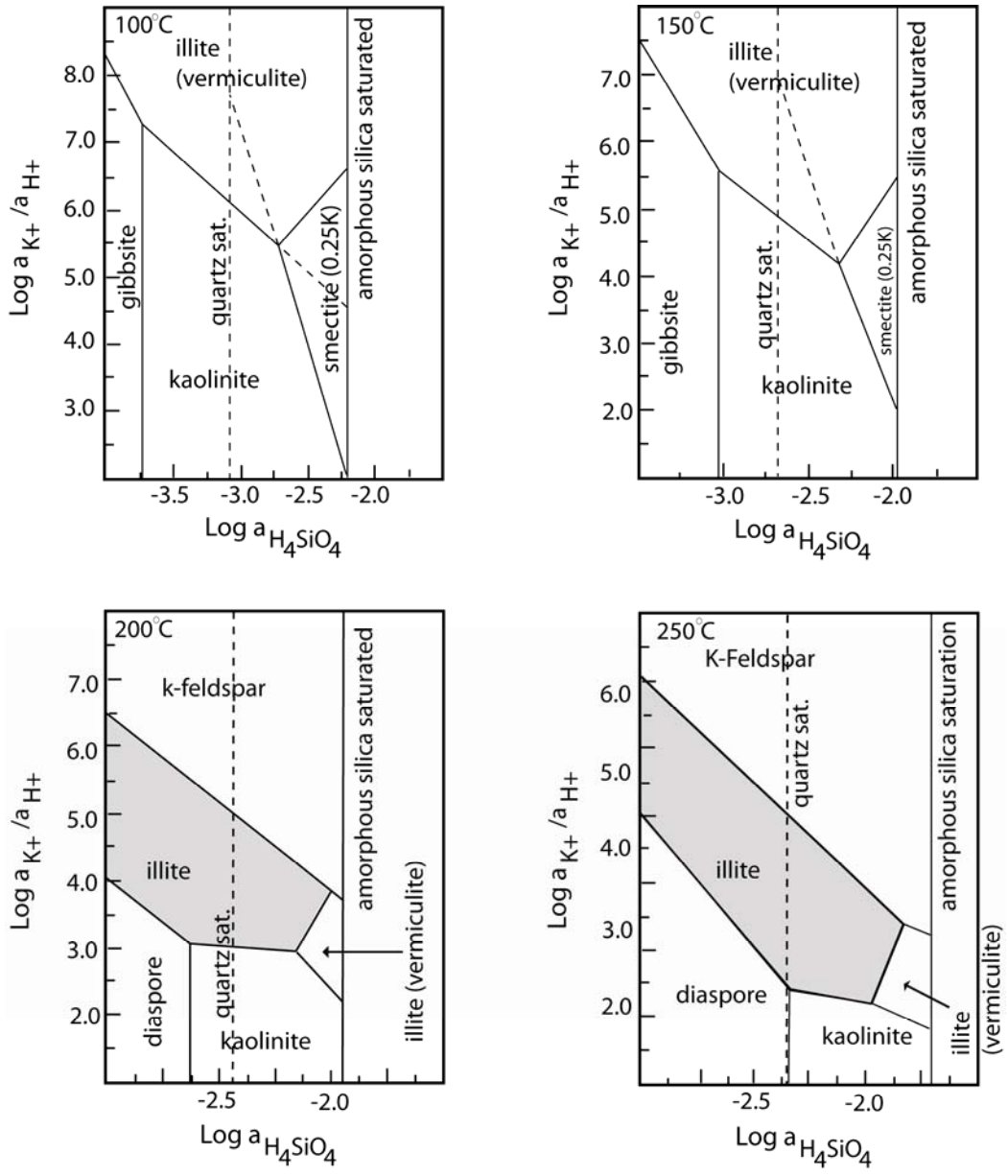

Fig. A7. Isothermal, isobaric phase diagrams derived from solution equilibration experiments by Yates and Rosenberg (1997) showing the stability fields of illite, illite-smectite (vermiculite) and smectite. Metastable phase boundaries are indicated by dashed lines. As temperature increases, expandable phases in the illite-smectite interlayered clay structure tend more toward illite. At 200°C we see the appearance of pure, end-member illite with no expandable phases and smectite is no longer stable. The smectite field has now been replaced by illite-smectite interlayered clay. The temperature of Carlin-type hydrothermal fluid has been placed between 180-240°C (Cline et al., 2005). At this range in temperature, illite is not stable, but illite, illite-smectite interlayered clay, and kaolinite are stable depending on fluid composition.

Illite crystallinity and illite composition have been identified as important geothermometers (Meunier and Velde, 2004; Battaglia, 2004, Ji and Browne, 2000; Kruse and Hauff, 1991). Crystallinity of the illite structure increases with temperature from 1M – 2M illite; where 1 and 2 represent the structural stacking of octahedral layers. XRD analysis of argillaceous material is fundamental in unraveling the structure of clays, particularly illite. The crystallinity of illite increases and this can be quantified using the full width at half the maximum (FWHM) value of the primary illite diffraction peak at 10Å (Kubler, 1967). Well crystallized illite has a peak position close to 10Å and a small FWHM (<~0.4) value. Poorly crystallized illite has a peak position ~10.2 Å and higher FWHM values ~0.8. Illite smectite interlayered clay has a peak position closer to 11.0Å and very high FWHM values of in the range of ~1.2. Pure smectite exhibits a peak closer to 14Å unglycolated and 17Å glycolated. Therefore a shift to higher peak positions indicates the presence of smectite layers in the mineral structure. The occurrence of smectite interlayers in the structure of illite further narrows the composition-temperature bounding box of a hydrothermal system.

Lithogeochemistry

Given the fairly consistent pattern of Au deposition with As, Sb, Hg, Tl and Te, the presence of a similar trace element suite at the Elder Creek property may be significant. To help understand the relationship of gold to other trace elements, concentrations of As, Hg, Sb, Tl, and Te were plotted in order of increasing gold value; a “gold ordered diagram”. This type of plot was first introduced by Sinclair and Tessari (1980). They used Ag ordered diagrams to evaluate metal zonation patterns around Ag-Pb-Zn veins from the Keno Hill area, Yukon Territory, Canada. From these diagrams, they were able to identify different trace element halos around mineralized veins. Although gold ordered diagrams are not referenced with respect to geographic orientation, they highlight patterns in trace element content with varying Au content.

METHODOLOGY

Samples for this study were collected from within the Elder Creek open pit to investigate lithologies and structures that host gold, alteration assemblages, and the presence of a trace element relationship with gold precipitation. Figure A8 is a map detailing the location of all samples collected for this study. For comparative analytical purposes, samples were also collected distal to the deposit from unmineralized regions to the north-west and south-east. These unmineralized regions have been mapped as part of the same stratigraphic package (T. Chapin, Barrick Gold Corporation; unpublished data).

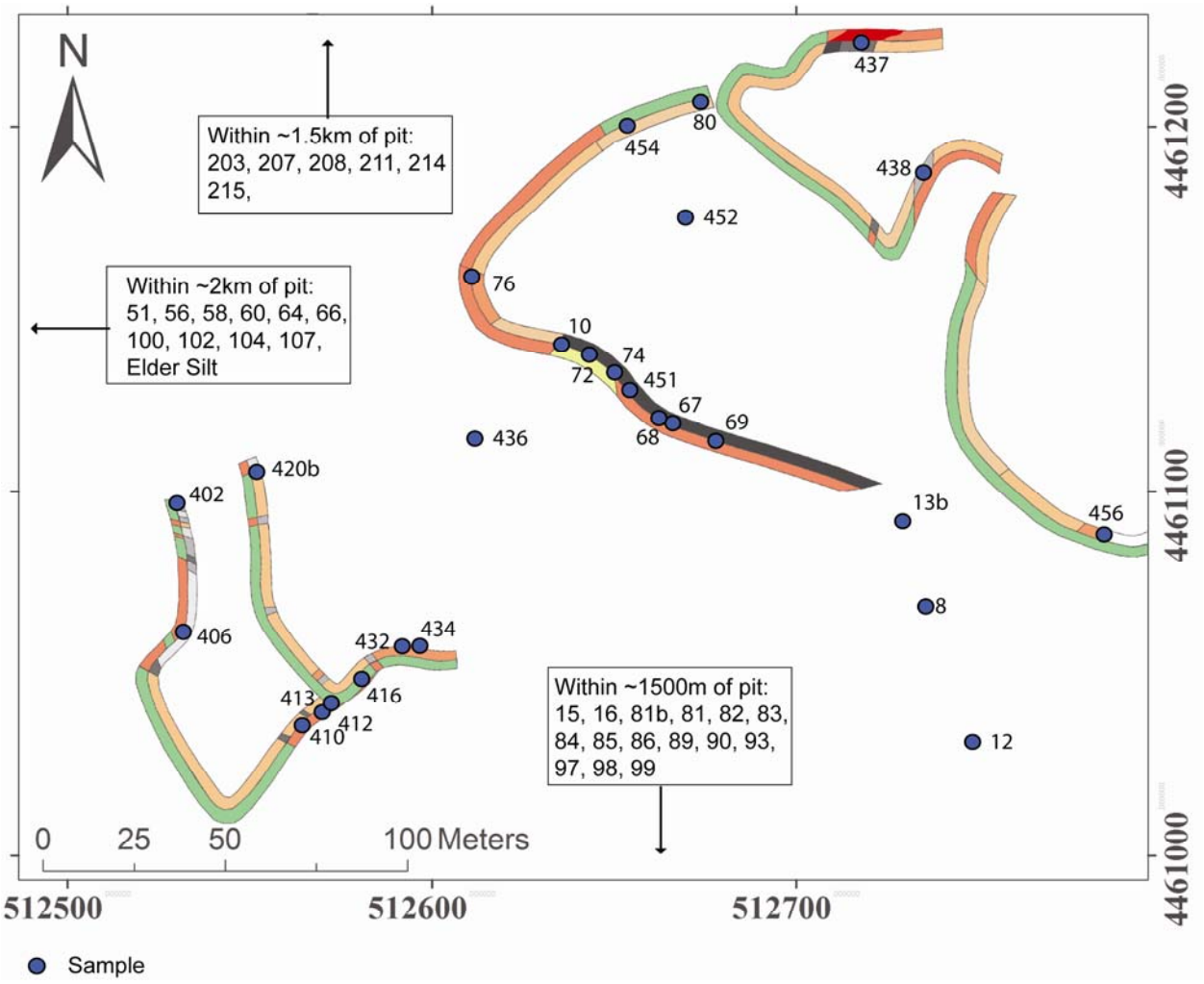

Fig. A8. Sample location map

The methods of X-ray diffraction, scanning electron microscopy, and near and shortwave infrared spectroscopy were applied to argillaceous samples both proximal and distal to the Elder Creek deposit to determine whether a Carlin-type clay alteration assemblage was present. The x-ray diffraction methods of Moore and Reynolds (1997) were used to separate clastic and carbonate samples into clastic aggregates and clay size fractions (<2μm) which involved a combination of sonic dispersion and centrifugation. Qualitative x-ray diffraction methods were carried out using a *Bruker D5000 X-ray diffractometer*. Following initial analyses the same suite of samples was treated with glycol following the methods outlined by Moore and Reynolds (1997). The glycolation of clay-rich samples facilitates the identification of swelling clays (smectite) by shifting either the 14Å or the 10Å clay peak to the left. Two standards were used to calibrate crystallinity: pegmatitic muscovite from the Bonanza mine near Tete Jaune Cache, British Columbia, and diagenetic 1Mt illite sample of Cambrian Shale from Silver Hill, Montana. The XRD pattern for these standards is shown in Figure A9.

The Terraspec© analytical spectral device (ASD) was employed to provide preliminary observations regarding clay assemblages and to distinguish between kaolinite and dickite. The Terraspec© provides rapid analysis of clay minerals by producing characteristic light reflectance spectra based on composition, bond strength, and vibrational energy. Kaolinite exhibits a characteristic reflectance doublet at 2164nm while dickite exhibits the same doublet but at 2185nm. X-ray diffraction is unable to consistently distinguish between these two mineral polymorphs.

Two polished thin sections and four clay separated fractions were analyzed using the scanning electron microscope (SEM) to determine the morphology of illite grains, and the relationship between gold and clay. Samples collected for petrographic analyses were chosen based on gold assay results, intensity of alteration, or conversely lack of visible alteration.

Approximately 58 rock samples were submitted to ALS Chemex Ltd., in Vancouver, British Columbia, for multi-element litho-geochemical analyses to determine whether the same trend between As, Hg, Sb, Tl +/- Te and Au associated with Carlin-style gold mineralization could be identified at the Elder Creek deposit. Major elements were processed by lithium borate fusion and ICP-AES (inductively coupled plasma – atomic emission spectrometry) analysis. Carbon and sulfur were determined by Leco furnace method. REE and trace elements were processed using lithium borate fusion and ICP-MS, and volatiles were processed using aqua regain digestion and ICP-MS. Fire assay fusion (FA-FUSPG1 & FA-FUSPG2) was used to isolate gold. Gold was analyzed using ICP-AES.

RESULTS

Clay mineralogy

Combined XRD, ASD, and SEM analyses indicate that 2M illite, illite-smectite interlayered clay, smectite, and kaolinite are present in the study area. Samples 432, and 437 from two of the three zones of extreme argillization mentioned previously, contain illite. Illite was identified in the matrix material of

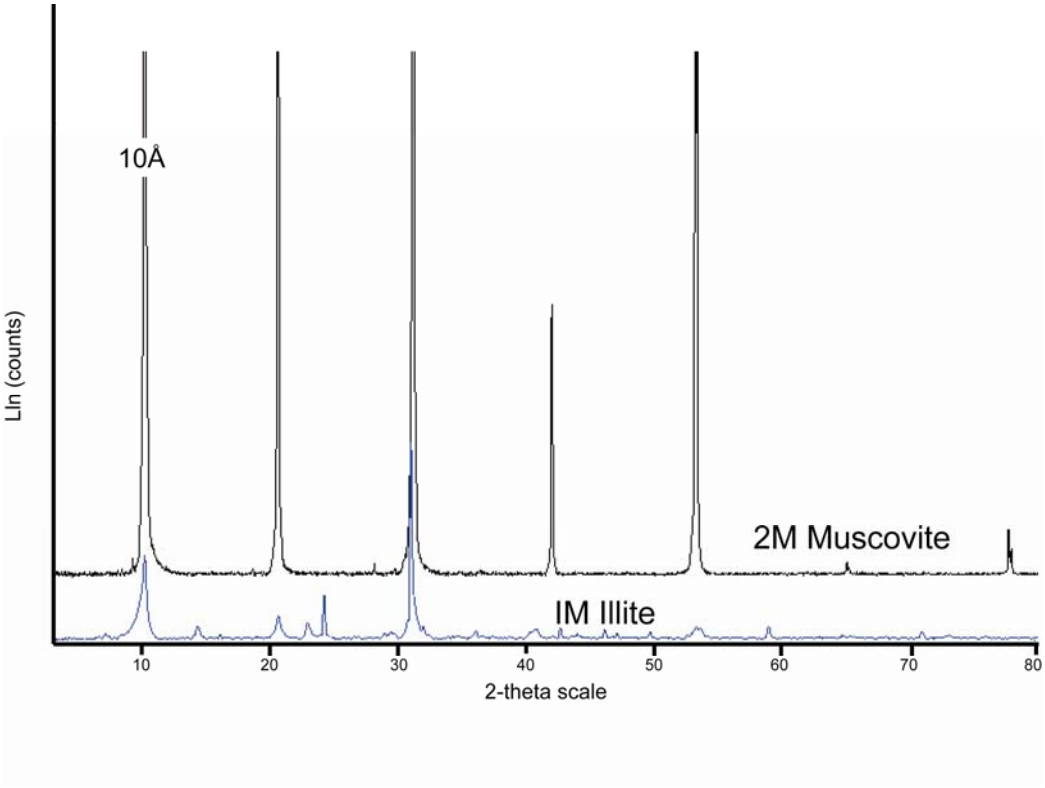

Fig. A9. Two standards were used for calibration of XRD patterns for crystallinity analysis: Bonanza igneous muscovite and Cambrian shale illite. Note the difference in the width of the 10Å peak. Igneous muscovite exhibits a full width at half the maximum (FWHM) value of 0.083 2θ while 1Mt Cambrian shale illite exhibits a FWHM value of 0.497. Crystalline muscovite exhibits a much narrower, symmetrical peak than illite.

gold hosting quartz arenite-clay breccia (sample 8). Strongly argillized siltstones contain crystalline illite with minor interlayered illite-smectite clay. Illite-smectite interlayers were identified in XRD based onthe glycolation of randomly oriented powder mount samples, and the subsequent shift of either the 14Å or 10 Å peak to lower d-spacings. Figure A10 exhibits data for all 21 samples in the dataset. Samples 'Elder Silt' and '64' exhibited distinct shifts in the 14Å peak of their diffraction patterns. Both clinochlore and smectite exhibit peaks in the 14Å range, however only the presence of smectite will cause a peak shift to the left. A number of samples exhibited uncharacteristic narrowing of the 10Å peak. These samples likely contain small amounts of illite-smectite interlayered clay, however the amounts were not of significant quantity to shift the peak to lower d-spacings.

Kaolinite was differentiated from illite by a lack of K in EDS results using the SEM, by the presence of a diffraction peak at 7.5Å in XRD, and also in the analysis of spectra from the Terraspec©. There does not appear to be one lithology prone to kaolinization as quartz arenite, chert clast breccia, claystone, and fault gouge all contain kaolinite.

SEM imaging of argillaceous samples indicates that the texture of illite varies depending on its occurrence (Figure A11). In the groundmass of pervasively altered siltstone and argillite, illite occurs as ~20 micron long laths. Each lath is made of up of stacked hexagonally shaped sheets. In quartz arenite clast breccia matrix infill, illite occurs as <10 micron microcrystalline fabric. The composition of illite, based on energy dispersive spectra (EDS), appears uniform within and between samples with different textures exhibiting high silicon, aluminum, potassium, and oxygen +/- sodium, magnesium and iron.

The crystallinity of illite was based on a measurement of the full width at half the maximum intensity value of the 10Å diffraction peak following glycolation, and by the decomposition of the 10Å diffraction peak into weakly crystalline illite (WCI), poorly crystalline illite (PCI), and illite-smectite interlayers (ISI). Figure A12 demonstrates the same trend observed by Meunier and Velde (2004) between FWHM values and the position of the 10Å illite peak. As FWHM values increase, the peak positions shifts to higher values. All samples from the Elder Creek deposit fall within the WCI and PCI crystallinity regions outlined by Meunier and Velde (2004). Studies conducted by Heller-Kalai and Kalman (1972) indicate that the 10Å illite peak may shift to higher values with the presence of illite-smectite interstratifications. Upon glycolation the 10Å illite peak is not affected by the glycol solution, however the illite-smectite interlayers are affected and shift to higher angles. Given that none of the FWHM data falls within the illite- smectite interlayered clay category according to Meunier and Velde (2004), this likely means that only very small quantities of illite-smectite exist in the sample within the Elder Creek pit. Samples 'Elder Creek Silt, and 64' contain smectite. These samples are located within 1.5-2km from the centre of the Elder Creek pit.

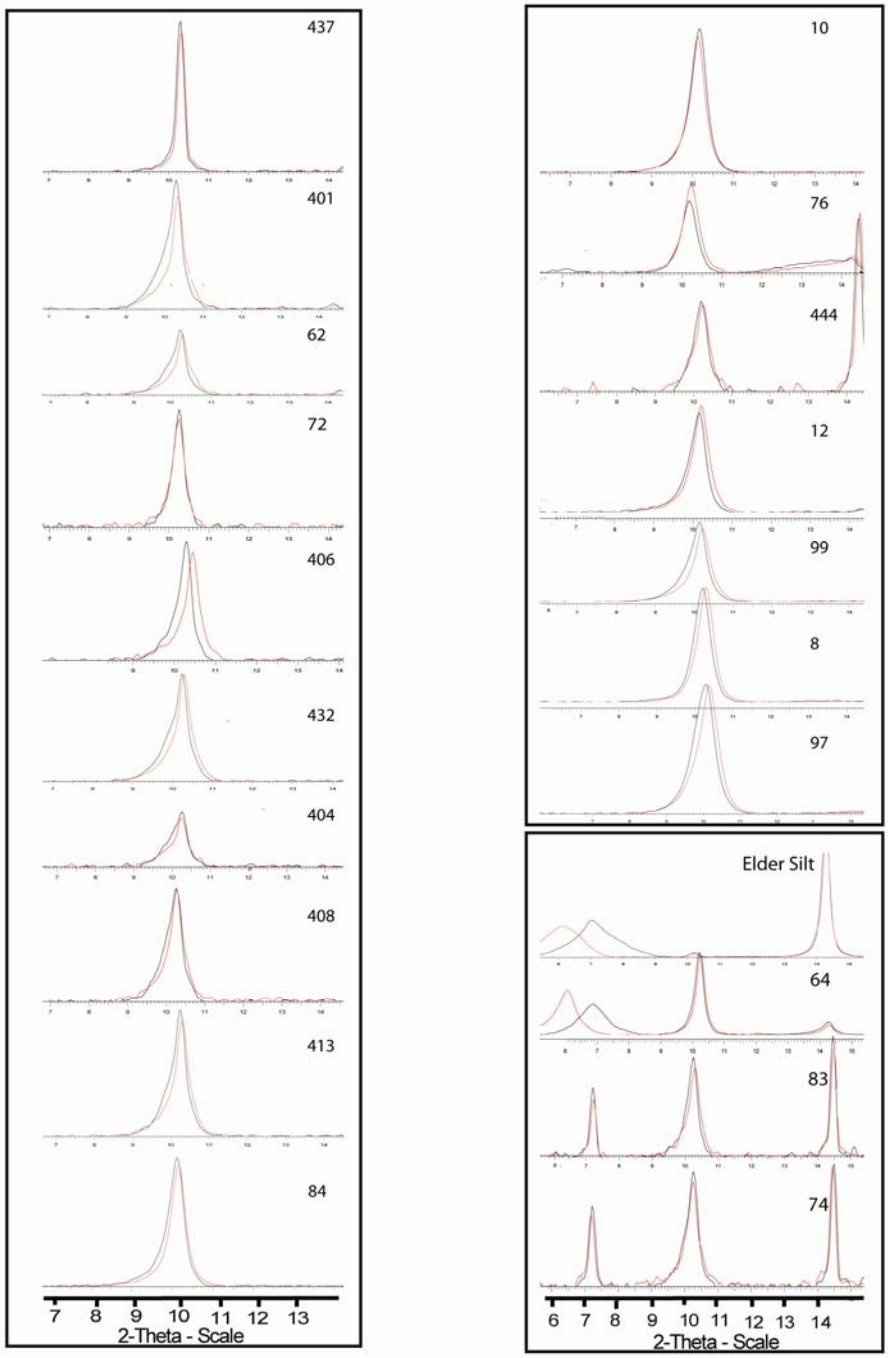

Fig. A10. Glycolated (red) and non-glycolated (black) x-ray diffraction patterns for Elder Creek samples. Samples are stacked from lowest FWHM value (top left) to highest FWHM value (bottom right). Samples a - q exhibit minor shifts in the 10Å peak indicating either poorly crystalline illite containing <5% interlayered smectite (PCI) or well crystallized illite (WCI) containing <1% interlayered smectite. Samples r – u have been separated from the rest due to the presence of other phyllosilicate phases in the sample. Samples r and s contain smectite, as evidenced by the distinct shift of the 12Å peak to left following glycolation, and kaolinite which exhibits a strong peak at 7Å. Samples t and u contain illite, kaolinite, and chlorite.

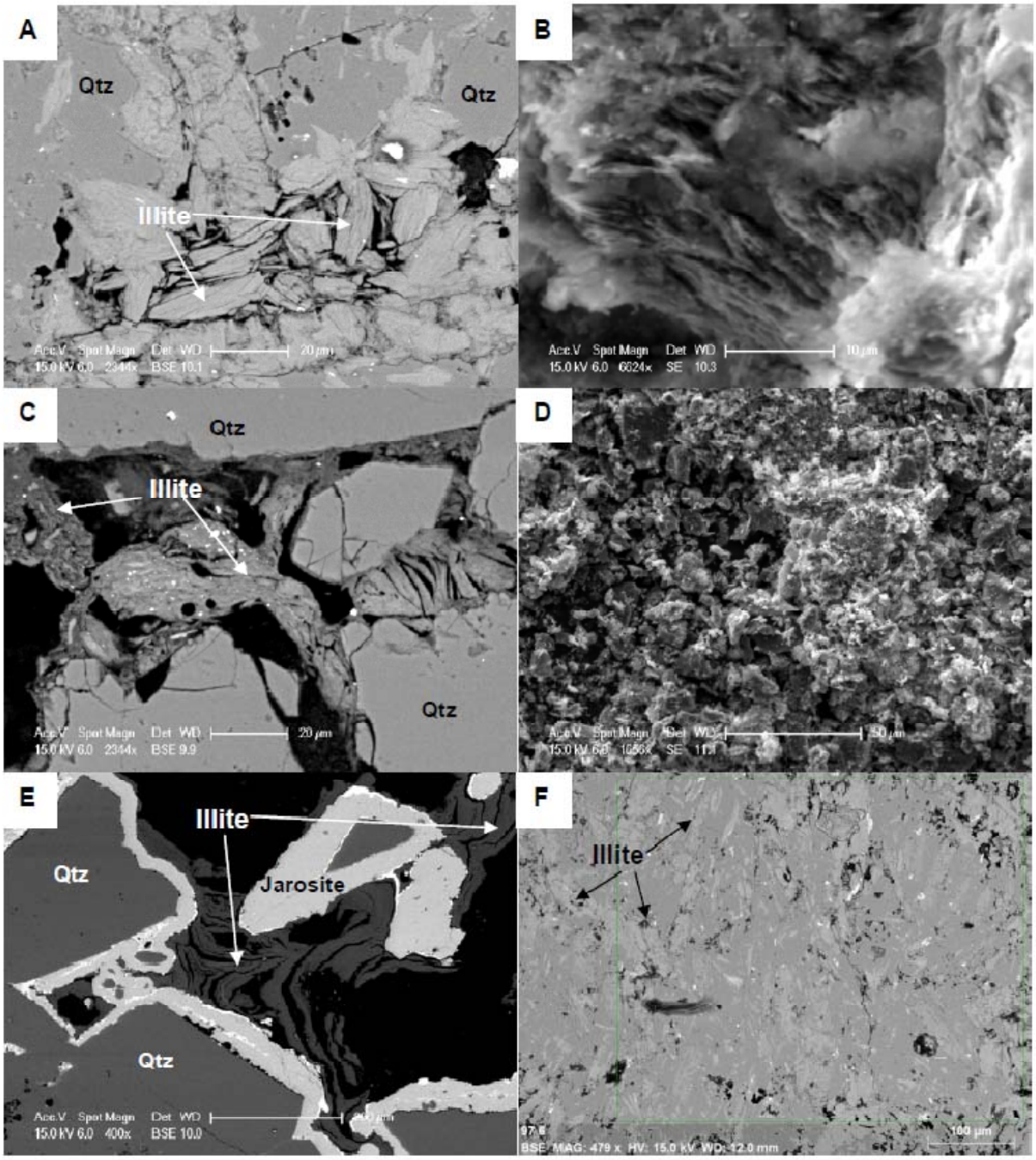

Fig. A11. Hydrothermal illite textures: A) Illite occurs as platy, euhedral grains in a strongly argillized siltstone B) Smear powder mount: illite occurs as distinct stacked sheets of octagonal shape in the same argillized siltstone as A B) Illite occurs within the matrix of a mineralized brecciated quartzite D) Powder mount: illite occurs as a microcrystalline aggregate in the same sample as C E) Polished section: Quartzite clasts are rimmed with jarosite forming after pyrite. Microcrystalline illite occurs in the matrix F) Illite occurs as euhedral laths in the groundmass of strongly argillized arkosic siltstone.

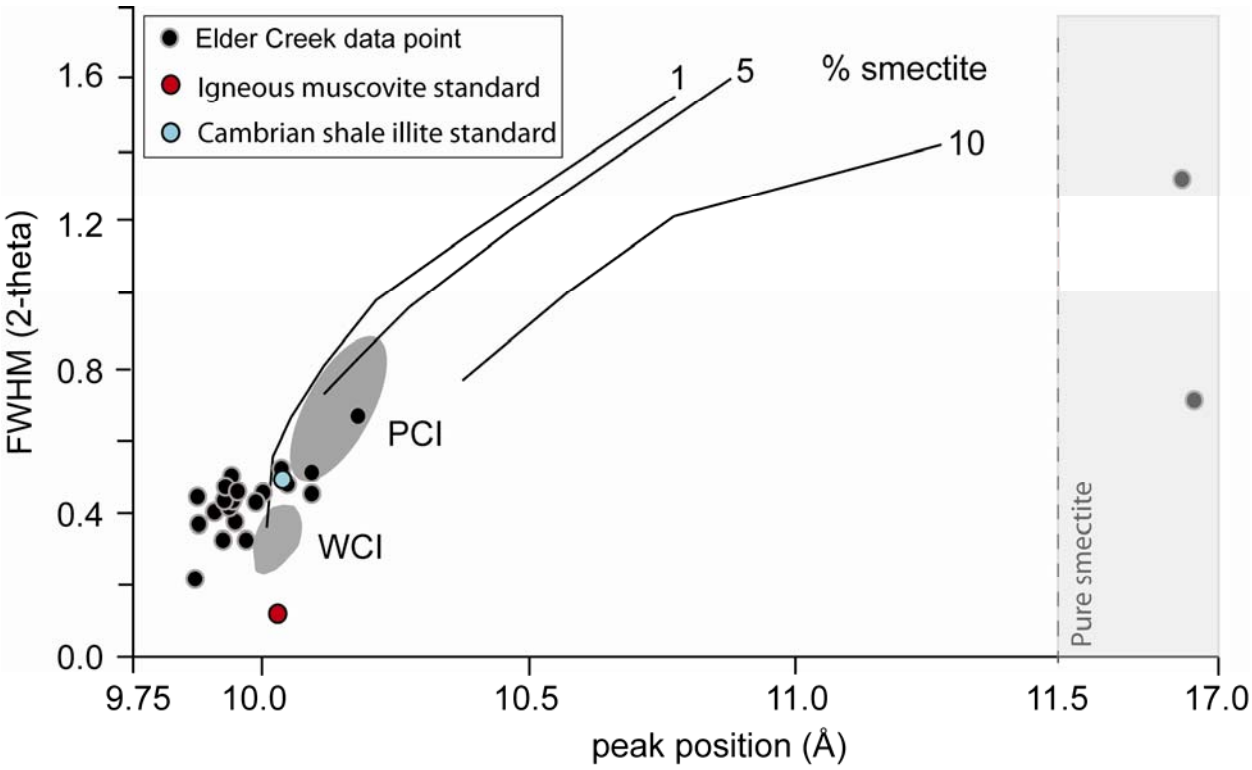

Fig. A12. Graph illustrating the relationship between the location of the 10Å illite diffraction peak, and corresponding full width at half the maximum 2θ values (After Lanson et al., 1998). Data from the Elder Creek deposit have been superimposed on this graph, illustrating the locations of well crystallized illite (WCI) and poorly crystallized illite (PCI). Both the igneous muscovite and Cambrian shale illite standards have been plotted for reference. Low full width at half the maximum (FWHM) values correspond to low 10Å peak positions indicating illite, whereas higher FWHM values and the presence of smectite correspond to higher 10Å peak positions. Note that all the samples proximal to the Elder Creek deposit fall within or very near to the WCI and PCI fields indicating low (<5% interlayered smectite). Two samples from locations distal to the deposit contain pure smectite. Pure smectite plots at ~17Å and higher FWHM. The Cambrian shale illite standard falls in the middle of the Elder Creek deposit data while the igneous muscovite standard plots at lower FWHM (more crystalline) values than Elder Creek samples. FWHM values may shift ~+/-0.1 2θ relative to the data plotted by Lanson et al (1998) due differences in x-ray diffractometer calibration. As such the important point to note in this graph is the overall trend, not exact values. Note: On the original graph taken from Meunier and Velde (2004) the lines indicating % smectite were mislabelled 99, 95, and 90%, when they are actually 1, 5, and 10% smectite.

Lithogeochemistry

Gold

All geochemical data is detailed in Appendix B. Gold values attained by ICP-AES indicate that quartz arenite clast breccia and fault cataclasite appear to be the main hosts for gold mineralization (based on samples 8, 10, 402, 434, 454) with gold values reaching 6.27g/t (sample 8). Unbrecciated quartz arenite samples returned values below 0.03g/t, indicating that brecciation likely created the required permeability to precipitate gold. SEM analysis of sample 8 indicates that native gold can occur in the void space attached to quartz grains in the breccia matrix. Gold mineralization also appears to be hosted in massive pyrite replaced argillite. Sample 451, a fist-size nodule of massive pyrite within a carbonaceous argillaceous shale unit returned 0.193g/t gold. Previous studies indicate that in Carlin-type systems, gold occurs as submicron particles within arsenic-rich pyrite rims (Cline, 2005). SEM analyses of this sample and other pyrite-bearing samples was not able to detect gold, and pyrite grains did not show evidence of zoning or the presence of pyrite rims. Given that gold is not hosted in the pyrite, it must have precipitated in the argillite host rock. The final lithologic hosts for mineralization are the three strongly argillized zones interpreted as igneous intrusions. Sample 438 of this lithology returned 0.102g/t.

Other trace elements

As mentioned in a previous section, samples were collected distal to the main centre of mineralization were included in this study to determine the background quantity of gold in upper plate sediments. Samples 16, 203, 208, 211, and 214 were taken from approximately 500m-1.5km outside the deposit and were chosen based on lithologic similarity to rocks found within the Elder Creek pit. Mapping by Tom Chapin (Barrick Gold Corporation - unpublished data) confirm that samples collected for background gold analysis are in fact part of the same stratigraphic units as within the deposit proper. Lithogeochemical analyses of these samples indicate that background values for unaltered siliciclastic sediments range from <0.001g/t (the detection limit for gold) to 0.002g/t. These same samples exhibit very low concentrations of As, Hg, Sb, Tl, and Te indicating that these trace elements along with Au was added to the system during mineralization.

Figure A13 presents a series of gold ordered diagrams for As, Hg, Sb, Tl, and Te. A key pattern is immediately evident in trace element values with increasing gold content. The same trend of increasing variability with increasing gold concentration is present when ordered by individual lithologies. A major break in slope separates low-moderate gold values from high gold values (“ore”). At gold values near or below the detection limit, As, Hg, Sb, Tl, and Te have low concentration and low variability between samples. Only Sb and Te show minor perturbations from these low values. In between the detection limit and gold “ore”, all trace elements show a marked increase both in concentration and in variability; clearly defining a halo to high Au zones. At high concentrations of gold, variability is highest for all trace elements except Te. Due to the increase in variability, individual values in these groups range from near 0 to highest in the dataset, indicating that some samples within the “ore” zone show a negative

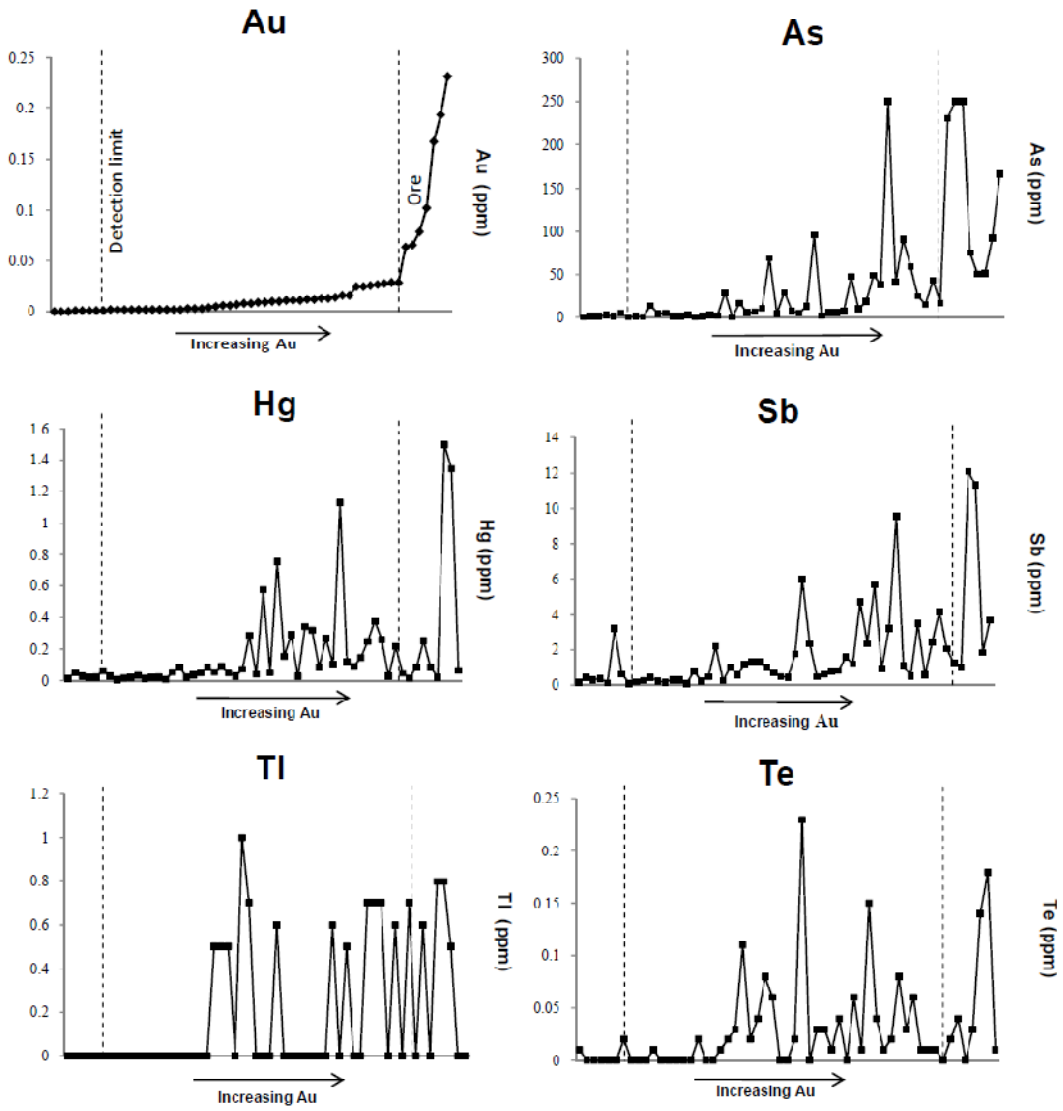

Fig. A13. Gold ordered variability diagrams for samples from the Elder Creek deposit. The trace element geochemical suite associated with gold in Carlin deposits is also associated with gold at the Elder Creek property: a) Au b) As c) Hg d) Sb e) Tl f)Te. The first dashed line on the Au plot marks samples with gold values at or below the detection limit (0.001ppm). The second dashed line marks the break in gold values from low-moderate to ore-grade. Both dashed lines shown on each trace element diagram. Below the detection limit for gold, we see low variability in As, Hg, Tl and Te, and low average values of all trace elements. As Au concentrations increases, the average concentrations of As, Hg, Sb, Tl, and Te increase, and the deviation from this average increases. Well outside of the high grade gold zone, all trace elements exhibit a large jump in concentration. At the break between moderate gold values and high gold values, only arsenic exhibits a coincident spike in concentration, while other trace elements show average, or even negative correlations to gold. On a broader scale however, the average concentration of each trace element increases with gold. Proximal to the pit (within the dashed line), well crystallized illite and poorly crystalline illite dominate the alteration sequence. Distal to the deposit (outside the dashed line), smectite and clinochlore are prevalent. Along with the geochemical data, this points to an obvious zone of fluid flow proximal to the Elder Creek deposit.

correlation with gold. This emphasizes the importance analyzing an entire dataset and looking for variability in values, not absolute values.

Figure A14 presents geochemical plots of Au, As, Hg, Sb, Tl, and Te respectively. Examination of the spatial association between ore and trace element geochemical halos indicates that high gold values are very patchy. Thallium appears to show the most consistent "high Tl" halo around gold with an interpreted halo diameter of ~150m. As, Hg, Sb, Tl, and Te all exhibit a mix of "medium" and "high" values in the main ore zone. None of the trace elements exhibited "low values" within ~200m of the main ore zone of the Elder Creek deposit.

INTERPRETATIONS

Physiochemical nature of fluid

The presence of the hydrothermal clay assemblage illite + kaolinite + dickite has been previously associated with gold deposition in Carlin-type systems (Cline et al., 2005; Cail and Cline, 2001). The presence of well-crystallized hydrothermal 2M illite at the Elder Creek deposit provides a lower limit for the hydrothermal system of >150°C (Figure A7). The lack of co-existing dickite with illite indicates that fluid was likely not very acidic (Figure A15). The presence of hydrothermal kaolinite would provide information on the acidity of the fluid, however the origin of kaolinite at the Elder Creek deposit is poorly constrained. Kaolinite occurs mostly on the weathered surface of rocks and along exposed fractures. Given the uncertainty in the origin of kaolinite, illite is our most robust indicator of hydrothermal fluid flow in the Elder Creek system.

Fluid flow pathways

Evaluation of gold data with respect to structure and lithology indicates that permeability likely controlled gold mineralization at the Elder Creek deposit. Auriferous fluid exploited pre-existing corridors of enhanced permeability: faults, fractures, and zones of brecciation. Hydrothermal fluid-rock interaction is demonstrated by the presence of anomalous Au, As, Hg, Sb, Tl, and/or Te values, and the presence of hydrothermal illite. Impermeable units such as massive unbrecciated quartz arenite show no evidence of having interacted with the mineralizing fluid.

Three zones of intense 2M-illite alteration were identified in the Elder Creek pit (Figure A3). Illite in these zones falls into the 'well crystallized illite' category identified by Meunier and Velde (2004) indicating that the mineral structure is organized relative to the lower temperature polymorph 1M-illite and illite-smectite interlayered clay. Illite of this nature has been associated with hydrothermal activity

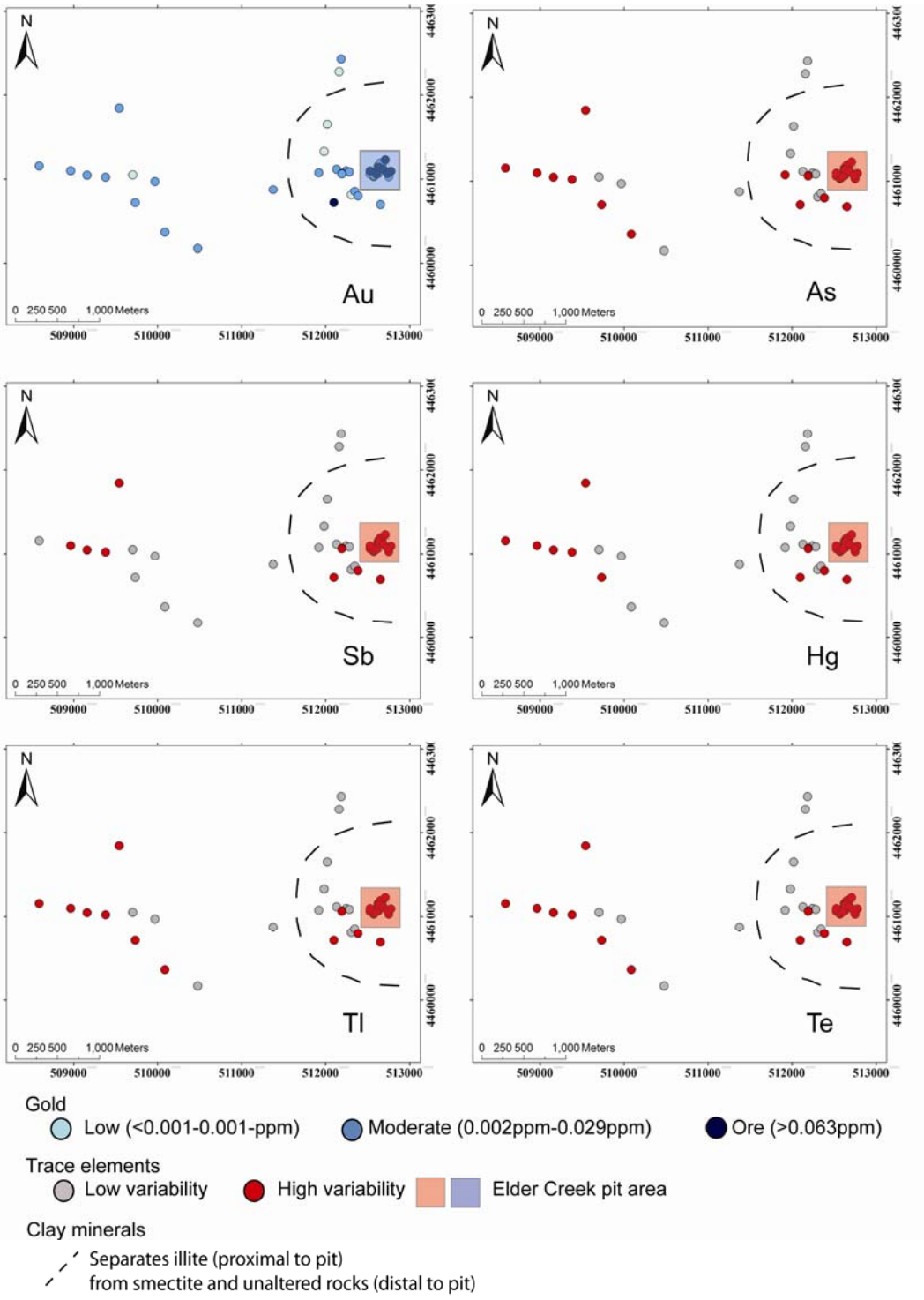
N
Au
As
Sb
Hg
Tl
Te
0 250 500 1,000 Meters
509000
510000
511000
512000
513000
4463000
4462000
4461000
4460000
Gold
Low (<0.001-0.001-ppm)
Moderate (0.002ppm-0.029ppm)
Ore (>0.063ppm)
Trace elements
Low variability
High variability
Elder Creek pit area
Clay minerals
Separates illite (proximal to pit)
from smectite and unaltered rocks (distal to pit)

Fig. A14. Geochemical halos plotted for Au, As, Sb, Hg, Tl, an Te. Gold values (Fig.13a) can be divided into "ore" and "non-ore" values based in a distinct break in slope of the values. Trace element values have been divided into two groups based on variability when assessed using the gold ordered diagrams from Figure A12. Low variability indicates both low average concentrations and little deviation from the median value. High variability indicates higher average concentrations and large fluctuations in concentrations. The occurrence of high Au-values (ore) is defined by the Elder Creek pit. The one sample sitting outside of the main Elder Creek pit comes from a roadcut to the South of the pit where mining also took place. The Elder Creek pit also exhibits high variability values in all the trace elements (As, Sb, Hg, Tl, and Te). Interestingly, variability is also high ~5km West of the deposit. This location marks the entrance to the road leading up to the deposit from the main haul road and may be a site of contamination. Distal to (>1000m) the main concentration of Au, we see dominantly low variability values in As, Hg, Sb, Tl, and Te. The same area exhibits low-moderate gold values, with only 3/17 samples containing >0.01 ppm Au. Therefore, the Elder Creek pits are characterized by high gold concentrations and high variability and average concentration of trace elements. Areas distal to the deposit are characterized by low gold values and low variability and low average concentrations of trace elements.

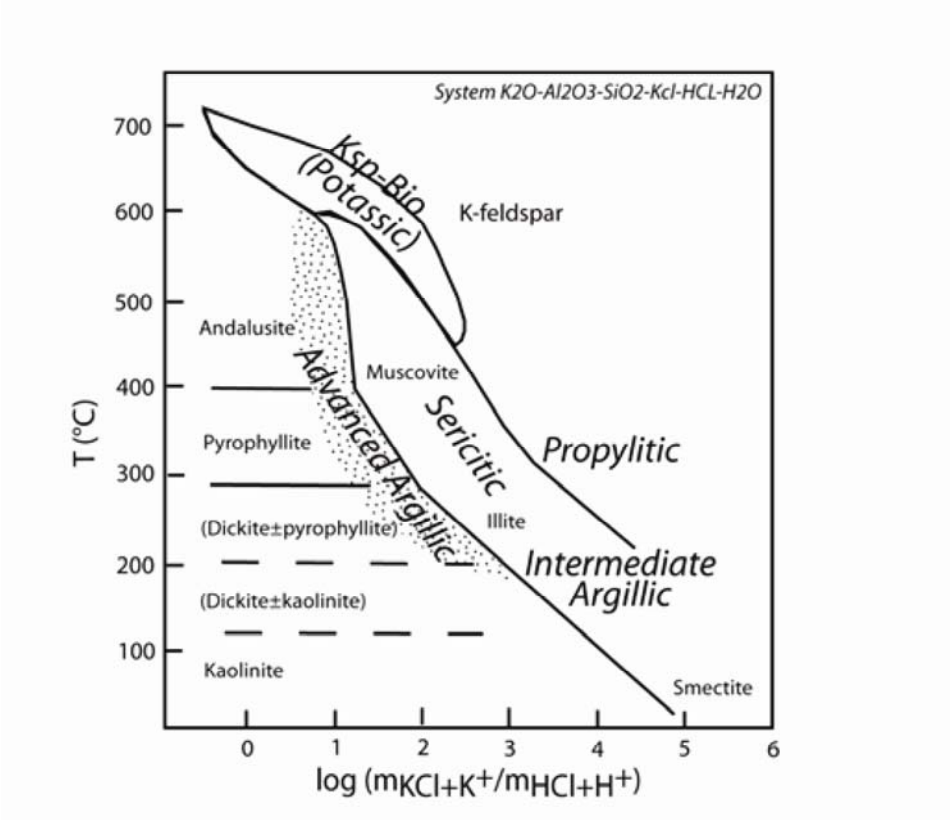

Fig. A15. Simplified stability field diagram for the system K_2O + Al_2O3 + SiO_2 + KCl + HCl+ H_2O. Dickite is the higher temperature aluminosilicate polymorph of kaolinite. Note that dickite is stable in higher acidity environments than illite. The lack of dickite in the Elder Creek system provides constraints on the acidity of the hydrothermal fluid (Seedorf et al., 2005).

indicating that the three zones of intense alteration are likely hydrothermal fluid pathways (Meunier and Velde, 2004). Zones of brecciation and faulting appear to be other conduits for hydrothermal fluid. 2M-illite was identified in the matrix of both quartz arenite clast breccia and cataclasite. Gold was indentified in the matrix of the quartz arenite clast breccia indicating at the very least a spatial relationship between illite and gold, if not one of co-genetic deposition. Some difficulty exists in distinguishing between clay minerals formed at the time of gold deposition from earlier hydrothermal and later supergene events. For this study, clay minerals were categorized by occurrences in: groundmass/ sedimentary matrix, veins, or as breccia matrix material. From these occurrences, it can be assumed that neither vein nor breccia matrix material formed from diagenetic processes.

DISCUSSION

Gold mineralization at the Elder Creek deposit was structurally controlled and concentrated in zones of high permeability. As, Sb, Hg, Tl, and Te precipitated with gold. Typical values for these trace elements are plotted in Table 1 along with gold values, for the giant Cortez Hills Carlin-type gold deposit, hosted in the lower plate. Trace element values appear as ratios to gold. As, Hg and Te values are comparable across the two deposits. Tl exhibits slightly higher values at the Elder Creek deposit than the Cortez Hills deposit. Of particular interest are Sb values which are on average an order of magnitude larger at the Elder Creek.

Although trace elements are enriched at the Elder Creek deposit, the average gold grade is still much lower than at the Cortez Hills deposit and most other Carlin-type gold deposits. The Alligator Ridge mining district is located along the southern extension of the Carlin trend and hosts a number of Carlin-style deposits in carbonate rocks (Nutt and Hofstra, 2003). Studies suggest that Carlin-style Au mineralization at Alligator Ridge differs from typical Carlin-style mineralization in both deposit size and Au grade being much lower. Two explanations are offered by Nutt and Hofstra (2003) for this difference: either the mineralizing fluid transported less Au than typical Carlin systems, or host rocks were less suitable at fixing Au from these fluids. The latter explanation would correspond to scenario 1 of Figure A6 whereby mineralizing fluid was not buffered by lower plate carbonate rocks, however the lack of a carbonate trap for gold in the upper plate lead to the precipitation of only minor amounts of gold in siliciclastic rocks. T

he second explanation is that gold was trapped previously by carbonate rocks of the lower plate and the fluid has been partially rock buffered losing most of its gold and some of its trace elements, but retaining most of its heat. This explanation corresponds to scenario 2 of Figure A6 and suggests that the Elder Creek deposit is genetically linked to mineralization at depth, possibly a Carlin-type system. Only further drilling of Elder Creek deposit would resolve this possibility.

Table A1. Assay and trace element values for four high grade ore samples (1-4) from the Cortez Hills deposit located ~14km southeast of the Elder Creek deposit. Trace element values are presented as ratios to gold. Samples highlighted in grey are samples from the Elder Creek deposit shown for comparison. As, Hg, and Te values for both deposits are comparable. Sb values are on average an order of magnitude higher at the Elder Creek deposit than the giant Cortez Hills deposit. Elder Creek Tl values are also higher at than at the Cortez Hills deposit.

Sample	Au (ppm)	As:Au	Hg:Au	Sb:Au	Tl:Au	Te:Au
1	9.68	119.32	3.87	1.93	2.59	0.05
2	10.8	18.24	1.54	0.77	0.31	0.02
3	12.6	107.94	2.98	3.38	1.02	0.10
4	64.2	233.64	0.58	1.12	0.99	0.05
434	0.064	3906.25	1.33	65.16	3.91	0.31
10	0.066	3787.88	3.85	31.36	9.09	0.61
402	0.079	946.84	1.08	15.70	3.16	0.06
438	0.102	496.08	0.19	9.90	7.84	0.29
100	0.167	304.19	8.95	72.46	4.79	0.84
451	0.193	478.76	6.97	58.55	2.59	0.93
456	0.231	720.78	0.27	8.01	1.08	0.04
8	6.27	59.81	0.02	0.59	0.04	0.00

Deposit classification

The Shoshone range is host to a plethora of metal deposits located within three geographical districts: Hilltop, Lewis and Buillion (Kelson et al., 2008). Three deposit types are prevalent in the area: Miocene epithermal deposits, Eocene porphyry deposits, and Eocene Carlin deposits (Kelson et al., 2008). Mineralization in the area has been associated with early Eocene to late Oligocene igneous rocks (Maher et al.,1993, Kelson et al., 2005 in Kelson et al., 2008). Carlin deposits have been explained by some as simply being distal sediment hosted expressions of either porphyry or high sulfidation epithermal systems or at the very least being of Eocene magmatic origin (Johnston and Ressel, 2004; Henry and Ressel, 2000; Sillitoe and Bonham, 1990). Low sulfidation deposits have been excluded from the discussion on the origin of Carlin-systems due to a lack of shared characteristics. The same exclusion will take place here with regards to the Elder Creek deposit due to a lack of evidence for boiling, and the stark difference in ore assemblage and vein quartz association between Elder Creek and typical low sulfidation systems.

The defining features of high sulfidation systems include pyrite-rich, high sulphidation-state sulfide assemblages typified by enargite, luzonite, digenite, chalcocite and covellite; and advanced argillic alteration assemblages typified by quartz, alunite, pyrophyllite and kaolinite/dickite (Arribas, 1995). The Elder Creek deposit lacks alunite, pyrophyllite, and dickite. Additionally, the Elder Creek deposit lacks any of the sulfide minerals typically associated with high sulphidation-state ore assemblage.

Porphyry gold deposits and related epithermal deposits are intrusion centered, and formed at <4km depth, from exsolved magmatic fluid (Sillitoe and Hedenquist, 2004). Mineralizing fluids in these systems are oxidized, and carry some trace metals; Cu, Au, Ag, Zn, W, As, and Sb. Given the data presented in this paper, the clay assemblage observed at the Elder Creek deposit would coincide with distal porphyry-style alteration. While alteration assemblages can be explained by a porphyry system, the trace-element suite observed in both Carlin deposits and Elder Creek does not contain significant amounts of Cu, Ag, Zn, or W. A more plausible link, however, can be made between mineralization at the Elder Creek property and models for distal disseminated sediment-hosted Au deposits (Sillitoe and Bonham, 1990). Distal concentrations of Au-As-Sb can be explained in the context of the liberation of metal-bearing magmatic hydrothermal brines from centrally located intrusions and their progressive cooling as fluids move up and out through connate and meteoric waters (Sillitoe and Bonham, 1990). On the peripheries of these intrusions, salinities are too low to complex appreciable amounts of base metals and only Au, As, and Sb are capable of further transport as bisulfide complexes. Distal disseminated Au and trace element deposition has been reported at the Bingham deposit, Utah, as far as 8 km away from the magmatic centre (Sillitoe and Bonham, 1990). Such distances negate the need of a large intrusion proximal to Au mineralization. Given the extent of Eocene magmatism in the north-west Shoshone range, the possibility cannot be ruled out that Elder Creek deposit, if not all Carlin deposits are in fact distal disseminated gold deposits.

Carlin gold systems are extremely variable between deposits but previous studies indicate a fluid temperature between 180-240°C, with an alteration signature consisting of decalcification, silicification, argillization, and sulfidation (Cline et al., 2005). The geochemical signature associated with these deposits typically includes anomalous values of Au, As, Hg, Sb, Tl, +/- Te. Disseminated gold ore is

hosted in carbonate sediments, and the ore assemblage appears to lack major concentrations of other sulfide phases such as chalcopyrite, molybdenite, or pyrrhotite. Although many Carlin deposits are spatially associated with major igneous bodies (Cortez Hills, Pipeline, Goldstrike), there is no direct indication that mineralization is associated with magmatic activity. The Elder Creek deposit shares many of these characteristics: 1) low temperature argillic alteration (illite + kaolinite) 2) gold +/- pyrite ore assemblage 3) anomalous concentrations of or moreover increased variability in arsenic, antimony mercury, thallium, and tellurium with increased gold concentrations. Given these similarities, it is possible that the Elder Creek deposit is in fact the upper plate expression of a Carlin-style hydrothermal system.

CONCLUSIONS

Results from this study of the Elder Creek gold deposit indicate that Carlin-type hydrothermal fluid may have transgressed the upper plate following mineralization of the lower plate, and precipitated gold in siliciclastic sedimentary rocks. This study determined that a fluid of temperature >150°C, relatively low acidity, carrying Au, As, Hg, Sb, Tl, and Te precipitated gold (along with associated trace elements) in zones of high permeability including breccia and cataclasite. This description is consistent with Carlin-style gold mineralization.

Recognizing upflow zones of Carlin-style hydrothermal fluid may provide a robust vector toward gold ore at depth. Identifying characteristics of Carlin gold mineralization in upper plate siliciclastic rocks redefines existing models for Carlin gold deposits. We suggest here that in order to further develop a process model for Au-deposition, Carlin deposits must be studied in the context of large-scale hydrothermal systems. The process of Carlin gold mineralization in the Eocene may not have ended with gold deposition in lower plate carbonate rocks, it is possible that mineralizing fluid continued through into the upper plate.

REFERENCES

Arehart, G., 1996, Characteristics and origin of sediment-hosted disseminated gold deposits: A review: Ore Geology Reviews, v. 11, p. 383-403.

Arehart, G., Chakurian, A., Tretbar, D., Christensen, J., McInnes, B., and Donelick, R., 2003, Evaluation of radioisotope dating of Carlin-type deposits in the Great Basin, western North America, and implications for deposit genesis: Economic Geology, v. 98, p. 235.

—, 2003, Evaluation of radioisotope dating of Carlin-type deposits in the Great Basin, western North America, and implications for deposit genesis: Economic Geology, v. 98, p. 235.

Arribas Jr, A., 1995, Characteristics of high-sulfidation epithermal deposits, and their relation to magmatic fluid: Mineralogical Association of Canada Short Course Series, v. 23.

Battaglia, S., 2004, Variations in the chemical composition of illite from five geothermal fields: a possible geothermometer: Clay Minerals, v. 39, p. 501.

Cail, T., and Cline, J., 2001, Alteration associated with gold deposition at the Getchell Carlin-type gold deposit, north-central Nevada: Economic Geology, v. 96, p. 1343.

Cline, J., Hofstra, A., Muntean, J., Tosdal, R., and Hickey, K., 2005, Carlin-type gold deposits in Nevada: Critical geologic characteristics and viable models: Economic Geology, 100th Anniversary Volume, p. 451-484.

Cluer, J., Cellura, B., Keith, S., Finney, S., and Bellert, S., 1997, Stratigraphy and structure of the Bell Creek nappe (Antler orogen), Ren property, northern Carlin trend, Nevada: The RMT, Elko and Eureka counties, Nevada: Nevada Petroleum Society, p. 41–54.

Gilluly, J., and Gates, O., 1965, Tectonic and igneous geology of the northern Shoshone Range, Nevada, US Gov. Print. Off.

Heller-Kallai, L., and Kalman, Z., 1972, Some naturally occurring illite-smectite interstratifications: Clay Clay Minerals, v. 20, p. 165–168.

Henry, C., and Ressel, M., 2000, Eocene magmatism of northeastern Nevada: The smoking gun for Carlin-type gold deposits: Geology and ore deposits, p. 15–18.

Heyl, A., 1991, The Elder Creek Mine, Lander County, Nevada, p. 53-55.

Hofstra, A., Snee, L., Rye, R., Folger, H., Phinisey, J., Loranger, R., Dahl, A., Naeser, C., Stein, H., and Lewchuk, M., 1999, Age constraints on Jerritt Canyon and other carlin-type gold deposits in the Western United States; relationship to mid-Tertiary extension and magmatism: Economic Geology, v. 94, p. 769.

Ji, J., and Browne, P., 2000, Relationship between illite crystallinity and temperature in active geothermal systems of New Zealand: Clays and Clay Minerals, v. 48, p. 139.

Kelson, C., Crowe, D., and Stein, H., 2005, Geochronology and geochemistry o£ the Hilltop, Lewis, and Bullion mining districts and surrounding area, Battle Mountain-Eureka trend, Nevada, Geological Society of Nevada, p. 25.

—, 2008, Geochemical and Geochronological Constraints on Mineralization within the Hilltop, Lewis, and Bullion Mining Districts, Battle Mountain-Eureka Trend, Nevada: Economic Geology, v. 103, p. 1483.

Kruse, F., Identification of illite polytype zoning in disseminated gold deposits using reflectance spectroscopy and X-ray diffraction-potential for mapping with imaging spectrometers.

Lanson, B., Velde, B., and Meunier, A., 1998, Late-stage diagenesis of illitic clay minerals as seen by decomposition of X-ray diffraction patterns: Contrasted behaviors of sedimentary basins with different burial histories: Clays and Clay Minerals, v. 46, p. 69-78.

Maher, B., Browne, Q., and McKee, E., 1993, Constraints on the age of gold mineralization and metallogenesis in the Battle Mountain-Eureka mineral belt: Nevada: Economic Geology, v. 88, p. 469-478.

Montoya, J., and Hemley, J., 1975, Activity relations and stabilities in alkali feldspar and mica alteration reactions: Economic Geology, v. 70, p. 577.

Moore, D., and Reynolds Jr, R., 1997, X-ray diffraction and the identification and analysis of clay minerals, 378 p, Oxford University Press, New York.

Muntean, J., Cline, J., Johnston, M., Ressel, M., Seedorff, E., and Barton, M., 2004, Controversies on the origin of world-class gold deposits: Part I, Carlin-type gold deposits in Nevada: Society of Economic Geologists Newsletter, v. 59, p. 1-18.

Noble, P., and Finney, S., 1999, Recognition of fine-scale imbricate thrusts in lower Paleozoic orogenic belts—An example from the Roberts Mountains allochthon, Nevada: Geology, v. 27, p. 543.

Nutt, C., and Hofstra, A., 2003, Alligator Ridge district, east-central Nevada: Carlin-type gold mineralization at shallow depths: Economic Geology, v. 98, p. 1225.

—, 2003, Alligator Ridge district, east-central Nevada: Carlin-type gold mineralization at shallow depths: Economic Geology, v. 98, p. 1225.

Price, J.G., Muntean, J.L., Davis, D.A., and Hess, R.H., 2007, The Nevada mineral industry-2007: Nevada Bureau of Mines and Geology, v. Special Publication, p. 178.

Russell, R.H., 2004, Technical report for the North Mill Creek, Elder Creek and NAD exploration properties in Lander County, Nevada, USA: 43-101 Report.

Seedorff, E., Dilles, J., Proffett Jr, J., Einaudi, M., Zurcher, L., Stavast, W., Johnson, D., and Barton, M., 2005, Porphyry deposits: Characteristics and origin of hypogene features: Economic Geology, v. 100, p. 251–298

Sillitoe, R., and Bonham Jr, H., 1990, Sediment-hosted gold deposits: Distal products of magmatic-hydrothermal systems: Geology, v. 18, p. 157.

Sillitoe, R., and Hedenquist, J., 2003, Linkages between volcanotectonic settings, ore-fluid compositions, and epithermal precious metal deposits: SPECIAL PUBLICATION-SOCIETY OF ECONOMIC GEOLOGISTS, v. 10, p. 315-343.

Sinclair, A., and Tessari, O., 1981, Vein geochemistry, an exploration tool in Keno Hill camp, Yukon Territory, Canada: Journal of Geochemical exploration, v. 14, p. 1-24.

Stewart, J., McKee, E., and Stager, H., 1977, Geology and mineral deposits of Lander County: Nevada: Nevada Bureau of Mines and Geology Bulletin, v. 88, p. 06.

Teal, L., and Jackson, M., 2002, Geologic overview of the Carlin trend gold deposits: Gold deposits of the Carlin trend: Nevada Bureau of Mines and Geology Bulletin, v. 111, p. 204.

Theodore, T., Kotlyar, B., Singer, D., Berger, V., Abbott, E., and Foster, A., 2003, Applied Geochemistry, Geology, and Mineralogy of the Northernmost Carlin Trend, Nevada: Economic Geology, v. 98, p. 287.

Winterer, E., 1968, Tectonic Erosion in the Roberts Mountains, Nevada: The Journal of Geology, p. 347-357.

Yates, D., and Rosenberg, P., 1997, Formation and stability of endmember illite: II. Solid equilibration experiments at 100 to 250 C and Pv, soln: Geochimica et Cosmochimica Acta, v. 61, p. 3135-3144.

APPENDIX B– APATITE FISSION TRACK THERMOCHRONOLOGY DATA

Table. B1. Apatite fission track data from the Northern Carlin trend (Chakurian et al., 2003; Cline et al., 2005; Hickey et al., 2010). All ages and errors are reported in Ma.

East	North	# Grains	# Tracks	Dpar (um)	Age (Ma)	(-) 2σ	(+) 2σ	Mean Lm(um)	Lm SD(um)	Mean Lc(um)	Lc SD(um)	MeanDpar (um)	DparSE (um)	DparSD (um)	Dpar_SE (um)
555048	4540720	6	1	2.06	23.8	9.6	16.1	14.11		14.34	1.86	0.09	0.21	1.86	
559128	4539741	21	60	1.8	51.1	7.8	9	13.45	2.12	14.61	1.95	0.06	0.29	0.25	0.4
560198	4538825	6	9	2.39	32.4	8.8	12.2	13.38	1.71	14.34	3.13	0.28	0.7	1.04	1.37
561114	4537287	40	74	1.94	79.9	10.2	11.6	13.16	2.05	14.51	2.06	0.05	0.32	0.24	0.36
558312	4537259	27	40	1.85	76.5	13.1	15.8	13.38	1.55	14.53	1.91	0.06	0.3	0.3	0.33
558184	4536152	24	26	1.77	60.4	12.1	15.2	13.13	2.16	14.44	1.98	0.07	0.32	0.39	0.38
559697	4533592	14	18	1.92	38	8.4	10.8	13.64	1.66	14.79	2.1	0.1	0.38	0.5	0.44
557521	4533602	5	3	1.98	22.7	7.6	11.2	12.38	1.77	13.76	1.98	0.15	0.33	1.14	0.21
553111	4536180	40	135	1.92	45.8	7.4	8.9	13.27	2.59	14.58	2.35	0.05	0.31	0.2	0.28
552812	4535590	25	117	2.01	45.5	8.5	10.5	14.38	1.27	15.27	1.97	0.03	0.15	0.18	0.19
557070	4533008	12	102	2.31	91.6	11.4	13	13.72	2	14.78	2.24	0.04	0.15	0.22	0.2
476228	4561643	25	130	1.8	78.8	9.7	11.1	14.52	1.47	15.34	1.97	0.03	0.16	0.17	0.34
558335	4532802	11	34	2.74	14.3	2.9	3.8	15.03	1.48	15.71	2.84	0.15	0.48	0.49	0.39
558167	4532551	14	136	2.38	113	15	17.4	13.44	2.29	14.65	2.19	0.08	0.3	0.19	0.22
558074	4529287	37	200	2.01	56.1	6.1	6.8	13.39	2.64	14.68	2.1	0.03	0.19	0.15	0.21
557760	4528910	12	19	1.65	18.6	7.2	11.6	13.67	2.2	14.65	1.68	0.05	0.16	0.39	0.13
555037	4529041	22	28	1.84	32.5	6.1	7.4	14.15	1.44	15.18	1.95	0.04	0.19	0.37	0.38
557488	4528267	16	63	2.19	40.9	7.3	8.9	13.66	2.31	14.88	2.12	0.06	0.24	0.27	0.27
558079	4526758	5	14	1.68	36.7	9.8	13.3	13.03	2.24	14.28	1.75	0.05	0.12	0.47	0.16
559166	4528248	13	16	1.94	34.8	5.3	6.2	13.87	1.97	14.79	2.02	0.08	0.27	0.5	0.22
559492	4525044	25	13	1.69	58.8	10	12.1	12.52	2.82	13.99	1.53	0.05	0.24	0.42	0.06
557406	4526268	6	11	1.56	27.7	10.8	17.6	12.96	2.18	14.47	1.57	0.06	0.14	0.47	0.18

East	North	# Grains	# Tracks	Dpar (um)	Age (Ma)	(-) 2σ	(+) 2σ	Mean Lm(um)	Lm SD(um)	Mean Lc(um)	Lc SD (um)	MeanDpar (um)	DparSE (um)	DparSD (um)	Dpar_SE (um)
556429	4525786	7	1	1.59	16	8.1	16.4	9.07		12.5	1.29	0.05	0.13	1.29	
554103	4523739	29	19	1.62	28.1	8.1	11.4	14.2	1.2	15.18	1.71	0.03	0.17	0.39	0.11
556997	4524747	17	25	1.82	20.6	4.1	5.1	13.71	2.18	14.77	2	0.05	0.21	0.4	0.16
553576	4528871	16	83	2.21	33	5.3	6.3	14.78	1.12	15.51	2.25	0.06	0.24	0.25	0.2
552713	4530356	12	74	1.7	35.5	6.6	8.1	14.22	1.26	15.16	1.91	0.05	0.16	0.22	0.25
552058	4539373	24	134	2.11	53.7	6.8	7.7	13.23	2.28	14.41	2.19	0.04	0.17	0.19	0.21
552506	4537399	24	14	1.84	31.6	7.3	9.4	14.1	1.38	15.14	2.38	0.09	0.44	0.64	0.86
552363	4536299	40	192	2.56	41.3	4.6	5.1	14.93	1.45	15.61	2.64	0.04	0.24	0.19	0.45
551480	4538430	11	23	2.06	53.1	14.4	19.7	13.94	2.32	14.88	2.14	0.08	0.28	0.45	0.35
548708	4538750	28	47	1.75	38.4	8.6	11.2	14.15	1.55	15.13	1.86	0.05	0.29	0.27	0.29
551522	4537236	10	2	1.99	24.4	8.8	13.9	15.26	2.09	15.96	2.29	0.07	0.22	1.62	0.14
551377	4537158	25	163	1.97	43.2	5.3	6.1	14.35	1.59	15.24	2.16	0.03	0.13	0.17	0.42
555418	4533245	37	200	2.37	129	13.8	15.3	13.4	2.45	14.64	2.53	0.03	0.16	0.18	0.21
555418	4533245	25	202	2.29	119	12.8	14.4	13.29	2.53	14.49	2.28	0.03	0.13	0.16	0.17
555418	4533245	24	200	1.83	75.1	11.4	13.4	14.07	1.82	15.05	1.98	0.05	0.25	0.14	0.3
555418	4533245	33	200	1.83	69.7	9.6	11.2	13.92	1.52	14.99	1.97	0.02	0.13	0.14	0.15
552767	4535055	20	132	1.95	63.4	6.9	7.7	13.15	2.23	14.42	2.03	0.03	0.12	0.18	0.14
552789	4535070	23	135	2.07	59.8	6.6	7.4	12.75	2.29	14.21	2.02	0.04	0.18	0.17	0.23
558184	4536152	24	26	1.77	60.4	12.1	15.2	13.13	2.16	14.44	1.98	0.07	0.32	0.39	0.38
552942	4535192	24	133	2.09	60.4	7.2	8.1	13.11	2.23	14.38	2.13	0.04	0.19	0.18	0.18
553150	4535306	21	135	1.91	60.2	9.1	10.6	13.34	1.99	14.5	1.96	0.04	0.19	0.17	0.17
552794	4535585	26	198	2.13	70.4	10	11.5	12.81	2.42	14.28	2.07	0.03	0.16	0.15	0.26
552794	4535585	40	139	1.94	58.1	8.3	9.6	13.3	2.26	14.51	1.95	0.02	0.16	0.17	0.15
552794	4535585	38	200	1.93	58.1	6.7	7.6	13.14	2.13	14.45	2.03	0.02	0.12	0.14	0.14
552794	4535585	33	136	2.17	80.4	10.7	12.3	13.09	2.32	14.46	2.08	0.03	0.2	0.18	0.24
552794	4535585	39	196	2.12	56.3	6.6	7.4	12.59	2.07	14.03	2.24	0.02	0.14	0.16	0.18

Table. B2. Pooled apatite fission track ages for the Shoshone Range area, * denotes absence of asymmetric ages, symmetric ages shown

East	North	# Grains	# Tracks	Dpar (um)	Age (Ma)	(-) 2σ	(+) 2σ	Mean Lm(um)	Lm SD(um)	Mean Lc(um)	Lc SD(um)	MeanDpar(um)	DparSE(um)	DparSD(um)	Dpar_SE (um)	Dpar_SD (um)
493088	4501907	40	210	1.83	36	3.4	3.7	14.58	1.56	15.4	1	1.86	0.13	0.23	0.02	0.15
493240	4493545	40	155	1.63	42.5	5.4	6.1	14.36	1.68	15.27	1.07	1.69	0.14	0.18	0.03	0.18
493399	4497239	40	201	1.68	37.6	3.6	4	14.12	1.32	15.05	0.9	1.71	0.12	0.16	0.02	0.15
498741	4438208	35	12	1.62	13.6	2.6	3.2	12.23	2.61	13.67	2.13	1.82	0.53	0.16	0.03	0.17
499938	4462388	12	28	1.93	108.2	15.8	18.6	12.97	1.99	14.35	1.22	1.91	0.36	0.27	0.07	0.23
500648	4409038	40	92	1.6	8.9	1.6	1.9	14.96	1.25	15.62	0.85	1.87	0.19	0.57	0.02	0.15
503237	4461618	27	54	1.67	55.1	9.8	11.9	13.58	2.21	14.67	1.44	1.63	0.22	0.13	0.03	0.18
504789	4473185	23	53	2.4	16.5	3.8	4.9	13.85	2.29	14.78	1.58	2.57	0.35	0.33	0.07	0.35
504888	4457292	21	23	1.76	32.7	6.1	7.5	14.57	1.07	15.27	0.77	1.97	0.41	0.34	0.09	0.43
505537	4465781	24	35	2	45.7	7.4	8.9	14.02	1.54	14.97	0.99	2.13	0.36	0.39	0.06	0.31
505662	4466508	20	4	1.76	15.1	7	13.2	12.74	4.98	14.88	1.99	1.82	0.91	0.35	0.05	0.2
506133	4471855	28	11	1.74	12.9	3.6	5	13.21	1.91	14.39	1.15	1.78	0.54	0.14	0.05	0.27
506757	4414389	29	91	2.73	84.2	11.3	13.1	13.9	1.57	14.9	1.07	2.94	0.31	0.84	0.19	1.03
508155	4465581	23	-	1.57	18.2	4.0*	-	-	-	-	-	-	-	-	-	-
508167	4471393	32	19	1.7	17.2	4.2	5.6	12.72	1.94	14.17	1.23	1.81	0.42	0.29	0.03	0.19
508294	4461372	38	100	1.84	64.7	8.1	9.2	12.43	2.5	13.93	1.57	1.91	0.19	0.19	0.04	0.25
508588	4461155	-	-	-	77.4		-	-	-	-	-	-	-	-	-	-
509501	4460863	-	-	-	27.4		-	-	-	-	-	-	-	-	-	-
509691	4513620	38	130	1.77	33	4.3	4.9	13.88	1.67	14.94	1.03	1.94	0.17	0.36	0.03	0.19
509974	4471329	18	21	1.74	13.9	4.1	5.7	13.16	1.56	14.58	0.93	1.86	0.41	0.2	0.07	0.28
510975	4460491	16	18	1.73	39.5	7.1	8.6	14.22	2.14	15.18	1.37	1.77	0.42	0.15	0.05	0.18
511183	4476760	33	9	1.83	16.6	3.8	4.9	13.92	1.42	14.96	0.79	1.78	0.59	0.26	0.06	0.32
511695	4466671	20	22	1.71	28.9	4.9	5.9	13.23	2.44	14.46	1.36	1.81	0.39	0.18	0.05	0.23
512055	4475222	31	48	1.67	13.7	2.6	3.2	13.41	1.87	14.52	1.28	1.82	0.26	0.23	0.04	0.24
512602	4464254	15	14	1.79	35.7	8.6	11.3	14.42	1.83	15.23	1.27	1.75	0.47	0.22	0.07	0.28
512634	4461137	40	199	1.63	28.9	2.2*	-	-	-	-	-	-	-	-	-	-

East	North	# Grains	# Tracks	Dpar (um)	Age (Ma)	(-) 2σ	(+) 2σ	Mean Lm(um)	Lm SD(um)	Mean Lc(um)	Lc SD(um)	MeanDpar(um)	DparSE(um)	DparSD(um)	Dpar_SE (um)	Dpar_SD (um)
512750	4461028	33	171	1.61	31.3	2.6*	-	-	-	-	-	-	-	-	-	-
512977	4461269	24	26	1.99	35	4.6	5.3	13.68	1.61	14.57	1.16	1.85	0.36	0.21	0.12	0.58
514197	4460178	23	38	2.02	34.8	5.5	6.5	13.59	2.01	14.68	1.3	1.86	0.3	0.19	0.1	0.49
514403	4473950	28	18	1.69	29.8	3.9	4.6	13.2	1.93	14.33	1.43	1.72	0.41	0.17	0.05	0.24
514895	4464693	16	24	1.72	23.1	7.6	11.4	13.22	2.56	14.56	1.39	1.86	0.38	0.22	0.06	0.25
515617	4481696	28	8	1.74	9.2	3.1	4.7	12.22	2.45	14.08	0.99	1.68	0.59	0.21	0.05	0.27
516019	4478794	28	51	1.96	27	4.4	5.2	13.76	1.47	14.8	1.01	2.02	0.28	0.3	0.06	0.3
516566	4468846	24	13	1.69	28.6	4.6	5.6	14.02	1.55	14.97	1.01	1.74	0.48	0.16	0.04	0.2
516990	4460609	40	61	1.85	38.6	4.3	4.8	14.52	1.06	15.28	0.75	2.09	0.27	0.21	0.04	0.24
518283	4477234	30	38	1.79	33.8	5.6	6.8	12.66	2.14	14.18	1.21	1.87	0.3	0.18	0.04	0.22
519194	4451324	25	105	1.88	33.6	9	12.3	14.89	0.9	15.59	0.6	2.07	0.2	0.18	0.05	0.25
519408	4457072	19	33	1.78	51.1	8.2	9.7	13.77	1.48	14.8	1.01	1.85	0.32	0.11	0.05	0.24
519945	4456913	24	23	1.69	48	7.5	8.9	14.08	1.23	15.11	0.79	1.96	0.41	0.22	0.05	0.25
520029	4459464	17	22	1.79	37.9	8	10.3	12.98	2.21	14.41	1.16	1.92	0.41	0.22	0.12	0.49
520192	4468590	25	34	1.83	43.7	5.5	6.2	13.72	1.59	14.83	1.03	1.8	0.31	0.18	0.04	0.18
520529	4469759	24	131	2.08	33.4	4.4	5.1	14.45	1.69	15.29	1.12	2.24	0.2	0.15	0.03	0.15
520900	4456419	13	12	1.71	25	5.4	6.8	13.64	1.23	14.81	0.66	1.78	0.51	0.2	0.05	0.19
521187	4455472	25	157	1.69	36.8	5.2	6.2	14.14	1.33	15.08	0.89	1.77	0.14	0.25	0.02	0.12
521205	4461734	19	22	1.97	33.9	5.7	6.9	14.78	1.08	15.52	0.78	2.17	0.46	0.22	0.06	0.25
521232	4454441	35	117	1.79	66.9	7.6	8.6	12.71	2.42	14.1	1.52	1.97	0.18	0.24	0.03	0.21
521451	4481657	15	30	1.96	38	6.1	7.1	13.98	1.82	15	1.18	1.93	0.35	0.25	0.05	0.2
521535	4455966	30	26	1.69	33.5	8.4	11.3	14.69	1.65	15.46	0.97	1.62	0.32	0.16	0.03	0.16
521535	4455966	33	31	1.6	49.7	12	15.8	13.95	1.87	14.83	1.34	1.56	0.28	0.17	0.03	0.17
521543	4456127				34.8											
522454	4462891	26	36	1.85	41.3	6	7.1	14.46	1.04	15.36	0.71	2.02	0.34	0.17	0.04	0.2
522635	4456190	9	14	1.68	39.1	8.4	10.8	14.17	1.38	15.02	0.96	1.86	0.5	0.18	0.12	0.37
522821	4467016	15	14	1.71	24.5	4.8	6	14.16	1.41	15.19	0.86	1.77	0.47	0.17	0.05	0.21
522996	4455574	12	4	1.8	22.7	8.1	12.6	14.88	1.6	15.7	1.04	2.06	1.03	0.59	0.09	0.31

East	North	Grains	# Tracks	Dpar (um)	Age (Ma)	(-) 2σ	(+) 2σ	Mean Lm(um)	Lm SD(um)	Mean Lc(um)	Lc SD(um)	MeanDpar(um)	DparSE(um)	DparSD(um)	Dpar_SE (um)	Dpar_SD (um)
523014	4458204	29	42	1.8	42.5	6.4	7.6	14.19	1.4	15.12	0.91	1.9	0.29	0.28	0.08	0.45
523187	4454258	8	6	1.78	25.7	8.4	12.5	13.51	1.56	14.64	0.99	1.66	0.68	0.22	0.07	0.19
523841	4455858	18	10	1.91	27.4	5.7	7.1	14.16	1.8	15.07	1.25	2.1	0.66	0.68	0.1	0.42
523872	4455651	15	8	1.9	20.8	5.4	7.3	12.96	3.97	14.54	1.85	1.8	0.64	0.21	0.12	0.45
523934	4455152	28	50	1.93	45	7.2	8.6	13.21	1.59	14.46	1.25	1.99	0.28	0.25	0.05	0.29
524212	4475592	29	96	2	37.3	6.2	7.4	13.86	1.8	14.83	1.24	1.8	0.18	0.14	0.08	0.45
524282	4466538	22	25	1.84	33.8	5.9	7.3	14.19	1.23	15.04	0.81	1.8	0.36	0.23	0.08	0.38
524336	4456245	35	49	1.65	35.6	7.3	9.1	13.83	1.47	14.81	1.01	1.72	0.25	0.19	0.06	0.38
524477	4454981	38	67	2.2	19.8	3.8	4.6	13.11	2.34	14.5	1.31	2.26	0.28	0.46	0.11	0.67
524518	4454411	18	49	1.93	37.7	6	7.2	14.64	1.91	15.49	1.17	2.01	0.29	0.24	0.07	0.29
524555	4455727	26	27	1.87	42.5	6.6	7.8	14.12	1.8	15.17	0.94	1.84	0.35	0.29	0.07	0.35
524877	4454151	27	38	1.92	29	5.3	6.4	13.65	1.82	14.67	1.29	1.98	0.32	0.3	0.08	0.42
525153	4453997	20	54	2.06	41.2	8.3	10.5	13.61	1.39	14.63	0.98	1.93	0.26	0.29	0.07	0.31
525367	4433446	24	34	1.82	37.5	8.1	10.2	13.79	1.77	14.83	1.12	1.68	0.29	0.16	0.1	0.5
526536	4452839	12	25	1.76	65.4	10.2	12	13.08	1.84	14.5	1.14	1.85	0.37	0.33	0.08	0.28
526651	4436509	35	68	1.87	43.3	5.7	6.5	14.02	1.89	15.04	1.14	2.04	0.25	0.33	0.05	0.29
526721	4471144	18	30	1.9	36.1	8	10.4	13.36	2.25	14.57	1.46	1.86	0.34	0.27	0.15	0.63
526776	4465413	14	21	1.77	39.7	5.7	6.6	13.92	2.39	15.11	1.07	1.87	0.41	0.23	0.05	0.2
526805	4462487	24	125	1.85	45.1	7.4	8.7	14.91	1.05	15.62	0.75	2.02	0.18	0.18	0.02	0.09
527005	4441549	34	147	1.8	44.6	5.9	6.8	12.27	2.33	13.83	1.46	2.1	0.17	0.29	0.02	0.13
532289	4449090	12	64	1.86	30.7	8.6	11.9	13.13	2.11	14.43	1.37	2	0.25	0.23	0.08	0.27
532292	4449041	27	101	1.96	44.4	7.9	9.5	13.45	2	14.63	1.26	2.06	0.21	0.23	0.04	0.22
532408	4448971	24	36	1.87	27.5	5.8	7.4	13.33	1.81	14.52	1.19	2.13	0.35	0.45	0.07	0.32

APPENDIX C – SAMPLE INFORMATION

Table C1. Sample data

Sample ID	Easting	Northing	XRD	Terraspec	Microprobe	Colour	Lithology	Clay content
PP1	524528	4454902	o	o	o	Medium grey	Silty limestone	1-10%
1	516229	4460135		o		Orange	Sandy siltstone	1-10%
2	516225	4460153		o		Translucent	Vein	<1%
3	516227	4460140		o		Orange	Sandy siltstone	1-10%
4	515886	4460158		o		Medium grey	Sandstone	1-10%
5	515879	4460174		o		Medium grey	Sandstone	1-10%
6	515879	4460174		o		Translucent	Vein	<1%
7	515740	4460116		o		Medium grey	Argillite	1-10%
8	512737	4461065	o	o	o	Light grey	Quartzite	<1%
9	512634	4461137		o		Light grey	Quartzite	<1%
10	512634	4461137	o	o		Medium orange brown	Conglomerate	1-10%
11	512634	4461137		o		Beige + dark grey	Mudstone	1-10%
12	512750	4461028		o		Light orange brown	Siltstone	1-10%
13a	512750	4461028	o	o		Dark grey	Siltstone	1-10%
13b	512750	4461028		o		Dark grey	Siltstone	1-10%
13c	512750	4461028		o		Dark grey	Quartzite	<1%
14	524188	4469903	o	o	o	Light beige	Dyke	Dyke
15	516654	4460003		o		Light grey	Quartz arenite	<1%
16	516658	4459982		o		Light grey	Quartzite	<1%
17	516669	4459988		o		Medium grey	Breccia	1-10%
18	516682	4459989		o		Light grey	Quartzite	<1%
19	516615	4459657		o		Light grey	Siltstone	1-10%
20	516710	4459572		o		Light grey	Chert	<1%
21a	516733	4459519		o		Medium grey	Breccia	1-10%
21b	516733	4459519		o		Dark grey	Chert	<1%
21c	516733	4459519		o		Light grey	Silstone	1-10%
22	516795	4459482		o		Translucent	Quartz vein	<1%
23	510480	4460155		o		Medium beige	Sandstone	1-10%
24	515597	4460030		o		Medium grey	Siltstone	1-10%
25	515376	4460778		o		Dark grey	Chert	<1%
26	515409	4460748		o		Medium grey	Sandstone	1-10%
27	515464	4460772		o		Dark grey	Chert	<1%
28	514995	4461220		o		Dark grey	Chert	<1%
29	515212	4461343		o		Medium grey	Sandstone	1-10%
30	515133	4460767		o		Light grey	Siltstone	1-10%
31	515221	4460772		o		Light grey	Quartz arenite	<1%
32	515144	4459984		o		Medium grey	Conglomerate	1-10%
33	515043	4459875		o		Medium grey	Conglomerate	1-10%
34	514384	4461726		o		Dark grey	Chert	<1%
35	514375	4461765		o		Light grey	Chert	<1%
36	514375	4461765		o		Dark grey	Siltstone	1-10%
37	514075	4462080		o		Medium to dark grey	Chert	<1%
38	514054	4462090		o		Light to medium grey	Chert	<1%
39	514019	4462100		o		Dark grey	Siltstone	1-10%
40	513967	4462053		o		Light grey	Quartzite	<1%
41	513888	4462027		o		Dark grey	Silt	Silt
42a	509726	4467952		o		Medium grey	Sandstone	1-10%
42b	509726	4467952		o		Medium grey	Sandstone	1-10%
43	*509726	*4467952		o		Translucent	Quartz vein	<1%
44	*509726	*4467952		o		Translucent	Sandstone	1-10%
45	*509726	*4467952		o		Medium grey	Sandstone	1-10%
46a	508830	4466178		o		Black	Carbonate vein	<1%
46b	508830	4466178		o		Medium grey	Sandstone	1-10%
47	508830	4466178		o		Dark grey	Siltstone	1-10%
48	508490	4466219		o		Light grey	Chert	<1%
49a	508389	4466289		o		Medium grey	Quartzite	<1%
49b	508389	4466289		o		Medium grey	Quartzite	<1%
50	508531	4466201		o		Medium grey	Sandstone	1-10%

Sample ID	Easting	Northing	XRD	Terraspec	Microprobe	Colour	Lithology	Clay content
51b	509380	4461021		o		Dark grey	Chert	<1%
52	509362	4461022		o		Dark grey	Chert	<1%
53	509366	4461011		o		Dark grey	Chert	<1%
54	509501	4460863		o		Light grey	Quartzite	<1%
55	509440	4460835	o	o		Dark grey	Chert	<1%
56	509731	4460714		o		Dark grey	Chert	<1%
57	509990	4460430		o		Light grey	Quartzite	<1%
58	510084	4460366		o		Medium grey	Mudstone	1-10%
59	510084	4460366		o		Medium grey	Quartzite	<1%
60	510476	4460172		o		Medium grye	Quartzite	<1%
61	510572	4460114		o		Light grey	Quartzite	<1%
62	510617	4460216	o	o		Light grey	Quartzite	<1%
63	510845	4460388	o	o		Light grey	Quartzite	<1%
64	511374	4460870	o	o		Light grey	Mudstone	1-10%
65	511995	4461080		o		Light grey	Quartzite	<1%
66	511917	4461075		o		Medium grey	Chert	<1%
67	512678	4461122	o	o		Dark grey	Siltstone	1-10%
68	512663	4461108	o	o		Medium grey	Siltstone	1-10%
69	512663	4461108		o		Medium grey	Sandstone	1-10%
70	512658	4461112		o		Dark grey	Silstone	1-10%
71	512652	4461115		o		Medium grey	Sandstone	1-10%
72	512639	4461124	o	o		Medium grey	Silstone	1-10%
73	512636	4461128		o		Dark grey	Siltstone	1-10%
74	512624	4461135	o	o		Medium grey	Stilstone	1-10%
75	512620	4461144		o		Medium grey	Siltstone	1-10%
76	512621	4461153	o	o			Sandstone	1-10%
77	512624	4461161		o		Medium grey	Siltstone	1-10%
78	512637	4461181	o	o		Medium grey	Siltstone	1-10%
79	512624	4461161		o		Orange	Clay	Clay
80	512677	4461187	o	o		Light beige	Quartzite	<1%
81	512128	4461114		o		Light beige	Quartzite	<1%
82	512193	4461068	o	o		Light grey	Breccia	
83	512193	4461068	o	o		Medium grey	Silstone	1-10%
84	512191	4461062	o	o		Dark grey	Siltstone	1-10%
85	512243	4461096		o		Medium grey	Quartzite	<1%
86	512281	4461084	o	o		Medium grey	Sandstone	1-10%
87	512316	4461057		o		Light grey	Quartzite	<1%
88	512403	4460896		o		Light grey	Siltstone	1-10%
89	512345	4460851	o	o		Medium grey	Quartzite	<1%
90	512305	4460808		o		Medium grey	Quartzite	<1%
91	512256	4460745		o		Medium grey	Quartzite	<1%
92	512328	4460780		o		Medium grey	Quartzite	<1%
93	512385	4460794		o		Light grey	Sandstone	1-10%
94	512452	4460818		o		Medium grey	Siltstone	1-10%
95	512549	4460831		o		Light grey	Quartzite	<1%
96	512663	4460873		o		Light grey	Quartzite	<1%
97	512651	4460692	o	o	o	Light grey	Sandstone	1-10%
98	512651	4460692		o		Light grey	Quartzite	<1%
99	512651	4460692	o	o		Light grey	Siltstone	1-10%
100	512096	4460714		o		Dark grey	Siltstone	1-10%
101	512149	4460636		o		Dark grey	Chert	<1%
102	509157	4461046		o		Dark grey	Chert	<1%
103	509067	4461046	o	o		Dark grey	Chert	<1%
104	508963	4461097		o		Dark grey	Siltstone	1-10%
105	508898	4461187		o		Dark grey	Chert	<1%
106	508953	4461227		o		Dark grey	Chert	<1%
107	508588	4461155		o		Light grey	Quartzite	<1%
108	509298	4461415		o		Light grey	Quartzite	<1%
109	509472	4461702		o		Light grey	Quartzite	<1%
110	509541	4461846		o		Dark grey	Chert	<1%
111	509646	4461941		o		Dark grey	Chert	<1%
112	509787	4462073		o		Light grey	Quartzite	<1%
113	509691	4462139		o		Medium grey	Sandstone	1-10%
114	509651	4462220		o		Meidum grey	Quartzite	<1%
115	509515	4462197		o		Medium grey	Chert	<1%

Sample ID	Easting	Northing	XRD	Terraspec	Microprobe	Colour	Lithology	Clay content
116	509389	4462243		o		Medium grey	Quartzite	<1%
117	509256	4461874		o		Dark grey	Chert	<1%
118	508999	4461629		o		Medium grey	Quartzite	<1%
119	522885	4456429		o		Medium grey	Limestone	<1%
120	522826	4456338		o		Medium grey	Limestone	<1%
121	522642	4456260		o		Medium grey	Limestone	<1%
122	521924	4456532		o		Light grey	Quartzite	<1%
123	521508	4456297	o	o		Light grey	Siltstone	1-10%
124	521196	?		o		Dark grey	Siltstone	1-10%
125	521096	4456264		o		Translucent	Quartz vein	<1%
126	520957	4456208		o		Light grey	Chert	<1%
127	521156	4456585		o		Medium grey	Chert	<1%
128	520695	4457267		o		Dark grey	Siltstone	1-10%
129	520551	4457465		o		Light grey	Quartzite	<1%
130	520941	4457547		o		Medium grey	Lamprophyre	1-10%
131	521335	4457617		o		Medium grey	Chert	<1%
132	521643	4457704		o		Black	Chert	<1%
133	520199	4456914		o		Light grey	Chert	<1%
134	519899	4456795	o	o		Light grey	Chert	<1%
135	519379	4456665		o		Light grey	Chert	<1%
136	519261	4456552		o		Light grey	Chert	<1%
137	518664	4457020		o		Light grey	Chert	<1%
138	519458	4456994		o		Light grey	Chert	<1%
138b	519540	4457241		o		Translucent	Quartz vein	<1%
139	519558	4457373		o		Medium grey	Chert	<1%
140	519830	4457586		o		Medium grey	Chert	<1%
141	520192	4457991		o		Medium grey	Chert	<1%
142	521132	4458223		o		Medium grey	Chert	<1%
143	518541	4457561		o		Light grey	Quartzite	<1%
144	518298	4457363		o		Light grey	Quartzite	<1%
145	517944	4457217		o		Light grey	Quartzite	<1%
146	518029	4456868		o		Light grey	Quartzite	<1%
147	517689	4457189		o		Light grey	Quartzite	<1%
148	517592	4457616		o		Light grey	Quartzite	<1%
149	517566	4457861		o		Light grey	Quartzite	<1%
150	517731	4458308		o		Light grey	Quartzite	<1%
151	518433	4458229		o		Light grey	Quartzite	<1%
152	518562	4457943		o		Light grey	Quartzite	<1%
153	518596	4457815		o		Light grey	Siltstone	1-10%
154	518884	4457931		o		Light grey	Quartzite	<1%
155	519055	4457926		o		Light grey	Quartzite	<1%
156	519549	4457619		o		Medium grey	Chert	<1%
157	519836	4457569		o		Medium grey	Chert	<1%
158	520712	4458395		o		Medium grey	Chert	<1%
159	522040	4457784		o		Light grey	Quartzite	<1%
160	523100	4457873		o		Medium grey	Limestone	<1%
161	517627	4459565		o		Light grey	Quartzite	<1%
162	517432	4459362		o		Light grey	Quartzite	<1%
163	517228	4459369		o		Light grey	Quartzite	<1%
164	517083	4459602		o		Light grey	Quartzite	<1%
165	516767	4458988		o		Light grey	Quartzite	<1%
166	517045	4458843		o		Light grey	Quartzite	<1%
167	517281	4458745		o		Light grey	Quartzite	<1%
168	517175	4458290		o		Light grey	Quartzite	<1%
169	517395	4458266		o		Light grey	Quartzite	<1%
170	518430	4458462		o		Light grey	Quartzite	<1%
171	518519	4458697		o		Light grey	Quartzite	<1%
172	518625	4459138		o		Medium grey	Chert	<1%
173	519175	4459029		o		Medium grey	Chert	<1%
174	514113	4461668		o		Dark grey	Chert	<1%
175	513992	4461707		o		Dark grey	Chert	<1%
176	513948	4461487		o		Dark grey	Chert	<1%
177	513511	4461871		o		Light grey	Quartzite	<1%
178	513477	4461911		o		Dark grey	Chert	<1%
179	513544	4462083		o		Dark grey	Chert	<1%

Sample ID	Easting	Northing	XRD	Terraspec	Microprobe	Colour	Lithology	Clay content
180	513527	4462167		o		Dark grey	Chert	<1%
181	513602	4462283		o		Medium grey	Chert	<1%
182	513869	4462144		o		Dark grey	Chert	<1%
183	513869	4462141		o		Medium grey	Siltstone	1-10%
184	514685	4461370		o		Dark grey	Siltstone	1-10%
203	509701	4461051		o		Light grey	Quartzite	<1%
204	509863	4461018		o		Light grey	Quartzite	<1%
205	510048	4461070		o		Light grey	Quartzite	<1%
206	510054	4461055		o		Medium grey	Chert	<1%
207	509966	4460970		o		Medium grey	Quartzite	<1%
208	511980	4461327		o		Dark grey	Siltstone	1-10%
209	511951	4461453		o		Medium green	Chert	<1%
210	511957	4461629		o		Medium grey	Mudstone	1-10%
211	512018	4461652		o		Medium grey	Limestone	<1%
212	512202	4461886		o		Medium grey	Siltstone	1-10%
213	512206	4462142		o		Medium green	Chert	<1%
214	512159	4462279		o		Light grey	Quartzite	<1%
215	512185	4462435		o		Light grey	Quartzite	<1%
216	512423	4462765		o		Medium grey	Chert	<1%
217	512669	4462849		o		Light grey	Argillite	1-10%
218	512779	4462802		o		Dark grey	Argillite	1-10%
219	512887	4462210		o		Dark grey	Chert	<1%
220	512066	4461139		o		Light grey	Quartzite	<1%
221	511964	4461151		o		Dark grey	Mudstone	1-10%
222	511862	4461220		o		Medium grey	Siltstone	1-10%
223	511803	4461281		o		Medium grey	Siltstone	1-10%
224	511707	4461339		o		Dark grey	Siltstone	1-10%
225	511559	4461345		o		Medium grey	Quartzite breccia	<1%
226	511559	4461345		o		Medium grey	Quartzite	<1%
227	511328	4461184		o		Medium grey	Quartzite	<1%
228	511286	4461125		o		Dark grey	Siltstone	1-10%
229	511286	4461125		o		Medium grey	Chert	<1%
230	511176	4461079	o	o		Medium grey	Quartzite breccia	<1%
231	504072	4469411		o		Dark grey	Siltstone	1-10%
232	504076	4469315		o		Light grey	Limestone	<1%
233	504019	4469240		o		Medium grey	Limestone	<1%
234	504071	4469153		o		Light grey	Quartzite	<1%
235	504165	4469022		o		White	Quartzite	<1%
236	504180	4469003		o		Medium grey	Limestone	<1%
237	504300	4468770		o		Medium grey	Limestone	<1%
238	504355	4468775		o		White	Quartzite	<1%
239	504245	4468706		o		White	Limestone	<1%
240	505295	4468520		o		White	Quartzite	<1%
241	504085	4468553		o		Light grey	Dirty sandstone	1-10%
242	507660	4464047		o		Light grey	Quartzite	<1%
243	507846	4464378		o		Light grey	Quartzite	<1%
244	507736	4464577		o		Dark grey	Siltstone	1-10%
245	507756	4464821		o		Dark grey	Silty limestone	1-10%
246	507922	4464944		o		Medium grey	Silty limestone	1-10%
247	507976	4465139		o		Medium grey	Siltstone	1-10%
248	507939	4465256		o		Dark grey	Siltstone	1-10%
249	507992	4465449		o		Dark grey	Limestone	<1%
250	508073	4465593		o		Dark grey	Mudstone	1-10%
251	508155	4465581		o		Light grey	Quartzite	<1%
252	507955	4463783		o		Medium grey	Chert	<1%
253	508072	4463780		o		Light grey	Quartzite	<1%
254	508841	4463804		o		Light grey	Calcareous sandstone	1-10%
255	509251	4463648		o		Light brown	Sandstone	1-10%
256	509527	4463849		o		Light grey	Quartzite	<1%
257	509127	4463429		o		Light grey	Quartzite	<1%
258	509100	4463159		o		Reddish-brown	Quartzite	<1%
259	508741	4463139		o		Light grey	Quartzite	<1%
260	508286	4462930	o	o		Medium grey	Chert	<1%
261	522009	4455410		o		Dark grey	Siltstone	1-10%
262	521991	4455426		o		Dark grey	Siltstone	1-10%

Sample ID	Easting	Northing	XRD	Terraspec	Microprobe	Colour	Lithology	Clay content
263	521974	4455451		o		Medium grey	Sandstone	1-10%
264	521962	4455430	o	o		Dark grey	Calcareous chert	<1%
265	521898	4455478		o		Light grey	Calcareous chert	<1%
266	521906	4455568		o		Dark grey	Silty limestone	1-10%
267	521852	4456111		o		Dark grey	Silty limestone	1-10%
268	521902	4456108	o	o		Light grey	Silty limestone	1-10%
269	521969	4456101		o		Cream	Silty limestone	1-10%
270	522044	4456119		o		Medium grey	Silty limestone	1-10%
271	521991	4455979		o		Dark grey	Silty limestone	1-10%
272	521977	4455929		o		Cream	Silty limestone	1-10%
273	521702	4456173		o		Medium grey	Silty limestone	1-10%
274	521564	4456166	o	o		Light grey	Silty claystone	1-10%
275	521558	4456151		o		Cream	Chert	<1%
276	521543	4456127		o		Light grey	Siltstone	1-10%
277	521526	4456056		o		Light grey	Siltstone	1-10%
278	521724	4456114		o		Light grey	Limestone	<1%
279	521746	4455933		o		Beige	Silty limestone	1-10%
280	521734	4455885	o	o		Black	silty limestone	1-10%
281	521636	4455996		o		Black	Silty limestone	1-10%
282	521695	4456054		o		Dark grey	Silty limestone	1-10%
283	521788	4455919		o		Light grey	Silty limestone	1-10%
284	521815	4455909	o	o		Dark grey	Clay	Clay
285	521896	4455843	o	o		Light grey	Siltstone	1-10%
286	521856	4455832		o		Medium grey	Silty limestone	1-10%
287	521735	4456242		o		Medium grey	Limestone	<1%
288	521676	4456256		o		Medium grey	Siltstone	1-10%
289	521612	4456263		o		Dark grey	Siltstone	1-10%
290	521582	4456217		o		Medium grey	Chert	<1%
291	522243	4455823		o		Medium grey	Silty limestone	1-10%
292	522202	4455626	o	o		Light grey	Siltstone	<50%
293	521906	4455616		o		Beige	Calcareous siltstone	1-10%
294	521856	4455582		o		Light grey	Silty limestone	1-10%
295	521830	4455648		o		Light grey	Chert	<1%
296	522161	4455432		o		Light grey	Marble	<1%
297	522174	4455407		o		Light grey	Marble	<1%
298	522213	4455381		o		Dark grey	Silstone	1-10%
299	522112	4455347		o		Dark grey	Silty limestone	1-10%
300	522112	4455347		o		Light grey	Silty limestone	1-10%
301	522114	4455394		o		Light grey	Silty limestone	1-10%
302	524456	4455183		o		Beige	Silty limestone	1-10%
302b	524456	4455183		o		Bige	Silty limestone	1-10%
303	524456	4455183	o	o		Beige	Silty limestone	1-10%
304	524447	4455123		o		Dark grey	Silty limestone	1-10%
305	524422	4454908		o		Medium grey	Silty limestone	1-10%
306	523819	4454956		o		Light grey	Silty limestone	1-10%
307	524012	445928	o	o		Light grey	Siltstone	1-10%
308	522112	4455262		o		Medium grey	Silty limestone	1-10%
309	522170	4455204		o		Light grey	Marble	<1%
310	522408	4455386		o		Medium grey	Greenstone	1-10%
311	521935	4455421		o		Orange-brown	Quartz monzonite	10-50%
312	521893	4455453		o		Beige	Chert	<1%
313	521792	4455584		o		Medium grey	Siltstone	1-10%
314	522099	4455454		o		Light grey	Siltstone	1-10%
315	522244	4455790		o		Medium grey	Silty limestone	1-10%
316	507878	4466950		o		Medium grey	Limestone	<1%
400	512590	4461052	o	o		Dark grey	Siltstone	1-10%
401	512527	4461102	o	o		Medium grey	siltstone	1-10%
402	512527	4461096		o		Medium grey	quartzite	<1%
403	512533	4461082		o		Medium grey	quartzite	<1%
404	512528	4461083	o	o		Medium grey	siltstone	1-10%
405	512530	4461063		o		Medium grey	quartzite	<1%
406	512528	4461059	o	o		Cream	dyke	dyke
407	512525	4461049		o		Cream	undifferentiated dyke	10-50%
408	512529	4461043	o	o		Medium grey	siltstone	1-10%
409	512528	4461035		o		Medium grey	quartzite	<1%

Sample ID	Easting	Northing	XRD	Terraspec	Microprobe	Colour	Lithology	Clay content
410	512571	4461030		o		Medium grey	quartzite	<1%
411	512593	4461049		o		Medium grey	quartzite	<1%
412	512573	4461033		o		Medium grey	siltstone	1-10%
413	512576	4461041	o	o		Medium grey	siltstone	1-10%
414	512578	4461050		o		Medium grey	siltstone	1-10%
415	512561	4461018		o		Medium grey	silstone	1-10%
416	512576	4461041		o		Medium grey	Quartzite breccia	<1%
420b	512576	4461041		o		Reddish-brown	Quartzite Breccia	<1%
420	512576	4461041		o		Reddish-brown	Quartzite	<1%
421	512576	4461041		o		Reddish-brown	Quartzite	<1%
422	512576	4461041		o		Medium grey	Quartzite	<1%
423	512576	4461041		o		Light grey	Mudstone	1-10%
424	512576	4461041		o		Medium grey	Quartzite	<1%
425	512576	4461041		o		Medium grey	Quartzite	<1%
426	512576	4461041		o		Light grey	Mudstone	1-10%
427	512576	4461041		o		Meidum grey	Quartzite	<1%
428	512576	4461041		o		Medium grey	Quartzite	<1%
429	512576	4461041		o		Light grey	Mudstone	1-10%
430	512576	4461041		o		Medium grey	Quartzite	<1%
431	512576	4461041		o		Light grey	Sandy siltstone	1-10%
432	512576	4461041	o	o		Light grey	Mudstone	1-10%
433	512576	4461041		o		Dark grey	Siltstone	1-10%
434	512576	4461041		o		Light grey	Quartzite breccia	<1%
436	512576	4461041		o		Dark grey	Quartzite	<1%
437	512576	4461041	o	o		Light grey	Quartzite	<1%
438	512576	4461041		o		Light grey	Quartzite	<1%
444	512576	4461041	o	o		Light grey	Cataclasite	>50%
445	512576	4461041		o		Dark grey	Siltstone	1-10%
446	512576	4461041		o		Dark grey	Siltstone	1-10%
447	512576	4461041		o		Medium grey	SIltstone	1-10%
448	512576	4461041		o		Medium grey	Siltstone	1-10%
449	512576	4461041		o		Medium grey	Quartzite	<1%
450	512576	4461041		o		Light grey	Argillite	1-10%
451	512576	4461041		o		Dark grey	Argillite	1-10%
452	512576	4461041		o		Dark grey	Argillite	1-10%
453	512630	4461188		o		Light grey	Siltstone	1-10%
454	512650	4461190		o		Medium grey	Quartzite	<1%
454b	512775	4461094		o		Reddish-brown	Cataclasite	>50%
455	512777	4461092		o		Reddish-brown	Fault breccia	Fault
456	512777	4461092		o		Reddish-brown	Fault breccia	Fault
470	558572	4529983		o		Beige	Siltstone	1-10%
471	558575	4529978		o		Beige	Siltstone	1-10%
472	558582	4529976	o	o		Light grey	Feldspar porphyry	10-50%
473	558585	4529980	o	o		Light grey	Chert	<1%
473a	558595	4529963	o	o		Light grey	Clay seam	>50%
473b	558614	4529960		o		Dark grey	Silstone	1-10%
474	558533	4530263		o		Light grey	Chert	<1%
475	558785	4530341		o		Reddish-brown	Chert	<1%
476	558396	4530295	o	o		Reddish-brown	Chert breccia	<1%
477a	558239	4530121	o	o		White	Clay seam	>50%
477b	556239	4530121		o		Reddish-brown	Clay gouge	>50%
478a	558226	4530125	o	o		Light grey	Feldspar porphyry	10-50%
478b	558226	4530125		o		Reddish-brown	Feldspar porphyry	10-50%
479	558228	4530123		o		Light grey	Chert	<1%
480	558239	4530121	o	o		Light grey	Siltstone	1-10%
480a + b	558458	4530052		o		Reddish-brown	Chert	<1%
482	558632	4532710		o		Reddish-brown	Siltstone	1-10%
483	558624	4532649		o		Reddish-brown	Quartzite breccia	<1%
484	558946	4532756	o	o		Light grey	Intrusive	10-50%
485	559958	4533940		o		Light grey	Chert	<1%
486a	560192	4533861	o	o		Light grey	Chert	<1%
486b	560192	4533861		o		Light grey	Chert breccia	<1%
487	557848	4530829	o	o		White	Siltstone	1-10%
488	557848	4530829		o		Light grye	Siltstone	1-10%
489a	557848	4530829		o		Reddish-brown	Chert	<1%

Sample ID	Easting	Northing	XRD	Terraspec	Microprobe	Colour	Lithology	Clay content
489b	557848	4530829		o		Reddish-brown	Chert	<1%
490	557852	4530859		o		Medium grey	Chert	<1%
491	558208	4532389		o		Light grey	Siltstone	1-10%
492	558485	4532221	o	o		Reddish-brown	Quartzite breccia	<1%
493	558490	4532203		o		Dark grey	Mudstone	1-10%
494	558606	4532015		o		Light grey	Siltstone	1-10%
495	558947	4532014	o	o		Light grey	Chert breccia	<1%
496	559154	4531970	o	o	o	Light grey	Sandstone	1-10%
497	559533	4531891		o		Medium grey	Chert	<1%
498	558165	4531821	o	o		Light grey	Intrusive	10-50%
499a	558135	4531803		o		White	Clay seam	>50%
499b	558135	4531803		o		Light grey	siltstone	1-10%
499c	558135	4531803	o	o		Light grey	Clay gouge	>50%
499d	558135	4531803		o		Reddish-brown	Clay gouge	>50%
500	558345	4532871		o		Light grey	Chert	<1%
501	558331	4532954		o		Medium grey	Siltstone	1-10%
502	558335	4532822	o	o	o	Medium grey	Quartzite	<1%
503	558145	4532642		o		Light grey	Quartzite	<1%
504	557477	4533694		o		White	Siltstone	1-10%
505	557243	4533546		o		Whie	Chert	<1%
506	557243	4533546	o	o		Light grey	Silt	Silt
507	557261	4533543	o	o		White	Clay seam	>50%
508	557086	4533408	o	o		Light grey	Mudstone	1-10%
508 b	557086	4533408		o		Medium grey	Intrusive	10-50%
509	557277	4533334	o	o		Dark grey	Lamprophyre	<1%
510a	556352	4530874	o	o		Beige	Clay gouge	>50%
510b	556356	4530870	o	o	o	Beige	Intrusive	10-50%
510c	556371	4530876		o		White	Clay seam	>50%
510d	556374	4530877		o		Light grey	Chert	<1%
510e	556374	4530877		o		Light pink	Siltstone	1-10%
510f	556366	4530872		o		Biege	Intrusive	10-50%
511a	556535	4531050		o		Light grey	Chert	<1%
511b	556535	4531050		o		Light grey	Intrusive	10-50%
511c	556535	4531054	o	o		Medium grey	Cataclasite	>50%
512a	557254	4530909		o		Reddish-brown	Chert breccia	<1%
512b	557266	4530904		o		Reddish-brown	Chert breccia	<1%
513a	557359	4530284		o		White	Clay gouge	>50%
513b	557349	4530282	o	o	o	White	Clay gouge	>50%
513c	557338	4530279	o	o		White	Clay gouge	>50%
514	556944	4530167		o		Reddish-brown	Chert breccia	<1%
515a	556669	4530269		o		Reddish-brown	Chert	<1%
515b	556627	4530448		o		Medium grey	Chert	<1%
516a	557550	4531273		o		Light grey	Clay gouge	>50%
516b	557579	4531311	o	o		Light grey	Clay seam	>50%
516c	557581	4531317		o		Light grey	Clay gouge	>50%
516d	557590	4531333	o	o		Light grey	Clay gouge	>50%
517	557529	4531651		o		Medium grey	Chert	<1%
518	557328	4531670		o		Dark purple	Chert	<1%
519	557245	4531785	o	o		Light grey	Siltstone	1-10%
520a	557243	4531813		o		Reddish-brown	Chert breccia	<1%
520b	557243	4531813		o		Reddish-brown	Chert breccia	<1%
521a	556987	4532927	o	o	o	Reddish-brown	Chert breccia	<1%
521b	557023	4532929		o		Reddish-brown	Chert breccia	<1%
522	557242	4532903		o		Dark grey	Diorite (Vivian Stock)	<1%
523	556555	4532437	o	o		Light grey	Intrusive	10-50%
524a	557416	4530700	o	o		Light grey	Clay gouge	>50%
524b	557409	4530702		o		Light grey	Chert	<1%
524c	557409	4530702		o		Light grey	Chert	<1%
525a + b	557314	4530712	o	o	o	Reddish-brown	Chert breccia	<1%
525c	557295	4530684		o		Light grye	Clay gouge	>50%
525d	557295	4530684		o		White	Clay gouge	>50%
526a	556706	4533887	o	o		White	Siltstone	1-10%
526b	556706	4533887	o	o		Light green	Intrusive	10-50%
526c	556706	4533887		o		White	Clay gouge	>50%
526d	556706	4533887		o		Light green	Intrusive	10-50%

Sample ID	Easting	Northing	XRD	Terraspec	Microprobe	Colour	Lithology	Clay content
527a	556803	4533540		o		White	Clay gouge	>50%
527b	556803	4533540	o	o	o	Reddish-brown	Intrusive	10-50%
528a	557087	4532110	o	o		White	Clay gouge	>50%
528b	557087	4532110		o		White	Clay gouge	>50%
528c	557087	4532110	o	o		Reddish-brown	Chert	<1%
528d	557087	4532100	o	o		Beige	Barite	<1%
529	557468	4531605		o		Light grye	Chert	<1%
530	557704	4530302		o		Light grey	Chert	<1%
UL-18	Leeville	underground	o	o		Beige	Intrusive	>50%
UL-19	Leeville	underground	o	o		Beige	Intrusive	>50%
			n=76	n=459	n=9			

APPENDIX D – X-RAY DIFFRACTION PATTERNS

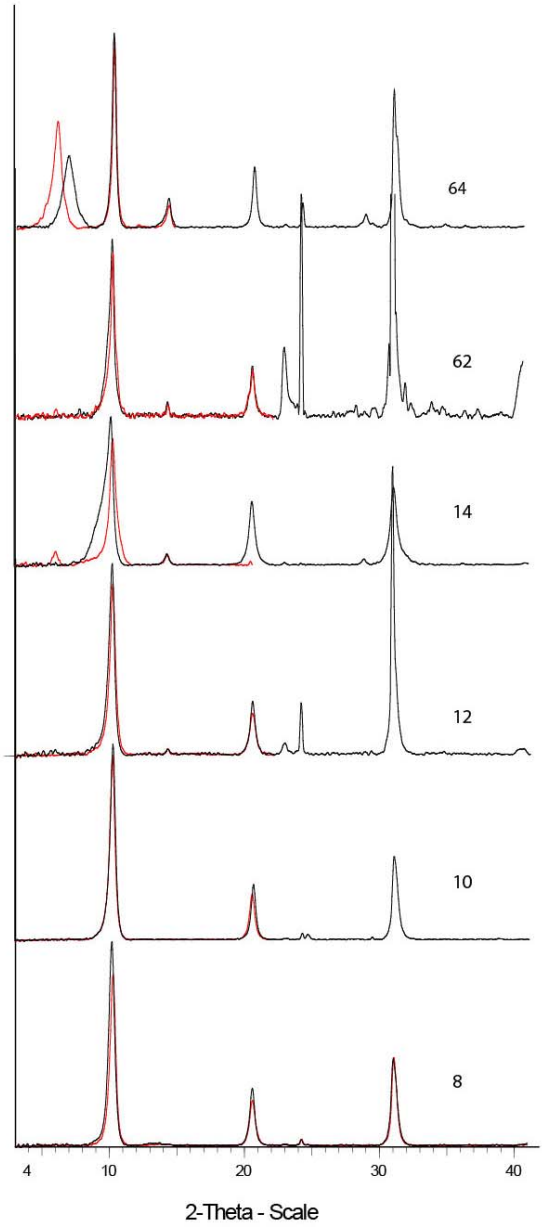

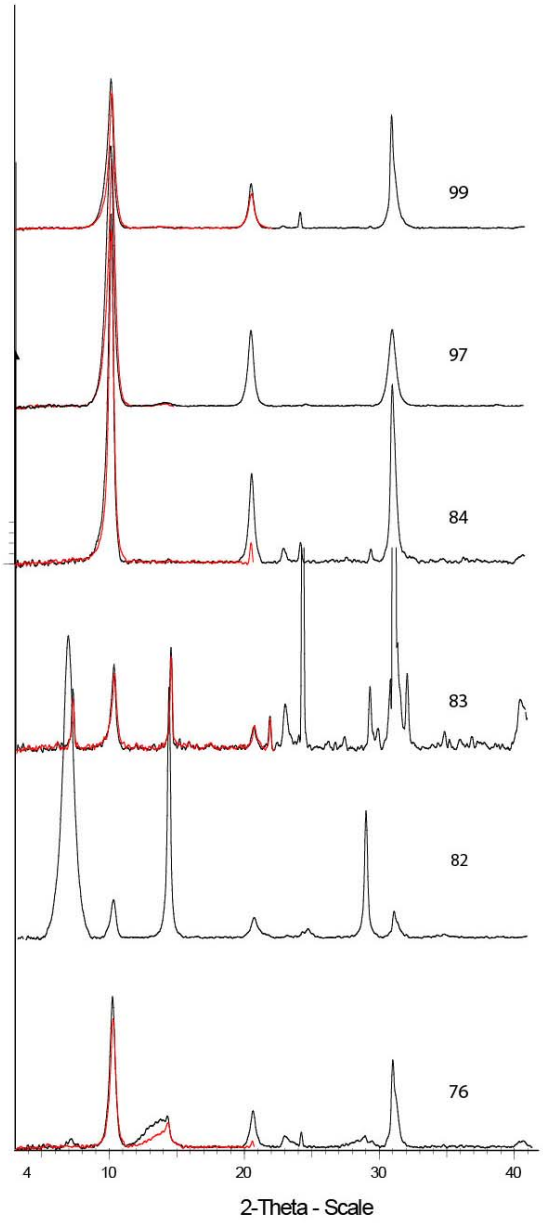

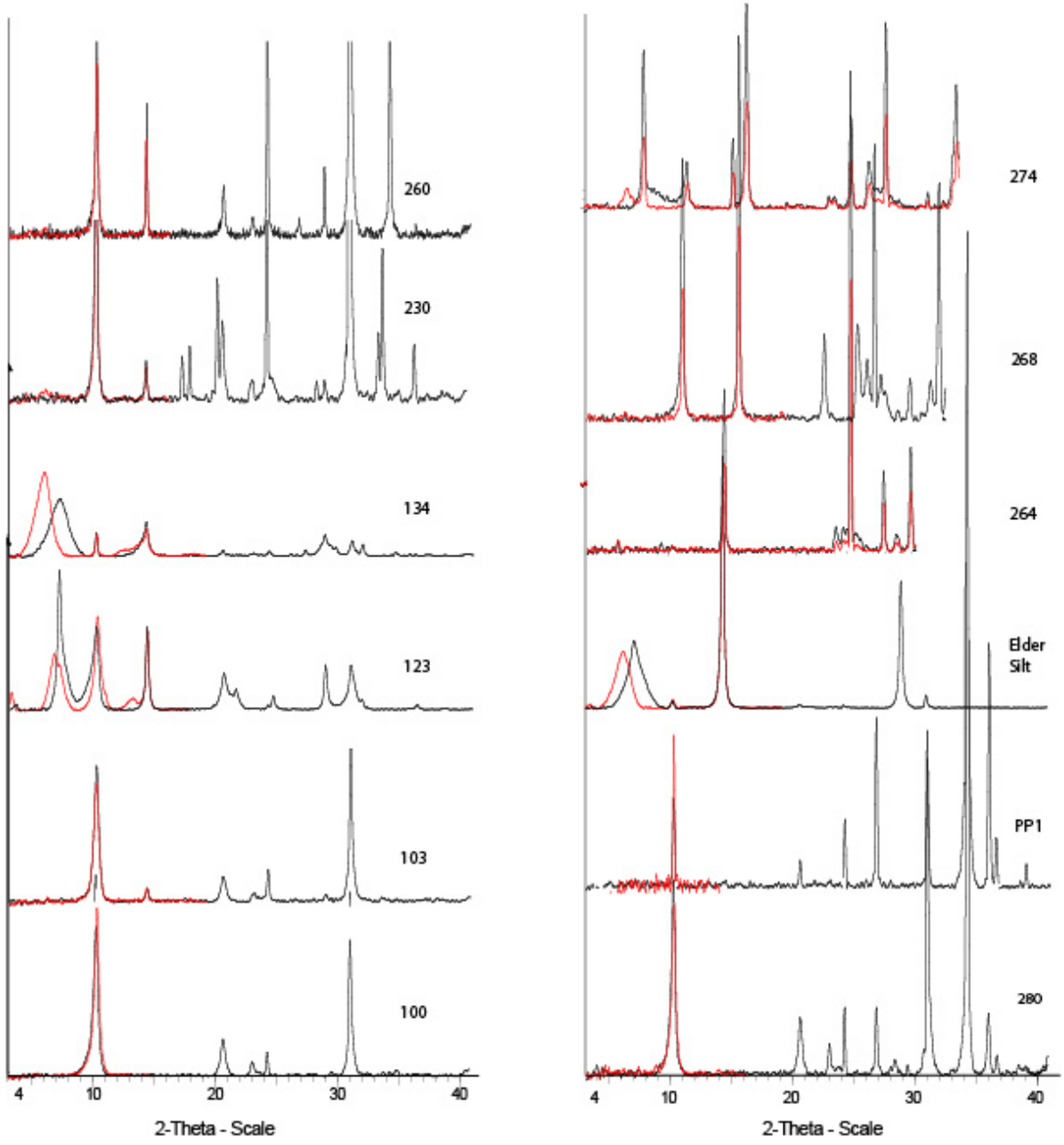
260
230
134
123
103
100
4
10
20
30
40
2-Theta - Scale
274
268
264
Elder
Silt
PP1
280
4
10
20
30
40
2-Theta - Scale

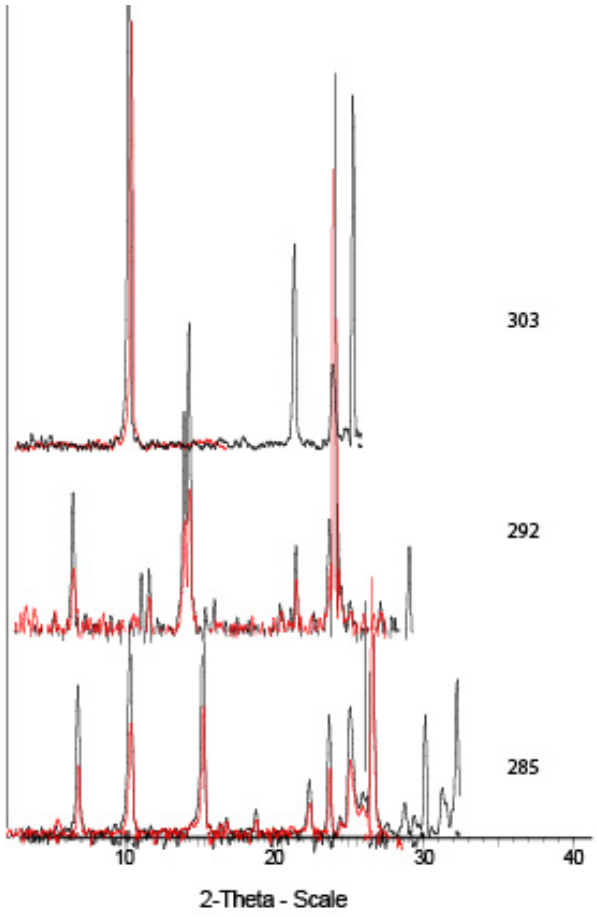
303
292
285
10
20
30
40
2-Theta - Scale

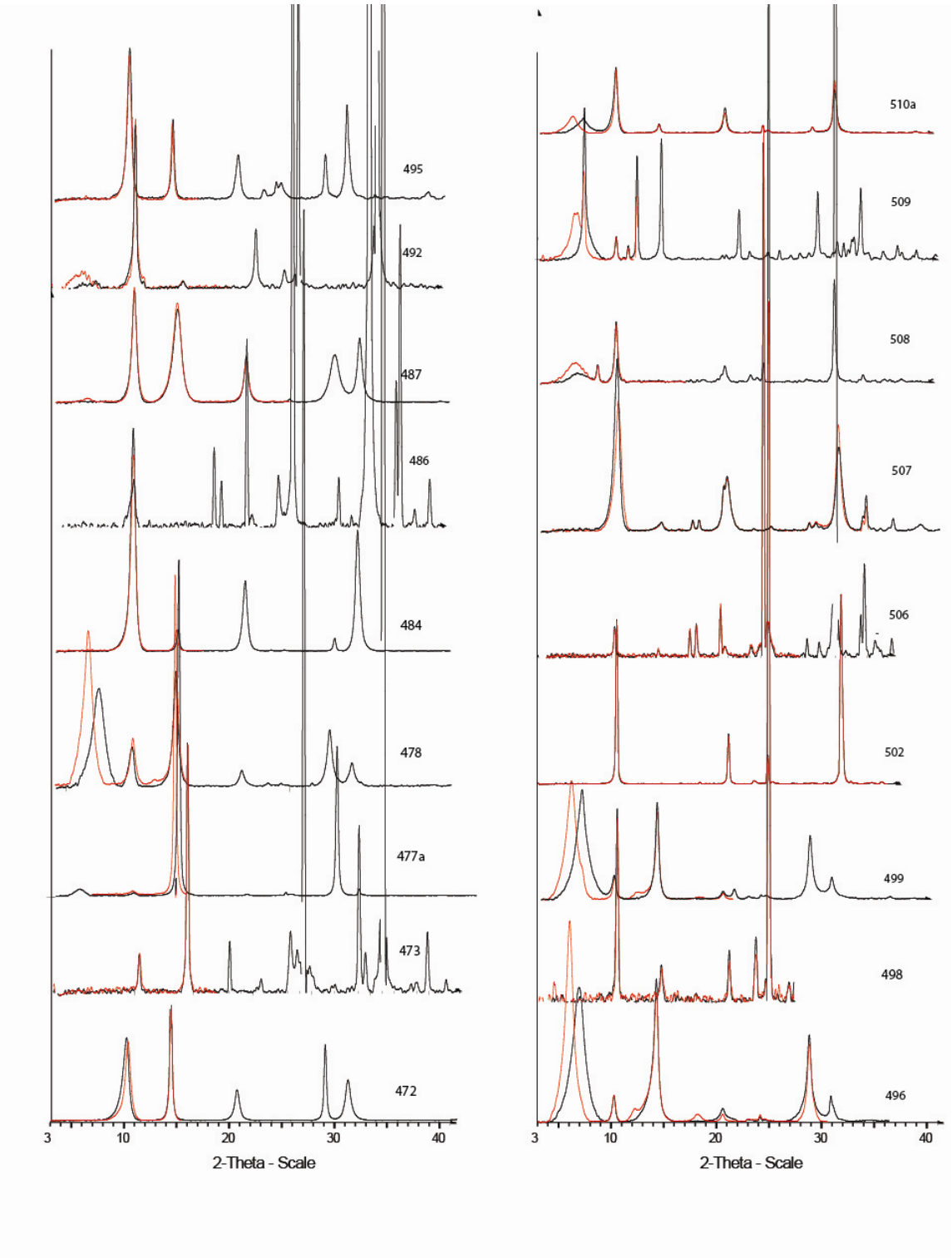
495
492
487
486
484
478
477a
473
472
3
10
20
30
40
2-Theta - Scale
510a
509
508
507
506
502
499
498
496
3
10
20
30
40
2-Theta - Scale

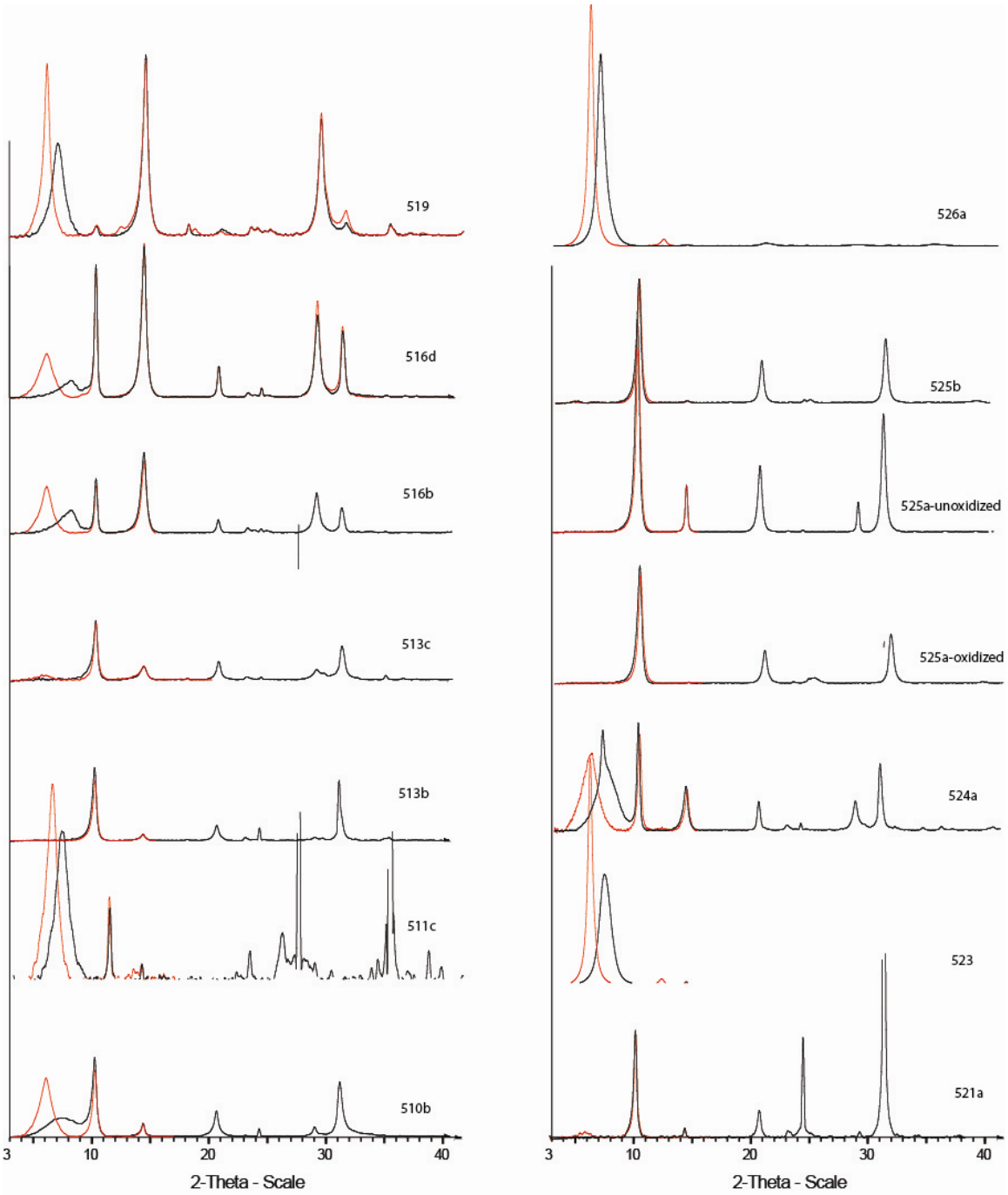
519
516d
516b
513c
513b
511c
510b
3
10
20
30
40
2-Theta - Scale
526a
525b
525a-unoxidized
525a-oxidized
524a
523
521a
3
10
20
30
40
2-Theta - Scale

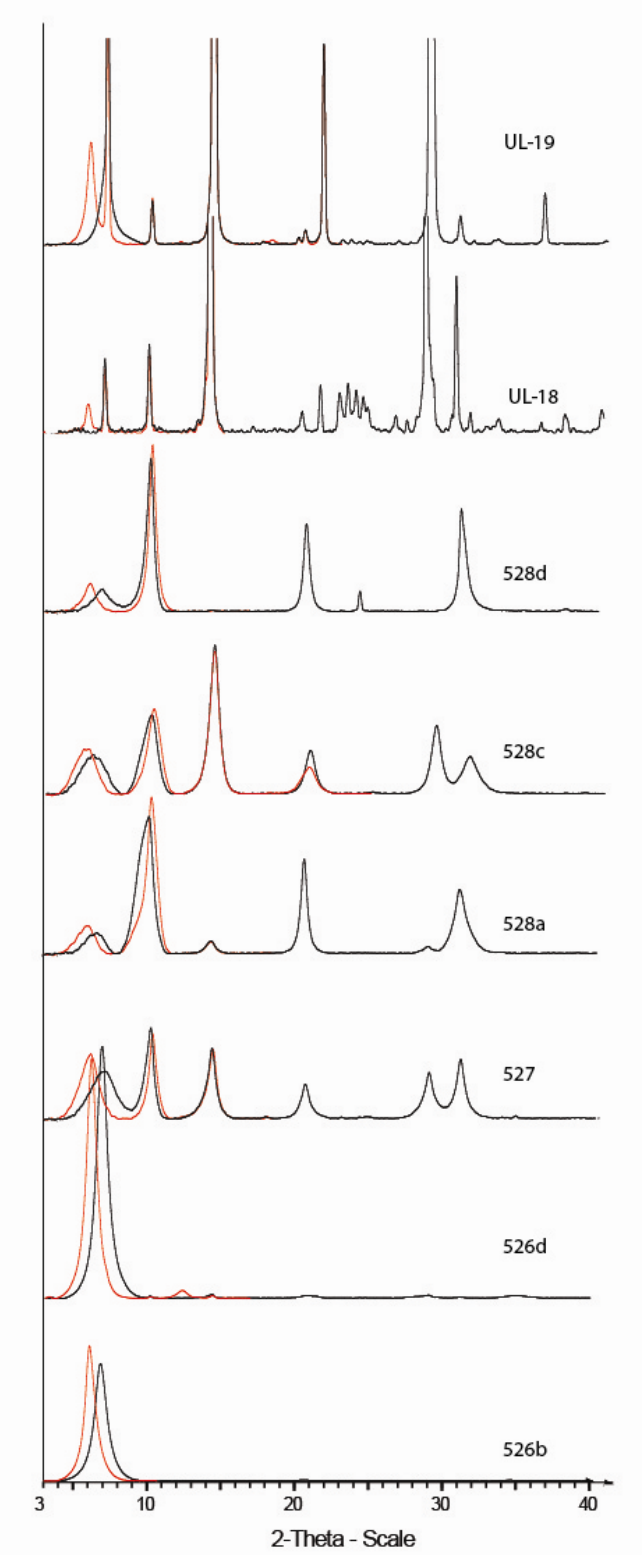
UL-19
UL-18
528d
528c
528a
527
526d
526b
3
10
20
30
40
2-Theta - Scale

APPENDIX E – MICROPROBE DATA

Table E1. Illite microprobe compositional data

Sample	Si	Ti	Al	Cr	Fe	Mn	Mg	Ca	Na	K	Total (%)	K+(Fe-Mg)	T (°C)
525b-1	3.47	0.01	2.27	0.01	0.07	0.01	0.16	0.01	0.01	0.75	75.13	0.85	258.95
525b-2	3.56	0.03	2.04	0.01	0.04	0.00	0.28	0.01	0.01	0.82	88.49	1.05	313.88
525b-3	3.55	0.03	2.07	0.01	0.04	0.00	0.27	0.00	0.01	0.83	86.77	1.06	315.75
525b-4	3.72	0.01	1.92	0.01	0.07	0.00	0.25	0.02	0.01	0.62	76.37	0.80	246.09
525b-5	3.61	0.00	2.11	0.01	0.05	0.00	0.18	0.03	0.01	0.64	71.80	0.77	238.05
525b-6	3.70	0.01	1.98	0.00	0.06	0.00	0.19	0.01	0.01	0.71	76.92	0.83	253.59
525b-7	3.83	0.00	1.85	0.00	0.05	0.00	0.17	0.01	0.01	0.67	75.51	0.79	242.60
525b-8	3.46	0.01	2.27	0.01	0.05	0.00	0.17	0.00	0.01	0.79	77.18	0.91	275.83
525b-9	3.37	0.01	2.38	0.01	0.12	0.00	0.15	0.01	0.01	0.75	81.07	0.79	242.60
525b-10	3.39	0.01	2.35	0.01	0.10	0.00	0.17	0.01	0.01	0.76	82.10	0.82	251.98
525b-11	3.42	0.01	2.35	0.01	0.07	0.00	0.16	0.00	0.03	0.75	79.98	0.84	256.81
525b-12	3.49	0.01	2.25	0.01	0.07	0.00	0.15	0.01	0.01	0.74	80.02	0.82	251.45
525b-13	3.41	0.01	2.33	0.00	0.08	0.00	0.16	0.01	0.05	0.77	77.98	0.86	261.09
525b-14	3.43	0.02	2.26	0.01	0.06	0.01	0.19	0.00	0.06	0.85	74.67	0.98	293.25
525b-15	3.39	0.01	2.34	0.01	0.10	0.00	0.18	0.01	0.02	0.73	78.97	0.82	249.84
525b-16	3.43	0.01	2.30	0.02	0.06	0.00	0.18	0.01	0.01	0.81	56.51	0.92	278.24
525b-17	3.45	0.01	2.30	0.01	0.08	0.00	0.16	0.00	0.01	0.74	80.19	0.82	252.25
525b-18	3.44	0.01	2.31	0.00	0.09	0.00	0.17	0.01	0.01	0.74	78.05	0.81	248.23
525b-19	3.45	0.01	2.29	0.01	0.07	0.00	0.17	0.00	0.01	0.79	77.73	0.88	268.33
525b-20	3.46	0.01	2.27	0.01	0.06	0.00	0.17	0.01	0.01	0.75	81.39	0.86	262.97
525b-21	3.71	0.00	1.95	0.00	0.07	0.00	0.25	0.02	0.00	0.61	72.61	0.80	245.02
525b-22	3.78	0.00	1.82	0.01	0.03	0.00	0.34	0.01	0.02	0.63	80.64	0.94	282.53
525b-23	3.75	0.00	1.87	0.01	0.02	0.00	0.34	0.01	0.00	0.63	81.65	0.95	286.28
525b-24	3.85	0.00	1.72	0.00	0.03	0.00	0.40	0.01	0.00	0.57	85.41	0.94	283.87
525b-25	3.69	0.00	1.94	0.00	0.03	0.00	0.32	0.01	0.01	0.66	76.99	0.94	284.40

Sample	Si	Ti	Al	Cr	Fe	Mn	Mg	Ca	Na	K	Total (%)	K+(Fe-Mg)	T (°C)
525b-26	3.83	0.00	1.76	0.01	0.03	0.00	0.37	0.01	0.01	0.57	80.83	0.90	272.88
525b-27	3.81	0.00	1.78	0.00	0.03	0.00	0.37	0.01	0.03	0.58	81.42	0.92	277.44
525b-28	3.68	0.00	1.98	0.01	0.04	0.00	0.27	0.01	0.01	0.65	79.41	0.88	267.52
525b-29	3.74	0.00	1.88	0.01	0.04	0.00	0.31	0.01	0.00	0.64	73.17	0.92	277.44
525b-30	3.81	0.00	1.79	0.01	0.03	0.00	0.34	0.01	0.00	0.61	80.57	0.91	276.10
525b-31	3.76	0.00	1.84	0.01	0.04	0.00	0.34	0.01	0.00	0.61	77.33	0.91	275.83
525b-32	3.83	0.00	1.74	0.01	0.03	0.00	0.38	0.02	0.00	0.58	82.26	0.93	279.58
525b-33	3.38	0.01	2.37	0.01	0.06	0.01	0.18	0.01	0.01	0.82	75.49	0.94	282.80
525b-34	3.46	0.01	2.27	0.01	0.07	0.00	0.17	0.00	0.01	0.78	75.75	0.88	266.45
525b-35	3.47	0.01	2.26	0.01	0.08	0.00	0.17	0.01	0.01	0.77	73.53	0.86	262.70
525b-36	3.45	0.01	2.27	0.01	0.09	0.00	0.18	0.01	0.03	0.73	73.16	0.82	250.64
525b-37	3.46	0.01	2.27	0.02	0.04	0.00	0.15	0.01	0.01	0.86	77.16	0.97	292.18
525b-38	3.55	0.01	2.16	0.02	0.05	0.01	0.14	0.01	0.00	0.83	79.17	0.93	280.92
525b-39	3.49	0.03	2.15	0.02	0.06	0.00	0.22	0.01	0.01	0.82	82.56	0.97	292.44
525b-40	3.47	0.04	2.19	0.04	0.07	0.00	0.17	0.01	0.01	0.80	81.10	0.89	269.40
525b-41	3.40	0.03	2.16	0.01	0.15	0.00	0.27	0.01	0.01	0.97	84.15	1.09	323.26
525b-42	3.41	0.02	2.21	0.01	0.09	0.00	0.25	0.01	0.01	0.92	82.17	1.08	320.04
525b-43	3.39	0.01	2.24	0.01	0.08	0.00	0.25	0.01	0.01	0.93	85.40	1.10	325.94
525b-44	3.34	0.01	2.39	0.02	0.04	0.00	0.17	0.01	0.01	0.92	87.86	1.05	312.54
525b-45	3.32	0.02	2.30	0.01	0.10	0.00	0.28	0.01	0.02	0.91	79.28	1.09	324.06
502-1	3.19	0.01	2.46	0.00	0.17	0.00	0.28	0.01	0.02	0.90	93.15	1.01	302.89
502-2	3.26	0.00	2.56	0.00	0.10	0.00	0.12	0.00	0.03	0.82	90.02	0.84	257.61
502-3	3.21	0.01	2.62	0.01	0.09	0.00	0.10	0.01	0.03	0.83	90.25	0.84	257.34
502-4	3.16	0.01	2.57	0.00	0.20	0.00	0.15	0.01	0.03	0.89	91.33	0.93	280.39
502-5									0.00		59.96		
502-6	3.18	0.01	2.60	0.00	0.08	0.00	0.17	0.01	0.03	0.91	91.05	1.00	300.21
502-7	3.18	0.00	2.62	0.00	0.09	0.00	0.14	0.02	0.03	0.88	92.45	0.93	281.19
502-8	3.55	0.01	2.21	0.00	0.03	0.00	0.14	0.00	0.01	0.79	93.99	0.90	272.88
502-9	3.10	0.00	2.43	0.00	0.42	0.00	0.24	0.08	0.03	0.78	86.98	0.96	289.50

Sample	Si	Ti	Al	Cr	Fe	Mn	Mg	Ca	Na	K	Total (%)	K+(Fe-Mg)	T (°C)
502-10	3.56	0.04	2.01	0.01	0.11	0.00	0.53	0.00	0.18	0.09	88.39	0.51	167.85
502-11	3.52	0.00	2.14	0.00	0.12	0.00	0.25	0.01	0.02	0.71	90.40	0.85	258.95
502-12	3.19	0.01	2.59	0.00	0.08	0.00	0.15	0.00	0.02	0.95	90.74	1.02	303.97
502-13	3.19	0.00	2.59	0.00	0.16	0.00	0.11	0.00	0.06	0.85	91.45	0.89	270.74
502-14	3.27	0.00	2.51	0.00	0.05	0.00	0.18	0.01	0.02	0.88	93.13	1.01	302.36
502-16	3.20	0.00	2.63	0.00	0.05	0.00	0.15	0.01	0.04	0.87	92.88	0.97	291.10
502-17	3.27	0.01	2.50	0.00	0.04	0.00	0.18	0.01	0.01	0.91	94.13	1.05	312.00
502-18	3.16	0.01	2.59	0.00	0.09	0.00	0.21	0.00	0.06	0.90	92.53	1.01	303.16
502-19	3.15	0.01	2.60	0.00	0.06	0.00	0.23	0.00	0.05	0.91	93.47	1.08	320.31
502-20	3.18	0.01	2.59	0.00	0.07	0.00	0.18	0.01	0.04	0.90	91.81	1.01	301.02
502-21	3.18	0.06	2.51	0.00	0.13	0.00	0.18	0.01	0.06	0.82	89.68	0.87	263.77
502-22	3.28	0.00	2.41	0.01	0.16	0.00	0.22	0.01	0.03	0.84	90.22	0.90	271.54
502-23	3.23	0.01	2.51	0.00	0.06	0.00	0.23	0.00	0.01	0.93	93.46	1.10	325.94
502-24	3.18	0.01	2.55	0.00	0.16	0.00	0.17	0.01	0.03	0.90	91.72	0.92	276.63
502-25	3.22	0.01	2.46	0.00	0.21	0.00	0.19	0.01	0.04	0.88	88.56	0.90	272.08
502-26	3.16	0.00	2.58	0.00	0.20	0.00	0.14	0.01	0.03	0.83	86.74	0.89	269.67
527B-2	3.21	0.00	2.59	0.00	0.01	0.00	0.22	0.00	0.03	0.88	92.94	1.08	321.51
527B-3	3.24	0.04	2.41	0.00	0.03	0.00	0.30	0.00	0.02	0.94	94.88	1.21	355.85
527B-4	3.22	0.01	2.47	0.00	0.08	0.00	0.30	0.02	0.04	0.84	94.20	1.06	316.62
527B-5	3.14	0.01	2.62	0.00	0.05	0.00	0.24	0.01	0.06	0.88	93.65	1.07	316.95
527B-6	3.25	0.03	2.42	0.00	0.03	0.00	0.31	0.00	0.02	0.90	94.92	1.18	347.74
527B-7	3.26	0.02	2.44	0.00	0.03	0.00	0.28	0.00	0.02	0.88	93.00	1.13	334.57
527B-8	3.15	0.02	2.61	0.00	0.04	0.00	0.21	0.00	0.06	0.91	94.68	1.09	323.31
527B-9	3.24	0.03	2.42	0.00	0.03	0.00	0.31	0.00	0.03	0.94	93.08	1.22	358.75
527B-10	3.16	0.03	2.54	0.00	0.04	0.00	0.29	0.00	0.05	0.92	95.36	1.18	347.30
527B-11	3.21	0.01	2.45	0.00	0.06	0.00	0.38	0.01	0.03	0.86	94.07	1.18	347.83

Sample	Si	Ti	Al	Cr	Fe	Mn	Mg	Ca	Na	K	Total (%)	K+(Fe-Mg)	T (°C)
527B-12	3.51	0.02	2.19	0.00	0.04	0.00	0.21	0.00	0.08	0.75	92.77	0.92	279.19
527B-14	3.16	0.01	2.56	0.00	0.04	0.00	0.29	0.01	0.06	0.87	94.61	1.13	334.13
527B-15	3.17	0.02	2.65	0.00	0.02	0.00	0.12	0.00	0.06	0.89	94.26	0.99	297.55
527B-16	3.22	0.00	2.40	0.00	0.10	0.00	0.43	0.01	0.03	0.82	93.83	1.15	340.65
527B-17	3.26	0.01	2.44	0.00	0.08	0.00	0.30	0.01	0.03	0.80	84.08	1.01	303.08
527B-18	3.35	0.01	2.31	0.01	0.10	0.00	0.28	0.02	0.01	0.78	51.87	0.96	288.63
527B-19	3.22	0.00	2.49	0.00	0.05	0.00	0.32	0.01	0.03	0.85	94.70	1.12	330.45
527B-20	3.16	0.02	2.66	0.00	0.02	0.00	0.16	0.01	0.06	0.89	94.87	1.03	307.08
496-1	3.27	0.04	2.39	0.01	0.13	0.00	0.18	0.01	0.03	0.89	94.14	0.94	284.15
496-2	3.26	0.05	2.42	0.00	0.12	0.00	0.16	0.01	0.04	0.87	91.66	0.91	275.08
496-3	3.48	0.02	2.00	0.00	0.33	0.00	0.24	0.01	0.02	0.80	89.77	0.89	270.19
496-4	3.41	0.04	2.15	0.00	0.25	0.00	0.19	0.00	0.02	0.86	91.96	0.92	276.77
496-5	3.43	0.04	2.13	0.00	0.23	0.00	0.20	0.01	0.02	0.81	62.10	0.84	256.46
496-6	3.71	0.05	1.71	0.00	0.26	0.00	0.28	0.01	0.01	0.74	93.33	0.76	234.36
496-7	3.49	0.05	1.88	0.00	0.32	0.00	0.30	0.01	0.01	0.89	93.48	0.90	273.82
496-8	3.23	0.07	2.45	0.00	0.13	0.00	0.11	0.00	0.04	0.91	92.36	0.93	279.75
496-9	3.21	0.07	2.47	0.00	0.14	0.00	0.11	0.00	0.04	0.91	92.44	0.93	281.82
496-10	3.15	0.07	2.57	0.00	0.11	0.00	0.11	0.00	0.04	0.93	94.46	0.93	280.96
496-11	3.20	0.05	2.55	0.00	0.09	0.00	0.12	0.01	0.06	0.85	93.22	0.87	265.84
496-12	3.22	0.02	2.57	0.00	0.09	0.00	0.13	0.01	0.11	0.77	93.70	0.82	249.86
496-13	3.24	0.02	2.46	0.00	0.18	0.00	0.14	0.00	0.05	0.88	93.83	0.92	277.32
496-14	3.13	0.02	2.75	0.00	0.04	0.00	0.06	0.00	0.14	0.80	95.26	0.81	248.84
496-15	3.90	0.02	1.80	0.00	0.05	0.00	0.08	0.00	0.09	0.55	96.54	0.58	187.21
496-16	3.25	0.03	2.43	0.00	0.17	0.00	0.17	0.01	0.04	0.85	93.12	0.85	259.26
496-17	3.26	0.02	2.64	0.00	0.10	0.00	0.12	0.01	0.03	0.49	86.89	0.51	169.14
496-18	4.89	0.01	0.66	0.00	0.04	0.00	0.05	0.00	0.02	0.24	98.99	0.25	97.90
496-19	3.49	0.02	2.19	0.00	0.12	0.00	0.15	0.00	0.06	0.76	94.83	0.79	242.58
496-20	3.55	0.05	2.07	0.00	0.14	0.00	0.15	0.01	0.03	0.78	91.58	0.80	244.57
496-21	3.85	0.02	1.85	0.00	0.08	0.00	0.09	0.00	0.03	0.63	92.17	0.63	200.71

Sample	Si	Ti	Al	Cr	Fe	Mn	Mg	Ca	Na	K	Total (%)	K+(Fe-Mg)	T (°C)
496-22	3.24	0.02	2.56	0.00	0.11	0.00	0.10	0.00	0.03	0.83	91.22	0.83	254.57
496-23	3.14	0.04	2.62	0.00	0.11	0.00	0.12	0.01	0.07	0.87	93.11	0.88	267.74
496-24	3.19	0.02	2.64	0.00	0.07	0.00	0.11	0.00	0.14	0.74	85.51	0.77	238.75
496-25	3.20	0.02	2.62	0.00	0.07	0.00	0.12	0.01	0.14	0.73	92.94	0.78	241.19
496-26	3.80	0.03	1.92	0.00	0.05	0.00	0.06	0.00	0.05	0.62	94.45	0.63	199.81
496-27	3.32	0.01	2.35	0.00	0.20	0.00	0.15	0.01	0.02	0.88	92.97	0.92	277.73
496-28	3.55	0.03	2.04	0.00	0.18	0.00	0.20	0.01	0.02	0.79	92.77	0.81	249.16
496-29	3.35	0.03	2.11	0.00	0.34	0.01	0.25	0.00	0.02	0.93	90.75	1.02	304.23
496-30	3.21	0.02	2.52	0.00	0.13	0.00	0.15	0.01	0.07	0.87	93.69	0.89	270.05
496-31	3.20	0.02	2.56	0.00	0.11	0.00	0.14	0.00	0.08	0.86	94.43	0.89	269.39
496-32	3.47	0.03	2.31	0.00	0.06	0.00	0.06	0.00	0.06	0.77	94.86	0.77	238.16
496-33	3.35	0.03	2.26	0.00	0.21	0.00	0.15	0.00	0.03	0.88	94.09	0.95	284.75
496-34	3.39	0.03	2.41	0.00	0.04	0.00	0.07	0.00	0.20	0.62	93.40	0.65	205.86
496-35	3.15	0.02	2.69	0.00	0.06	0.00	0.09	0.01	0.20	0.72	94.08	0.76	234.53
510a-1	3.69	0.04	1.35	0.01	0.50	0.00	0.90	0.06	0.02	0.07	79.25	0.46	154.88
510a-2	3.86	0.01	1.45	0.00	0.25	0.00	0.72	0.04	0.02	0.10	86.38	0.57	184.64
510a-3	2.89	0.00	1.94	0.00	0.33	0.01	1.87	0.07	0.03	0.04	77.38	1.58	455.47
510a-4	2.93	0.00	2.06	0.00	0.28	0.01	1.67	0.03	0.01	0.09	82.46	1.48	429.15
510a-5	3.76	0.07	1.31	0.01	1.08	0.00	0.18	0.05	0.02	0.10	77.78	1.00	298.65
510a-6	3.21	0.03	0.93	0.00	2.89	0.01	0.13	0.07	0.00	0.04	59.75	2.80	782.84
510a-7	2.87	0.00	1.66	0.00	0.51	0.01	2.17	0.04	0.01	0.11	81.56	1.77	505.35
510a-8	3.28	0.01	2.11	0.00	0.38	0.00	0.77	0.04	0.01	0.13	80.42	0.51	168.15
510a-9	3.74	0.00	1.67	0.00	0.34	0.00	0.59	0.04	0.01	0.07	87.19	0.32	117.85
510a-10	3.20	0.03	0.79	0.00	3.05	0.00	0.15	0.10	0.02	0.09	74.37	3.00	834.23
510a-11	2.72	0.01	1.67	0.00	0.54	0.01	2.39	0.07	0.02	0.07	84.40	1.91	543.66
510a-12	3.26	0.00	2.27	0.00	0.38	0.00	0.62	0.04	0.01	0.03	84.09	0.27	103.41
510a-13	2.95	0.00	1.95	0.00	0.45	0.01	1.62	0.05	0.01	0.06	80.76	1.23	362.12
510a-14	3.04	0.00	2.35	0.00	0.20	0.00	1.14	0.03	0.01	0.02	85.51	0.96	289.06
510a-15	3.61	0.00	1.99	0.01	0.28	0.00	0.29	0.08	0.01	0.23	82.77	0.24	95.32

Sample	Si	Ti	Al	Cr	Fe	Mn	Mg	Ca	Na	K	Total (%)	K+(Fe-Mg)	TT (°C)
510a-16	2.94	0.00	1.76	0.00	0.33	0.01	2.04	0.07	0.04	0.02	83.54	1.73	494.50
510a-17	3.01	0.00	2.23	0.00	0.27	0.00	1.29	0.04	0.01	0.04	85.26	1.06	316.42
510a-18	3.02	0.00	2.06	0.00	0.32	0.00	1.46	0.05	0.02	0.03	82.39	1.18	348.01
510a-19	2.86	0.00	1.81	0.00	0.36	0.01	2.08	0.06	0.02	0.06	85.26	1.78	508.33
510a-20	3.16	0.00	2.01	0.00	0.28	0.01	1.29	0.04	0.01	0.07	86.93	1.08	320.48
513b-1	3.52	0.02	2.14	0.00	0.34	0.01	0.18	0.05	0.01	0.28	74.40	0.44	150.45
513b-2	3.97	0.02	1.64	0.00	0.24	0.00	0.13	0.03	0.01	0.26	81.09	0.38	131.98
513b-3	3.47	0.03	2.20	0.01	0.32	0.00	0.18	0.05	0.02	0.32	71.89	0.46	155.02
513b-4	3.62	0.03	2.03	0.00	0.32	0.00	0.15	0.05	0.01	0.27	55.34	0.44	148.85
513b-5	3.43	0.04	2.24	0.00	0.30	0.00	0.18	0.02	0.01	0.40	76.94	0.53	172.84
513b-6	3.48	0.03	2.20	0.00	0.33	0.00	0.17	0.01	0.01	0.33	84.36	0.49	163.31
513b-7	3.25	0.01	2.66	0.00	0.02	0.00	0.08	0.01	0.06	0.72	58.99	0.78	241.37
513b-8	3.66	0.01	2.16	0.00	0.02	0.00	0.09	0.00	0.06	0.58	49.31	0.66	207.29
513b-9	3.48	0.03	2.18	0.00	0.32	0.00	0.18	0.05	0.01	0.32	70.66	0.46	154.46
513b-10	3.61	0.02	2.06	0.00	0.21	0.00	0.16	0.03	0.02	0.44	76.49	0.50	164.12
513b-11	3.52	0.03	2.13	0.00	0.33	0.01	0.17	0.04	0.01	0.31	73.08	0.46	155.66
513b-12	3.50	0.03	2.17	0.00	0.29	0.00	0.17	0.04	0.02	0.36	73.68	0.48	159.51
513b-13			3.43	0.03	2.25	0.00	0.30	0.00	0.17	0.04	0.01	0.38	75.00
513b-14	3.48	0.03	2.16	0.00	0.36	0.00	0.18	0.05	0.01	0.29	70.39	0.47	156.86
513b-15	3.71	0.03	1.94	0.00	0.19	0.00	0.15	0.02	0.02	0.46	76.14	0.50	165.98
513b-16	3.51	0.03	2.17	0.00	0.22	0.00	0.17	0.03	0.02	0.44	77.97	0.50	164.66
513b-17	3.41	0.04	2.23	0.00	0.39	0.00	0.17	0.04	0.01	0.30	73.99	0.52	170.07
513b-18	3.71	0.03	1.93	0.00	0.23	0.00	0.14	0.04	0.02	0.41	54.59	0.51	168.12
513b-19	3.43	0.03	2.18	0.00	0.42	0.00	0.17	0.04	0.02	0.31	74.64	0.56	182.52
513b-20	3.42	0.02	2.27	0.00	0.27	0.00	0.17	0.04	0.02	0.43	84.04	0.53	173.87
513b-21	3.47	0.03	2.16	0.00	0.34	0.00	0.19	0.05	0.01	0.34	63.63	0.49	162.52
513b-22	4.15	0.02	1.47	0.00	0.21	0.00	0.11	0.04	0.01	0.23	81.32	0.33	119.86
513b-23	3.73	0.03	1.92	0.00	0.26	0.00	0.13	0.04	0.01	0.33	77.54	0.45	151.59
513b-24	3.40	0.03	2.26	0.00	0.37	0.01	0.16	0.05	0.01	0.31	70.02	0.53	173.24

Sample	Si	Ti	Al	Cr	Fe	Mn	Mg	Ca	Na	K	Total (%)	K+(Fe-Mg)	T (°C)
521a-1	3.22	0.02	2.38	0.02	0.06	0.00	0.38	0.00	0.02	0.95	90.62	1.27	372.78
521a-2	3.26	0.02	2.34	0.02	0.07	0.00	0.34	0.01	0.02	0.94	89.05	1.21	356.54
521a-3	3.41	0.13	2.08	0.02	0.05	0.00	0.29	0.01	0.02	0.81	93.57	1.05	313.85
521a-4	3.49	0.04	2.10	0.03	0.05	0.00	0.24	0.00	0.02	0.87	91.76	1.06	314.25
521a-5	3.37	0.02	2.21	0.02	0.09	0.01	0.29	0.02	0.03	0.89	88.52	1.10	326.26
521a-6	3.37	0.05	2.32	0.01	0.11	0.00	0.13	0.03	0.03	0.77	87.29	0.79	242.10
521a-7	3.26	0.03	2.30	0.02	0.09	0.01	0.34	0.00	0.03	0.98	87.73	1.23	362.17
521a-8	3.16	0.02	2.41	0.01	0.12	0.01	0.42	0.01	0.03	0.92	93.70	1.23	360.33
521a-9	3.16	0.01	2.47	0.01	0.08	0.00	0.39	0.01	0.04	0.89	93.96	1.19	351.37
521a-10	3.16	0.00	2.44	0.01	0.15	0.00	0.39	0.01	0.04	0.86	92.73	1.11	328.60
521a-11	3.27	0.01	2.31	0.01	0.10	0.01	0.42	0.01	0.03	0.84	94.52	1.16	341.23
521a-12	3.17	0.01	2.43	0.01	0.09	0.00	0.40	0.01	0.03	0.91	91.78	1.22	357.90
521a-13	3.17	0.01	2.45	0.01	0.09	0.00	0.39	0.00	0.04	0.90	94.38	1.20	354.10
521a-14	3.19	0.02	2.35	0.02	0.18	0.00	0.34	0.01	0.04	0.94	90.04	1.11	327.77
521a-15	3.20	0.02	2.40	0.01	0.11	0.00	0.34	0.00	0.03	0.94	92.55	1.17	345.14
521a-16	3.12	0.00	2.44	0.00	0.10	0.00	0.49	0.01	0.03	0.92	94.12	1.31	383.81
521a-17	3.41	0.01	2.13	0.01	0.09	0.00	0.43	0.01	0.03	0.78	92.98	1.12	332.77
521a-18	3.16	0.01	2.40	0.01	0.10	0.00	0.47	0.01	0.03	0.90	92.32	1.28	373.45
521a-19	3.19	0.01	2.39	0.01	0.09	0.00	0.43	0.01	0.03	0.89	91.21	1.23	361.09
521a-20			3.21	0.03	2.31	0.01	0.13	0.01	0.40	0.02	0.03	0.92	91.43
521a-21	3.17	0.01	2.40	0.01	0.14	0.00	0.41	0.02	0.03	0.89	92.54	1.16	342.77
521a-22	3.21	0.01	2.31	0.01	0.19	0.00	0.42	0.03	0.03	0.84	92.55	1.07	319.26
AKS-8-1	3.55	0.00	2.20	0.00	0.05	0.00	0.16	0.03	0.05	0.65	88.72	0.76	234.61
AKS-8-2	3.47	0.00	2.33	0.00	0.03	0.00	0.12	0.03	0.05	0.69	86.47	0.78	240.44
AKS-8-3	3.26	0.00	2.71	0.00	0.01	0.00	0.06	0.01	0.02	0.63	86.92	0.68	214.92
AKS-8-4	3.29	0.01	2.59	0.00	0.03	0.00	0.11	0.01	0.02	0.71	84.75	0.80	246.16
AKS-8-5	3.24	0.01	2.62	0.00	0.05	0.00	0.08	0.02	0.05	0.75	92.79	0.78	241.65
AKS-8-6	4.01	0.01	1.60	0.00	0.07	0.00	0.15	0.07	0.10	0.45	74.78	0.53	173.99
AKS-8-7	3.28	0.02	2.54	0.00	0.03	0.00	0.14	0.02	0.02	0.78	92.10	0.89	269.87

Sample	Si	Ti	Al	Cr	Fe	Mn	Mg	Ca	Na	K	Total (%)	K+(Fe-Mg)	T (°C)
AKS-8-8	3.52	0.02	2.13	0.00	0.15	0.00	0.24	0.03	0.03	0.58	74.21	0.67	211.79
AKS-8-9	3.52	0.02	2.12	0.00	0.16	0.00	0.25	0.02	0.02	0.58	81.81	0.67	210.94
AKS-8-10	3.51	0.02	2.14	0.00	0.15	0.00	0.25	0.02	0.02	0.62	81.15	0.72	224.53
AKS-8-11	3.50	0.02	2.14	0.00	0.17	0.00	0.25	0.03	0.02	0.58	80.02	0.66	209.14
AKS-8-12	3.51	0.03	2.12	0.00	0.17	0.00	0.24	0.03	0.01	0.59	82.20	0.67	210.47
AKS-8-13	3.37	0.10	2.31	0.00	0.10	0.00	0.16	0.02	0.02	0.60	80.99	0.66	209.12
AKS-8-14	3.37	0.01	2.39	0.00	0.05	0.00	0.21	0.02	0.02	0.73	90.72	0.89	268.83
AKS-8-15	3.21	0.00	2.73	0.00	0.01	0.00	0.06	0.02	0.02	0.72	93.04	0.77	238.25
AKS-8-16	3.23	0.00	2.74	0.00	0.01	0.00	0.06	0.02	0.03	0.66	91.07	0.71	222.52
AKS-8-17	3.37	0.00	2.53	0.00	0.02	0.00	0.07	0.03	0.06	0.62	89.03	0.67	210.56
AKS-8-18	3.41	0.00	2.48	0.00	0.02	0.00	0.07	0.04	0.06	0.58	87.65	0.63	200.40
PP1-1	3.20	0.02	2.47	0.00	0.01	0.00	0.36	0.03	0.03	0.91	94.59	1.26	368.90
PP1-2	3.13	0.02	2.44	0.00	0.01	0.00	0.45	0.08	0.04	0.90	92.98	1.34	391.10
PP1-3	3.18	0.02	2.46	0.01	0.02	0.00	0.40	0.02	0.05	0.89	92.05	1.28	373.18
PP1-4	3.18	0.02	2.51	0.00	0.01	0.00	0.33	0.02	0.05	0.91	93.06	1.23	361.69
PP1-5	3.16	0.02	2.46	0.01	0.02	0.00	0.44	0.02	0.03	0.91	93.14	1.33	386.96
PP1-6	3.18	0.01	2.49	0.00	0.02	0.00	0.39	0.02	0.03	0.90	93.43	1.27	371.25
PP1-7	3.16	0.02	2.49	0.00	0.02	0.00	0.39	0.02	0.03	0.91	93.74	1.28	375.61
PP1-8	2.87	0.01	2.30	0.01	0.02	0.00	0.64	0.72	0.03	0.78	82.29	1.40	405.32
PP1-9	3.17	0.01	2.44	0.01	0.01	0.00	0.38	0.14	0.04	0.85	92.98	1.21	356.74
PP1-10	3.20	0.01	2.50	0.00	0.02	0.00	0.32	0.02	0.03	0.89	88.46	1.20	352.53
PP1-11			3.45	0.01	2.24	0.00	0.01	0.00	0.31	0.01	0.01	0.78	94.87
PP1-12	3.41	0.00	2.29	0.00	0.01	0.01	0.30	0.01	0.01	0.80	93.70	1.10	325.14
PP1-13	3.28	0.01	2.42	0.00	0.01	0.00	0.24	0.16	0.01	0.76	92.68	0.99	296.60
PP1-14	3.22	0.00	2.30	0.00	0.01	0.00	0.25	0.50	0.01	0.70	89.60	0.94	284.04
PP1-15	3.13	0.01	2.47	0.00	0.00	0.00	0.29	0.31	0.03	0.82	90.28	1.11	327.58
PP1-16	3.18	0.01	2.48	0.00	0.01	0.00	0.36	0.07	0.03	0.87	93.88	1.22	358.37
PP1-17	3.15	0.01	2.70	0.00	0.01	0.00	0.22	0.15	0.02	0.49	89.49	0.70	219.99
PP1-18	3.20	0.01	2.50	0.00	0.01	0.00	0.33	0.02	0.03	0.89	94.06	1.21	355.84

Sample	Si	Ti	Al	Cr	Fe	Mn	Mg	Ca	Na	K	Total (%)	K+(Fe-Mg)	T (°C)
PP1-19	3.23	0.01	2.42	0.00	0.02	0.00	0.38	0.02	0.03	0.86	94.58	1.23	359.74
PP1-20	3.17	0.02	2.46	0.00	0.01	0.00	0.43	0.03	0.03	0.90	94.44	1.31	382.97
PP1-21	3.19	0.02	2.46	0.00	0.01	0.00	0.40	0.03	0.04	0.88	92.67	1.26	368.53
PP1-22	3.18	0.02	2.48	0.00	0.01	0.00	0.40	0.02	0.04	0.85	92.25	1.24	364.48
PP1-23	3.19	0.01	2.41	0.01	0.02	0.00	0.48	0.01	0.04	0.85	92.47	1.32	383.83
PP1-24	3.17	0.02	2.45	0.00	0.01	0.00	0.45	0.03	0.05	0.88	93.17	1.31	382.74
PP1-25	3.21	0.01	2.41	0.01	0.01	0.00	0.44	0.03	0.03	0.87	93.13	1.29	376.90
97-1	3.32	0.00	2.50	0.00	0.06	0.00	0.13	0.01	0.02	0.78	89.93	0.86	260.65
97-2	3.36	0.00	2.41	0.00	0.08	0.00	0.17	0.01	0.02	0.78	93.12	0.87	264.69
97-3	3.30	0.00	2.45	0.00	0.17	0.00	0.11	0.00	0.03	0.82	94.15	0.88	267.24
97-4	3.38	0.00	2.40	0.00	0.05	0.00	0.17	0.02	0.02	0.78	93.54	0.90	273.12
97-5	3.34	0.01	2.38	0.00	0.11	0.00	0.19	0.01	0.03	0.81	90.48	0.88	268.59
97-6	3.33	0.00	2.32	0.00	0.18	0.00	0.20	0.01	0.03	0.88	91.90	0.90	272.33
97-7	3.33	0.00	2.40	0.00	0.11	0.00	0.17	0.01	0.03	0.81	92.33	0.88	266.27
97-8	3.24	0.00	2.64	0.00	0.04	0.00	0.08	0.01	0.02	0.80	94.46	0.84	256.81
97-9	3.35	0.01	2.43	0.00	0.09	0.00	0.15	0.01	0.01	0.78	88.77	0.84	256.35
97-10	3.32	0.01	2.43	0.00	0.11	0.00	0.15	0.01	0.02	0.82	79.59	0.86	261.17
97-11	3.35	0.00	2.35	0.00	0.15	0.00	0.19	0.01	0.03	0.84	93.66	0.89	269.08
97-12	3.28	0.00	2.52	0.00	0.11	0.00	0.11	0.01	0.03	0.81	93.31	0.82	249.85
97-13	3.33	0.01	2.39	0.00	0.13	0.00	0.17	0.00	0.03	0.82	84.62	0.86	261.65
97-14	3.39	0.00	2.37	0.00	0.09	0.00	0.17	0.01	0.02	0.77	93.39	0.85	259.10
97-15	3.28	0.01	2.44	0.00	0.13	0.00	0.17	0.01	0.04	0.87	94.08	0.91	275.34
97-16	3.32	0.00	2.42	0.00	0.12	0.00	0.16	0.01	0.02	0.84	92.30	0.88	266.61
97-17			3.30	0.01	2.49	0.00	0.09	0.00	0.13	0.01	0.02	0.81	94.71
97-18	3.29	0.01	2.48	0.00	0.09	0.00	0.15	0.02	0.03	0.84	92.70	0.90	272.20
97-19	3.23	0.00	2.57	0.00	0.13	0.00	0.09	0.00	0.02	0.90	94.67	0.94	284.33
97-20	3.31	0.00	2.44	0.00	0.13	0.00	0.14	0.00	0.03	0.83	94.33	0.84	257.70
97-21	3.31	0.01	2.47	0.00	0.08	0.00	0.15	0.01	0.02	0.81	94.29	0.88	267.30
97-23	3.23	0.01	2.59	0.00	0.11	0.00	0.09	0.00	0.02	0.86	94.65	0.89	268.74

Sample	Si	Ti	Al	Cr	Fe	Mn	Mg	Ca	Na	K	Total (%)	K+(Fe-Mg)	T (°C)
97-24	3.36	0.00	2.41	0.00	0.06	0.00	0.18	0.01	0.01	0.79	94.27	0.90	273.09
97-25	3.33	0.01	2.46	0.00	0.06	0.00	0.15	0.01	0.02	0.80	92.98	0.89	268.87
97-26	3.31	0.00	2.52	0.00	0.04	0.00	0.13	0.01	0.02	0.77	89.74	0.86	262.63
97-27	3.31	0.01	2.38	0.00	0.13	0.00	0.20	0.01	0.02	0.84	84.01	0.91	275.95

APPENDIX F - ISOTOPIC VARIATION BETWEEN LITHOLOGICAL FORMATIONS

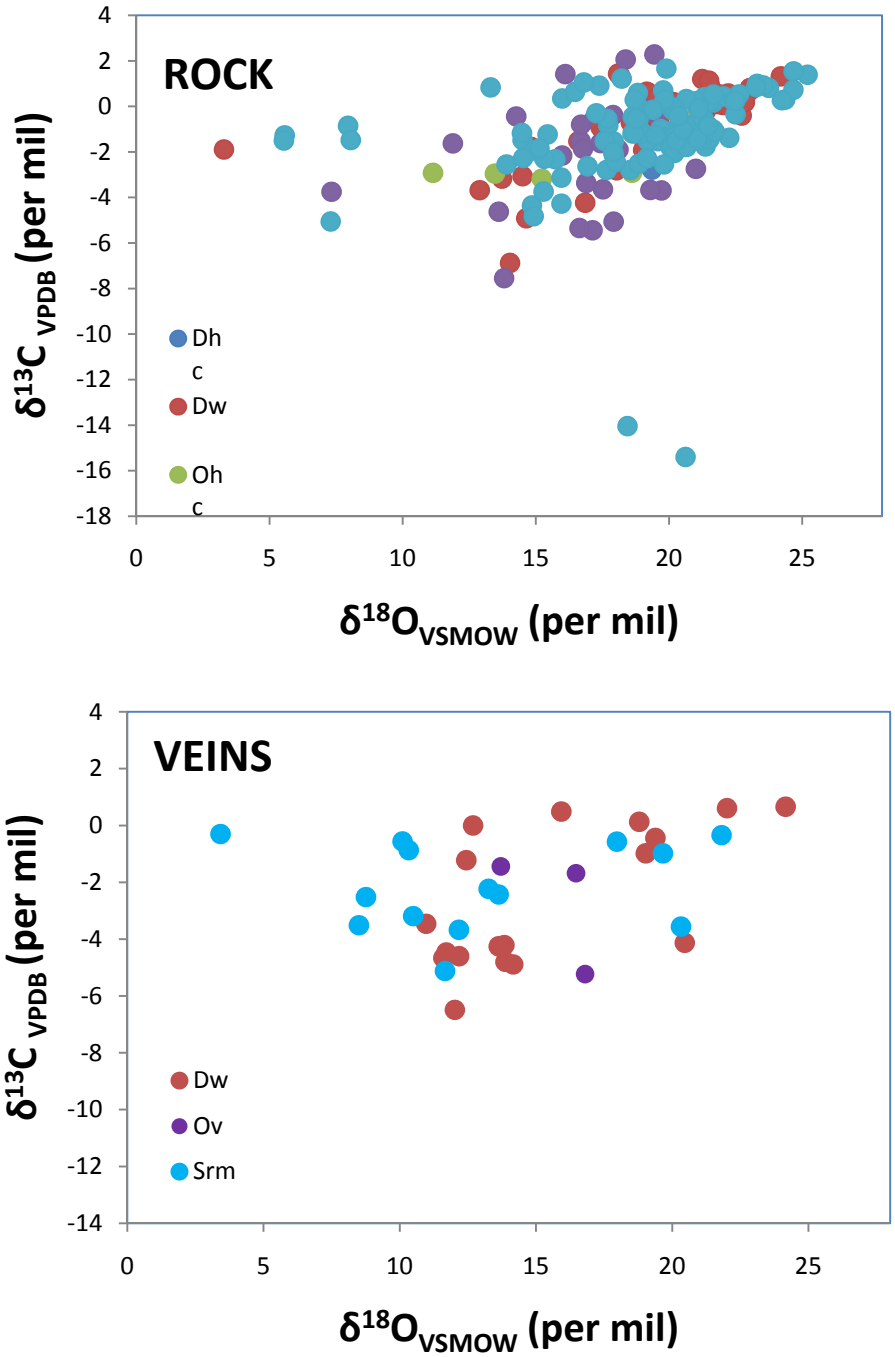

Fig. F1. Graph showing the stable isotope value of rock samples. Colours indicate different rock formations. Ordovician Valmi Formation does not show values any higher than 21 per mil, however this is within range of lower Paleozoic carbonate isotope values described by table 1. There is no apparent correlation between stratigraphic formation and stable isotope composition of rock samples.